BIOPHYSICAL PROPERTIES AND GENE EXPRESSION PROFILE OF SINGLE PERIAQUEDUCTAL GRAY NEURONS

DISSERTATION
submitted in partial fulfilment
of the requirements for the degree of
Doctor of Philosophy
in Neuroscience

by
Oriol Pavón Arocas

Sainsbury Wellcome Centre for Neural Circuits and Behaviour
University College London

London, March 2022

PREFACE

I, Oriol Pavón Arocas, confirm that the work presented in this thesis is my own. Where information has been derived from other sources, I confirm that this has been indicated in the thesis.

All the work described in this thesis was carried out at the Sainsbury Wellcome Centre for Neural Circuits and Behaviour – University College London, under the supervision of Professor Tiago Branco. This dissertation is my own work and contains nothing which is the outcome of work done in collaboration with others except as specified in the text and summarised in the Statement of Contributions.

This dissertation is not substantially the same as any that I have submitted, or is being concurrently submitted, for a degree or diploma or other qualification at University College London or any other University or similar institution except as declared in the Preface and specified in the text. It does not exceed 100,000 words, including footnotes, tables, and figures but excluding bibliography, appendices, and supporting data.

Oriol Pavón Arocas

March 2022

ACKNOWLEDGEMENTS

The work presented in this thesis would not have been possible without the help of a myriad of extraordinary people, to whom I am indebted. I would like to start by thanking my supervisor, Tiago Branco, for having the door open whenever I needed it, for helping me cut through the weed to find a way forward when I got stuck, and for giving me the freedom to carve my own path. I would also like to thank David Attwell, Sarah-Jayne Blakemore, Alasdair Gibb, and Patricia Salinas, the committee of the UCL Wellcome 4-year PhD Programme in Neuroscience, for their trust, their mentoring, and for offering me the opportunity to embark on this journey in the first place. I am also grateful to the funders for supporting and ultimately enabling this project. This work was funded by a UCL Wellcome 4-year PhD Programme in Neuroscience Fellowship (203729/Z/16/Z) (to Oriol Pavón Arocas) and by a Wellcome Senior Research Fellowship (214352/Z/18/Z) and a Sainsbury Wellcome Centre Core Grant from the Gatsby Charitable Foundation and Wellcome (090843/F/09/Z) (to Tiago Branco).

I wouldn't have been able to complete a single one of my experiments without the support of my fantastic colleagues in the Branco Lab, the Sainsbury Wellcome Centre, and the wider Neuroscience community. First and foremost, to Yiota Iordanidou, for being the pillar upon which so much of what happens in the lab stands on. Thank you for your unwavering help, the lunchtime chats and laughs, and your friendship. To Kostas Betsios, for programming the software I used for data acquisition and for helping me troubleshoot and upgrade it when the experiments required. To Philip Shamash and Federico Claudi, for creating SHARP-Track and Brainrender and for helping me use them to register the hundreds of PAG images I acquired during my project. To the fellow patch-clamp initiates that selflessly shared the hard-won secrets of our trade: Yaara Lefler, Yu Lin Tan, Simon Weiler, Mateo Vélez-Fort, Sara Mederos, Hedi Young, Nicolas Wanaverbecq, Annalisa Scimemi,

Christian Madry, Diogo Pimentel, Maarten Kole, Marko Popovic, Arne Battefeld, Mustafa Hamada, and many others in the virtual world and in the real one. To the instructors, TAs, and fellow patch-clamp enthusiasts in the 2019 CSHL Ion Channels Course, thank you for teaching me so much and for making it the best experience of my PhD. To everyone that helped me see the transcriptomics project from a vague sketch of a plan to completion, I couldn't have done it without you: Sarah Olesen, Yoh Isogai, Petr Znamenskyi, Yiota Iordanidou, Mathew Edwards, Molly Strom, Jonny Kohl, Miguel Branco, Eirinn Mackay, Joaquin Rapela, the instructors of the 2019 EBI-EMBL RNA-sequence Analysis course, and the wonderful Bioconductor and scRNA-seq online community. Last but definitely not least, to the MSc students I have had the privilege to supervise on their projects: Sarah Olesen, Lucille Duquenoy, and Tinya Chang – I hope I managed to pass on at least a fraction of the number of things I learned from you.

I was incredibly lucky to work with and be able to count with the support of the professional and scientific staff at the Sainsbury Wellcome Centre. To the NRF staff, past and present, for taking such good care of our animals. To the past and current SWC Lab Managers, Yanai Duran, Kristina Britchford, and Eve McLoughlin, for ensuring everything run as it was supposed to. To the Stores magicians Ian Blaney and Jake Roberts, who pulled out some amazing tricks to ensure I had everything I needed to succeed in my experiments. I will neither confirm nor deny this, but rumour has it they have been spotted conjuring Thorlabs treats out of thin air (and making them disappear even faster). In all seriousness, thank you both for your incredible support and for the shared smiles. To the FabLabs heroes Robb Barrett and Del Halpin, who showed me again and again that Fab stands for fabulous. I very much doubt anyone can come up with a challenge you and your team can't solve. Thank you for turning my poorly described ideas into reality. To the IT crowd and, in particular, the late Richard Bennet, for always finding a solution while generously sharing more knowledge that I could absorb. To Alexandra Boss and Brian Fenelon, for helping me navigate the intricacies of the convoluted world of grants and finances. To the incredible Karen Fergus, for being a force of nature and making so many things

happen, from attending to conferences and courses, to PhD retreats and in-house events.

We don't always have the power to choose our companions and those who sit by our side, but I couldn't have chosen better desk mates if I had tried. To Federico Claudi, for literally being always by my side, for answering my thousand and one questions about coding, and for reminding me there is nothing we can't learn if we set our mind to it. It's been a pleasure to grow with you. To Yaara Lefler, for constantly gifting me the benefit of a different perspective, for sharing the expertise of a seasoned electrophysiologist, and for reminding me of the things that truly matter when I got lost. To Dario Campagner, thank you for being the Gandalf of our little Shire, and for always sharing your wisdom when I needed it most. So much of what I wrote here would not have been possible without your help and stimulating discussions. Let the GABA stay closed and the boundaries of the PAG be wherever you want them to be.

And because there is more to life than science, I wanted to thank the friends that kept me sane through it all. To all the fellow judokas I have had the privilege to train with at the University of London Judo Club, for all the throws, the laughs, the crunches and muscle pain, the competitions, and for the weekly reminder to keep standing up whenever we fall. To the First Floor Fish and Friends Football Club, for all the kickabouts, the goals, and for keeping the fun going when things were tough. To Gonçalo Ferreira, the Ping Pong Lord Supreme, for all the games we played in the sun, in the rain, and in the cold, dark winter. Thank you for being an amazing friend, and for letting me win a couple of times.

This thesis is the culmination of a journey that started way before my joining the SWC and even my moving to London and starting the PhD. One of the greatest benefits of having followed science across different countries has been the opportunity to meet inspiring people wherever I have gone, many of whom I have the privilege to call friends. To the amazing mentors, friends, and colleagues I have had over the years, you have been a constant source of inspiration: Jason Rihel, Sabine Reichert, Declan Lyons, Anya Suppermpool, Shannon Shibata, Marcus Ghosh, Joanna Lau, and Paride

Antinucci; Christian Madry, Ross Nortley, and Nils Korte; Diogo Pimentel and Michael Song; Boris Chagnaud, Andreas Genewsky, and Carsten Wotjak; Marko Popovic, Arne Battefeld, and Mustafa Hamada. And in particular to Ksenia Yashina, Vilim Štih, Judita Huber, Elena Dragomir, Jaime Eugenín, and the Biomed gang for proving throughout the years that our friendship has no borders.

Finally, I would like to thank my family, for I wouldn't have made it without your support. To my parents, for guiding me, trusting me, and letting me spread my wings to find my own path. An especially heartfelt thank you to el meu avi, Benvi, who left us last Christmas: gràcies per tot el que m'has ensenyat. And above all, to Marta, for lifting me up, pushing me forward, and carrying me up to el Mont del Fat when I faltered.

To that curious entity that kindles a child to keep asking but why?

May its flame never extinguish.

May its light guide us as we grow.

THE PROBLEM

"It's the questions we can't answer that teach us the most. They teach us how to think. If you give a man an answer, all he gains is a little fact. But give him a question and he'll look for his own answers."

— Patrick Rothfuss, The Wise Man's Fear

"I think the problem, to be quite honest with you, is that you've never actually known what the question is." […] "So once you do know what the question actually is, you'll know what the answer means."

– Deep Thought. Douglas Adams, The Hitchhiker's Guide to the Galaxy

THE PLAN

"The mice will see you now"

– Douglas Adams, The Hitchhiker's Guide to the Galaxy

*"Huh… What the hell just happened? For real? … but how? Oh, for f***'s sake!"*

– Overheard at a patch-clamp rig.

"No plan survives contact with the enemy"

– Helmut von Moltke The Elder (quoted by Joshua Schimel, Writing Science)

THE SOLUTION

"That's very good thinking, you know. […] Hey, kid, you just saved our lives, you know that?"

"Oh," said Arthur, "well, it was nothing really…"

"Was it?" said Zaphod. "Oh well, forget it, then. OK, computer, take us in to land."

"But …"

"I said forget it."

– Douglas Adams, The Hitchhiker's Guide to the Galaxy

ABSTRACT

The midbrain periaqueductal gray (PAG) is a longitudinal columnar structure where instinctive behaviours as diverse as escaping from predators, vocalising, and pup grooming segregate onto distinct anatomical subdivisions. This parallel between behaviour and brain circuit anatomy provides a unique opportunity for investigating how neural mechanisms support the computation of different adaptive actions. In this work, I aimed to characterise the biophysical properties and gene expression profile of single neurons across PAG subdivisions.

First, I used loose-seal cell-attached and whole-cell patch-clamp recordings to characterise the biophysical properties of PAG neurons in acute midbrain slices of transgenic mice. I found that, even in the absence of synaptic inputs, GABAergic neurons defined by the expression of the VGAT promoter fire action potentials spontaneously, whereas glutamatergic neurons defined by the expression of the VGluT2 promoter are mostly silent. In addition, $VGAT^+$ neurons had a higher input resistance and a lower action potential threshold than $VGluT2^+$ neurons.

Next, to link the expression of ion channels, receptors, and molecular effectors to specific PAG subdivisions, I established a pipeline to perform single-cell RNA-sequencing while preserving the anatomical origin of each neuron. I obtained detailed transcriptomic profiles from $VGAT^+$ and $VGluT2^+$ neurons across PAG subdivisions by individually isolating fluorescently labelled neurons from acute midbrain slices of transgenic mice and processing them with the Smart-seq2 protocol and a target sequencing depth of 4 million reads per sample. Unsupervised clustering of the resulting data revealed putative subpopulations of neurons that mapped onto different PAG subdivisions, whereas differential expression analysis identified candidate genes for setting and regulating key biophysical properties of PAG neurons.

By leveraging the unique relationship between PAG circuit anatomy and behavioural output, this work uses anatomical location as an anchor to provide a framework for studying how molecularly defined biophysical properties might underpin behavioural control by the PAG.

IMPACT STATEMENT

The periaqueductal gray (PAG) is an evolutionarily conserved brain structure that regulates and coordinates the execution of a plethora of instinctive behaviours, from predator avoidance, reproductive behaviour, and hunting to analgesia, stress, and cardiovascular function. Even though its functional heterogeneity has been known for decades, a systematic biophysical and molecular characterisation of the main cell types across PAG subdivisions is still lacking. The results of this thesis begin to address this gap and provide a biophysical and molecular framework for future studies trying to achieve a mechanistic understanding of how the PAG acts as an integrator, gating the behavioural output that maximises an individual's survival.

The results from the experiments investigating the biophysical properties of PAG neurons support the idea that glutamatergic and GABAergic neurons in this brain area have profoundly different electrophysiological profiles and suggest a biophysical blueprint upon which its different neural circuits are built. In line with recent studies (La-Vu, Sethi, et al., 2022), these results underscore the importance of using cell type-specific approaches to record and manipulate the activity of PAG neurons and can help contextualise the outcome of past and future studies aimed at dissecting the physiological roles of the PAG.

To better understand the main cellular components of the neuronal circuits within the PAG, I established a pipeline to perform cell type-specific deep transcriptomic profiling of PAG neurons while preserving their anatomical origin. To the best of my knowledge, this study is the first to use such targeted approach to link the expression of ion channels, receptors, and molecular effectors to specific PAG subdivisions. The resulting dataset will be made publicly available as a resource to the wider academic community. I hope that, by interpreting the gene expression data in light of the electrophysiological properties of the two main cell types in the PAG, the results of

this thesis will prove to be an asset to the field and will ultimately lead to a better understanding of the many roles of this fascinating brain area.

Inter alia, some of the potential benefits of this thesis will likely extend beyond academia and translate into new lines of research leading to improved medical treatment. Of note, the PAG has been implicated in panic attacks, post-traumatic stress disorder, and anxiety (Brandão and Lovick, 2019). Leveraging this gene expression data could help design experiments with the potential to bridge the gap between neuronal physiology and neuropsycopharmacological observations in humans. For instance, understanding the effects that gabapentinoids or monoamine neuromodulators have on the electrophysiological properties of PAG neurons could lead to the development of better treatments for epilepsy, neuropathic pain, and anxiety disorders.

STATEMENT OF CONTRIBUTIONS

Due to the interdisciplinary nature of this project, some of the data presented in this dissertation was acquired in collaboration with colleagues in the Branco Lab. I designed all experiments, collected all the data, and performed all analyses presented in this dissertation under the supervision of Professor Tiago Branco and in collaboration with other researchers, as detailed below.

In the following I state the contribution of other people to the data presented by chapter:

Chapter 4. A pipeline for topographic and cell type-specific deep transcriptomic profiling of periaqueductal gray neurons: the implementation and troubleshooting of this pipeline and all the subsequent experiments were done in collaboration with Sarah F. Olesen. I aspirated all the neurons in the dataset. Sarah F. Olesen processed all the samples with Smart-seq2, purified the resulting cDNA, and performed all the quality controls. cDNA library preparation, sequencing, and the initial analysis steps, including read alignment and quantification, were performed externally by the Barts London Genome Centre at the Blizard Institute (Barts and The London School of Medicine and Dentistry, Queen Mary University of London).

Chapter 5. Gene expression profiling of single periaqueductal gray neurons: the single-cell RNA-sequencing data analysed and presented in this chapter were obtained from the experiments done in collaboration with Sarah F. Olesen and the Barts London Genome Centre at the Blizard Institute (Barts and The London School of Medicine and Dentistry, Queen Mary University of London). I did all the analysis.

CONTENTS

LIST OF FIGURES

LIST OF TABLES

ABBREVIATIONS

ACSF	artificial cerebrospinal fluid
AgCl	silver chloride
AHP	afterhyperpolarisation
AMP	adenosine monophosphate
API	application programming interface
Aq	aqueduct
AUC	area under the curve
bp	base pairs
$CaCl_2$	calcium chloride
CCF	common coordinate framework
cDNA	complementary deoxyribonucleic acid
CO_2	carbon dioxide
CV	coefficient of variation
CV^2	squared coefficient of variation
dlPAG	dorsolateral periaqueductal gray
dmPAG	dorsomedial periaqueductal gray
DNA	deoxyribonucleic acid
dNTP	deoxynucleotide triphosphate
DTT	1,4-dithiothreitol
EGTA	ethylene glycol tetraacetic acid
ERCC	external RNA controls consortium
EYFP	enhanced yellow fluorescent protein
FACS	fluorescence activated cell sorting
FU	fluorescence units
g	g force or relative centrifugal force
GABA	gamma-aminobutyric acid
Hz	hertz
HCl	hydrochloric acid

HEPES	4-(2-hydroxyethyl)-1-piperazineethanesulfonic acid
ID	identification
KCl	potassium chloride
kHz	kilohertz
$KMeSO_3$	potassium methanesulfonate
KOH	potassium hydroxide
LNA	locked nucleic acid
lPAG	lateral periaqueductal gray
M	molar
MΩ	megaohm
Mg-ATP	adenosine triphosphate, magnesium salt
$MgCl_2$	magnesium chloride
$MgSO_4$	magnesium sulfate
min	minute
ml	millilitre
ml/min	millilitre per minute
mm	millimetre
mM	millimolar
mOsm/kg	milliosmoles per kilogram
ms	millisecond
mV	millivolt
mRNA	messenger ribonucleic acid
NA	numerical aperture
Na_2-GTP	guanosine triphosphate, disodium salt
NaCl	sodium chloride
$NaHCO_3$	sodium bicarbonate
NaH_2PO_4	sodium monobasic phosphate
NaOH	sodium hydroxide
nm	nanometre
NMDG-Cl	N-methyl-D-glucamine chloride
O_2	oxygen

pA	picoampere
PAG	periaqueductal gray
PC	principal component
PCA	principal component analysis
PCR	polymerase chain reaction
RNA	ribonucleic acid
RNAse	ribonuclease
R_s	series resistance
RT-qPCR	reverse transcription quantitative real-time PCR
s	second
SEM	standard error of the mean
t-SNE	t-distributed stochastic neighbour embedding
TSO	template switching oligonucleotide
UMAP	uniform manifold approximation and projection
UV	ultraviolet
U/µL	unit per microlitre
VGAT	vesicular GABA transporter
VGluT2	vesicular glutamate transporter 2
vlPAG	ventrolateral periaqueductal gray
°C	degrees Celsius
3D	three-dimensional
µL	microlitre
µm	micrometre
µM	micromolar

FOREWORD

The motivation behind this foreword is to briefly lay out the way I have structured the thesis with the hope that this will facilitate the digestion of its contents and make it a more enjoyable read. I envisioned the first chapter as a general introduction, the purpose of which is to summarise the most relevant aspects of the periaqueductal gray, the brain region that is the focal point of this work, and to present the overarching aims of the thesis. To expand on the main introduction, in each of the results chapters I incorporated further introductory sections that delve into the topics and techniques directly relevant to the chapter in hand. After the general introduction in chapter one, the second chapter describes the methods I used to obtain and analyse the data presented in the results sections. The ensuing three chapters contain the results of two complementary lines of investigation: on the one hand, chapter three covers the biophysical characterisation of periaqueductal gray neurons, and on the other hand, chapter four describes the steps I took to devise, implement, and troubleshoot a method to generate a single-cell RNA-sequencing dataset from periaqueductal gray neurons, whereas chapter five summarises the biological insights derived from the gene expression data. Each results chapter is capped with a brief interim summary that highlights the main findings. In the last chapter I attempt to bring both research lines together, discussing and interpreting the main findings in an integrated manner before outlining the experimental outlook and proposing some potentially interesting follow up experiments that could build on the work you are about to read.

1 INTRODUCTION

1.1 THE MIDBRAIN PERIAQUEDUCTAL GRAY MATTER

The midbrain periaqueductal gray matter (PAG, Figure 1.1) is an evolutionarily conserved structure that has long been proposed as an essential part of the neural circuits integrating and coordinating defensive behavioural responses to stressors and imminent dangers (de Molina and Hunsperger, 1962; Bandler and Carrive, 1988; Bandler and Depaulis, 1991; Carrive, 1993; Vianna and Brandão, 2003; Linnman, Moulton, *et al.*, 2012; Franklin, 2019; Lefler, Campagner, and Branco, 2020). When prey species like mice venture beyond their safe and familiar territory to find food or mate, they become exposed to potential threats. Such threats are encoded by salient sensory stimuli and can trigger innate defensive behaviours such as escaping to a known shelter or freezing (Yilmaz and Meister, 2013; De Franceschi, Vivattanasarn, *et al.*, 2016; Tovote, Esposito, *et al.*, 2016; Vale, Evans, and Branco, 2017; Evans, Stempel, *et al.*, 2018; Branco and Redgrave, 2020). For example, a rapidly expanding overhead visual stimulus suggests the approach of an object in collision course or a predator and would trigger immediate escape to a safe place (Yilmaz and Meister, 2013; De Franceschi, Vivattanasarn, *et al.*, 2016; Vale, Evans, and Branco, 2017; Evans, Stempel, *et al.*, 2018), whereas a sweeping object cruising overhead might indicate to the prey that it has not yet been detected, in which case freezing would be a better strategy (Yilmaz and Meister, 2013; De Franceschi, Vivattanasarn, *et al.*, 2016).

Besides being considered the exit relay for defensive behaviours (de Molina and Hunsperger, 1962; Vianna and Brandão, 2003), the PAG has also been critically involved in a variety of physiological functions and behaviours key to an animal's survival. These include, but are not limited to, pain processing and analgesia, vocalisation, lordosis, anxiety, micturition, and cardiovascular function (Bandler and Depaulis, 1991; Behbehani, 1995; Linnman, Moulton, *et al.*, 2012; Silva and McNaughton, 2019). The neural mechanisms and the precise role the PAG has in some of these behaviours are only now beginning to be understood at a cellular level (see section 1.1.3).

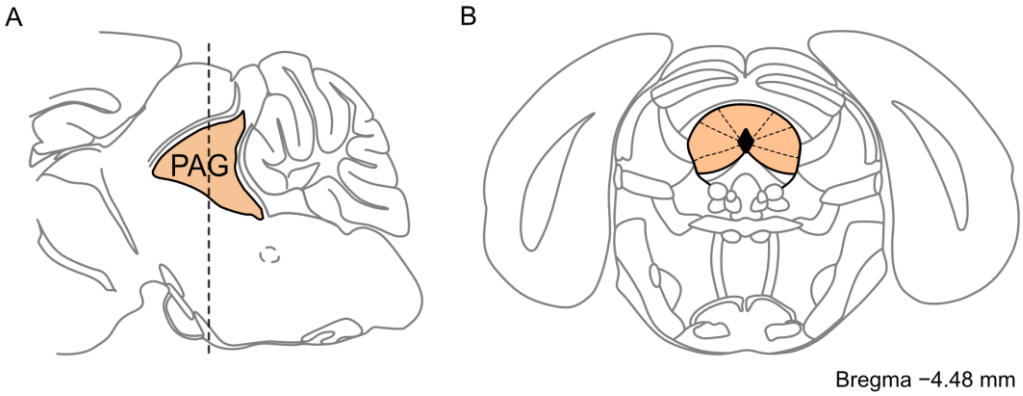

Figure 1.1. Anatomical location of the midbrain periaqueductal gray matter. Schematics illustrating the anatomical location of the PAG, highlighted in yellow, in a sagittal (**A**) and a coronal (**B**) section of a mouse brain. The dashed line in (**A**) indicates the position of the coronal section shown in (**B**). PAG, periaqueductal gray. Adapted from Franklin and Paxinos (2008).

In this first chapter, I provide an overview of previous efforts directed at understanding the structural and functional aspects of this highly complex and heterogenous brain region that is the focal point of this thesis.

1.1.1 Anatomy and input-output connectivity of the periaqueductal gray

The PAG, also known as the central gray, is a region of gray matter that surrounds the cerebral aqueduct along the rostro-caudal axis (Figure 1.1 and Figure 1.2) (Bandler and Depaulis, 1991; Franklin and Paxinos, 2008). This elongated structure is found within the midbrain or mesencephalon, and as such is part of the brainstem. At its rostral end, as the third ventricle becomes the aqueduct, the PAG forms as a structure adjacent to the periventricular gray matter of the thalamus and the hypothalamus; caudally, the PAG ends as the aqueduct becomes the fourth ventricle and the pontine gray matter forms its floor (Bandler and Depaulis, 1991; Keay and Bandler, 2015). Besides these rostro-caudal borders, two fibre-streams set the confines of the PAG: the tectobulbospinal fibres stemming from the deep white layer of the superior colliculus separate the PAG from the colliculi, whereas the mesencephalic trigeminal tract separates the PAG from the cuneiform nucleus (Franklin and Paxinos, 2008; Chon, Vanselow, *et al.*, 2019). The PAG has been commonly seen as an area structurally and functionally distinct from the following nuclei found within the same anatomical limits: the oculomotor and trochlear nuclei, the Edinger-Westphal nucleus, the interstitial nucleus of Ramón y Cajal, the dorsal raphe nucleus, the mesencephalic trigeminal nucleus, and the dorsal tegmental nuclei (Keay and Bandler, 2015).

Far from being a homogeneous structure, the PAG has been divided into longitudinal columns, with each column named after its location with respect to the aqueduct (Figure 1.2): a dorsomedial column (dmPAG), a dorsolateral column (dlPAG), a lateral column (lPAG), and a ventrolateral column (vlPAG). These columns have traditionally been defined based on the inputs they receive and on the physiological consequences elicited by their stimulation or lesion (Bandler and Carrive, 1988; Bandler and Depaulis, 1991; Carrive, 1993; Vianna and Brandão, 2003; Franklin and Paxinos, 2008; Benarroch, 2012; Linnman, Moulton, *et al.*, 2012; Keay and Bandler, 2015; Chon, Vanselow, *et al.*, 2019; Silva and McNaughton, 2019).

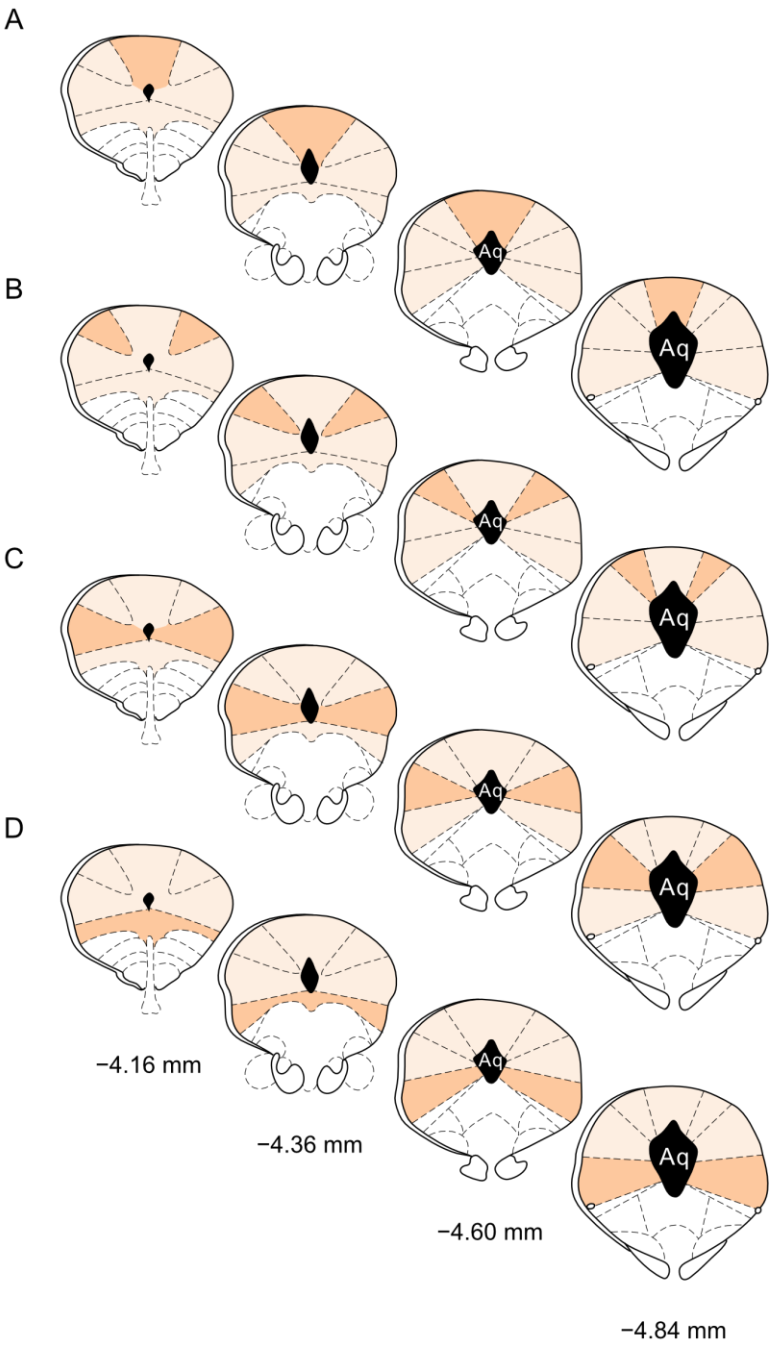

Figure 1.2. Columnar structure of the midbrain periaqueductal gray matter. Schematics illustrating the structure of the PAG, highlighted in light shaded yellow, and its different subdivisions along the rostro-caudal axis of a mouse brain. For each panel, the dark shaded yellow area represents the extent of a PAG subdivision: (**A**) dorsomedial column of the PAG, (**B**) dorsolateral column of the PAG, (**C**) lateral column of the PAG, and (**D**) ventrolateral column of the PAG. Aq, cerebral aqueduct. The numbers at the bottom indicate the coronal coordinates from bregma. Adapted from Franklin and Paxinos (2008).

In terms of its connectivity, the PAG receives inputs from multiple cortical and subcortical brain areas, as well as ascending inputs from the spinal cord and the spinal trigeminal nucleus. These inputs show various degrees of specificity towards different PAG subdivisions (summarised in Figure 1.3), suggesting that incoming projections can differentially modulate potentially segregated circuit modules with distinct physiological functions (Bandler and Depaulis, 1991; Vianna and Brandão, 2003; Benarroch, 2012; Keay and Bandler, 2015; Silva and McNaughton, 2019).

The most prominent cortical input to the PAG comes from the medial prefrontal cortex. This brain area has been implicated in the regulation of numerous cognitive functions, including attention, inhibitory control, and habit and memory formation (Jobson, Hase, *et al.*, 2021), but has also been linked to the development of defensive strategies during escape behaviour (Mobbs, Petrovic, *et al.*, 2007; Mobbs, Trimmer, *et al.*, 2018). Several studies suggest that the projections from medial prefrontal cortex to PAG are topographically organised. The CG1 and CG2 subdivisions of the anterior cingulate cortex have been shown to specifically target the dlPAG (Floyd, Price, *et al.*, 2000; Silva and McNaughton, 2019). The anterior part of the prelimbic cortex preferentially projects to vlPAG and dorsal raphe, whereas the posterior part of the prelimbic cortex projects mainly to dmPAG and dlPAG (Floyd, Price, *et al.*, 2000; Franklin, Silva, *et al.*, 2017; Silva and McNaughton, 2019). The infralimbic cortex and the dorsal peduncular cortex have similar projection patterns, and mostly target the vlPAG and dorsal raphe (Floyd, Price, *et al.*, 2000; Silva and McNaughton, 2019). In rats, primary motor cortical areas preferentially project to lPAG and vlPAG, whereas primary auditory cortex and secondary visual areas mostly target the dlPAG (Vianna and Brandão, 2003).

There are also several subcortical areas that project to the PAG. In the case of the amygdaloid complex, only the central nucleus of the amygdala projects to the PAG. This projection mainly targets the lPAG and vlPAG and has been shown to constitute a disinhibitory pathway that drives immobility by targeting GABAergic neurons in the vlPAG (Vianna and Brandão, 2003; Tovote, Esposito, *et al.*, 2016; Silva and

McNaughton, 2019). Conversely, a monosynaptic connection from glutamatergic neurons in the deep layers of the superior colliculus to glutamatergic neurons in the dorsal PAG has been shown to implement a synaptic threshold mechanism that allows the PAG to initiate escape in response to salient threatening stimuli (Evans, Stempel, *et al.*, 2018; Branco and Redgrave, 2020).

Other subcortical inputs to the PAG can be found in the hypothalamus. Together with the dorsomedial portion of the ventromedial hypothalamic area, the dorsal premammillary nucleus and the anterior hypothalamic areas send dense projections to the dlPAG (Canteras and Swanson, 1992; Semenenko and Lumb, 1992; Keay and Bandler, 2015; Silva and McNaughton, 2019), while the ventrolateral portion of the hypothalamic area selectively projects to the lPAG and mediates aggression (Falkner, Wei, *et al.*, 2020). The lateral hypothalamic area, the zona incerta, and the medial preoptic area all send GABAergic projections to the l/vlPAG, each pathway involved in a different behaviour from predation (Li, Zeng, *et al.*, 2018), freezing (Chou, Wang, *et al.*, 2018), and pup grooming (Kohl, Babayan, *et al.*, 2018).

Finally, the spinal cord and the spinal trigeminal nucleus have been shown to send afferent projections to the lPAG and vlPAG in a topographically organised manner, some of which may be involved in nociception (Bandler and Depaulis, 1991; Keay, Feil, *et al.*, 1997; Keay and Bandler, 2001).

In turn, the PAG sends multiple ascending and descending projections to other areas. The dorsal PAG sends efferents to the paraventricular thalamic nuclei and the anterior hypothalamic area, whereas the vlPAG preferentially projects to the lateral hypothalamic area, the parafascicular and central medial thalamic nuclei, and the bed nucleus of the stria terminalis (Cameron, Khan, Westlund, Cliffer, *et al.*, 1995). The PAG also sends projections to the zona incerta, the ventral tegmental area, the preoptic area, the substantia nigra pars compacta, the nucleus basalis of Meynert, the dorsal and posterior hypothalamic areas, and the midline thalamic nuclei (Cameron, Khan, Westlund, Cliffer, *et al.*, 1995; Keay and Bandler, 2015; Silva and McNaughton, 2019).

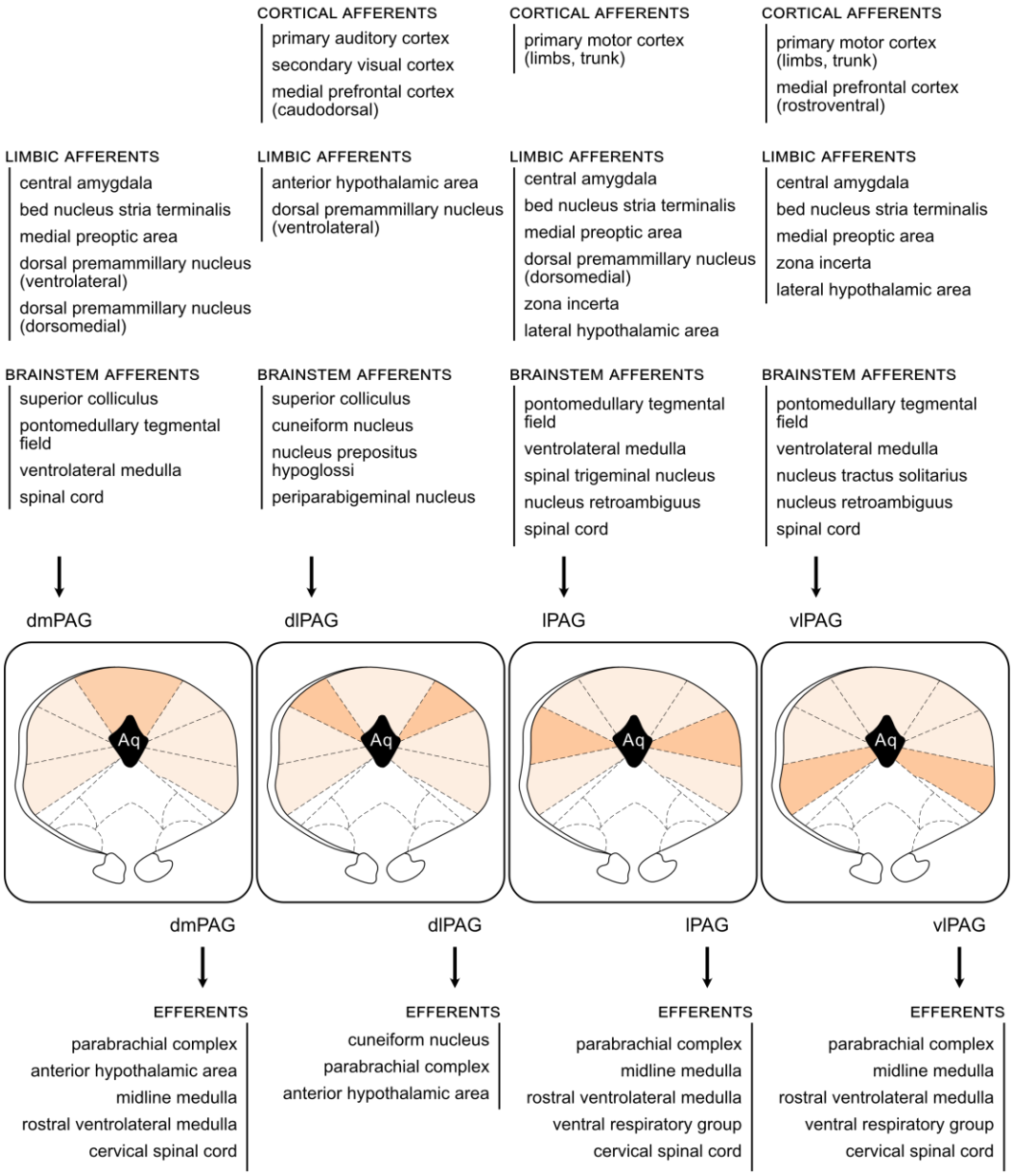

Figure 1.3. Input-output connectivity of the midbrain periaqueductal gray matter. Anatomical afferent (top) and efferent (bottom) connections of the PAG (centre), highlighted in light shaded yellow, and its different subdivisions, highlighted in dark shaded yellow. Each column corresponds to a PAG subdivision, from left to right: dorsomedial column of the PAG (dmPAG), dorsolateral column of the PAG (dlPAG), lateral column of the PAG (lPAG), and ventrolateral column of the PAG (vlPAG). Aq, cerebral aqueduct. Adapted from Faull, Subramanian, *et al.* (2019).

In terms of descending projections, the dorsal PAG has been shown to preferentially target the locus coeruleus, a noradrenergic nucleus involved in regulating attention, arousal, and stress responses (Cameron, Khan, Westlund, and Willis, 1995; Luppi, Aston-Jones, *et al.*, 1995), as well as the Barrington's nucleus, involved in micturition (Cameron, Khan, Westlund, and Willis, 1995; Verstegen, Klymko, *et al.*, 2019). In addition, the dlPAG sends projections to the cuneiform nucleus (Redgrave, Dean, *et al.*, 1988; Vianna and Brandão, 2003), which is part of the mesencephalic locomotor region that controls gait and locomotion (Caggiano, Leiras, *et al.*, 2018). The lPAG has been shown to contain jaw-projecting neurons (Falkner, Wei, *et al.*, 2020), whereas the vlPAG sends direct projections to the dorsal and median raphe nuclei and the spinal cord (Cameron, Khan, Westlund, and Willis, 1995; Keay and Bandler, 2015; Silva and McNaughton, 2019).

1.1.2 Cellular composition of periaqueductal gray circuits

The cytoarchitecture of the PAG is similar across mammals and consists of mostly small- and medium-size neurons with somata between 10 and 40 μm in diameter (Mantyh, 1982; Behbehani, 1995). Morphological studies using the Golgi, Nissl, and other staining methods in a variety of mammalian species have described different types of PAG neurons on the basis of the size and shape of the soma and the number and distribution of dendritic and axonic arborizations (Mantyh, 1982; Beitz and Shepard, 1985; Behbehani, 1995). *Fusiform* neurons are elongated and have a bipolar arrangement of their processes, with one or more primary dendrites arising from each pole and the axon typically stemming from a primary or secondary dendrite. Another major class, *pyramidal* neurons, are characterised by a triangularly shaped soma and dendritic arborizations which often spread far into the superior colliculus or the deep and intermediate tegmentum. Fusiform neurons tend to be most prominently found in regions closer to the aqueduct. Pyramidal neurons, on the other hand, are larger and more numerous towards the periphery of the PAG, far from the aqueduct. A third

morphological class consists of *multipolar* or *stellate* neurons, characterised by having extensive dendritic arborizations spreading mainly in the coronal plane. Although these three cell types can be found in all the PAG subdivisions, the size of the soma and the density of neurons tend to increase with distance from the aqueduct (Mantyh, 1982), something I also observed in the course of the experiments conducted for this thesis.

Early studies using immunohistochemistry identified two subpopulations of neurons based on the presence of glutamate decarboxylase, the enzyme that catalyses the decarboxylation of glutamate to gamma-aminobutyric acid (GABA) and carbon dioxide (CO_2): a group consisting of intrinsic neurons characterised by having a small size and expressing glutamate decarboxylase, and a group consisting of projection neurons which were larger and did not express glutamate decarboxylase (Barbaresi and Manfrini, 1988). Further experiments went on to show that the main neurotransmitters of PAG neurons are glutamate and GABA, with their major types of receptors being highly expressed throughout the PAG (Albin, Makowiec, *et al.*, 1990; Bandler and Depaulis, 1991). Importantly, recent experiments using fluorescence in situ hybridization to doubly label mRNA transcripts for the vesicular GABA transporter (VGAT) and the vesicular glutamate transporter 2 (VGluT2) have shown that GABAergic and glutamatergic neurons form two non-overlapping subpopulations, at least in the vlPAG (Samineni, Grajales-Reyes, *et al.*, 2017). GABAergic neurons account for approximately 20% of all PAG neurons (Barbaresi and Manfrini, 1988; Bandler and Depaulis, 1991), and have been described as local interneurons with very few efferent projections that exert a strong tonic inhibitory control over the outputs of the PAG (Brandão, De Aguiar, and Graeff, 1982; Audi and Graeff, 1987; Behbehani, Jiang, *et al.*, 1990; Bandler and Depaulis, 1991; Ogawa, Kow, and Pfaff, 1994; Behbehani, 1995; Brandão, Anseloni, *et al.*, 1999; Lee and Gammie, 2010).

In addition to expressing the main excitatory and inhibitory neurotransmitters, PAG neurons have been shown to release or be modulated by a strikingly large number of neurotransmitters, neuropeptides, and neuromodulators (for a review, see Silva and McNaughton, 2019). Nitric oxide synthase, the enzyme that catalyses the synthesis of

nitric oxide, has been found to be highly expressed in dlPAG neurons (Onstott, Mayer, and Beitz, 1993), where it may modulate defensive behaviours (Guimarães, Beijamini, *et al.*, 2005; Braga, Aguiar, and Guimarães, 2009). The neuropeptides substance P, oxytocin, and thyrotropin-releasing hormone have all been shown to have an excitatory neuromodulatory effect on PAG neurons *in vitro*, and may be involved in facilitating lordosis (Ogawa, Kow, and Pfaff, 1992). Conversely, the endogenous opioid peptide met-enkephalin has been shown to have an inhibitory effect on a subset of PAG neurons (Ogawa, Kow, and Pfaff, 1994). Several other transmitters, including dopamine (Messanvi, Eggens-Meijer, *et al.*, 2013; Vander Weele, Siciliano, *et al.*, 2018; Vaaga, Brown, and Raman, 2020), serotonin (Schütz, de Aguiar, and Graeff, 1985; Graeff, 2004; Jeong, Lam, *et al.*, 2013), and both adrenaline and noradrenaline (Jiang, Chandler, *et al.*, 1992; Estrada, Matsubara, *et al.*, 2016), have also been shown to induce neuromodulatory effects on the PAG and its functions (for a review see Brandão, Anseloni, *et al.*, 1999 and Silva and McNaughton, 2019).

1.1.3 Physiological functions of the periaqueductal gray and its subdivisions

Early and more recent studies depict a picture in which dorsal and ventral PAG coordinate opposing defensive behaviours: electrical, optical, and neurochemical stimulation of the dmPAG and dlPAG elicits strong flight responses, whereas stimulation of the vlPAG produces immobility and freezing (Bandler and Carrive, 1988; Bandler and Depaulis, 1991; Carrive, 1993; Behbehani, 1995; Fanselow, Decola, *et al.*, 1995; Brandão, Anseloni, *et al.*, 1999; Keay and Bandler, 2001; Vianna and Brandão, 2003; Tovote, Esposito, *et al.*, 2016; Evans, Stempel, *et al.*, 2018). In human patients, electrically stimulating the dorsal PAG induces a sensation of fear and panic (Nashold, Wilson, and Slaughter, 1969; Amano, Tanikawa, *et al.*, 1978), with one patient reporting that *"somebody is now chasing me, I am trying to escape from him"* (Amano, Tanikawa, *et al.*, 1978), suggesting that this PAG function is highly conserved across species (Branco and Redgrave, 2020; Lefler, Campagner, and Branco, 2020).

This anatomical and functional dichotomy can be recapitulated by recording and manipulating the activity of genetically defined subtypes of neurons. Experiments using calcium imaging to record neuronal activity in freely behaving mice have shown that glutamatergic neurons of the dorsal PAG are silent until just before the initiation of escape, and are maximally active during escape (Evans, Stempel, *et al.*, 2018). Optogenetic activation of glutamatergic neurons in the dorsal PAG evokes an escape response in the absence of a threatening stimulus, whereas optogenetic inhibition of the same neurons switches the response to threats from escape to freezing (Evans, Stempel, *et al.*, 2018). Conversely, other studies have shown that optogenetic activation of glutamatergic neurons in the ventral PAG induces freezing in the absence of a threat (Tovote, Esposito, *et al.*, 2016).

Importantly, and as I have described in the previous sections, the PAG is a highly heterogeneous structure that has been involved in a wide variety of functions beyond defensive behaviours. These include, but are not limited to, nociception, analgesia, vocalisation, lordosis, anxiety, micturition, and cardiovascular function (Bandler and Depaulis, 1991; Behbehani, 1995; Linnman, Moulton, *et al.*, 2012; Silva and McNaughton, 2019). And although most of these functional modules have been mapped onto the anatomical substructure of the PAG, their underlying neural mechanisms are only beginning to be unravelled at the cellular level.

The ability to identify and manipulate cell type-specific projections has been a major catalyst in PAG research and has allowed researchers to start teasing apart the subtler details underlying the many functions of the PAG. Two very fine examples of such an approach have already been described above, the results of which further consolidate the functional dichotomy between dorsal and ventral PAG in coordinating active and passive defensive behaviours. On one hand, a monosynaptic connection from glutamatergic neurons in the deep layers of the superior colliculus to glutamatergic neurons in the dorsal PAG has been shown to implement a synaptic threshold mechanism that allows the PAG to initiate escape in response to salient threatening stimuli (Evans, Stempel, *et al.*, 2018). On the other hand, an inhibitory

projection between the central nucleus of the amygdala and the ventral PAG has been shown to mediate freezing by disinhibition, in particular by targeting GABAergic neurons in the vlPAG that in turn synapse onto the vlPAG glutamatergic outputs to pre-motor neurons in the magnocellular nucleus of the medulla (Tovote, Esposito, *et al.*, 2016).

Other studies using similar approaches have implicated the lPAG in aggression and hunting. For instance, a recent study has identified a projection from glutamatergic neurons in the ventrolateral portion of the ventromedial hypothalamus to glutamatergic neurons in the lPAG that mediates aggression (Falkner, Wei, *et al.*, 2020). Their conclusions outline a role for the lPAG in coordinating the activity of multiple muscle groups rather than regulating the aggressive state of the animal. Another study has implicated two cell type-specific projections from the lateral hypothalamus to lPAG in driving predatory attack or evasion, with GABAergic neurons driving the former and glutamatergic neurons the latter (Li, Zeng, *et al.*, 2018). Experiments using optrode recordings have shown that GABAergic neurons in the lPAG are recruited during prey detection, chase, and attack, whereas glutamatergic neurons in the lPAG are necessary for predatory attack (Yu, Xiang, *et al.*, 2021). Besides hunting, predation, and aggression, different subpopulations of l/vlPAG neurons have been shown to be important for social vocalisations (Tschida, Michael, *et al.*, 2019), itch-scratching behaviour (Gao, Chen, *et al.*, 2019), and micturition (Verstegen, Klymko, *et al.*, 2019).

The vlPAG has also been implicated in a variety of behaviours via a suite of different projections and cell types. Projections from GABAergic neurons in the bed nucleus of the stria terminalis or the lateral hypothalamus to GABAergic neurons in the vlPAG have been shown to regulate feeding behaviour (Hao, Yang, *et al.*, 2019). A population of neurotensin-expressing glutamatergic neurons in the vlPAG has been shown to promote and be active during non-rapid eye movement sleep (Zhong, Zhang, *et al.*, 2019). And a subpopulation of GABAergic neurons in the vlPAG has been described to receive inhibitory inputs from galanin-expressing neurons in the

medial preoptic area and regulate certain motor aspects of pup grooming behaviour by disinhibition (Kohl, Babayan, *et al.*, 2018).

In addition to the anatomical location and the input-output connectivity, two recent studies have highlighted the importance of adding the molecular identity of PAG neurons to the list of key drivers of functional heterogeneity when investigating the physiological implications of PAG circuits. The first study used cell type-specific chemogenetic manipulations to show that glutamatergic and GABAergic neurons in the vlPAG can have opposing effects on nociception: inhibition of GABAergic neurons or activation of glutamatergic neurons was found to have an antinociceptive or analgesic effect, whereas activation of GABAergic neurons or inhibition of glutamatergic neurons was found to have a pronociceptive effect (Samineni, Grajales-Reyes, *et al.*, 2017). The second study found that while pan-neuronal activation of l/vlPAG neurons promoted freezing, a subset of cholecystokinin-expressing neurons in the same area selectively elicited flight to safety upon activation (La-Vu, Sethi, *et al.*, 2022).

1.2 AIMS OF THIS STUDY

The body of work on the different functions of this highly heterogeneous and conserved brain area strongly supports the existence of microcircuits consisting of cell type-specific modules across the anatomical subdivisions of the PAG. Many brain areas have been shown to project to specific subdivisions and cell types within the PAG, driving or modulating a wide array of behaviours critical for an animal's survival. Even though some of the studies I have reviewed have begun to dissect the roles these different projections and PAG cell types have, it is still not clear what determines the specificity of each projection or how does the PAG integrate all this barrage of inputs to give rise to a coordinated behavioural response.

While there is a wealth of information on the cytoarchitecture and connectivity of the PAG and its anatomical columns, our knowledge of the molecular complexity of PAG neurons and how it relates to their physiological functions is still very shallow. Achieving a mechanistic understanding of the PAG network computations underlying its many functions requires understanding how their principal components work. Both the intrinsic biophysical properties and the computations neurons can perform are in part determined by their gene expression profile, including the differential expression of specific ion channels and neuromodulator receptors. However, a comprehensive and systematic biophysical and molecular profiling of the main cell types within the PAG is still lacking.

In this study, I attempted to fill this gap by using a multidisciplinary approach to characterise the electrophysiological properties and gene expression profile of PAG neurons, with the goal of identifying molecularly defined circuit motifs that may underpin the functional heterogeneity of the midbrain PAG. Briefly, the overarching aims of this thesis were to:

(1) Characterise the biophysical properties of PAG neurons in a cell type-specific manner by obtaining targeted patch-clamp recordings from glutamatergic and GABAergic neurons across PAG subdivisions.

(2) Establish a pipeline to perform topographic and cell type-specific deep transcriptomic profiling of single PAG neurons.

(3) Extract biological insights from the gene expression profile of glutamatergic and GABAergic neurons across PAG subdivisions, with a focus on ion channel subunits and neuromodulator receptors with the potential to set and modulate the electrophysiological properties identified in (1).

2 METHODS

2.1 MOUSE BREEDING AND HUSBANDRY

All experiments were carried out under the UK Animals (Scientific Procedures) Act of 1986 (PPL 70/7652 and PFE9BCE9) following local ethical approval by the Sainsbury Wellcome Centre Animal Welfare Ethical Review Body. Young adult female or male mice between 6-10 weeks were obtained from the SWC animal facility. Mice were housed (<5 mice per cage) with free access to food and water on a 12:12 hour light:dark cycle and tested during the light phase. Transgenic mouse strains on a C57BL/6J background were used to target GABAergic or glutamatergic neurons. Cre driver lines targeting the vesicular GABA transporter (VGAT-ires-Cre, Jackson Laboratory, Stock No. 016962) and the vesicular glutamate transporter (VGluT2-ires-Cre, Jackson Laboratory, Stock No. 016963) were crossed with Cre-dependent reporter lines (R26R-EYFP, Jackson Laboratory, Stock No. 006148 and Ai14, Jackson Laboratory, Stock No. 007914; EYFP, enhanced yellow fluorescent protein) to express fluorescent proteins and label genetically-defined cell populations (Srinivas, Watanabe, *et al.*, 2001; Borgius, Restrepo, *et al.*, 2010; Vong, Ye, *et al.*, 2011).

Unless otherwise indicated, the Cre recombinase-expressing mouse strains used in all experiments were VGAT::EYFP, VGAT::tdTomato, VGluT2::EYFP, and VGluT2::tdTomato. Animals in test and control groups were littermates and randomly selected.

2.2 PREPARATION OF ACUTE MIDBRAIN SLICES

Acute midbrain slices were prepared following one of the two protocols detailed below. Path A is the simpler of the two approaches: the solutions are easier to prepare, and the brain extraction is preceded by terminal anaesthesia and decapitation. Path B is more elaborated: it requires three solutions instead of two, it has an additional incubation step, and the decapitation and brain extraction are preceded by intracardial perfusion. I originally followed path A with great results and used it for all the experiments involving aspiration of neurons via patch pipettes and some of the initial experiments involving loose-seal and whole-cell patch-clamp recordings. Towards the later stages of the project, I transitioned to path B as it produced acute slices of higher quality.

In line with recent efforts to improve the accessibility and reproducibility of scientific methods, the methods described in this section have also been made available as a detailed step-by-step protocol for the preparation of acute midbrain slices containing the superior colliculus and periaqueductal gray for patch-clamp recordings (Pavón Arocas and Branco, 2022).

2.2.1 Path A. Decapitation under terminal isoflurane anaesthesia

Briefly, this slicing approach consisted of decapitation under terminal isoflurane anaesthesia, brain extraction and slicing in ice-cold slicing artificial cerebrospinal fluid (ACSF), slice incubation in slicing ACSF for 30 minutes at 35°C, followed by a second incubation in recording ACSF for at least 30 minutes at room temperature (19-23°C) and then for the remainder of the day until transfer of the slices to the recording chamber perfused with recording ACSF at 32-34°C or room temperature. Solutions were made fresh at least once per week.

Slicing ACSF (in mM): 87 NaCl, 2.5 KCl, 26 $NaHCO_3$, 1.25 NaH_2PO_4, 10 D-glucose, 50 sucrose, 0.5 $CaCl_2$, and 3 $MgCl_2$. The solution was equilibrated with 95% O_2 and 5% CO_2 and the pH adjusted to 7.3-7.4 with HCl or NaOH before adding the $CaCl_2$ and $MgCl_2$. Osmolality was verified to be ~280 mOsm/kg.

Recording ACSF (in mM): 125 NaCl, 2.5 KCl, 26 $NaHCO_3$, 1 NaH_2PO_4, 10 D-glucose, 2 $CaCl_2$, and 1 $MgCl_2$. The solution was equilibrated with 95% O_2 and 5% CO_2 and the pH adjusted to 7.3-7.4 with HCl or NaOH before adding the $CaCl_2$ and $MgCl_2$. Osmolality was verified to be between 295-305 mOsm/kg.

Solutions were bubbled with a mixture of 95% O_2 and 5% CO_2 for at least 30 minutes and allowed to equilibrate to the desired temperature using a dry block heating system (QBD4, Grant Instruments) prior to slicing. pH was again verified to be between 7.3-7.4 and adjusted with HCl or NaOH if necessary. Animals were anaesthetised with 5% isoflurane anaesthesia and killed by decapitation. Brains were quickly removed and immediately immersed in ice-cold slicing ACSF, constantly equilibrated with 95% O_2 and 5% CO_2. Acute coronal slices (250 μm thick) were prepared at the level of the PAG and the superior colliculus (−4.9 to −3.9 mm from bregma) using a vibrating microtome (Leica VT1200S, Leica Biosystems or Ci7000smz-2, Campden Instruments). Slices were collected and transferred to a recovery chamber containing slicing ACSF and stored under submerged conditions at near-physiological temperature (35°C) for 30 minutes, constantly equilibrated with 95% O_2 and 5% CO_2. After this time, slices were transferred to a different recovery chamber containing recording ACSF, constantly equilibrated with 95% O_2 and 5% CO_2. Slices were allowed to further recover at room temperature (19-23°C) for at least 30 more minutes prior to electrophysiological recordings or aspiration of single neurons.

2.2.2 Path B. Intracardial perfusion with ACSF under terminal isoflurane anaesthesia

Over the course of this study, I continuously strived to improve the quality of the acute slice preparation. From the several modifications I tested, the following had a positive impact on slice quality and were incorporated to the slicing procedure: intracardially perfusing the animals with ice-cold slicing ACSF before extracting the brain, switching to solutions optimised for adult brain tissue, and sterilising the glassware by baking it for 2 hours at 200°C in an oven (E28, Binder) before every use.

The modified procedure was used for the majority of electrophysiological recordings, and briefly consisted of intracardially perfusing the mouse with ice-cold slicing ACSF under terminal isoflurane anaesthesia, followed by decapitation, brain extraction, and slicing in ice-cold slicing ACSF, incubation in slicing ACSF for 10-12 minutes at 32°C, followed by a second incubation in holding ACSF for at least 1 hour at room temperature (19-23°C) and then for the remainder of the day until transfer of the slices to the recording chamber perfused with recording ACSF at 32-34°C or room temperature.

Slicing ACSF (in mM): 96 NMDG-Cl, 2.5 KCl, 1.25 NaH_2PO_4, 25 $NaHCO_3$, 20 HEPES, 25 D-glucose, 5 sodium L-ascorbate, 2 thiourea, 3 sodium pyruvate, 3 myo-inositol, 12 N-acetyl-L-cysteine, 0.01 taurine, 0.5 $CaCl_2$, and 10 $MgSO_4$. pH was adjusted to 7.3-7.4 with HCl before adding the $CaCl_2$ and $MgSO_4$. The solution was equilibrated with 95% O_2 and 5% CO_2 and the pH adjusted to 7.3-7.4 with HCl or NMDG-Cl. Osmolality was verified to be between 295-305 mOsm/kg.

Holding ACSF (in mM): 87 NaCl, 2.5 KCl, 1.25 NaH_2PO_4, 25 $NaHCO_3$, 20 HEPES, 25 D-glucose, 5 sodium L-ascorbate, 2 thiourea, 3 sodium pyruvate, 3 myo-inositol, 12 N-acetyl-L-cysteine, 0.01 taurine, 2 $CaCl_2$, and 2 $MgSO_4$. pH was adjusted to 7.3-7.4 with NaOH before adding the $CaCl_2$ and $MgSO_4$. The

solution was equilibrated with 95% O_2 and 5% CO_2 and the pH adjusted to 7.3-7.4 with HCl or NaOH. Osmolality was verified to be between 295-305 mOsm/kg.

Recording ACSF.I (in mM): 126 NaCl, 2.5 KCl, 1.25 NaH_2PO_4, 26 $NaHCO_3$, 12.5 D-glucose, 2 $CaCl_2$, and 1 $MgSO_4$. The solution was equilibrated with 95% O_2 and 5% CO_2 and the pH adjusted to 7.3-7.4 with HCl or NaOH before adding the $CaCl_2$ and $MgSO_4$. Osmolality was verified to be between 295-305 mOsm/kg.

Recording ACSF.II (in mM): 125 NaCl, 2.5 KCl, 1.25 NaH_2PO_4, 26 $NaHCO_3$, 5 HEPES, 10 D-glucose, 2 $CaCl_2$, 1 $MgSO_4$, 2 ascorbic acid, 2 sodium pyruvate, and 3 myo-inositol. The solution was equilibrated with 95% O_2 and 5% CO_2 and the pH adjusted to 7.3-7.4 with HCl or NaOH before adding the $CaCl_2$ and $MgSO_4$. Osmolality was verified to be between 295-305 mOsm/kg.

Solutions were bubbled with a mixture of 95% O_2 and 5% CO_2 for at least 30 minutes and allowed to equilibrate to the desired temperature using a dry block heating system (QBD4, Grant Instruments) prior to slicing. pH was adjusted to ~7.3-7.4 right before use. Animals were anaesthetised with 5% isoflurane anaesthesia and intracardially perfused with 25 ml of ice-cold slicing ACSF. Brains were quickly removed and immediately immersed in ice-cold slicing ACSF, constantly equilibrated with 95% O_2 and 5% CO_2. Acute coronal slices (250 μm thick) were prepared at the level of the PAG and the superior colliculus (−4.9 to −3.9 mm from bregma) using a vibrating microtome (Leica VT1200S, Leica Biosystems or Ci7000smz-2, Campden Instruments). Slices were collected and transferred to a recovery chamber containing slicing ACSF and stored under submerged conditions at near-physiological temperature (32°C) for 10 minutes, constantly equilibrated with 95% O_2 and 5% CO_2. After this time, slices were transferred to a different recovery chamber containing holding ACSF at room temperature (19-23°C), constantly equilibrated with 95% O_2

and 5% CO_2. Slices were allowed to further recover at room temperature (19-23°C) for at least 1 more hour prior to electrophysiological recordings.

2.3 SLICE ELECTROPHYSIOLOGY

Acute midbrain slices were individually transferred to a submersion type recording chamber (Scientifica) and continuously perfused with recording ACSF constantly equilibrated with 95% O_2 and 5% CO_2. The solution was perfused at a flow rate of 2 ml/min by means of a peristaltic pump (PPS2, MultiChannel Systems) and either left at room temperature (19-23°C) or warmed to 32-34°C using a feedback-controlled in-line Peltier heater (Scientifica) for the length of the experiment. Slices were allowed to equilibrate for 10-20 minutes before the beginning of the recording. Neurons within the PAG were visualised with oblique illumination on an upright SliceScope Pro 1000 (Scientifica) using a 60× water-immersion objective (LUMPlanFLN, 1.0 numerical aperture, 2 mm working distance, Olympus) and a CMOS camera (Ximea MQ013MG-E2, Lambda Photometrics). $VGAT^+$ or $VGluT2^+$ neurons were identified based on fluorescence from EYFP or tdTomato expression using LED illumination (pE-100, CoolLED) at wavelengths of 490 nm (VGAT::EYFP and VGluT2::EYFP animals) or 565 nm (VGAT::tdTomato and VGluT2::tdTomato animals).

Patch pipettes were pulled from standard-walled filament-containing borosilicate glass capillaries (GC150F-10, 1.5 mm outer diameter, 0.85 mm inner diameter, 100 mm length, Harvard Apparatus) using a vertical micropipette puller (PC-10 or PC-100, Narishige). Pipettes with 4-7 MΩ resistance were backfilled with recording ACSF or intracellular solution and were inserted into the pipette holder of a patch-clamp headstage (EPC 800, HEKA), controlled by a motorised micromanipulator (PatchStar, Scientifica). A silver wire (0.35 mm diameter, GoodFellow, Cat. No. AG005145) coated with silver chloride (AgCl) was present inside the pipette and was in contact with the solution, and either an Ag-AgCl pellet electrode (E206, 2.0 mm diameter, Warner Instruments, Cat. No. 641310) or a coiled AgCl coated silver wire was

immersed in the bath and used as ground electrode. The bath and pipette solutions contained chloride ions to allow a reversible exchange of ions: $Ag + Cl^- \Leftrightarrow AgCl + e^-$. To ensure that this ionic exchange occurred at all times, both the silver wire and bath electrode were regularly chlorided or, in the case of the ground pellet, replaced for a new one.

2.3.1 Loose-seal patch-clamp recordings and pharmacology

Patch pipettes with 4-7 MΩ resistance were backfilled with recording ACSF solution (see section 2.2). The liquid junction potential between the electrode and the bath was approximately 0 because both solutions were the same. Each patch pipette was used for several recordings and was replaced if tissue debris got attached to the tip. Before its first use, the pipette tip was exposed to brain tissue by inserting it in the slice and releasing the positive pressure for several seconds.

Loose-seal cell-attached recordings were obtained by approaching the soma of the target neuron with minimal positive pressure applied to the patch pipette and positioning the tip in gentle contact with the cell membrane (Perkins, 2006; Alcami, Franconville, *et al.*, 2012; Mlinar, Montalbano, *et al.*, 2016). Mechanical stress to the neuron associated with membrane-glass contact was minimised by pre-exposing the pipette tip to brain tissue and by applying minimum suction during seal formation. The resistance of the pipette and the developing seal were continuously monitored using a voltage-clamp protocol with a holding potential of 0 mV and a test pulse of 5 mV with 50 ms duration repeated every 90 ms. Weak positive pressure was released, and gentle suction was slowly applied until the seal resistance was in the 10-20 MΩ range. Following the sealing procedure, action potential currents were continuously recorded for 5-6 minutes in voltage-clamp using an EPC 800 amplifier (HEKA). A test pulse of 5 mV with 50 ms duration was repeated every 5 or 10 s to monitor the seal resistance throughout the duration of the experiment. The command potential was continuously

updated to the value at which the amplifier read 0 pA current (Perkins, 2006). Signals were low-pass Bessel filtered at 5 kHz, sampled at 25 kHz, digitised with 16-bit resolution using a PCIe-6353 board (National Instruments), and recorded in LabVIEW using custom software.

Upon termination of the recording, the anatomical location of the neuron within the PAG was recorded using a 4× objective (PLN, 0.1 numerical aperture, 18.5 mm working distance, Olympus). The rostro-caudal level of each slice was assigned based on comparisons with a mouse stereotaxic atlas (Franklin and Paxinos, 2008) and was used to approximate the coordinates and the PAG subdivision of each recorded neuron.

2.3.1.1 Pharmacology

To assess the baseline firing properties of $VGAT^+$ neurons after blocking fast glutamatergic and GABAergic synaptic transmission, as well as tonic $GABA_A$ receptor activation, 2 mM kynurenic acid (Sigma, Cat. No. K3375-5G) and 50 μM picrotoxin (Tocris, Cat. No. 1128) were added to the recording ACSF, respectively. Kynurenic acid is an antagonist of AMPA, NMDA, and Kainate glutamate receptors (Perkins and Stone, 1982; Elmslie and Yoshikami, 1985), whereas picrotoxin binds $GABA_A$ receptors and stabilises their shut state (Newland and Cull-Candy, 1992). To assess the baseline firing properties of $VGluT2^+$ neurons after blocking fast GABAergic synaptic transmission as well as tonic $GABA_A$ receptor activation, 50 μM picrotoxin (Tocris, Cat. No. 1128) was added to the recording ACSF. When switching from normal recording ACSF to perfusing ACSF with drugs, slices were allowed to equilibrate for 10-20 minutes before the beginning of the recording.

2.3.1.2 Data analysis

The code used to analyse data from loose-seal cell-attached recordings can be found on GitHub. Loose-seal recordings were analysed in Python 3.8 using custom-written routines. To minimise any distortions in the recorded firing frequencies, only the recording period between 2-4 minutes after seal formation was considered for analysis. The first minute after seal formation was discarded as it is corrupted by seal instability, and recordings were only used up to five minutes after seal formation as the measured firing frequency has been shown to increase after that time, most likely due to increased activity of mechanosensitive stretch-activated channels (Alcami, Franconville, *et al.*, 2012). In addition, the following metrics were used to quality check the final dataset:

(1) The seal resistance was <40 MΩ and stable across the duration of the recording.

(2) The neuron remained healthy for the entirety of the recording. For example, the health status of a neuron was considered to have degraded if a large increase in firing frequency was observed and was followed by a progressive decrease in the action potential amplitude and subsequent silence.

(3) The current injected through the recording pipette to maintain a holding potential of 0 mV was on average within ±20 pA.

(4) No signs of changes in amplitude, irregular shape, or inward current events likely to be caused by opening of stretch-activated channels were observed in the baseline current between spikes.

(5) Action potentials did not show tail currents and the action potential shape did not change from its normal form corresponding to the time derivative of action potential to an action potential-like shape, which is thought to reflect a decreased resistance of the membrane patch caused by compromised integrity

of cell membrane in unhealthy neurons (Alcami, Franconville, *et al.*, 2012; Mlinar, Montalbano, *et al.*, 2016).

Neurons that did not meet the above quality criteria were excluded from analysis.

The *seal resistance* was calculated on a sweep-by-sweep basis using Ohm's Law by dividing the magnitude of the test pulse voltage command over the recorded membrane's current response. The resulting values from each sweep were then averaged to obtain a seal resistance value for each neuron.

Action potentials were detected using the `find_peaks` function from SciPy (Virtanen, Gommers, *et al.*, 2020). Detected peaks were then inspected and seven quality metrics were used to remove the peaks corresponding to noise and keep only the ones corresponding to action potentials. The quality metrics were based on the following parameters obtained from the `find_peaks` function: `prominence`, `width_heights`, `widths`, `peak_heights`, `peak_baselined`, `left_bases`, and `right_bases`. The detected action potentials were then cut, baselined, and averaged, and parameters including the action potential *magnitude* and *duration* were calculated. The action potential *magnitude* was defined as the value of the negative peak in the averaged trace. The action potential *duration* was calculated as the time difference between the onset and end of the averaged action potential trace. The action potential *onset* was defined as the point at which four consecutive samples fell outside the baseline distribution comprised by the values corresponding to the 3 ms period at the beginning of the cut, baselined, and averaged action potential. The action potential *end* was defined as the point, starting from the end of the average spike trace, at which four consecutive samples fell outside the baseline distribution comprised by the values corresponding to the 3 ms period at the end of the cut, baselined, and averaged action potential.

Firing frequencies and inter-spike intervals (ISI) for each neuron were obtained between minutes two and four of loose-seal cell-attached recordings. The *firing frequency* was calculated by dividing the number of detected action potentials over the recording

duration. ISIs were calculated on a sweep-by-sweep basis by subtracting the time of the action potential peak from the time of the next action potential peak, and an average ISI was obtained for each neuron. For each neuron, the coefficient of variation (CV) of the ISI was calculated by dividing the standard deviation over the mean.

Statistical analysis was performed in GraphPad Prism (v9.3.1). Cells were pooled across animals for comparisons between cell types, PAG subdivision, and drug condition. The Mann-Whitney test was used to assess whether samples from two independent groups (e.g. cell types) originated from the same distribution without assuming a Gaussian distribution. The Kruskal-Wallis one-way analysis of variance was used to test whether samples from two or more independent groups (e.g. PAG subdivisions) originated from the same distribution without assuming a Gaussian distribution. Where significance was detected using the Kruskal-Wallis test, the *post hoc* Dunn's test was used to analyse specific sample pairs, adjusting for multiple comparisons. A simple linear regression was used to model the relationship between the baseline firing frequency and the seal resistance or the age of the mouse.

Figures were composed using Affinity Designer.

2.3.2 Whole-cell patch-clamp recordings and pharmacology

Patch pipettes with 4-7 MΩ resistance were backfilled with intracellular solution. The reported membrane potential values were not corrected for liquid junction potentials.

> **Potassium methane sulfonate based intracellular solution (in mM):** 130 $KMeSO_3$, 10 KCl, 10 HEPES, 4 NaCl, 4 Mg-ATP, 0.5 Na_2-GTP, 5 Na-Phosphocreatine, 1 EGTA, and biocytin (1 mg/mL). pH was adjusted to 7.3-7.4 with KOH before adding the Na_2-GTP. Osmolality was verified to be between 285-295 mOsm/kg. The final solution was filtered (0.22 μm, Millex), divided in 250 μL or 500 μL aliquots, and stored in a freezer at −20°C until use.

Whole-cell patch-clamp recordings were obtained using an EPC 800 amplifier (HEKA) and following the procedure originally implemented by Neher and Sakmann (Hamill, Marty, *et al.*, 1981; Sakmann and Neher, 1984; Edwards, Konnerth, *et al.*, 1989; Gibb and Edwards, 1994). Signals were low-pass Bessel filtered at 5 kHz, sampled at 25 kHz, digitised with 16-bit resolution using a PCIe-6353 board (National Instruments), and recorded in LabVIEW using custom software. The soma of the target neuron was approached with positive pressure applied to the patch pipette and the tip was positioned in gentle contact with the cell membrane until a dimple was formed. The resistance of the pipette and the developing seal were continuously monitored using a voltage-clamp protocol with a holding potential of 0 mV and a test pulse of 5 mV with 50 ms duration repeated every 90 ms. Once a clear dimple was observed on the surface of the target neuron, positive pressure was released, holding current was applied to aid seal formation (voltage command was brought to −60 mV), and gentle suction was slowly applied until a gigaohm seal was obtained. Following the sealing procedure, pipette capacitance was cancelled, and brief suction pulses of growing intensity were applied to rupture the membrane patch and achieve whole-cell configuration. The resting membrane potential was determined immediately after

establishing the whole-cell configuration and experiments were continued only if neurons had a resting membrane potential more hyperpolarised than −45 mV. Whole-cell capacitance and series resistance (R_s) were estimated and compensated using the amplifier compensation controls. Input resistance and R_s were monitored continuously throughout the experiment, and R_s was compensated in current-clamp recordings. Only recordings from neurons with a stable R_s < 35 MΩ were analysed.

Upon termination of the recording, the anatomical location of the neuron within the PAG was recorded using a 4× objective (PLN, 0.1 numerical aperture, 18.5 mm working distance, Olympus). The rostro-caudal level of each slice was assigned based on comparisons with a mouse stereotaxic atlas (Franklin and Paxinos, 2008) and was used to approximate the coordinates and the PAG subdivision of each recorded neuron.

2.3.2.1 Pharmacology

To block fast glutamatergic and GABAergic synaptic transmission, as well as tonic $GABA_A$ receptor activation, 2 mM kynurenic acid (Sigma, Cat. No. K3375-5G) and 50 μM picrotoxin (Tocris, Cat. No. 1128) were added to the recording ACSF, respectively. Kynurenic acid is an antagonist of AMPA, NMDA, and Kainate glutamate receptors (Perkins and Stone, 1982; Elmslie and Yoshikami, 1985), whereas picrotoxin binds $GABA_A$ receptors and stabilises their shut state (Newland and Cull-Candy, 1992). When switching from normal recording ACSF to perfusing ACSF with drugs, slices were allowed to equilibrate for 10-20 minutes before the beginning of the recording.

2.3.2.2 Data analysis

The code used to analyse data from whole-cell patch-clamp recordings can be found on GitHub. Whole-cell recordings were analysed in Python 3.8 using custom-written routines.

The *input resistance* was calculated from the steady-state voltage measured in response to a hyperpolarising test pulse of either 500 ms or 1 s duration from a holding potential of −62.4 ± 2.7 mV (mean ± standard deviation, n=85 from 29 mice) in current-clamp mode. The seal resistance was calculated using Ohm's Law by dividing the recorded membrane's potential response over the magnitude of the test pulse current command. In the cases where several repetitions were available, the values from each sweep were averaged to obtain a seal resistance value for each neuron.

A depolarising step of either 500 ms or 1 s duration from a holding potential of −62.8 ± 2.8 mV (mean ± standard deviation, n=69 from 29 mice) was used to elicit a single action potential in current-clamp mode. In a minority of cases where none of the repetitions managed to elicit a single action potential, the first action potential of the sweeps in which two or a maximum of three action potentials were elicited was used. For each action potential, the peak was defined as the most positive value in the trace. For each neuron, the single action potentials across sweeps were cut, aligned at their peak, and averaged. The *trough* of the average action potential was defined as the most negative value within 3 ms after the action potential peak. The *afterdepolarisation* was defined as the most positive value within 8 ms after the trough. The *slow afterhyperpolarisation* was calculated by subtracting the most negative value within 40 ms after the trough, excluding the 8 ms used to detect the afterdepolarisation value, from the afterdepolarisation value. The *action potential half-width* was calculated as the time difference between the two points that cross the half-peak value, calculated by subtracting half the absolute magnitude (peak to trough) from the peak value. The *action potential threshold* was defined as the point where the derivative of the membrane potential (dV/dt) exceeded 20 mV/ms.

Statistical analysis was performed in GraphPad Prism (v9.3.1). Cells were pooled across animals for comparisons between cell types, PAG subdivision, and drug condition. The Mann-Whitney test was used to assess whether samples from two independent groups (e.g. cell types) originated from the same distribution without assuming a Gaussian distribution. The Kruskal-Wallis one-way analysis of variance was

used to test whether samples from two or more independent groups (e.g. PAG subdivisions) originated from the same distribution without assuming a Gaussian distribution. Where significance was detected using the Kruskal-Wallis test, the *post hoc* Dunn's test was used to analyse specific sample pairs, adjusting for multiple comparisons.

Figures were composed using Affinity Designer.

2.4 SINGLE-CELL RNA-SEQUENCING

In line with recent efforts to improve the accessibility and reproducibility of scientific methods, the methods described in this section have also been made available as a detailed step-by-step protocol for the isolation, processing, and sequencing of single PAG neurons (Pavón Arocas, Olesen, and Branco, 2021).

2.4.1 Isolation of single neurons from acute midbrain slices

$VGAT^+$ or $VGluT2^+$ neurons within the PAG of acute midbrain slices of transgenic mice were identified as described in section 2.3. Pipettes for aspiration were pulled with a horizontal micropipette puller (P-1000, Sutter) to yield a tip with 1-2 MΩ resistance. Prior to pulling, capillaries were flamed to smooth the edges and baked in an oven (E28, Binder) at 200°C for 2 hours to sterilise them. Pipettes were backfilled with recording ACSF (see section 2.2) containing 2 U/µL recombinant RNase inhibitor (Clontech, Cat. No. 2313A) and inserted into the pipette holder of the patch-clamp system described in section 2.3.

Prior to aspiration, the anatomical location of the neuron within the PAG was recorded using a 4× objective (PLN, 0.1 numerical aperture, 18.5 mm working distance, Olympus). The soma of the target neuron was approached with positive

pressure applied to the pipette to prevent any dirt or unwanted tissue from being aspirated. The tip was carefully positioned in gentle contact with the cell membrane of the target neuron and its fluorescence expression was confirmed. Positive pressure was released, and gentle suction was slowly applied to aspirate the neuron into the tip of the glass pipette. Suction was then stopped and replaced by minimal positive pressure while the pipette was carefully retracted from the slice tissue to avoid aspirating surrounding processes or tissue. Visual confirmation of successful single-cell isolation was obtained by examination of the pipette tip, where aspirated neurons typically remained attached. The pipette was removed from the bath and subsequently detached from the holder. The tip of the pipette was then broken into the bottom of a PCR tube (0.2 mL, Alpha Laboratories, Cat. No. LW2570), which had been kept on ice until use, containing 4 µL of lysis buffer: 1.8 µL 0.2% Triton X-100 (Sigma, Cat. No. T9284), 0.1 µL recombinant RNase inhibitor (Clontech, Cat. No. 2313A), 0.1 µL ERCC RNA spike-in Mix 1 (1:500,000 dilution, Thermo Fisher, Cat. No. 4456740), 1 µL oligo-$dT_{30}VN$ primer (10 µM, Sigma, Table 2.1), and 1 µL dNTP mix (10 µM, Thermo Fisher, Cat. No. R0192). Once broken, the pipette was quickly pulled out to avoid drawing the lysis buffer and the sample back into it by capillary action. Samples were vortexed for 10 seconds, spun down (700g for 10 seconds at room temperature), and immediately placed on dry ice, where they were kept until sample collection was complete. Samples were subsequently stored at −80°C until cDNA synthesis.

In a typical experiment, a total of 24 neurons were collected in equal proportions from each hemisphere and PAG subdivision (dmPAG, dlPAG, lPAG, vlPAG), following a sequence pseudo-randomised for each animal. A negative control containing only the 4 µL of lysis buffer was included for each batch of 24 neurons to assess DNA contamination during the processing steps. To assess the amount of ambient mRNA that was added by my isolation method, negative controls were obtained by inserting the glass pipette in the slice tissue without aspirating any neuron. In some instances, whole-cell patch-clamp recordings were obtained from the target neuron prior to aspiration, as described in section 0. A total of 588 neurons were collected from 25 mice (13 female, 12 male): 257 $VGAT^+$ neurons from 11 mice (7-9

weeks old, five females, six males) and 331 VGluT2$^+$ neurons from 14 mice (6-9 weeks old, eight females, six males).

2.4.1.1 Image registration

Images with the anatomical location of each isolated neuron were registered to the Allen Mouse Brain Common Coordinate Framework (Wang, Ding, *et al.*, 2020) using the Slice Histology Alignment, Registration, and Probe Track analysis tool (SHARP-Track) (Shamash, Carandini, *et al.*, 2018) as described in the GitHub wiki. Images obtained had a size of 1280x1024 pixels with a pixel size of 3.125 µm/pixel, as calibrated using a 1 mm stage microruler with 10 µm divisions (Thorlabs, Cat. No. R1L3S2P). Coordinates within the Common Coordinate Framework were obtained for each neuron and used to validate the PAG subdivision of each aspirated neuron and to generate 3D renderings using *brainrender* (Claudi, Tyson, *et al.*, 2021) and the BrainGlobe Atlas API (Claudi, Petrucco, *et al.*, 2020). The code for image registration using SHARP-Track and to generate plots with *brainrender* can be found on GitHub (here and here, respectively).

2.4.2 Smart-seq2 processing and sequencing of single neurons

Isolated neurons were processed following the Smart-seq2 protocol (Picelli, Faridani, *et al.*, 2014) using the primers listed in Table 2.1. When possible, all steps were performed under a UV-sterilised hood with laminar flow. To prevent degradation of RNA and cross-contamination with DNA from previous samples, all surfaces were cleaned with RNaseZap (Ambion or Invitrogen, Cat. No. AM9780) and DNA-OFF (Takara, Cat. No. 9036) solutions before placing the samples on them. Pipettes and gloves were sprayed with RNaseZap and all reagents were exclusively used for this procedure.

Name	Sequence (5'-3')	Use	Source
Oligo-dT primer (pi5)	AAGCAGTGGTATCAACGCAGA GTACT$_{30}$CG	Anneals to RNAs containing a poly(A) tail	Sigma
Oligo-dT primer (pi6)	AAGCAGTGGTATCAACGCAGA GTACT$_{30}$AG	Anneals to RNAs containing a poly(A) tail	Sigma
LNA-modified TSO	AAGCAGTGGTATCAACGCAGA GTACATrGrG+G	Template Switching Oligonucleotide	Qiagen
ISPCR	AAGCAGTGGTATCAACGCAGA GT	PCR preamplification primer	Sigma

Table 2.1. List of primers used in the Smart-seq2 protocol.

2.4.2.1 Optimisation of the Smart-seq2 protocol

Commercially available mouse brain total RNA (Takara, Cat. No. 636601) was used as sample material for the initial test runs of the protocol. 10-fold serial dilutions of the total RNA were prepared in nuclease-free water, aliquoted to minimise freeze-thaw cycles, and stored at −80°C until use. Samples of different starting RNA concentration were used to test the effectivity of Smart-seq2. Once good results were consistently obtained with this approach, the protocol was tested with individual neurons aspirated from acute midbrain slices.

2.4.2.2 Batch and experimental design

In single-cell RNA-sequencing experiments, *batch effects* refer to the systematic differences in the observed gene expression profiles that are introduced by processing samples in different batches and that are unrelated to the experimental questions at hand. To mitigate the chances of introducing confounding factors at the data collection stage that could mask biological differences related to the cell type and PAG subdivision, the two main variables of interest in this study, a pseudo-randomised order of aspiration was generated using a python script (available on GitHub). This ensured that, in any given experimental day, a total of 24 VGluT2$^+$ or VGAT$^+$ neurons

were aspirated, consisting of 6 dmPAG neurons, 6 dlPAG neurons, 6 lPAG neurons, and 6 vlPAG neurons, with half the neurons in each subdivision coming from each of the hemispheres.

Similar to the limit in the number of neurons that could be aspirated during one experiment (collection batch), there was a limit in the number of samples that could be processed at once with the Smart-seq2 protocol (processing batch). A properly balanced batch design would ensure that, in any given processing batch, the sample distribution equally covered different cell types, PAG subdivisions, animals, and experimental days. On the other hand, an unbalanced batch design would, for instance, consist of a processing batch were all the samples being processed belonged to the same cell type and originated from the same animal. In this study, approximately half of the processing batches followed an unbalanced design (i.e. all the samples in a processing batch came from the same animal and experimental day, and belonged to the same cell type), whereas the other half were successfully balanced (i.e. samples within a processing batch came from different animals and experimental days, and belonged to each cell type and PAG subdivision in the same proportions). The data analysis steps described in the following sections attempted to account for this in the best possible way.

Positive controls and negative controls were added in each collection and processing batch. As a positive control, ERCC spike-ins (RNA transcripts of known sequence and quantity) were added to the lysis buffer of each PCR tube. As a negative control, PCR tubes containing only lysis buffer were added to each processing batch to check for contamination. In earlier experiments, stab controls (in which the pipette tip went into the slice tissue, but no neuron was aspirated) were added to assess the amount of ambient mRNA introduced by the sample collection approach.

2.4.2.3 cDNA synthesis and preamplification

To obtain cDNA from the single-cell lysates, reverse transcription of mRNA was performed as follows. Frozen samples were thawed and incubated at 72°C in a thermal cycler (T100, Bio-Rad) for 3 minutes and subsequently kept on ice. All incubation steps in the Smart-seq2 protocol were done with a heated lid set to 105°C. Samples were spun down (700g for 10 seconds at room temperature) and placed back on ice. At this point, the oligo-dT primer had hybridized to the poly(A) tail of the mRNA molecules of the sample. Each sample containing approximately 4.3 µL lysis reaction was brought up to a volume of 10 µL by adding 5.7 µL reverse transcription master mix containing: 0.5 µL SuperScript II reverse transcriptase (200 U/µL, Invitrogen, Cat. No. 18064-014), 0.25 µL recombinant RNase inhibitor (40 U/µL, Clontech, Cat. No. 2313A), 2 µL SuperScript II first-strand buffer (5x, Invitrogen, Cat. No. 18064-014), 0.5 µL DTT (100 mM, Invitrogen, Cat. No. 18064-014), 2 µL betaine (5 M, Sigma, Cat. No. B0300-1VL), 0.06 µL $MgCl_2$ (1 M, Sigma, Cat. No. M8266), 0.1 µL template switching oligonucleotide (100 µM, TSO, Qiagen, Cat. No. 339412, Table 2.1), and 0.29 µL nuclease-free water (Qiagen, Cat. No. 10977035). Samples were spun down (700g for 10 seconds at room temperature) and then subjected to the reverse transcription program in the thermal cycler (Table 2.2).

Cycle	Temperature (°C)	Time
1	42	90 min
2-11	50	2 min
	42	2 min
12	70	15 min
13	4 or 10	Hold

Table 2.2. Reverse transcription program.

The resulting cDNA was amplified by adding 12.5 µL KAPA HiFi Hotstart ReadyMix (2x, KAPA Biosystems, Cat. No. KK2601), 0.25 µL ISPCR primer (10 µM,

Sigma, Table 2.1), and 2.25 µL nuclease-free water (Qiagen, Cat. No. 10977035) to a final volume of 25 µL. Samples were vortexed for 10 seconds, spun down (700g for 10 seconds at room temperature), and subjected to the PCR preamplification program in the thermal cycler (Table 2.3). Amplified samples were stored at −20°C until purification.

Cycle	Temperature (°C)	Time
1	98	3 min
2-19	98	20 s
	67	15 s
	72	6 min
20	72	5 min
21	4	Hold

Table 2.3. PCR preamplification program.

2.4.2.4 cDNA purification and quality control

Samples were thawed and then purified using Ampure XP beads (Beckman Coulter, Cat. No. A63880), which were allowed to equilibrate to room temperature for 15 minutes and vortexed well before use. 25 µL Ampure XP beads (1:1 ratio) were added to each sample and mixed by carefully pipetting up and down until the solution was homogeneous. Samples were incubated for 8 minutes at room temperature to let the cDNA bind to the beads and then placed on a magnetic stand (Invitrogen, Cat. No. AM10027) until the solution was clear and the beads had been collected at the bottom of the tube. With the samples still on the magnetic stand, the liquid was carefully removed without disturbing the beads. Samples were then washed twice by adding 200 µL 80% ethanol (VWR, Cat. No. 20821.330), incubating for 30 seconds, and removing the ethanol without disturbing the beads. Beads were then allowed to dry completely to remove any trace of ethanol by leaving at room temperature for 5 minutes. Samples

were eluted by adding 17.5 μL elution buffer solution (Qiagen, Cat. No. 19086), mixing ten times by pipetting up and down to resuspend the beads, and incubated off the magnetic stand for 2 minutes. Samples were placed back on the magnetic stand and left for 2 minutes or until the solution was clear and the beads had accumulated at the bottom of the tube. To ensure minimal bead carryover, 15 μL of the supernatant containing the purified cDNA from each sample was collected without disturbing the beads and transferred to a fresh PCR tube. Purified samples were stored at −20°C until quality checks were performed.

Three independent measures were typically used to quality check the purified samples. First, sample purity was estimated using a NanoDrop 2000 spectrophotometer (Thermo Scientific). The ratio of absorbance at 260 and 280 nm ($A_{260/280}$ ratio) is routinely used to assess the purity of RNA and DNA preparations (Wilfinger, Mackey, and Chomczynski, 1997; Walton and O'Connor, 2018). Samples with an $A_{260/280}$ ratio below 1.8 were considered to have failed this first quality check. Second, cDNA concentration of the purified samples was determined using the Qubit dsDNA High-Sensitivity Assay Kit (Invitrogen, Cat. No. Q32851) in a Qubit 2.0 fluorometer (Life Technologies). The fluorometer was used to measure the concentration of RNA or cDNA bound to a fluorescent dye. Samples with a Qubit-measured concentration below 1 ng/μL were considered to have failed this second quality check. Third, the size distribution of the cDNA of each sample was determined using Agilent High-Sensitivity DNA chips (Agilent Technologies, Cat. No. 5067-4626) run in an Agilent 2100 Bioanalyzer (Agilent Technologies). Bioanalyzer profiles with a peak in the 1500-3000 bp range, a small number of fragments below 500 bp, and small number of primer dimers indicated that the majority of cDNA had been produced from intact mRNA and the sample was considered of good quality. Samples that passed the NanoDrop and Qubit quality checks and showed good Bioanalyzer profiles were deemed of good quality and stored at −20°C until sequenced.

2.4.2.5 cDNA library preparation and sequencing

Out of the 588 collected and processed PAG neurons, a total of 516 neurons (253 $VGAT^+$ and 263 $VGluT2^+$) were of good quality and selected for sequencing. cDNA library preparation and sequencing were performed externally by the Barts London Genome Centre at the Blizard Institute (Barts and The London School of Medicine and Dentistry, Queen Mary University of London). Prior to library generation, cDNA samples were quantified using the Qubit dsDNA High-Sensitivity Assay Kit and the Qubit 2.0 Fluorometer (Life Technologies), and a subset of cDNAs were checked for quality using the Agilent 2200 Tapestation (Agilent Technologies). Libraries were prepared using the Illumina Nextera XT Sample Preparation Kit (Illumina Inc.) with an input of 150 pg of cDNA per sample. Resulting libraries were checked for average fragment size using the Agilent D1000 ScreenTape (Agilent Technologies) and were quantified using the Qubit dsDNA High-Sensitivity Assay Kit. Equimolar quantities of each sample library were pooled together and 75 bp paired-end reads were generated for each library using the Illumina NextSeq 500 High-output sequencing kit, with a target sequencing depth of ~4 million reads per sample.

2.4.3 RNA sequence alignment and quantification

The initial analysis steps, including read alignment and quantification, were performed externally by the Barts London Genome Centre at the Blizard Institute, Queen Mary University of London. Raw reads were quality checked with `FastQC` (Andrews, 2010) and trimmed from adaptor sequences and low-quality bases. Before proceeding with read alignment, custom genome reference sequences were created for the transgenes used to label neurons (Cre, EYFP, and tdTomato), the ERCC Mix 1, and TSO concatemers. Reads were aligned to the mouse genome (mm10, GRCm38.96) and the custom reference sequences using `STAR` (Dobin, Davis, *et al.*, 2013). A mapping quality of `MAPQ=255` was specified to identify and keep only the reads that uniquely mapped

to one genome locus. Reads with a mapping quality value below 255 (multimapping reads) were filtered out. Duplicated and unaligned reads were also removed.

Uniquely mapping reads were quantified using the `RefSeq Transcripts 83` annotation model, generating counts for both genes and transcripts. To avoid losing any reads, the minimum number of counts required for a read to be classified as detected was set to 0. A table in which each column was a PAG neuron and each row contained the number of counts for each gene or transcript was generated. The table containing the gene counts was used for downstream analysis.

2.4.4 Data pre-processing and analysis

Data were analysed with custom-written routines in R (v3.6.1) using software from the open-source Bioconductor project (v3.10) (Huber, Carey, *et al.*, 2015). The bulk of the code was written following the *simpleSingleCell* workflow package (Lun, McCarthy, and Marioni, 2016), the Orchestrating Single-cell Analysis book (Amezquita, Lun, *et al.*, 2020), and the course tutorial from the Hemberg Lab (Andrews, Kiselev, *et al.*, 2021). The different steps of the analysis pipeline are available as R Markdown files on GitHub.

Cell-level quality control. The expression matrix with the total gene counts per sample and the corresponding metadata were used to create `SingleCellExperiment` object. Several metrics were used to quality check the dataset. Samples that had a library size below 400,000 or above 4.6 million reads uniquely mapping to annotated genes were removed. Samples with less than 5,000 or more than 13,000 genes detected were also discarded. Samples that had more than 15% of reads mapping to mitochondrial genes, more than 1% of reads mapping to ERCC spike-ins, or more than 5% of reads mapping to TSO concatemers were excluded from further analysis. Samples with more than 20% (in the case of VGAT::Cre neurons) or 30% (in the case of VGluT2::Cre neurons) of reads mapping to ribosomal genes were discarded. To rule out any potential contamination, samples with reads mapping to the wrong fluorophore (i.e.

Cre::EYFP neurons with reads mapping to tdTomato or Cre::tdTomato neurons with reads mapping to EYFP) were also excluded. In addition, samples in which more than 60% of the reads were consumed by the 100 most expressed genes were discarded.

Gene-level quality control. Predicted genes, genes not expressed in any cell, and weakly expressed genes (to be kept, a gene had to be counted at least once in at least 3 or more cells) were removed from the dataset.

Normalisation. Size factors for each cell were estimated using the *scran* package (Lun, McCarthy, and Marioni, 2016) and used to calculate normalised expression values for each sample using *scater* (McCarthy, Campbell, *et al.*, 2017). Briefly, each normalised value was defined as the $\log_2$-ratio of each count to the size factor for the corresponding cell, after adding a pseudo-count of 1 to avoid undefined values at zero counts. The resulting normalised expression values were used for dimensionality reduction, clustering, and differential expression analysis.

Feature selection. The squared coefficient of variation (CV^2) and the mean of the expression values were calculated using the function `modelGeneCV2` from the *scran* package (Lun, McCarthy, and Marioni, 2016). Importantly, the expression values used corresponded to the counts *after* scaling them by the size factors but *prior* to log-transformation. A trend was then fitted with the `fitTrendCV2` function, and for each gene the fitted value was used as a proxy of technical noise. Under the assumption that most genes exhibit low baseline levels of variation that is not biologically interesting, the ratio of the total CV^2 to the trend was used to rank interesting genes, with large ratios being indicative of strong biological heterogeneity. The top 15% of genes with the largest ratio were selected. Before proceeding with downstream analysis, uninformative genes were removed from the dataset. These included spike-ins, TSO concatemers, mitochondrial genes, ribosomal genes, sex-specific genes (chromosomes X and Y), transgenes (Cre, EYFP, and tdTomato), and the transporters used to label and target the PAG neurons (VGAT or *Slc32a1*, and VGluT2 or *Slc17a6*). From the 19,574 genes left in the dataset after gene-level quality control, a total of 2,910 were selected as the most highly variable genes and used for downstream analysis.

Correction of batch effects. The `removeBatchEffect` function from the *limma* package (Ritchie, Phipson, *et al.*, 2015) was used to fit a linear model to the expression profile of each gene. For each cell, the *processing batch* was set as the blocking factor and the combination of both *cell type* and *PAG subdivision* was introduced as the design matrix to describe the comparisons between samples that should be left untouched. `removeBatchEffect` was then used to perform a linear regression on the data, set the coefficients corresponding to the blocking factor to zero, and recalculate a set of new expression values without the unwanted batch effect.

Principal component analysis. Principal component analysis (PCA) was performed with the `runPCA` function from *scater* (McCarthy, Campbell, *et al.*, 2017) on (1) the log-normalised and (2) the log-normalised and batch corrected gene expression values of the set of highly variable genes identified during feature selection. The `getClusteredPCs` function from *scran* (Lun, McCarthy, and Marioni, 2016) was used to determine the number of principal components (PCs) needed to capture as much of the variation stemming from biological signal as possible without retaining so much signal that the noise begins to mask the underlying structure of the data. After running `getClusteredPCs` on the dataset, the top 17 PCs when using the log-normalised values and the top 14 PCs when using the corrected values were selected for dimensionality reduction and unsupervised clustering.

Uniform manifold approximation and projection. The `runUMAP` function implemented in *scater* (McCarthy, Campbell, *et al.*, 2017) was used to perform uniform manifold approximation and projection (UMAP) on the log-normalised and batch corrected gene expression values of the set of highly variable genes identified during feature selection. To mitigate the computational intensity of the approach and leverage the noise removal provided by PCA, the `runUMAP` function was run on the top 14 PCs. To ensure reproducibility of the results, the function was tested with a range of hyperparameters and a set of seeds. The UMAP obtained with `n_neighbors=15` and `min_dist=0.01` was found to provide a clear visualisation that captured the main features obtained across hyperparameters and seeds.

Graph-based clustering. The `buildSNNgraph` function from the *scran* package (Lun, McCarthy, and Marioni, 2016) was used to identify the `k=5` nearest neighbours of each cell and build a graph based on the Euclidean distances between the log-normalised expression values of the set of highly variable genes, keeping only the top 17 PCs. The Jaccard similarity index was used to weight the edges between all pairs of cells that shared at least one neighbour, and the Louvain algorithm (Blondel, Guillaume, *et al.*, 2008) implemented by the *igraph* package (Csardi and Nepusz, 2006) was used to identify clusters. The `clusterModularity` function from *scran* was used to evaluate the modularity of the graph, and the `bootstrapCluster` function from *scran* was used to evaluate the stability of the graph-based clustering solution over 1000 bootstrap iterations.

Consensus clustering. As an alternative clustering approach, the Single-Cell Consensus Clustering (SC3) tool for unsupervised clustering of single-cell RNA-sequencing data was used on the data (Kiselev, Kirschner, *et al.*, 2017). After testing a range of parameters, the solution obtained with `k=4` was used to identify clusters in the dataset. To examine the stability of the identified clusters, a consensus matrix was calculated to represent the similarity between each pair of cells, with a similarity of 0 indicating that the two cells were always assigned to different clusters by the different clustering algorithms implemented by SC3, and a similarity of 1 indicating that the two cells were always assigned to the same cluster.

Differential expression analysis. The `findMarkers` function from the *scran* package (Lun, McCarthy, and Marioni, 2016) was used to identify marker genes differentially expressed between $VGAT^+$ and $VGluT2^+$ neurons, between the factor resulting from the combination of *cell type* and *PAG subdivision*, and between the identified clusters. To perform pairwise comparisons between the defined groups of observations, the Wilcoxon rank sum test (also known as the Wilcoxon-Mann-Whitney test) was used by setting `test=wilcox` on `findMarkers`. The Wilcoxon test statistic is proportional to the area-under-the curve (AUC). In a pairwise comparison, AUCs of 1 or 0 indicate that the two clusters or conditions have perfectly separated expression distributions.

To restrict the results from the pairwise comparisons to genes upregulated in a unique cluster or condition, the parameters `direction=up` and `pval.type=all` were used. To minimise the effects of unwanted factors of variation on the results, the sex of the mouse from which each cell was obtained was provided to the `block` parameter of `findMarkers`. Before performing the differential expression analysis and to avoid masking any effects related to the desired conditions, the cells belonging to the small cluster labelled with a high expression of macrophage-related genes were excluded from the dataset. Only genes with a Benjamini-Hochberg adjusted p-value of less than 0.05 were considered for interpretation.

3 BIOPHYSICAL PROPERTIES OF PERIAQUEDUCTAL GRAY NEURONS

In this first chapter, I used patch-clamp recordings to characterise the biophysical properties of PAG neurons in a cell type-specific manner. To that end, I obtained acute midbrain slices from transgenic mice in which either glutamatergic or GABAergic neurons expressed a fluorophore under the vesicular glutamate transporter 2 (VGluT2) or the vesicular GABA transporter (VGAT) promoter, respectively. In a first set of experiments, I employed targeted loose-seal cell-attached recordings to investigate the baseline firing properties of VGluT2^{+} and VGAT^{+} neurons across the four PAG subdivisions. Next, in a second set of experiments, I used whole-cell recordings to extract the intrinsic electrophysiological properties of VGluT2^{+} and VGAT^{+} neurons, this time focusing on the dorsal columns of the PAG (dmPAG and dlPAG), which have been shown to mediate the initiation of escape behaviour in response to imminent threats (Behbehani, 1995; Fanselow, Decola, *et al.*, 1995; Brandão, Anseloni, *et al.*, 1999; Deng, Xiao, and Wang, 2016; Tovote, Esposito, *et al.*, 2016; Watson, Cerminara, *et al.*, 2016; Evans, Stempel, *et al.*, 2018). The results from this two-pronged approach may have strong implications in the field's quest to dissect and understand the functional heterogeneity of the midbrain PAG.

3.1 EXPERIMENTAL APPROACH

3.1.1 Targeted patch-clamp recordings in acute midbrain slices of transgenic mice

The acute brain slice remains an essential preparation for studying the nervous system (Edwards, Konnerth, *et al.*, 1989). For decades, acute brain slices have been combined with the patch-clamp technique (Neher and Sakmann, 1976; Sakmann and Neher, 1984; Gibb and Edwards, 1994) for investigating the biophysical properties of different cell types in a multitude of brain areas and animal species, including humans (Blanton, Lo Turco, and Kriegstein, 1989; Madry, Kyrargyri, *et al.*, 2018; Gouwens, Sorensen, *et al.*, 2019; Dorst, Tokarska, *et al.*, 2020; McCauley, Petroccione, *et al.*, 2020; Campagnola, Seeman, *et al.*, 2021). More recently, the refinement of viral and gene-editing approaches and the development of techniques such as optogenetics, voltage and calcium imaging, and single-cell transcriptomics (Chiang, 1998; Carlson and Coulter, 2008; Miesenböck, 2011; Cadwell, Palasantza, *et al.*, 2016; Fuzik, Zeisel, *et al.*, 2016; Cadwell, Scala, *et al.*, 2017) have significantly expanded the range of questions that can be investigated with this preparation, from the workings of individual neurons (Muñoz-Manchado, Bengtsson Gonzales, *et al.*, 2018; Gouwens, Sorensen, *et al.*, 2020; Hanemaaijer, Popovic, *et al.*, 2020; Bakken, Jorstad, *et al.*, 2021; Berg, Sorensen, *et al.*, 2021; Callaway, Dong, *et al.*, 2021; Kalmbach, Hodge, *et al.*, 2021) to their roles in neural circuits and behaviour (Evans, Stempel, *et al.*, 2018; Weiler, Bauer, *et al.*, 2018; Mandelbaum, Taranda, *et al.*, 2019; Vale, Campagner, *et al.*, 2020; Fratzl, Koltchev, *et al.*, 2021).

Despite the long tradition of patch-clamp experiments, the success rate of the slice preparation and the quality of the resulting tissue can vary depending on the brain region of interest and the age of the animal. This has spurred the development of many adaptations of the slicing protocol (Aitken, Breese, *et al.*, 1995; Lipton, Aitken, *et al.*, 1995), seeking to find the optimal solution for specific animal ages (Moyer and Brown,

1998; Ting, Daigle, *et al.*, 2014), cell types (Tanaka, Tanaka, *et al.*, 2008; Ting, Kalmbach, *et al.*, 2018), and cellular compartments (Bischofberger, Engel, *et al.*, 2006). Some modifications involved adding specific compounds to reduce edema, such as ascorbate (Brahma, Forman, *et al.*, 2000) or HEPES (MacGregor, Chesler, and Rice, 2001). Others revolved around parameters like the temperature during slicing (Huang and Uusisaari, 2013; Eguchi, Velicky, *et al.*, 2020), the incubation system (Buskila, Breen, *et al.*, 2015), or the composition of the solutions (Ting, Daigle, *et al.*, 2014; Ting, Lee, *et al.*, 2018). It is thus important to test different combinations of solutions, brain extraction methods, and incubation strategies before starting a set of experiments, in order to find the approach that reliably provides the best tissue quality for the experiments at hand.

During the course of this thesis, I strived to continually improve the quality of my slices. In line with recent efforts to improve the accessibility and reproducibility of scientific methods, I elaborated a step-by-step guide for preparing acute slices from the midbrain of young adult mice and made it available online (Pavón Arocas and Branco, 2022). In this chapter, I combined the preparation of acute midbrain slices described in section 2.2 with the use of transgenic lines and pharmacology to perform patch-clamp recordings from genetically labelled subsets of neurons in the PAG and its anatomical subdivisions (Figure 3.1).

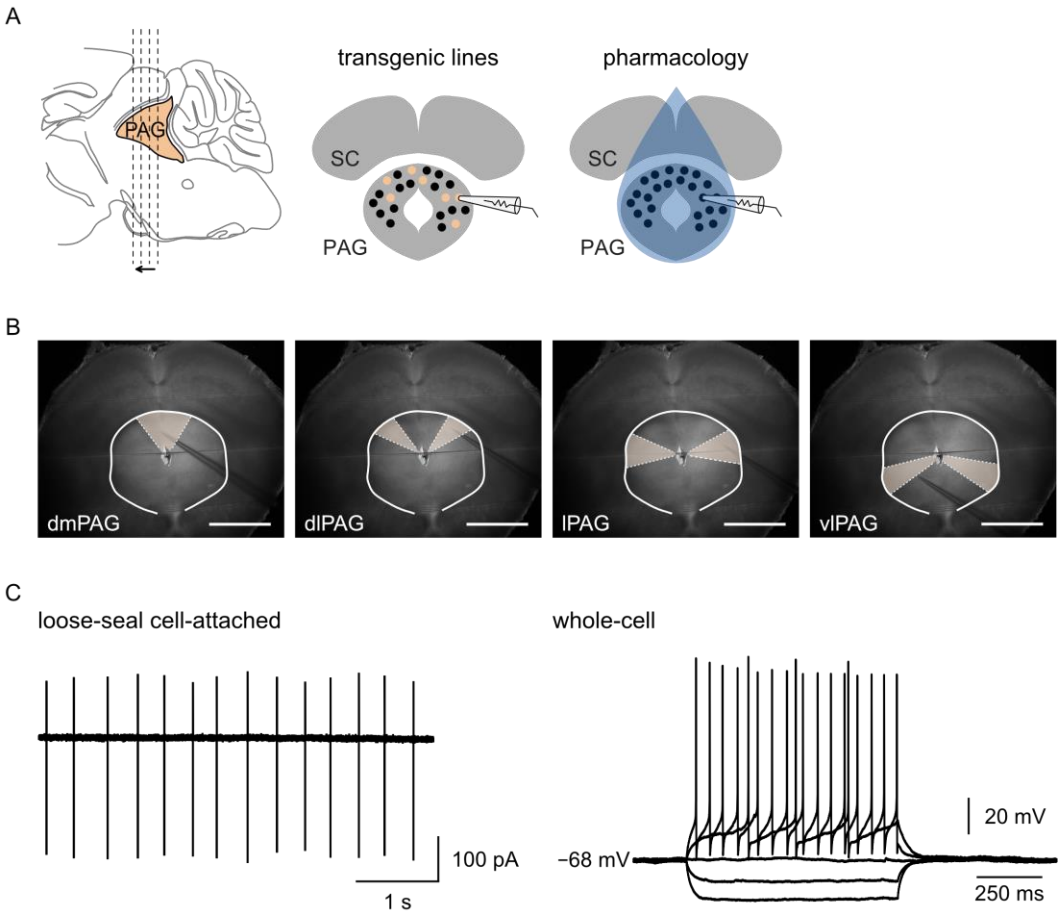

Figure 3.1. Targeted patch-clamp recordings in acute midbrain slices of transgenic mice. (**A**) Schematics illustrating the use of acute midbrain slices in combination with transgenic lines to target genetically defined subsets of cells and pharmacology to investigate neurons in a midbrain area of interest. On the left, PAG is highlighted in yellow, and the dashed lines and arrow indicate how coronal slices are obtained. In the middle, yellow circles represent a genetically identified subset of neurons labelled by the expression of a fluorophore under a specific promoter. On the right, the blue shading represents the wash-in of a drug dissolved in the solution bathing the slice. Adapted from Franklin and Paxinos (2008). (**B**) Example images from experiments targeting midbrain neurons in different anatomical subdivisions of the PAG in the same slice. Scale bars are 1 mm. Abbreviations indicate the different PAG subdivisions as described in Franklin and Paxinos (2008), highlighted in yellow: dorsomedial (dmPAG), dorsolateral (dlPAG), lateral (lPAG), and ventrolateral (vlPAG). (**C**) (Left) Spontaneous electrical activity of a PAG neuron during a loose-seal cell-attached recording. Each vertical line is the recorded current from an action potential. (Right) Voltage response to five step current injections of a PAG neuron during a whole-cell recording.

3.1.2 Cell-attached voltage-clamp recordings to measure action potential currents

The whole-cell patch-clamp technique remains the gold standard to record voltage or current dynamics of a cell with unparalleled resolution and sensitivity (Neher and Sakmann, 1976; Hamill, Marty, *et al.*, 1981; Fenwick, Marty, and Neher, 1982). However, to measure the baseline activity of a neuron without interfering with its internal milieu one needs to be able to record from it without rupturing the cell membrane. The cell-attached configuration, in which the glass pipette is attached to the cell membrane without breaking it, allows experimenters to achieve this and can be used to record the spontaneous firing activity of individual neurons in acute brain slices (Sakmann and Neher, 1984; Kondo and Marty, 1998). The popularity of this approach is likely due to the fact that these recordings are stable, relatively easy to achieve, and, if done properly, they allow the measurement of firing activity without changing it. But for this to remain true researchers must ensure that the right conditions are met. The mode at which the amplifier is set, the command potential, and the seal resistance are all determinants of the type of data that can be obtained with this technique and of how the cell will be affected during the experiment.

Under certain circumstances, setting the amplifier to current-clamp mode during a cell-attached recording might make it possible for the experimenter to measure synaptic potentials and estimate the resting membrane potential of a target neuron (Mason, Simpson, *et al.*, 2005; Perkins, 2006). Conversely, by switching the amplifier to voltage-clamp mode the cell-attached configuration can be used to easily record action potential currents (Barbour and Isope, 2000; Mason, Simpson, *et al.*, 2005; Hirono and Obata, 2006; Perkins, 2006; Alcami, Franconville, *et al.*, 2012; Mlinar, Montalbano, *et al.*, 2016). Even though the cell-attached voltage-clamp configuration will not voltage-clamp the cell, it is important to correctly use the command voltage, as the amplifier can generate current and the command set by the experimenter can change the firing activity of the cell that is being recorded (Barbour and Isope, 2000; Perkins, 2006). In voltage-clamp mode, the patch and cell resistance are in series with

each other but in parallel to the seal resistance (for a schematic of the circuit see Figure 6 of Perkins, 2006). This means that any current generated by the amplifier will split, with more current passing through the path of least resistance to the ground. Some of the generated current will pass across the patch of membrane and will then leave the cell through its membrane resistance, thus depolarising the cell (Barry and Lynch, 1991; Sherman-Gold, 2008). If the seal resistance is larger than the patch and cell resistance, as would be the case if using a tight seal, most of the current will flow across the cell. To record spontaneous firing activity in cell-attached voltage-clamp mode without affecting the cell membrane potential, the command potential needs to be set to the value at which no current flows from the amplifier through the patch. The correct value will be the one at which the amplifier current is at 0 pA (Perkins, 2006). This is crucial when recording in cell-attached mode with a tight seal but is less important with very loose seals, as in this case most of the current generated by the amplifier will flow through the seal (now the path of least resistance) rather than the patch.

The reason behind using voltage-clamp mode to record action potential currents and current-clamp mode to record synaptic potentials becomes apparent when looking at their respective circuit configurations (for a comparison of recordings obtained with the two modes and a schematic of the circuit see Figures 12 and 13 of Perkins, 2006). When the membrane potential of the cell being recorded in cell-attached is changing, the membrane patch acts as a resistor and capacitor in parallel. In voltage-clamp mode, the capacitor aspect of the membrane patch offers the path of lowest impedance for fast events (i.e. action potential currents) but not for slow events (i.e. synaptic potentials). This means that, in the cell-attached voltage-clamp configuration, most of the action potential current recorded will be capacitive current. On the other hand, in current-clamp mode the patch of membrane becomes a low-pass filter: due to the charging of the capacitor the membrane patch slows down the apparent kinetics of fast events and reduces the magnitude of fast changes in membrane potential. The cell-attached current-clamp configuration will let slow synaptic potentials pass largely unaffected but will highly filter the amplitude and kinetics of fast action potential currents (Perkins, 2006).

To summarise, cell-attached voltage-clamp recordings are well-suited to measure the firing activity of a target cell. They are easier and faster to achieve than perforated patch-clamp recordings (Horn and Marty, 1988; Kyrozis and Reichling, 1995) and, unlike whole-cell recordings, they do not disturb the intracellular contents of the cell of interest. Thus, if done properly, cell-attached voltage-clamp recordings can be used to successfully record the firing rate of a neuron without altering it.

3.1.3 Loose-seal cell-attached recordings to measure the firing activity of high-input resistance neurons

Besides the patch configuration (whole-cell or cell-attached), the amplifier mode (voltage-clamp or current-clamp), and the holding potential, it is necessary to consider how the other decisions made in terms of experimental approach will affect the data to be obtained. These decisions include the solution used in the pipette, the time from seal formation at which the data are obtained, and the value of the seal resistance.

As I have already discussed, the command potential in cell-attached voltage-clamp recordings can distort the firing rate one is trying to record (Perkins, 2006). In cells with a high input resistance such as those in the PAG (Lovick and Stezhka, 1999), the magnitude of this effect varies with the composition of the solution used in the pipette: potassium-based solutions have a larger effect on the neuron's firing rate than sodium-based solutions (Alcami, Franconville, *et al.*, 2012). Furthermore, if the pipette solution and the bath solution are different, there will be a liquid junction potential that will contribute to the distortion (Barry and Lynch, 1991; Neher, 1992). To avoid these pitfalls, one should opt for a sodium-based solution with the same composition of the bath solution.

Another variable that can impact the quality of the recorded data is the time lapsed since seal formation. During seal formation and up to a minute after establishing a seal,

the recorded action potential currents are variable in shape and magnitude, which has been suggested to reflect membrane instability or a transient elevation of intracellular calcium concentration (Alcami, Franconville, *et al.*, 2012). After that, the recorded firing rate remains stable during the first four minutes, beyond which it gradually increases with time (Alcami, Franconville, *et al.*, 2012). This may be due to mechanical stress originated from the glass-membrane contact, is more pronounced if using a tight seal instead of a loose one, and can be aggravated by applying suction, which would lead to an increased activity of mechanosensitive channels in the patch (Suchyna, Markin, and Sachs, 2009; Alcami, Franconville, *et al.*, 2012). These effects can be minimised by pre-exposing the tip of the pipette to slice tissue to avoid direct contact between the cell membrane and the pipette glass and by applying minimal suction when forming the seal (Barbour and Isope, 2000; Alcami, Franconville, *et al.*, 2012).

In these experiments, I took the factors described in this and the previous section into account and implemented the following strategy to minimise the introduction of errors and artifacts that could distort the firing rate measured from PAG neurons:

1. Used voltage-clamp cell-attached recordings to measure action potential currents without changing the intracellular milieu of the target neuron.

2. Set the command potential to the value at which the amplifier current was at 0 pA, to minimise the chances of any current generated by the amplifier flowing through the patch of membrane and changing the neuron's firing rate.

3. Filled the pipette with a sodium-based solution with the same composition of the bath solution, to avoid any errors introduced by the presence of a liquid junction potential, to weaken the pipette-cell coupling, and to reduce the effects that any current originating from the amplifier could have on the firing rate.

4. Pre-exposed the tip of the pipette to slice tissue and applied the minimum amount of suction needed to establish a loose seal (<40 MΩ), to minimise the mechanical stress associated with the glass-membrane contact.

5. Discarded the first minute of recording, when results were distorted by seal instability, and only used the data from minutes 2-4 for analysis, to avoid the artefactual increase in firing rate that gradually appears after minute five.

3.2 BASELINE FIRING PROPERTIES OF PERIAQUEDUCTAL GRAY NEURONS

To investigate the baseline firing properties of PAG neurons, I obtained targeted patch-clamp recordings from fluorescently labelled neurons in acute midbrain slices of VGAT::EYFP, VGAT::tdTomato, VGluT2::EYFP or VGluT2::tdTomato mice. For each mouse, I established a pseudo-random order to ensure I equally sampled the different PAG subdivisions (dmPAG, dlPAG, lPAG, vlPAG) and hemispheres (Figure 3.2). To minimise the risk of introducing any distortions to the recorded firing frequency of the target neuron, I established loose-seal cell-attached recordings (seal resistance 14.2 ± 0.2 MΩ, mean ± SEM; n=241 from 47 mice) in voltage-clamp mode, using regular ACSF in the recording pipette and carefully maintaining the holding current at 0 ± 20 pA. A summary of the anatomical location within the PAG of all the cells recorded following this approach can be found in Figure 3.2B (see section 2.3.1 for details).

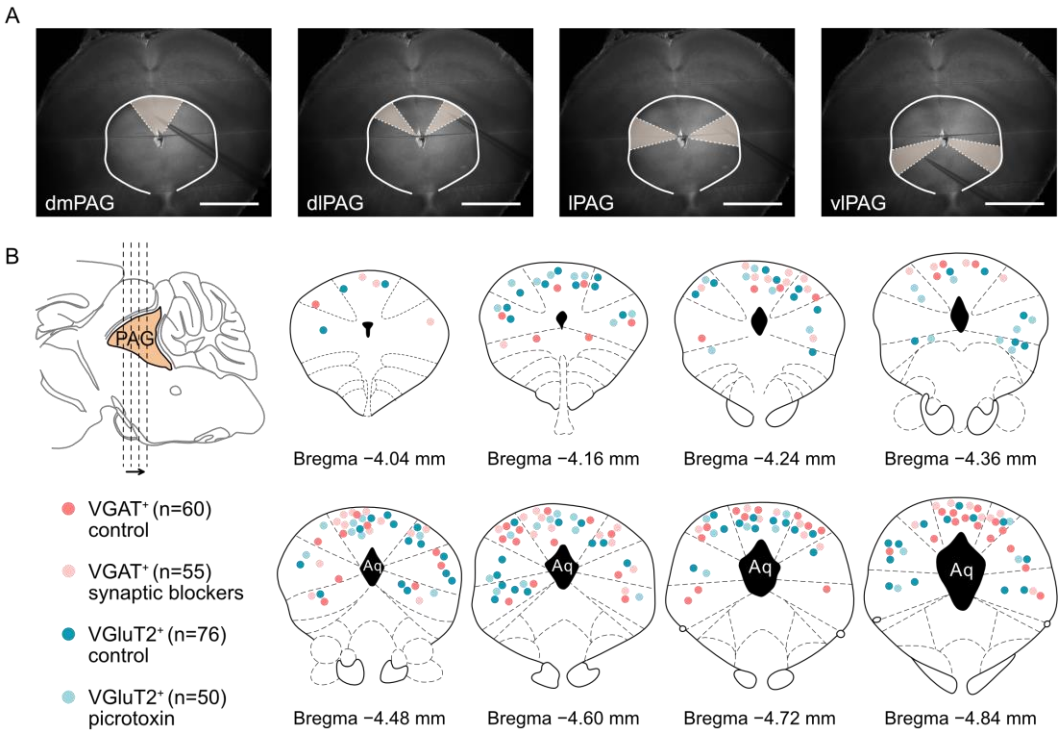

Figure 3.2. Overview of the anatomical location of all PAG neurons recorded using loose-seal cell-attached recordings. (**A**) Representative images illustrating the recording of target neurons located at different PAG subdivisions as described in Franklin and Paxinos (2008). Yellow shadings mark each of the PAG subdivisions, from left to right: dorsomedial (dmPAG), dorsolateral (dlPAG), lateral (lPAG), and ventrolateral (vlPAG). The white line delimitates the PAG. All scale bars are 1 mm. (**B**) The inset in the top left represents a sagittal section of the posterior half of a mouse brain. The PAG is highlighted in yellow, dashed lines represent different coronal sections along the rostro-caudal axis, and the arrow indicates the direction followed by the sequence of larger sections on the right. The schematics on the right show the distribution of all recorded neurons within coronal sections of the PAG along the rostro-caudal axis, coloured by cell type and shaded according to recording condition. Dark shading indicates that a neuron was recorded in control conditions. Light shading indicates that a neuron was recorded with synaptic blockers added to the recording ACSF (2 mM kynurenic acid and 50 µM picrotoxin in the case of VGAT$^+$ neurons, and 50 µM picrotoxin in the case of VGluT2$^+$ neurons). Aq, aqueduct. Adapted from Franklin and Paxinos (2008).

3.2.1 GABAergic neurons in the PAG fire action potentials spontaneously, whereas glutamatergic neurons are mostly silent

I first characterised the baseline firing properties of GABAergic and glutamatergic neurons in control conditions. I recorded a total of 60 $VGAT^+$ and 76 $VGluT2^+$ neurons, spanning the different PAG subdivisions along the rostro-caudal axis (Figure 3.2B). I observed that $VGAT^+$ neurons in the PAG are spontaneously active, with an average firing frequency of 4.59 ± 0.55 Hz (mean ± SEM, n=60 from 22 mice), whereas $VGluT2^+$ neurons are mostly silent, with a firing frequency of 0.12 ± 0.05 Hz (mean ± SEM, n=76 from 14 mice). The results from these recordings suggest that $VGAT^+$ neurons have a higher baseline firing rate than $VGluT2^+$ neurons in control conditions (two-tailed Mann-Whitney test, U=230, $p < 0.0001$, Figure 3.3).

Next, to investigate whether the spontaneous firing of PAG GABAergic neurons originated from synaptic activity in the slice, I obtained loose-seal cell-attached recordings from $VGAT^+$ neurons in the presence of 2 mM kynurenic acid and 50 μM picrotoxin to block glutamate receptors and $GABA_A$ receptors, respectively. Under these conditions, $VGAT^+$ neurons in the PAG continued to exhibit an average spontaneous firing frequency of 5.98 ± 0.73 Hz (mean ± SEM, n=55 from 13 mice, Figure 3.3).

To investigate whether a putative spontaneous firing activity in PAG glutamatergic neurons was being suppressed in baseline conditions due to the presence of tonically active inhibitory inputs or a tonic inhibitory conductance mediated by $GABA_A$ receptors, I recorded $VGluT2^+$ neurons in the presence of 50 μM picrotoxin to block $GABA_A$ receptors. In this situation, $VGluT2^+$ neurons in the PAG did not become spontaneously active, maintaining an average firing frequency of 0.03 ± 0.02 Hz (mean ± SEM, n=50 from 9 mice, Figure 3.3).

The results from this second set of experiments suggest that, even in the absence of synaptic inputs, VGAT$^+$ neurons are spontaneously active and have a higher firing frequency than VGluT2$^+$ neurons (two-tailed Mann-Whitney test, U=36, $p < 0.0001$, Figure 3.3).

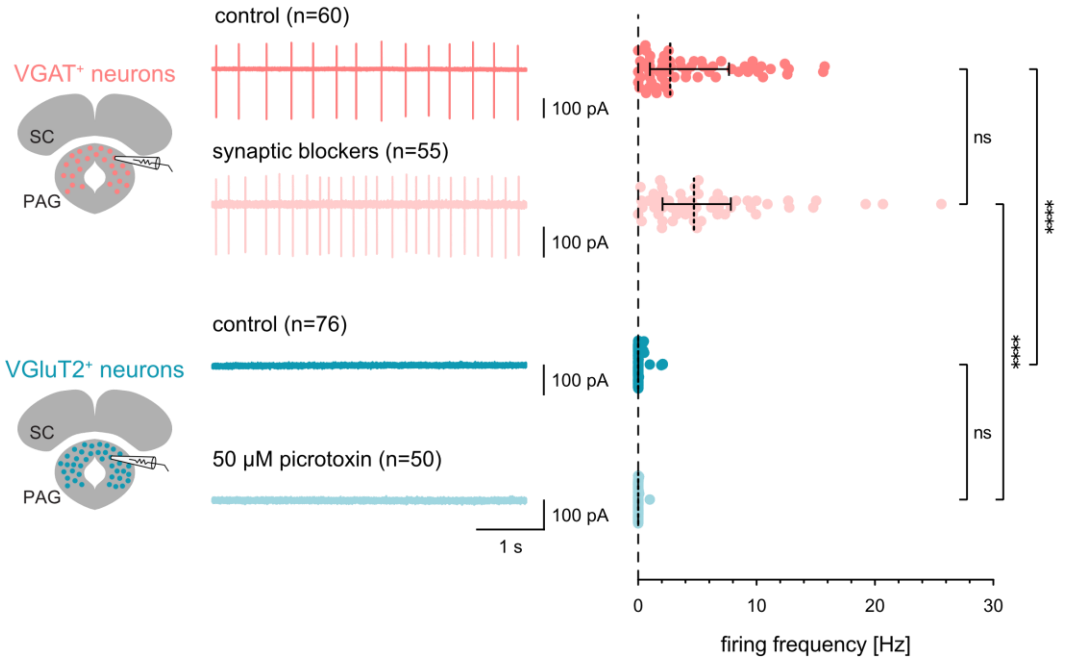

Figure 3.3. Firing frequency of VGAT$^+$ and VGluT2$^+$ neurons in the PAG. (**Left**) Schematics illustrating the use of acute midbrain slices in combination with transgenic lines to target VGAT$^+$ (top) or VGluT2$^+$ (bottom) neurons in the PAG. (**Middle**) Representative traces of the median firing frequency of VGAT$^+$ (top) or VGluT2$^+$ (bottom) neurons in the PAG, in control conditions (dark colour) or in the presence of synaptic blockers (light shading, 2 mM kynurenic acid and 50 µM picrotoxin in the case of VGAT$^+$ neurons, and 50 µM picrotoxin in the case of VGluT2$^+$ neurons). (**Right**) Summary of the average firing frequency of each recorded neuron. Dashed lines represent the median and whiskers represent the interquartile range. For the statistical comparisons, **** indicates $p < 0.0001$, and *ns* indicates not significant.

When comparing the firing frequency from VGAT$^+$ neurons under control conditions to that of VGAT$^+$ neurons in the presence of synaptic blockers, despite observing a slight increase in both the median (from 2.71 Hz to 4.72 Hz, Figure 3.3) and the mean firing rate (from 4.59 ± 0.55 Hz to 5.98 ± 0.73 Hz), I found no significant differences between the firing frequencies in control conditions and in synaptic

blockers of neither VGAT$^+$ (Kruskal-Wallis test, H=168.6, $p < 0.0001$; post-hoc multiple comparisons between control and synaptic blockers, Dunn's adjusted p=0.6109; Figure 3.3) nor VGluT2$^+$ neurons (Kruskal-Wallis test, H=168.6, $p < 0.0001$; post-hoc multiple comparisons between control and picrotoxin, Dunn's adjusted $p > 0.9999$; Figure 3.3).

3.2.2 The measured firing frequency is not explained by seal resistance, mouse age, nor mouse sex

I next wanted to check whether the measured firing frequencies across cell types and conditions could be explained by other experimental variables. I focused on the value of the seal resistance throughout the recording, as well as the age and sex of the mouse from which the acute midbrain slices were prepared.

A linear regression between the measured firing frequency and the seal resistance showed that the slope was not significantly different from zero, suggesting that there was no relationship between the seal resistance and the average firing frequency of the recorded neuron for any of the conditions (VGAT$^+$ control, F=0.44, p=0.5089, Figure 3.4A; VGAT$^+$ in synaptic blockers, F=1.24, p=0.2709, Figure 3.4B; VGluT2$^+$ control, F=0.092, p=0.7629, Figure 3.4C; VGluT2$^+$ in picrotoxin, F=0.67, p=0.4164, Figure 3.4D). This suggested that the experimental approach I followed did not distort the measurements.

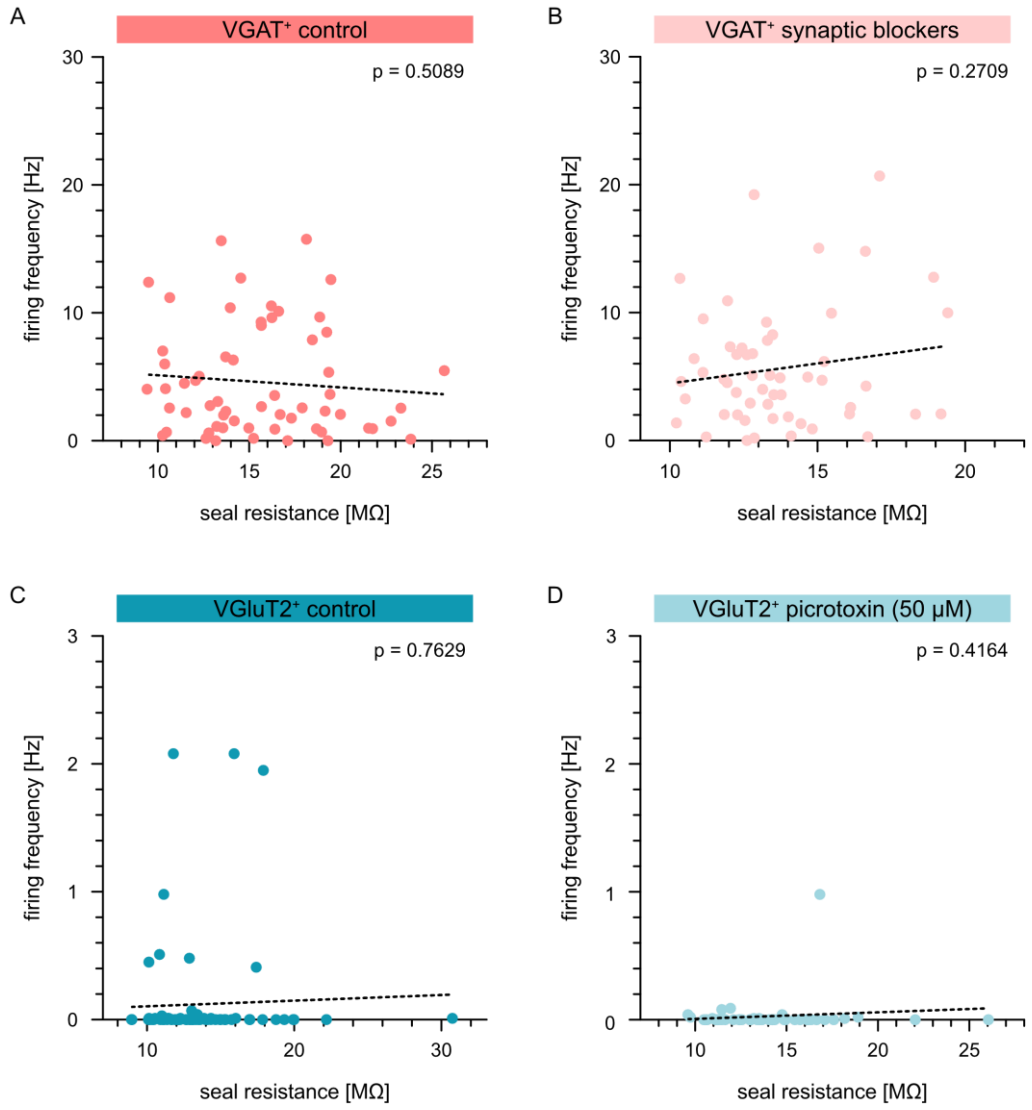

Figure 3.4. The measured firing frequency of PAG neurons is not explained by the seal resistance. (**A-D**) Scatter plots and linear regression (dashed lines) showing no relationship between the seal resistance and the measured firing frequency of VGAT$^+$ neurons in control conditions (**A**), of VGAT$^+$ neurons in the presence of 2 mM kynurenic acid and 50 µM picrotoxin (**B**), of VGluT2$^+$ neurons in control conditions (**C**), and of VGluT2$^+$ neurons in the presence of 50 µM picrotoxin (**D**).

Similarly, a linear regression between the measured firing frequency and age of the mouse also showed that the slope was not significantly different from zero, suggesting that there was no relationship between mouse age and the average firing frequency of the recorded neuron for any of the conditions (VGAT$^+$ control, F=0.47, p=0.4937,

Figure 3.5A; VGAT$^+$ in synaptic blockers, F=2.2, p=0.1436, Figure 3.5B; VGluT2$^+$ control, F=0.44, p=0.5099, Figure 3.5C; VGluT2$^+$ in picrotoxin, F=1.22, p=0.2746, Figure 3.5D).

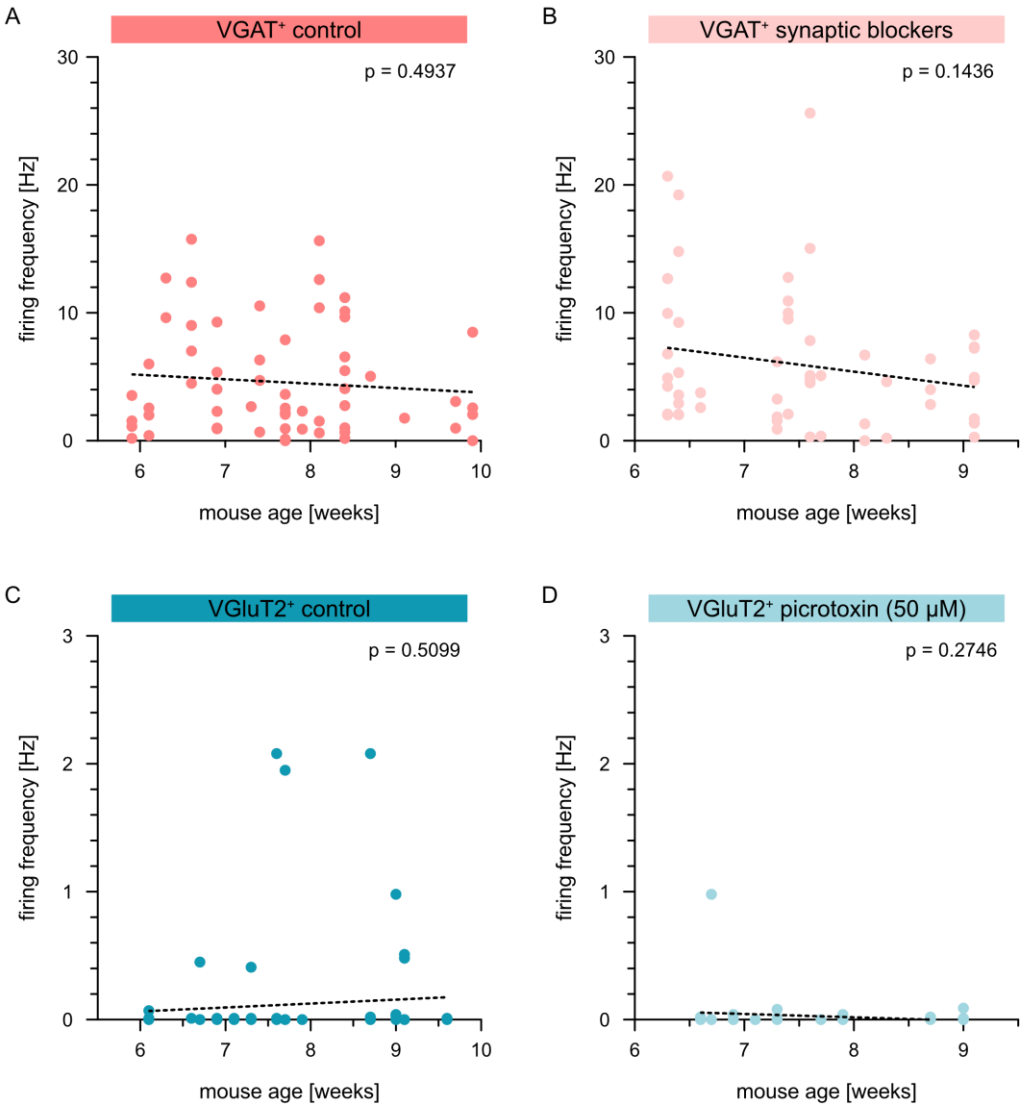

Figure 3.5. The measured firing frequency of PAG neurons is not explained by the age of the mouse. (**A-D**) Scatter plots and linear regression (dashed lines) showing no relationship between the mouse age and the measured firing frequency of VGAT$^+$ neurons in control conditions (**A**), of VGAT$^+$ neurons in the presence of 2 mM kynurenic acid and 50 µM picrotoxin (**B**), of VGluT2$^+$ neurons in control conditions (**C**), and of VGluT2$^+$ neurons in the presence of 50 µM picrotoxin (**D**).

Finally, I found no significant differences between the measured firing frequencies of male and female mice in any of the conditions tested (Kruskal-Wallis test, H=168.8, $p < 0.0001$; post-hoc multiple comparisons between the firing frequency of VGAT$^+$ neurons in control conditions from male and female mice, Dunn's adjusted $p > 0.9999$; of VGAT$^+$ neurons in synaptic blockers from male and female mice, Dunn's adjusted $p > 0.9999$; of VGluT2$^+$ neurons in control conditions from male and female mice, Dunn's adjusted $p > 0.9999$; and of VGluT2$^+$ neurons in picrotoxin from male and female mice, Dunn's adjusted $p > 0.9999$; Figure 3.6).

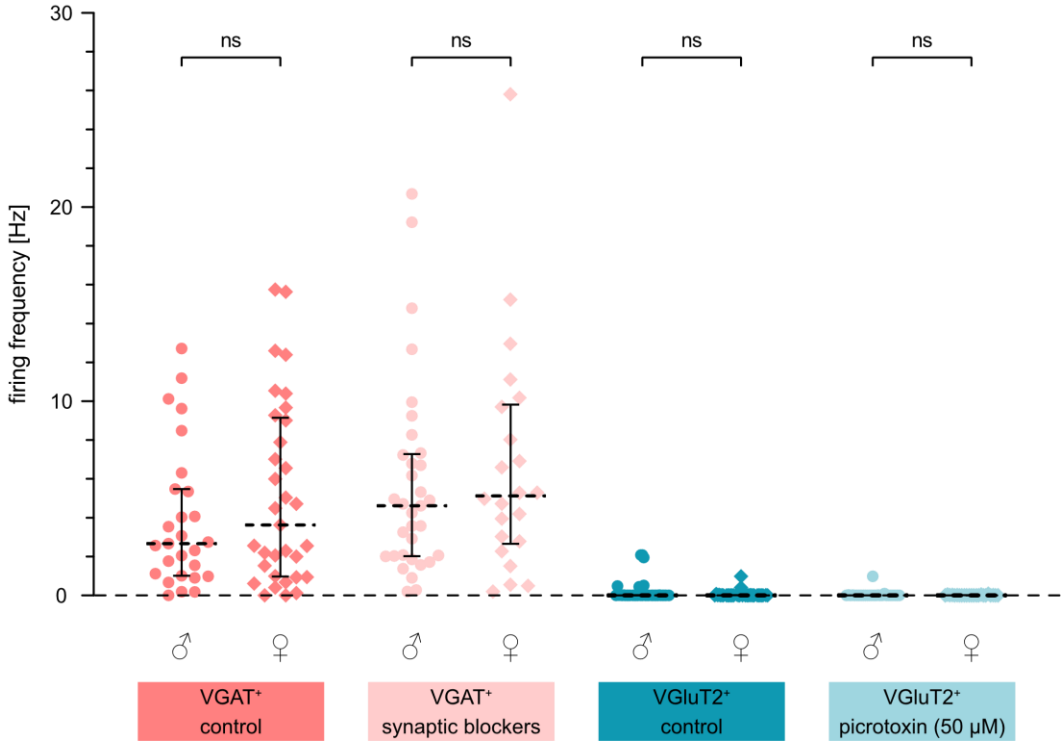

Figure 3.6. The measured firing frequency of PAG neurons is not explained by the sex of the mouse. From left to right, summary plots of the measured firing frequency of PAG neurons from male or female mice for VGAT$^+$ neurons in control conditions, for VGAT$^+$ neurons in the presence of 2 mM kynurenic acid and 50 µM picrotoxin, for VGluT2$^+$ neurons in control conditions, and for VGluT2$^+$ neurons in the presence of 50 µM picrotoxin. Dashed lines represent the median and whiskers represent the interquartile range. *ns* indicates not significant.

3.2.3 Baseline firing properties are similar across PAG subdivisions

After confirming that neither the seal resistance, the mouse age, nor the mouse sex introduced biases in the data, I proceeded to compare the firing frequencies of $VGAT^+$ and $VGluT2^+$ neurons from different PAG subdivisions. For each experimental condition ($VGAT^+$ neurons in control conditions, $VGAT^+$ neurons in synaptic blockers, $VGluT2^+$ neurons in control, and $VGluT2^+$ neurons in picrotoxin), I split the neurons according to the PAG subdivision they were recorded from (dmPAG, dlPAG, lPAG, and vlPAG).

I found that, only in the case of $VGAT^+$ neurons in control conditions, the average firing frequency of lPAG neurons was higher than that of vlPAG neurons (Kruskal-Wallis test, $H=9.26$, $p=0.026$; post-hoc multiple comparisons between the firing frequency of $VGAT^+$ neurons in control conditions in the lPAG and the vlPAG, Dunn's adjusted $p=0.0182$; Figure 3.7A). The rest of the comparisons yielded no significant differences, suggesting that, except in the case of lPAG and vlPAG, $VGAT^+$ neurons in the different PAG subdivisions exhibit similar baseline firing frequencies.

When adding 2 mM kynurenic acid and 50 µM picrotoxin to block glutamate receptors and $GABA_A$ receptors, the measured firing frequency of $VGAT^+$ neurons was comparable across PAG subdivisions (Kruskal-Wallis test, $H=1.23$, $p=0.7453$; Figure 3.7A). Furthermore, I found no differences in the average firing frequency of $VGluT2^+$ neurons across PAG subdivisions neither in control conditions (Kruskal-Wallis test, $H=1.21$, $p=0.7511$; Figure 3.7B) nor in the presence of 50 µM picrotoxin to block $GABA_A$ receptors (Kruskal-Wallis test, $H=3.38$, $p=0.3371$; Figure 3.7B).

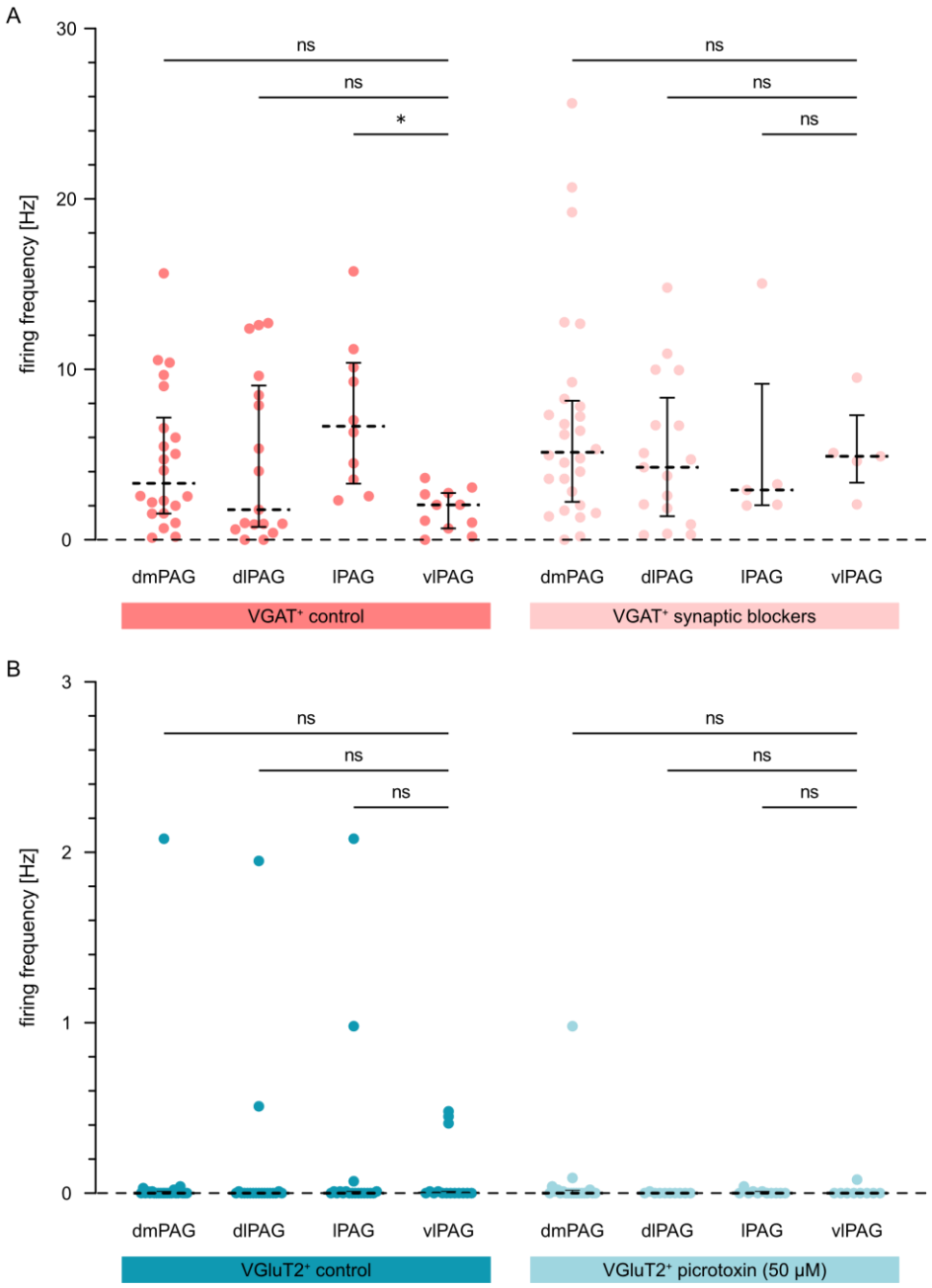

Figure 3.7. The firing frequency of VGAT⁺ and VGluT2⁺ neurons is similar across PAG subdivisions. (**A**) Summary plots of the measured firing frequency of VGAT⁺ PAG neurons across the different subdivisions in control conditions (left, dark colour) and in the presence of 2 mM kynurenic acid and 50 µM picrotoxin (right, light shading). (**B**) Summary plots of the measured firing frequency of VGluT2⁺ PAG neurons across the different subdivisions in control conditions (left, dark colour) and in the presence of 50 µM picrotoxin (right, light shading). Dashed lines represent the median and whiskers represent the interquartile range. For the statistical comparisons, * indicates an adjusted p value of $p < 0.05$, and *ns* indicates not significant.

3.2.4 Interspike intervals are similar across PAG subdivisions

I next sought to examine whether blocking synaptic inputs in the slice affected the interspike intervals of $VGAT^+$ neurons in the PAG. Given that, on average, the baseline firing frequency of $VGluT2^+$ neurons was 0.12 ± 0.05 Hz, I decided to focus on the interspike intervals of $VGAT^+$ neurons alone. Similar to what I observed for the firing frequency of $VGAT^+$ neurons (Figure 3.3), despite observing a slight decrease in both the median (from 275.3 ms to 210.4 ms, Figure 3.8A) and the mean (from 354.0 ± 41.3 ms to 293.5 ± 35.3 ms) interspike interval between control conditions and in the presence of 2 mM kynurenic acid and 50 μM picrotoxin, I found no significant differences between the interspike intervals of $VGAT^+$ neurons in control conditions and in synaptic blockers (two-tailed Mann-Whitney test, U=1381, p=0.3542, Figure 3.8A).

Not surprisingly, after splitting the dataset by PAG subdivision the results from the interspike intervals also mirrored those from the firing frequency. I found that, only in the case of $VGAT^+$ neurons in control conditions, the interspike intervals of vlPAG neurons were higher than that of lPAG neurons (Kruskal-Wallis test, H=8.60, p=0.0351; post-hoc multiple comparisons between the firing frequency of $VGAT^+$ neurons in control conditions in the lPAG and the vlPAG, Dunn's adjusted p=0.0236; Figure 3.8B). The rest of the comparisons yielded no significant differences, suggesting that, except in the case of lPAG and vlPAG, $VGAT^+$ neurons in the different PAG subdivisions exhibit similar interspike intervals.

When adding 2 mM kynurenic acid and 50 μM picrotoxin to block glutamate receptors and $GABA_A$ receptors, the measured interspike intervals of $VGAT^+$ neurons were comparable across PAG subdivisions (Kruskal-Wallis test, H=1.82, p=0.6104; Figure 3.8B).

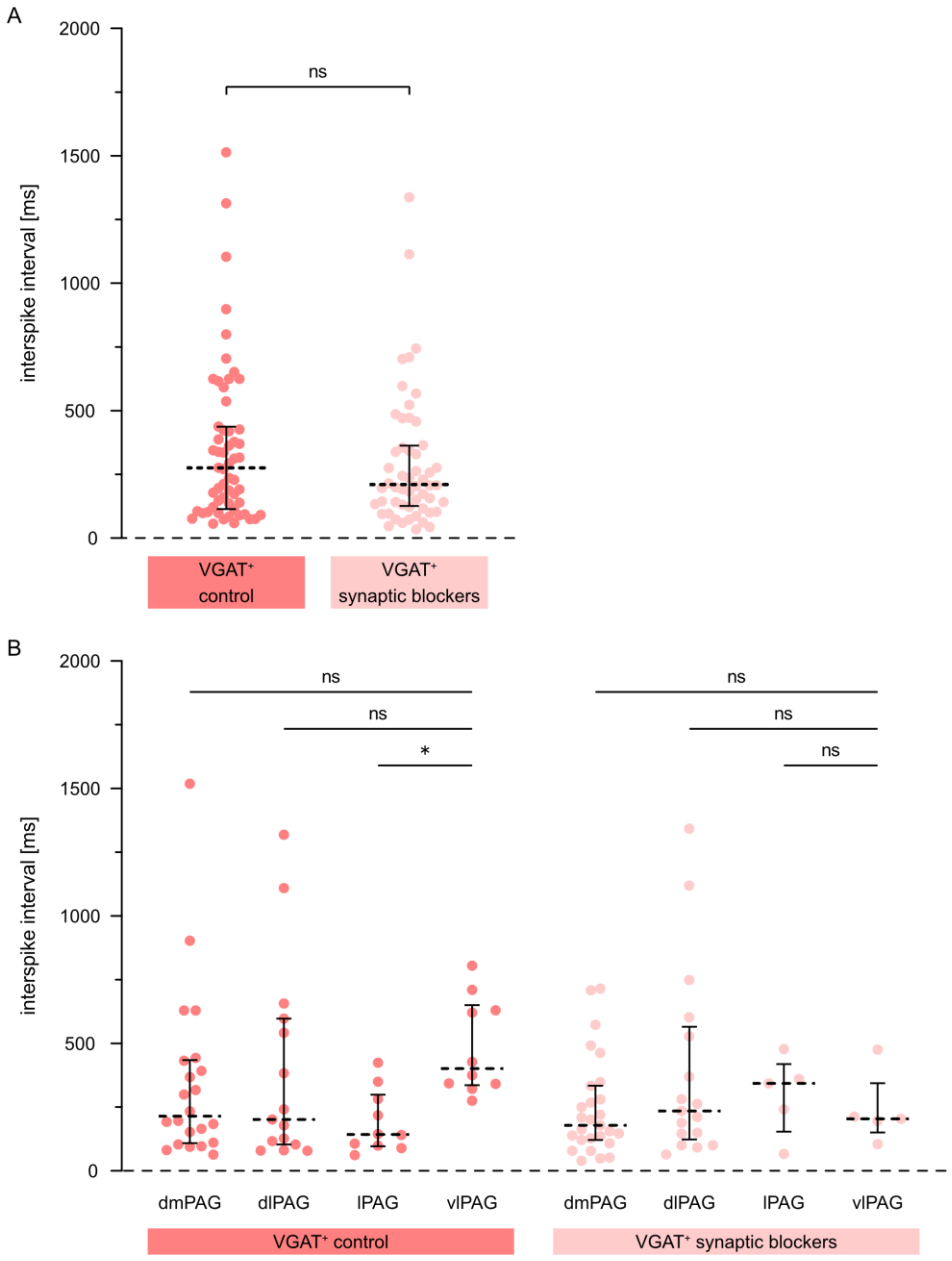

Figure 3.8. The average interspike interval of VGAT$^+$ neurons is similar between control conditions and in the presence of synaptic blockers, and across PAG subdivisions. (**A**) Summary plot of the average interspike interval of VGAT$^+$ PAG neurons in control conditions (left, dark colour) and in the presence of 2 mM kynurenic acid and 50 µM picrotoxin (right, light shading). (**B**) Summary plots of the average interspike interval of VGAT$^+$ PAG neurons across the different subdivisions in control conditions (left, dark colour) and in the presence of 2 mM kynurenic acid and 50 µM picrotoxin (right, light shading). Dashed lines represent the median and whiskers represent the interquartile range. For the statistical comparisons, * indicates an adjusted p value of $p < 0.05$, and *ns* indicates not significant.

To investigate whether the presence or absence of synaptic inputs in the slice affected the regularity of action potentials spontaneously fired by $VGAT^+$ neurons in the PAG, I examined the coefficient of variation of the interspike intervals. Despite observing a slight decrease in both the median (from 0.50 to 0.36, Figure 3.9A) and the mean (from 0.63 ± 0.06 to 0.54 ± 0.06), I found no significant differences between the coefficient of variation of the interspike intervals of $VGAT^+$ neurons in control conditions and in the presence of 2 mM kynurenic acid and 50 μM picrotoxin (two-tailed Mann-Whitney test, $U=1293$, $p=0.1480$, Figure 3.9A).

After splitting the dataset by PAG subdivision, I found that the coefficients of variation of the interspike intervals were similar across PAG subdivisions for both control conditions (Kruskal-Wallis test, $H=2.24$, $p=0.5233$; Figure 3.9B) and in the presence of 2 mM kynurenic acid and 50 μM picrotoxin to block glutamate receptors and $GABA_A$ receptors (Kruskal-Wallis test, $H=3.24$, $p=0.3557$; Figure 3.9B).

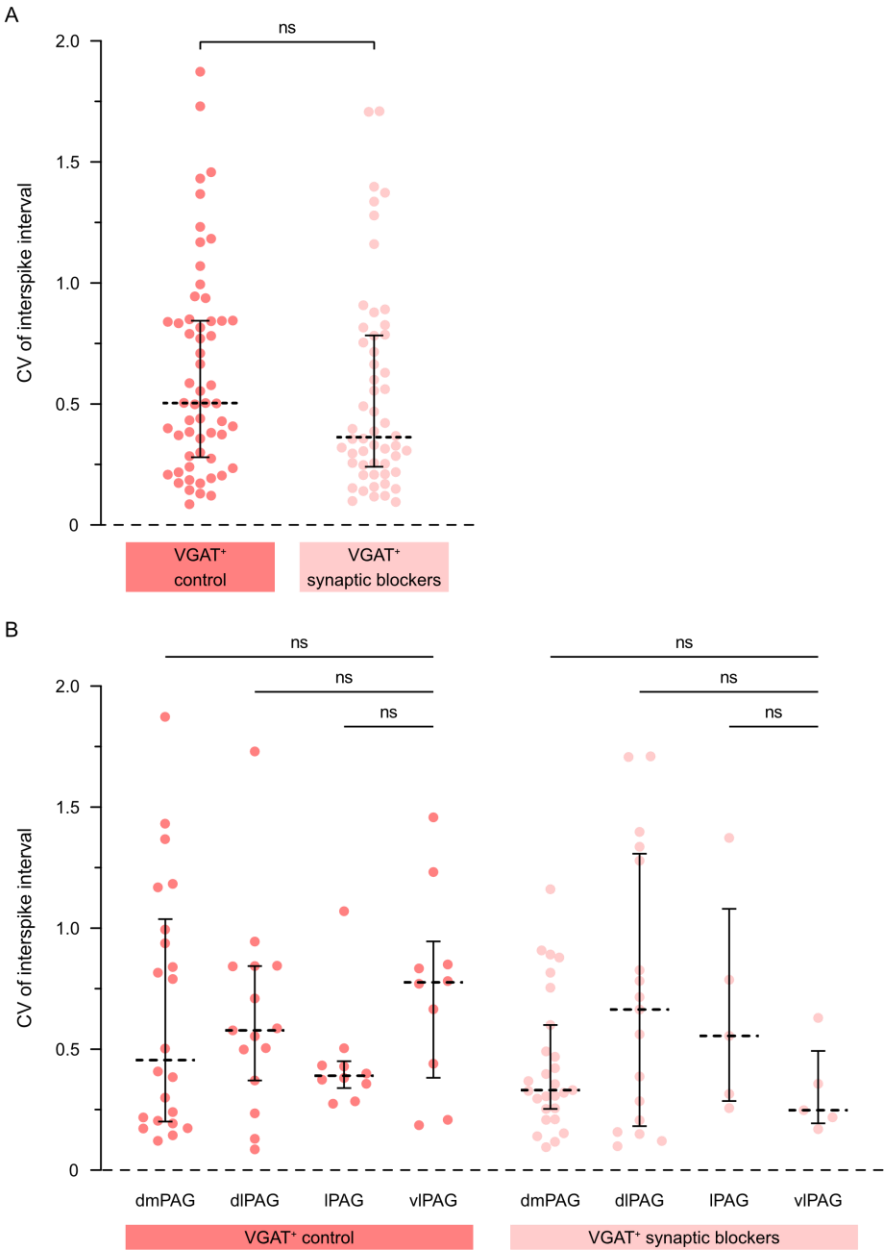

Figure 3.9. The coefficient of variation of the interspike intervals of VGAT⁺ neurons is similar between control conditions and in the presence of synaptic blockers, and across PAG subdivisions. (**A**) Summary plot of the coefficient of variation of the interspike intervals of VGAT⁺ PAG neurons in control conditions (left, dark colour) and in the presence of 2 mM kynurenic acid and 50 µM picrotoxin (right, light shading). (**B**) Summary plots of the coefficient of variation of the interspike intervals of VGAT⁺ PAG neurons across the different subdivisions in control conditions (left, dark colour) and in the presence of 2 mM kynurenic acid and 50 µM picrotoxin (right, light shading). Dashed lines represent the median and whiskers represent the interquartile range. For the statistical comparisons, *ns* indicates not significant.

3.2.5 Action current duration of GABAergic and glutamatergic neurons in the PAG

Finally, I set out to compare the duration of the action current waveform of $VGAT^+$ and $VGluT2^+$ neurons in the PAG. For each cell, I computed the average waveform from all the detected action currents and extracted the total duration (Figure 3.10A, see section 2.3.1.2 for details). It is important to note that, due to the low baseline firing frequency of $VGluT2^+$ neurons, their average action current waveform and the results derived from it were inherently noisier than that of their $VGAT^+$ counterparts.

I found that action currents from $VGAT^+$ neurons in control conditions lasted an average of 2.15 ± 0.1 ms (mean ± SEM, from 57 neurons), whereas action currents from $VGAT^+$ neurons in the presence of 2 mM kynurenic acid and 50 μM picrotoxin lasted an average of 2.32 ± 0.1 ms (mean ± SEM, from 54 neurons). In the case of $VGluT2^+$ neurons, I observed an average action current duration of 1.34 ± 0.1 ms (mean ± SEM, from 22 neurons) in control conditions, and of 1.41 ± 0.2 ms (mean ± SEM, from 12 neurons) in the presence of 50 μM picrotoxin (Figure 3.10).

Despite a slight increase in the average duration in the presence of synaptic blockers, I found no significant differences between the average action current duration of $VGAT^+$ neurons in control conditions and in synaptic blockers (Kruskal-Wallis test, $H=34.42$, $p < 0.0001$; post-hoc multiple comparisons between control and synaptic blockers, Dunn's adjusted $p=0.5588$; Figure 3.10B) nor between the average action current duration of $VGluT2^+$ neurons in control conditions and in picrotoxin (Kruskal-Wallis test, $H=34.42$, $p < 0.0001$; post-hoc multiple comparisons between control and picrotoxin, Dunn's adjusted $p > 0.9999$; Figure 3.10B).

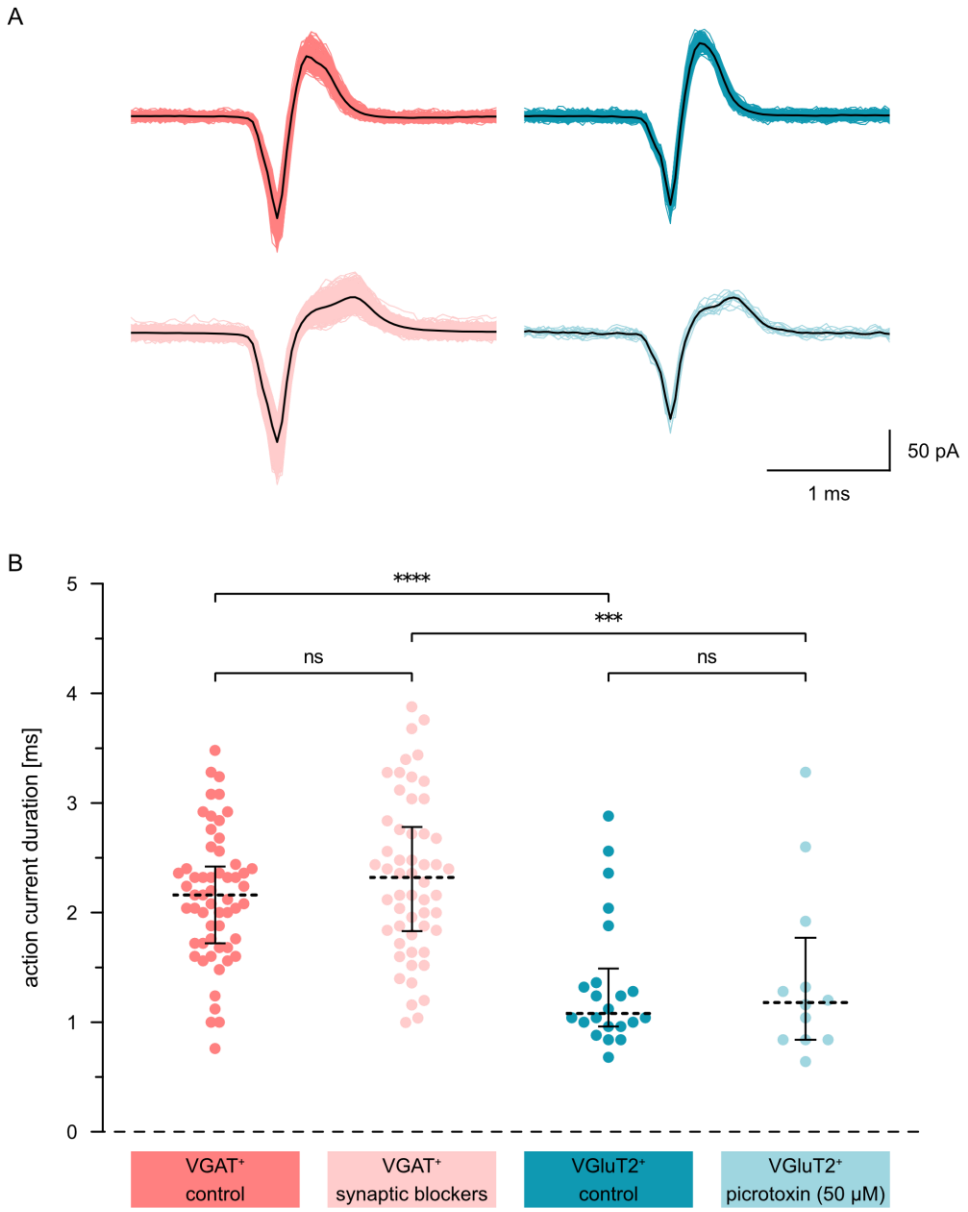

Figure 3.10. Action current duration of GABAergic and glutamatergic neurons in the PAG. (**A**) Traces of the recorded waveform of the action currents detected in an example PAG neuron for each condition. Coloured traces represent all the individual action currents recorded from the sample neuron. Black traces represent the average action current waveform of the sample neuron. (**B**) From left to right, summary plots of the action current duration calculated from the average action current trace of VGAT$^+$ neurons in control conditions, of VGAT$^+$ neurons in the presence of 2 mM kynurenic acid and 50 µM picrotoxin, of VGluT2$^+$ neurons in control conditions, and of VGluT2$^+$ neurons in the presence of 50 µM picrotoxin. Dashed lines represent the median and whiskers represent the interquartile range. For the statistical comparisons, **** indicates $p < 0.0001$, *** indicates $p < 0.001$, and *ns* indicates not significant.

When I compared the action current duration between VGAT$^+$ and VGluT2$^+$ neurons, I found that the action currents of VGAT$^+$ neurons were on average longer than those of VGluT2$^+$ neurons, both in control conditions (two-tailed Mann-Whitney test, U=220.5, $p < 0.0001$, Figure 3.10B) and in the presence of synaptic blockers (two-tailed Mann-Whitney test, U=117.5, p=0.0003, Figure 3.10B). However, and as I have mentioned earlier, this could be explained by an increase in noise in the average action current waveform of VGluT2$^+$ neurons due to their low baseline firing frequency.

Lastly, after splitting the dataset by PAG subdivision I found that the duration of the average action current waveform was similar across PAG subdivisions for all groups (Kruskal-Wallis test for VGAT$^+$ neurons in control conditions, H=2.8, p=0.4235; Kruskal-Wallis test for VGAT$^+$ neurons in synaptic blockers, H=2.67, p=0.4457; Kruskal-Wallis test for VGluT2$^+$ neurons in control conditions, H=7.15, p=0.0673; Kruskal-Wallis test for VGluT2$^+$ neurons in picrotoxin, H=1.16, p=0.8917; Figure 3.11).

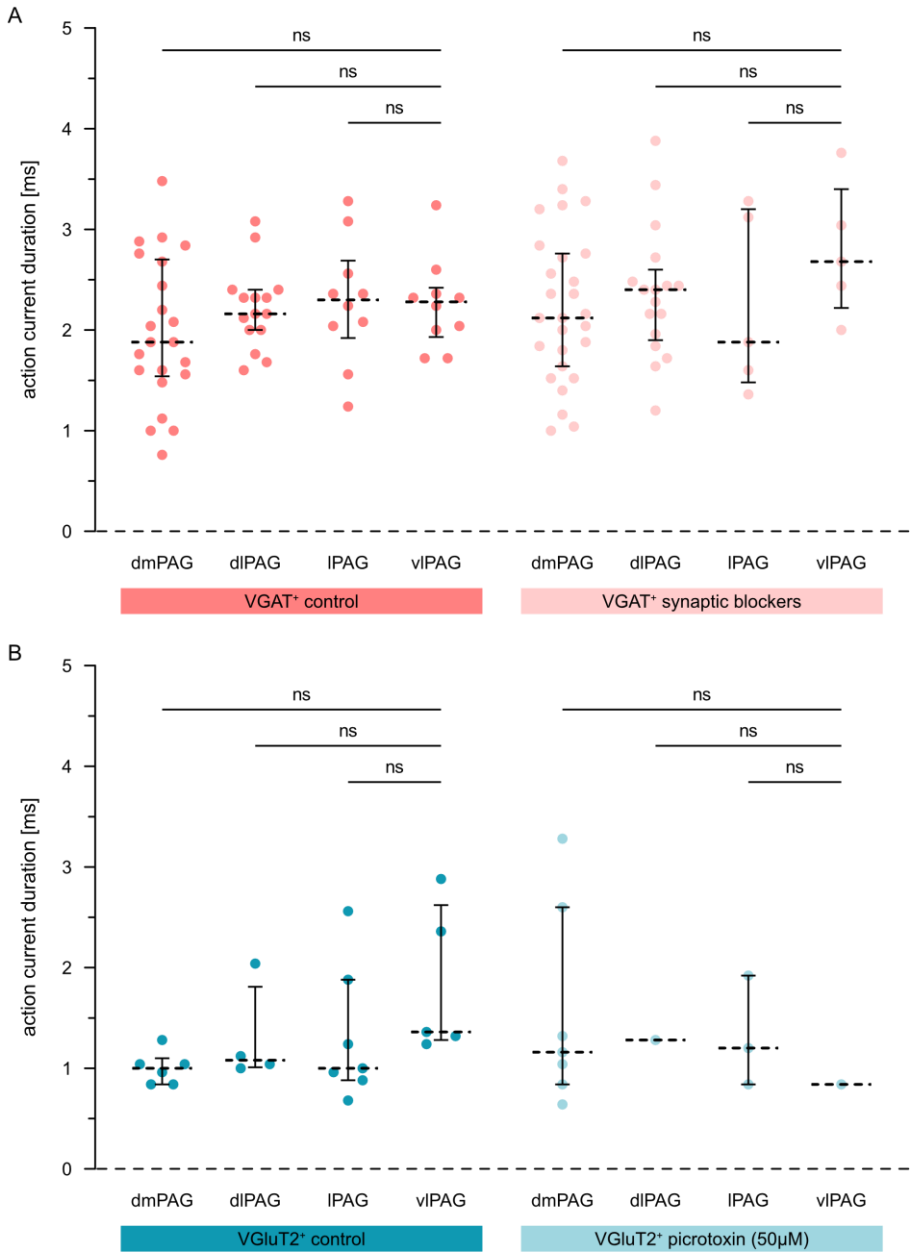

Figure 3.11. The action current duration of GABAergic and glutamatergic neurons is similar across PAG subdivisions. (**A**) Summary plots of the action current duration calculated from the average action current trace of VGAT$^+$ PAG neurons across the different subdivisions in control conditions (left, dark colour) and in the presence of 2 mM kynurenic acid and 50 µM picrotoxin (right, light shading). (**B**) Summary plots of the action current duration calculated from the average action current trace of VGluT2$^+$ PAG neurons across the different subdivisions in control conditions (left, dark colour) and in the presence of 50 µM picrotoxin (right, light shading). Dashed lines represent the median and whiskers represent the interquartile range. For the statistical comparisons, *ns* indicates not significant.

3.3 WHOLE-CELL CHARACTERISATION OF DORSAL PAG NEURONS

I next sought to further characterise the biophysical properties of PAG neurons by measuring several electrophysiological parameters, including the input resistance and the action potential threshold. To that end, I used targeted whole-cell patch-clamp recordings from fluorescently labelled neurons in acute midbrain slices of VGAT::EYFP, VGAT::tdTomato, VGluT2::EYFP or VGluT2::tdTomato mice. Given that I did not observe major differences between the loose-seal cell-attached recordings from $VGAT^+$ and $VGluT2^+$ neurons across PAG subdivisions, I decided to focus on dorsal PAG neurons (i.e. dmPAG and dlPAG), as they have been critically involved in the initiation of escape behaviour (Evans, Stempel, *et al.*, 2018).

3.3.1 $VGAT^+$ neurons in the dorsal PAG have a higher input resistance than $VGluT2^+$ neurons

The first parameter I examined was the input resistance, one of the measures of a neuron's excitability (Figure 3.12). I observed that, in control conditions, $VGAT^+$ neurons in the dorsal PAG had an average input resistance of 684.4 ± 36.0 MΩ (mean ± SEM, from 47 neurons), whereas the average input resistance of $VGluT2^+$ neurons in the dorsal PAG was 338.0 ± 44.7 MΩ (mean ± SEM, from 9 neurons). When I added 2 mM kynurenic acid and 50 μM picrotoxin to block glutamate receptors and $GABA_A$ receptors, I found that $VGAT^+$ neurons had an average input resistance of 795.0 ± 98.3 MΩ (mean ± SEM, from 22 neurons), whereas $VGluT2^+$ neurons had an average input resistance of 675.4 ± 116.8 MΩ (mean ± SEM, from 7 neurons).

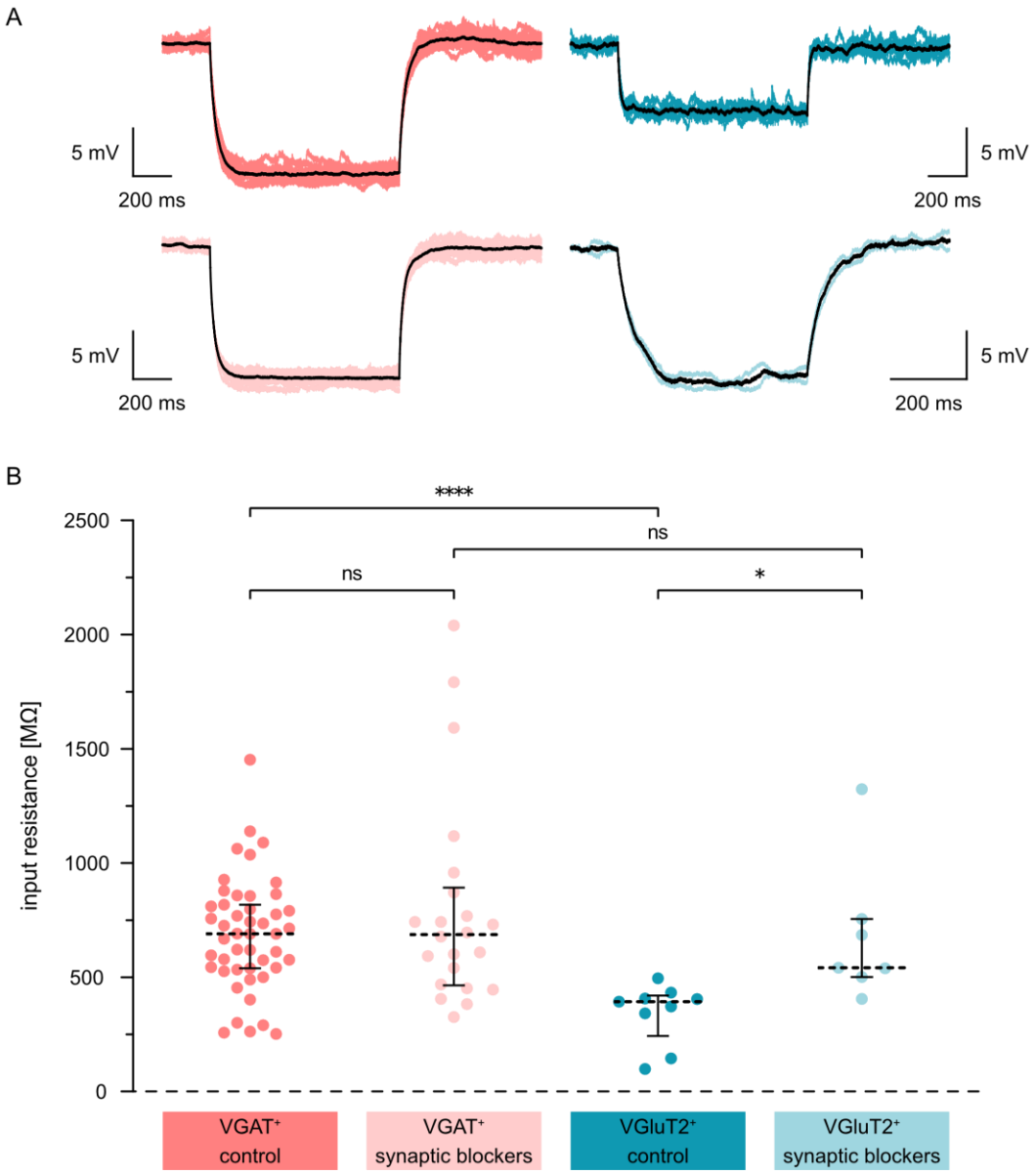

Figure 3.12. Input resistance of VGAT⁺ and VGluT2⁺ neurons in the dorsal PAG. (**A**) Traces of the recorded voltage response to a −20 pA step current injection of an example PAG neuron for each condition. Coloured traces represent individual trials. Black traces represent the average response of the sample neuron. Horizontal scale bars indicate 200 ms. Vertical scale bars indicate 5 mV. (**B**) Summary plots of the input resistance of VGAT⁺ and VGluT2⁺ neurons in the dorsal PAG, in control conditions (dark colour) or in the presence of synaptic blockers (light shading, 2 mM kynurenic acid and 50 µM picrotoxin). Dashed lines represent the median and whiskers represent the interquartile range. For the statistical comparisons, **** indicates $p < 0.0001$, * indicates an adjusted p value of $p < 0.05$, and *ns* indicates not significant.

These results suggested that $VGAT^+$ neurons in the dorsal PAG have a higher input resistance than their $VGluT2^+$ counterparts (two-tailed Mann-Whitney test, U=41, $p < 0.0001$, Figure 3.12B). Interestingly, I found no differences between $VGAT^+$ and $VGluT2^+$ neurons in the dorsal PAG in the presence of 2 mM kynurenic acid and 50 μM picrotoxin to block synaptic inputs (two-tailed Mann-Whitney test, U=67, p=0.6357, Figure 3.12B).

In line with this finding, removing synaptic inputs and tonic $GABA_A$ receptor activation from the slice by adding 2 mM kynurenic acid and 50 μM picrotoxin did not significantly change the input resistance of $VGAT^+$ neurons in the dorsal PAG (Kruskal-Wallis test, H=16.33, p=0.001; post-hoc multiple comparisons between control and synaptic blockers, Dunn's adjusted $p > 0.9999$; Figure 3.12B), but it did lead to an increase in the input resistance of $VGluT2^+$ neurons in the dorsal PAG (Kruskal-Wallis test, H=16.33, p=0.001; post-hoc multiple comparisons between control and synaptic blockers, Dunn's adjusted p=0.034; Figure 3.12B).

When comparing the results between PAG subdivisions, I found no significant differences between the average input resistance of dmPAG neurons and dlPAG neurons in any of the conditions tested (Kruskal-Wallis test, H=21.10, p=0.0036; post-hoc multiple comparisons between the input resistance of $VGAT^+$ neurons in control conditions from dmPAG and dlPAG, Dunn's adjusted $p > 0.9999$; of $VGAT^+$ neurons in synaptic blockers from dmPAG and dlPAG, Dunn's adjusted p=0.1766; of $VGluT2^+$ neurons in control conditions from dmPAG and dlPAG, Dunn's adjusted $p > 0.9999$; and of $VGluT2^+$ neurons in synaptic blockers from dmPAG and dlPAG, Dunn's adjusted $p > 0.9999$; Figure 3.13).

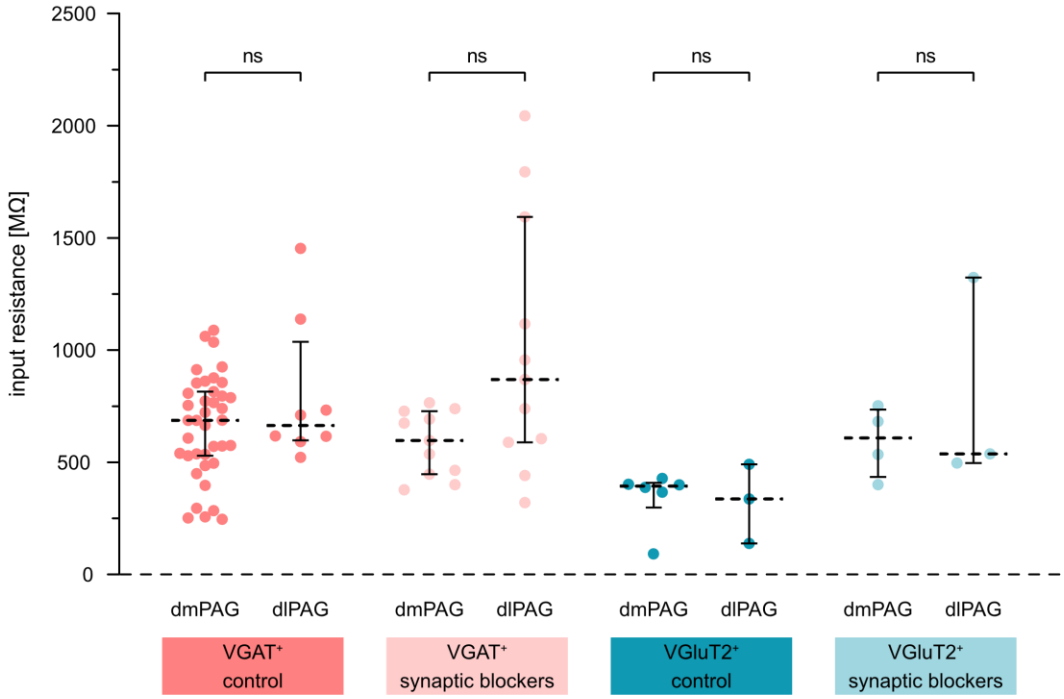

Figure 3.13. The input resistance of VGAT$^+$ and VGluT2$^+$ neurons is similar across PAG subdivisions. Summary plots of the input resistance of VGAT$^+$ and VGluT2$^+$ neurons in different PAG subdivisions, in control conditions (dark colour) or in the presence of synaptic blockers (light shading, 2 mM kynurenic acid and 50 µM picrotoxin). Dashed lines represent the median and whiskers represent the interquartile range. For the statistical comparisons, *ns* indicates not significant.

3.3.2 Action potential threshold of VGAT$^+$ and VGluT2$^+$ neurons in the dorsal PAG

The second parameter I looked at in dorsal PAG neurons was the action potential threshold, another measure of a neuron's excitability (Figure 3.14). I found that, in control conditions, VGAT$^+$ neurons in the dorsal PAG had an average action potential threshold of −38.2 ± 0.6 mV (mean ± SEM, from 34 neurons), whereas the action potential threshold of VGluT2$^+$ neurons in the dorsal PAG was on average −35.3 ± 1.2 mV (mean ± SEM, from 9 neurons). When I added 2 mM kynurenic acid and 50 µM picrotoxin to block glutamate receptors and $GABA_A$ receptors, I found that VGAT$^+$ neurons had an average action potential threshold of −36.6 ± 0.9 mV (mean

± SEM, from 19 neurons), whereas VGluT2$^+$ neurons had an average action potential threshold of −32.9 ± 0.9 mV (mean ± SEM, from 7 neurons).

Despite the average action potential threshold of VGAT$^+$ neurons in the dorsal PAG being slightly lower than that of VGluT2$^+$ neurons, I found that this difference was only significant in the presence of 2 mM kynurenic acid and 50 μM picrotoxin to block synaptic inputs (two-tailed Mann-Whitney test, U=27, p=0.0209, Figure 3.14C), but not in control conditions (two-tailed Mann-Whitney test, U=105, p=0.1573, Figure 3.14C).

Next, I examined the effects that removing synaptic inputs from the slice by adding 2 mM kynurenic acid and 50 μM picrotoxin had on the action potential threshold. Despite observing a slight increase of the median for both VGAT$^+$ (from −37.6 mV to −36.9 mV) and VGluT2$^+$ neurons (from −34.5 mV to −32.3 mV), I found no significant differences between the action potential threshold in control conditions and in synaptic blockers for either cell type (Kruskal-Wallis test, H=11.82, p=0.008; post-hoc multiple comparisons between control and synaptic blockers for VGAT$^+$ neurons, Dunn's adjusted p=0.4215; post-hoc multiple comparisons between control and synaptic blockers for VGluT2$^+$ neurons, Dunn's adjusted p=0.2615; Figure 3.14C).

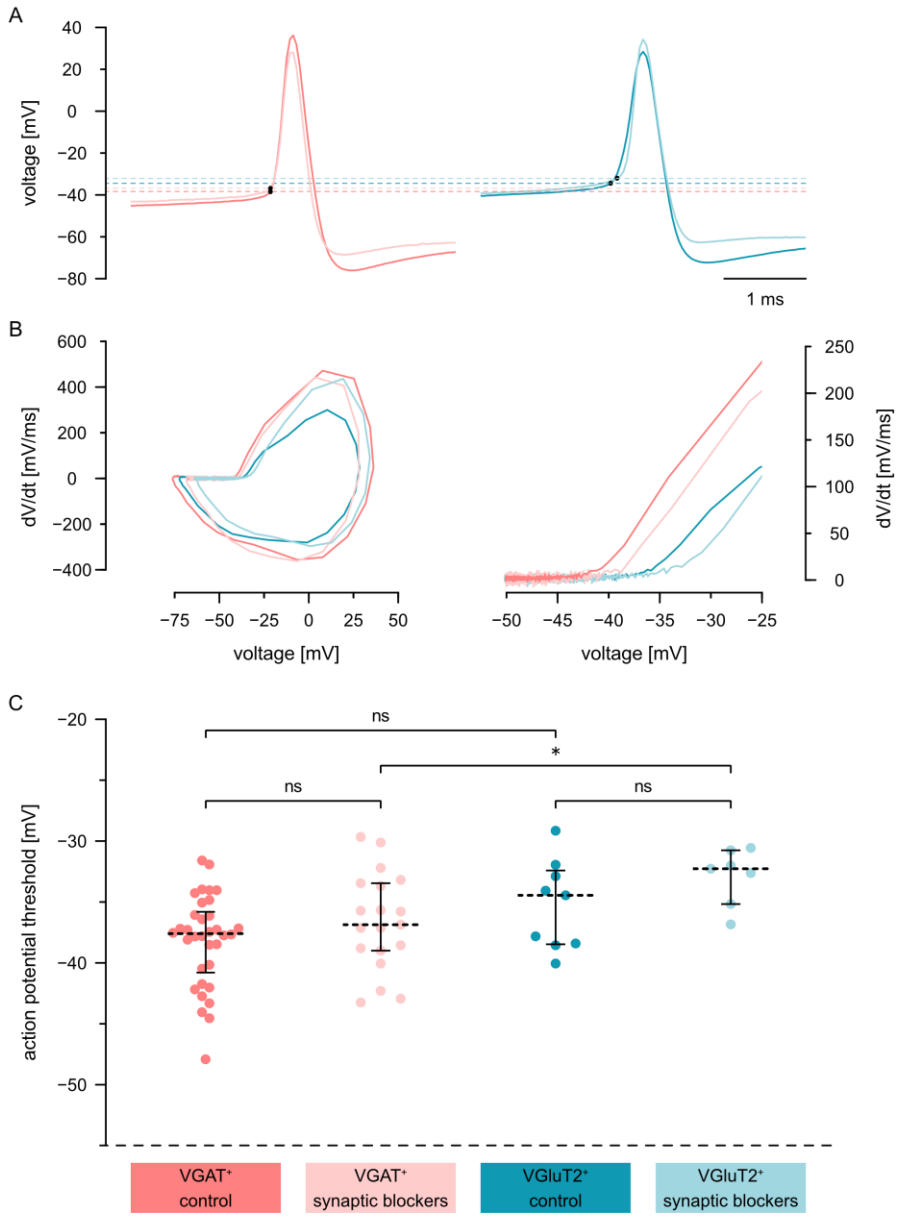

Figure 3.14. Action potential threshold of VGAT⁺ and VGluT2⁺ neurons in the dorsal PAG. (**A**) Traces of the average waveform of action potentials evoked by a step current injection in an example PAG neuron for each condition. Black dots and dashed lines indicate the action potential threshold of each example neuron. (**B**) (Left) Phase plots of the average action potential waveforms in (A). (Right) Magnified fragments of the phase plots depicted in the left. (**C**) Summary plots of the action potential threshold calculated from the average action potential trace of VGAT⁺ and VGluT2⁺ neurons in the dorsal PAG, in control conditions (dark colour) or in the presence of synaptic blockers (light shading, 2 mM kynurenic acid and 50 µM picrotoxin). Dashed lines represent the median and whiskers represent the interquartile range. For the statistical comparisons, * indicates $p < 0.05$, and *ns* indicates not significant.

Once again, I found that the action potential threshold of dmPAG neurons and dlPAG neurons was similar in all the conditions tested (Kruskal-Wallis test, H=15.45, p=0.0307; post-hoc multiple comparisons between the action potential threshold of VGAT$^+$ neurons in control conditions from dmPAG and dlPAG, Dunn's adjusted p=0.2738; of VGAT$^+$ neurons in synaptic blockers from dmPAG and dlPAG, Dunn's adjusted $p > 0.9999$; of VGluT2$^+$ neurons in control conditions from dmPAG and dlPAG, Dunn's adjusted $p > 0.9999$; and of VGluT2$^+$ neurons in synaptic blockers from dmPAG and dlPAG, Dunn's adjusted $p > 0.9999$; Figure 3.15).

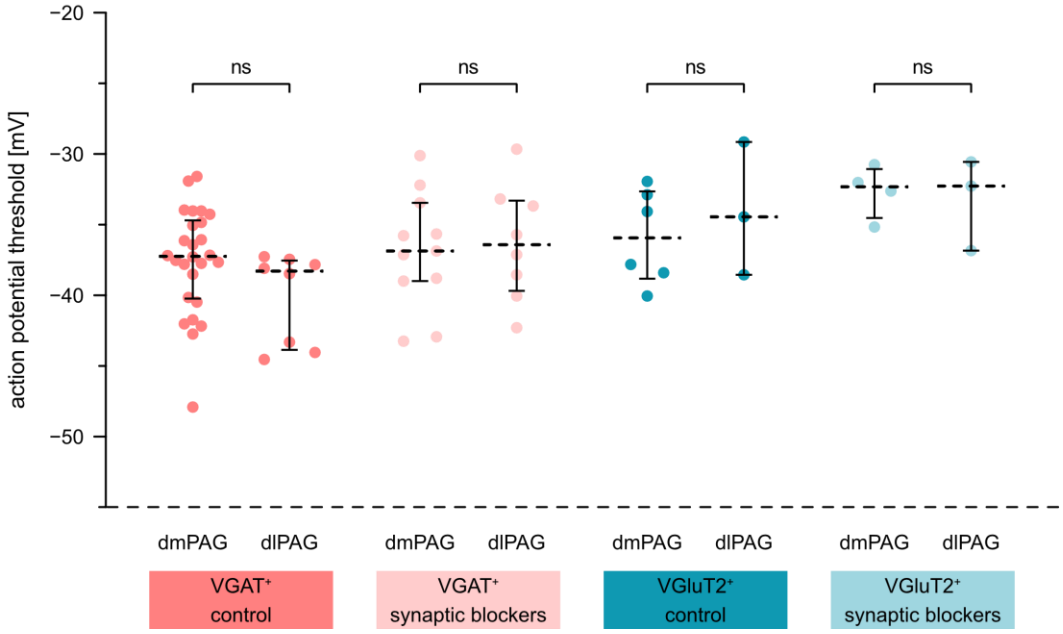

Figure 3.15. The action potential threshold of VGAT$^+$ and VGluT2$^+$ neurons is similar across PAG subdivisions. Summary plots of the action potential threshold calculated from the average action potential trace of VGAT$^+$ and VGluT2$^+$ neurons in different PAG subdivisions, in control conditions (dark colour) or in the presence of synaptic blockers (light shading, 2 mM kynurenic acid and 50 µM picrotoxin). Dashed lines represent the median and whiskers represent the interquartile range. For the statistical comparisons, *ns* indicates not significant.

3.3.3 Action potential half-width of VGAT$^+$ and VGluT2$^+$ neurons in the dorsal PAG

I next wanted to compare the action potential half-width of VGAT$^+$ and VGluT2$^+$ neurons in the dorsal PAG. I found that, in control conditions, VGAT$^+$ neurons have an average action potential half-width of 0.45 ± 0.03 ms (mean ± SEM, from 34 neurons), and VGluT2$^+$ neurons have an average action potential half-width of 0.45 ± 0.04 ms (mean ± SEM, from 9 neurons). In the presence of 2 mM kynurenic acid and 50 μM picrotoxin, the action potential half-width of VGAT$^+$ neurons was on average 0.47 ± 0.05 ms (mean ± SEM, from 19 neurons), and the action potential half-width of VGluT2$^+$ neurons was on average 0.46 ± 0.04 ms (mean ± SEM, from 7 neurons). These results suggest there are no significant differences between the action potential half-width of VGAT$^+$ and VGluT2$^+$ neurons in neither control conditions (two-tailed Mann-Whitney test, U=139, p=0.6919, Figure 3.16) nor in the presence of synaptic blockers (two-tailed Mann-Whitney test, U=56, p=0.5716, Figure 3.16). In addition, I found that the presence of 2 mM kynurenic acid and 50 μM picrotoxin had no effect on the action potential half-width of neither VGAT$^+$ neurons nor VGluT2$^+$ neurons (Kruskal-Wallis test, H=0.42, p=0.9352; Figure 3.16).

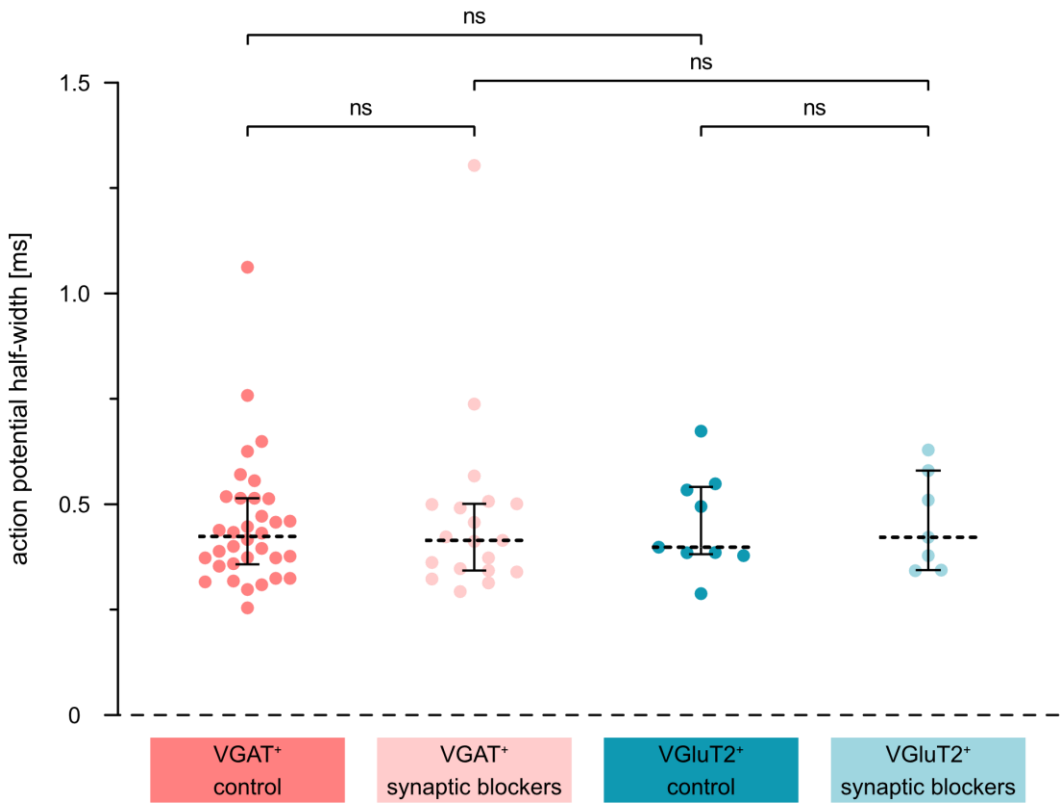

Figure 3.16. Action potential half-width of VGAT$^+$ and VGluT2$^+$ neurons in the dorsal PAG. Summary plots of the action potential half-width calculated from the average action potential trace of VGAT$^+$ and VGluT2$^+$ neurons in the dorsal PAG, in control conditions (dark colour) or in the presence of synaptic blockers (light shading, 2 mM kynurenic acid and 50 µM picrotoxin). Dashed lines represent the median and whiskers represent the interquartile range. For the statistical comparisons, *ns* indicates not significant.

Furthermore, after splitting the dataset by PAG subdivision I found that the action potential half-widths were also similar between dmPAG neurons and dlPAG neurons for all groups (Kruskal-Wallis test, H=7.15, p=0.4132; Figure 3.17).

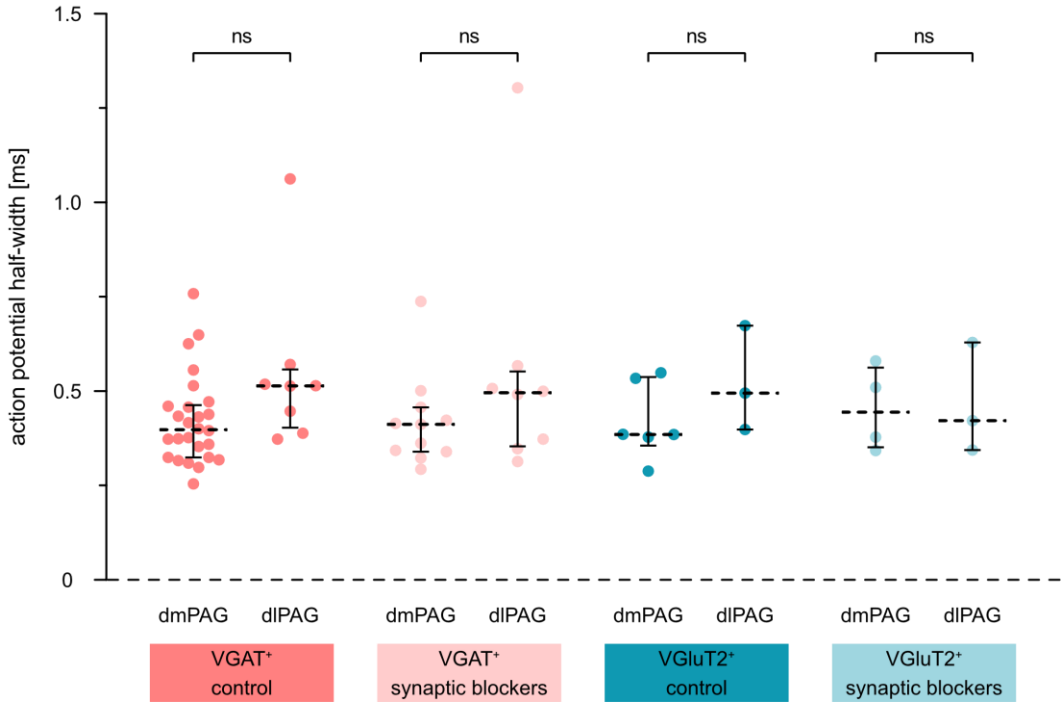

Figure 3.17. The action potential half-width of VGAT$^+$ and VGluT2$^+$ neurons is similar across PAG subdivisions. Summary plots of the action potential half-width calculated from the average action potential trace of VGAT$^+$ and VGluT2$^+$ neurons in different PAG subdivisions, in control conditions (dark colour) or in the presence of synaptic blockers (light shading, 2 mM kynurenic acid and 50 µM picrotoxin). Dashed lines represent the median and whiskers represent the interquartile range. For the statistical comparisons, *ns* indicates not significant.

3.3.4 Slow afterhyperpolarisation in action potentials of VGAT$^+$ and VGluT2$^+$ neurons in the dorsal PAG

The last metric I set out to characterise was the amplitude of the slow afterhyperpolarisation (AHP, Figure 3.18). I found that, in control conditions, VGAT$^+$ neurons in the dorsal PAG had an average slow AHP of −0.63 ± 0.2 mV (mean ± SEM, from 31 neurons), whereas the slow AHP of VGluT2$^+$ neurons in the dorsal PAG was on average −0.16± 0.1 mV (mean ± SEM, from 9 neurons). These results suggested that, in the dorsal PAG, the amplitude of the slow AHP between VGAT$^+$

neurons and VGluT2$^+$ neurons was similar in control conditions (two-tailed Mann-Whitney test, U=86, p=0.0862, Figure 3.18B). In the presence of 2 mM kynurenic acid and 50 μM picrotoxin to block glutamate receptors and $GABA_A$ receptors, the slow AHP of VGAT$^+$ neurons had an average of −1.15 ± 0.3 mV (mean ± SEM, from 19 neurons), whereas that of VGluT2$^+$ neurons had an average of −1.77 ± 0.5 mV (mean ± SEM, from 7 neurons). These results suggested that the amplitude of the slow AHP between VGAT$^+$ neurons and VGluT2$^+$ neurons was similar also in the presence of synaptic blockers (two-tailed Mann-Whitney test, U=48, p=0.3058, Figure 3.18B).

Despite the fact that removing synaptic inputs by adding 2 mM kynurenic acid and 50 μM picrotoxin resulted in a slight increase of the median slow AHP for both VGAT$^+$ (from −0.20 mV in control conditions to −0.68 mV) and VGluT2$^+$ neurons (from –0.06 mV in control conditions to −1.26 mV), these differences were significant only in the case of VGluT2$^+$ neurons (Kruskal-Wallis test, H=12.6, p=0.0056; post-hoc multiple comparisons between control and synaptic blockers for VGAT$^+$ neurons, Dunn's adjusted p=0.2211; post-hoc multiple comparisons between control and synaptic blockers for VGluT2$^+$ neurons, Dunn's adjusted p=0.0032; Figure 3.18B).

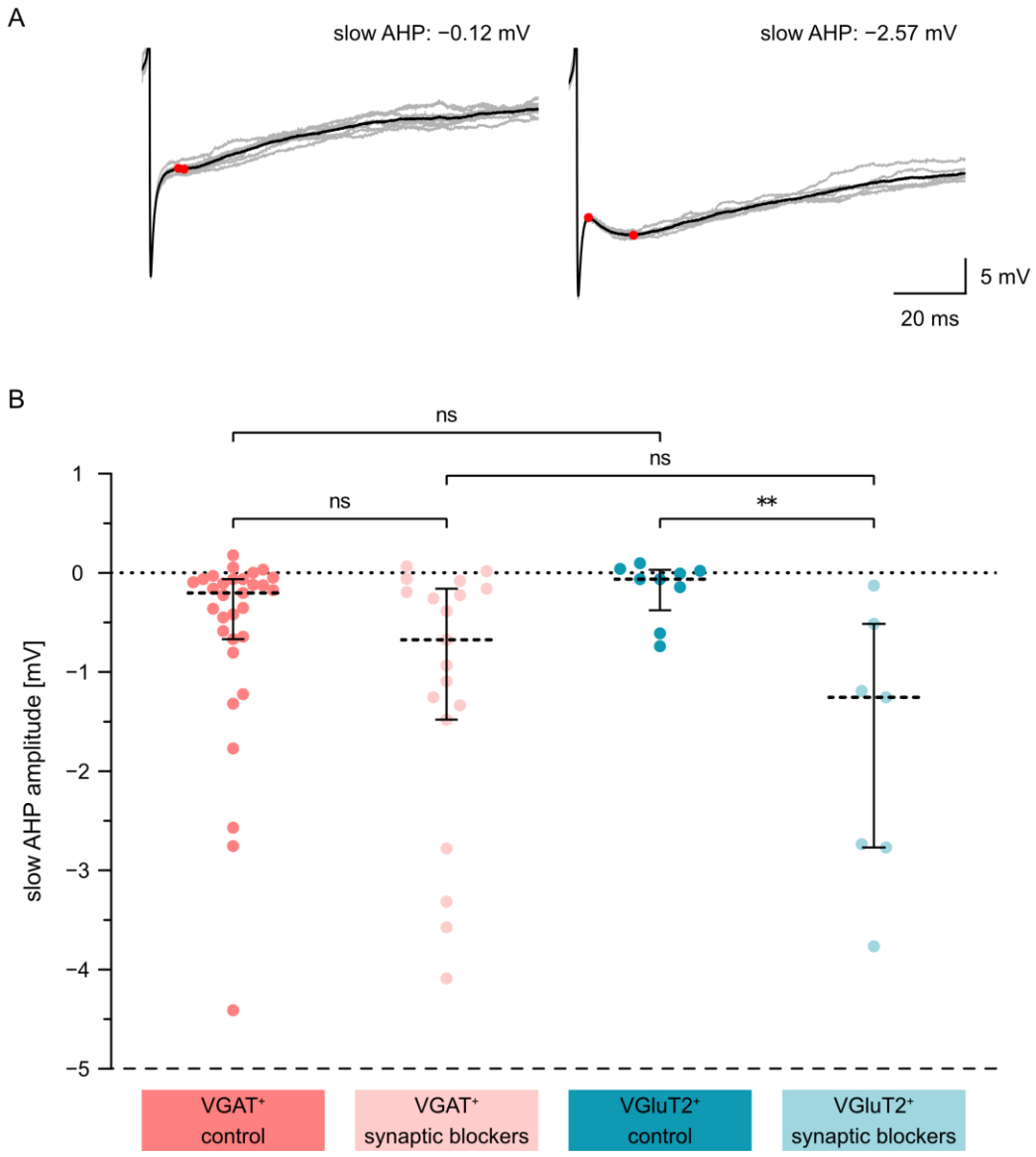

Figure 3.18. Amplitude of the slow afterhyperpolarisation in action potentials of VGAT⁺ and VGluT2⁺ neurons in the dorsal PAG. (**A**) Traces of the recorded action potentials evoked by a step current injection of an example PAG neuron without slow afterhyperpolarisation (AHP, left) and with slow afterhyperpolarisation (right). Gray traces represent individual action potentials. Black traces represent the average action potential waveform of the sample neuron. Horizontal scale bars indicate 20 ms. Vertical scale bars indicate 5 mV. (**B**) Summary plots of the magnitude of the slow AHP calculated from the average action potential trace of VGAT⁺ and VGluT2⁺ neurons in the dorsal PAG, in control conditions (dark colour) or in the presence of synaptic blockers (light shading, 2 mM kynurenic acid and 50 µM picrotoxin). Dashed lines represent the median and whiskers represent the interquartile range. For the statistical comparisons, ** indicates an adjusted p value of $p < 0.01$, and *ns* indicates not significant.

Finally, and in line with all previous results, I found that the magnitude of the slow AHP was similar between dmPAG neurons and dlPAG neurons for all groups (Kruskal-Wallis test, H=13.8, p=0.0548; Figure 3.19).

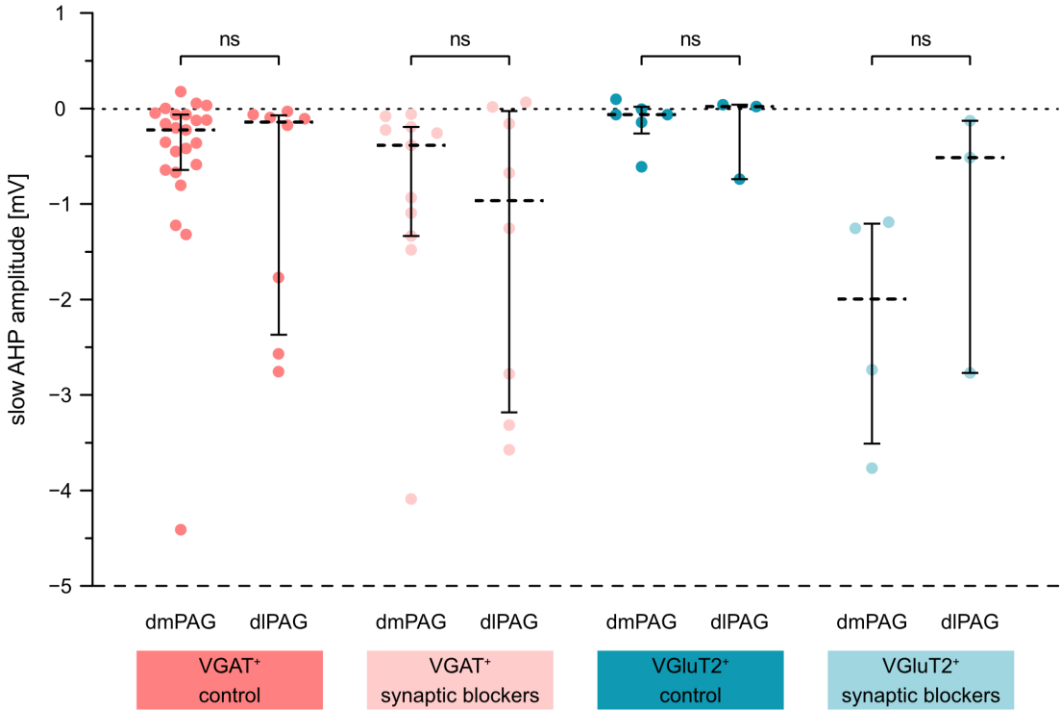

Figure 3.19. The amplitude of the slow afterhyperpolarisation in action potentials of VGAT⁺ and VGluT2⁺ neurons is similar across PAG subdivisions. Summary plots of the magnitude of the slow AHP calculated from the average action potential trace of VGAT⁺ and VGluT2⁺ neurons in different PAG subdivisions, in control conditions (dark colour) or in the presence of synaptic blockers (light shading, 2 mM kynurenic acid and 50 µM picrotoxin). Dashed lines represent the median and whiskers represent the interquartile range. For the statistical comparisons, *ns* indicates not significant.

3.4 SUMMARY

In this chapter, I have used loose-seal cell-attached patch-clamp recordings in acute midbrain slices of transgenic mice to measure the baseline firing properties of PAG neurons. I have found that, even in the absence of synaptic inputs, GABAergic neurons defined by the expression of the VGAT promoter fire action potentials spontaneously, whereas glutamatergic neurons defined by the expression of the VGluT2 promoter are mostly silent. These results were irrespective of the PAG subdivision in which the recorded neuron was found, as well as of other variables such as the age or the sex of the mouse, and are in agreement with previous studies indicating the existence of a tonically active GABAergic network within the PAG (Behbehani, Jiang, *et al.*, 1990; Bandler and Depaulis, 1991; Sánchez and Ribas, 1991; Jiang, Chandler, *et al.*, 1992; Ogawa, Kow, and Pfaff, 1994; Behbehani, 1995; Lovick and Stezhka, 1999; Chiou and Chou, 2000; Yu, Xiang, *et al.*, 2021).

At first glance, the results that neurons in different PAG subdivisions have similar electrophysiological traits can seem a bit surprising, especially when considering the number of publications that have used cell type agnostic techniques such as electrical stimulation, lesions, and extracellular recordings from multiple neurons to describe how a plethora of instinctive behaviours segregate onto the different anatomical subdivisions of the PAG (see section 1.1.3 for details). However, upon closer inspection these results suggest a common electrophysiological trait, disinhibition of a tonically active GABAergic network to gate behavioural output, upon which the different neural circuits within the PAG are built. This view is also supported by recent studies investigating similar questions using newly developed tools to record and manipulate the activity of neurons in a cell type-specific manner (Tovote, Esposito, *et al.*, 2016; Kohl, Babayan, *et al.*, 2018; Hao, Yang, *et al.*, 2019; Samineni, Grajales-Reyes, *et al.*, 2019; Roman-Ortiz, Guevara, and Clem, 2021, but see also section 1.1.3).

In a complementary set of experiments, I have used whole-cell patch-clamp recordings to further characterise the intrinsic biophysical properties of $VGAT^{+}$ and

VGluT2$^+$ neurons in the dorsal PAG. In addition to firing action potentials spontaneously, I have found that VGAT$^+$ neurons have a higher input resistance and a lower action potential threshold than VGluT2$^+$ neurons, making them more excitable.

Overall, these results suggest that GABAergic and glutamatergic neurons in the PAG have strikingly different electrophysiological signatures. In the next chapter, I lay the groundwork to obtain detailed gene expression profiles from VGAT$^+$ and VGluT2$^+$ neurons of the different PAG subdivisions. This will allow me to interrogate the molecular machinery underlying these biophysical traits and uncover the ways different brain circuits modulate and exploit them to give rise to the behavioural output that maximises an individual's survival.

4 A PIPELINE FOR TOPOGRAPHIC AND CELL TYPE-SPECIFIC DEEP TRANSCRIPTOMIC PROFILING OF PERIAQUEDUCTAL GRAY NEURONS

To achieve a mechanistic understanding of the network computations underlying a specific behaviour one must understand how the principal components of the circuit work. At the neuronal level, this might entail dissecting the characteristics of a neuron in terms of input-output connectivity, morphology, electrophysiological properties, and gene expression profile. Both the intrinsic biophysical properties and the computations neurons can perform are determined by the inputs they receive and their gene expression profile and molecular toolkit, including the differential expression of specific ion channels and receptors (Gjorgjieva, Drion, and Marder, 2016; Tripathy, Toker, *et al.*, 2017). While there is a wealth of information on the cytoarchitecture and connectivity of the PAG and its anatomical columns, a comprehensive molecular profiling of the different cell types within the PAG is still lacking.

A first step towards linking the expression of ion channels, neurotransmitter receptors, and molecular effectors to specific PAG subdivisions would be to obtain detailed transcriptomic profiles of genetically identified neurons while preserving their anatomical origin. Such an approach would leverage the unique relationship between

PAG circuit anatomy and behavioural output, allowing researchers to use anatomical location as an anchor to provide a framework for studying how molecularly defined biophysical properties might underpin behavioural control by the PAG.

The advent of single-cell RNA-sequencing has enabled quantitative analysis of the transcriptome of single cells in an unbiased manner (Tang, Barbacioru, *et al.*, 2009; Wang, Gerstein, and Snyder, 2009; Poulin, Tasic, *et al.*, 2016; Zeng and Sanes, 2017). Rapid technological developments (Pollen, Nowakowski, *et al.*, 2014; Klein, Mazutis, *et al.*, 2015; Macosko, Basu, *et al.*, 2015; Zheng, Terry, *et al.*, 2017), protocol improvements (Picelli, Faridani, *et al.*, 2014; Ziegenhain, Vieth, *et al.*, 2017), and novel bioinformatics methods for data analysis (Stegle, Teichmann, and Marioni, 2015; Bacher and Kendziorski, 2016) have recently made it possible for non-specialist laboratories to adopt this method (Shapiro, Biezuner, and Linnarsson, 2013; Saliba, Westermann, *et al.*, 2014; Kolodziejczyk, Kim, *et al.*, 2015; Cuevas-Diaz Duran, Wei, and Wu, 2017). Nonetheless, important considerations need to be made before choosing a single-cell RNA-sequencing protocol, including the type of information to be obtained, how the cells are to be isolated and processed, and the target sequencing depth at which data are to be generated (Haque, Engel, *et al.*, 2017; Baran-Gale, Chandra, and Kirschner, 2018; Lafzi, Moutinho, *et al.*, 2018; Mereu, Lafzi, *et al.*, 2020).

In this chapter, I first address the main aspects to be considered when designing a single-cell RNA-sequencing experiment and discuss the reasoning behind my decision to implement the chosen approach. I then go through the different steps of the pipeline, from cell isolation to library generation and sequencing. Finally, I proceed to curate, pre-process, and quality control the data to ready it for downstream analysis.

4.1 SINGLE-CELL RNA-SEQUENCING CONSIDERATIONS

The ability to profile the mRNA transcripts expressed in a single cell has been a major breakthrough in biological research. The development of new protocols has made it possible to apply next-generation sequencing technology to samples with small amounts of starting material (Tang, Barbacioru, *et al.*, 2009; Wang, Gerstein, and Snyder, 2009). Unlike earlier approaches like microarrays or single-cell RT-qPCR (Lambolez, Audinat, *et al.*, 1992; Bochet, Audinat, *et al.*, 1994; Sucher and Deitcher, 1995; Cauli, Audinat, *et al.*, 1997), which are limited in scope by a pre-selected set of transcripts to probe, single-cell RNA-sequencing quantifies the expression levels of all transcripts in a sample in an unbiased manner. This has led to an explosion of methods and experimental designs that have revolutionised the field, unlocking a myriad of possibilities to investigate old and new biological and medical questions (Svensson, Vento-Tormo, and Teichmann, 2018).

Nowadays, single-cell RNA-sequencing datasets are comprised of anything between hundreds to millions of cells (La Manno, Gyllborg, *et al.*, 2016; Tasic, Menon, *et al.*, 2016; Allen, DeNardo, *et al.*, 2017; Romanov, Zeisel, *et al.*, 2017; Svensson, Vento-Tormo, and Teichmann, 2018; Zeisel, Hochgerner, *et al.*, 2018; Cao, Spielmann, *et al.*, 2019; Kim, Yao, *et al.*, 2019). Some projects have focused on cataloguing the cell types present in a tissue or even a whole organism, generating comprehensive atlases for many tissues (Chen, Wu, *et al.*, 2017; Carter, Bihannic, *et al.*, 2018; Hrvatin, Hochbaum, *et al.*, 2018; Tasic, Yao, *et al.*, 2018; The Tabula Muris Consortium, 2018; Asp, Giacomello, *et al.*, 2019; Mickelsen, Bolisetty, *et al.*, 2019; Han, Zhou, *et al.*, 2020), animal models (Cao, Packer, *et al.*, 2017; Fincher, Wurtzel, *et al.*, 2018; Sebé-Pedrós, Saudemont, *et al.*, 2018; Cao, Lemaire, *et al.*, 2019; Norimoto, Fenk, *et al.*, 2020; Bakken, van Velthoven, *et al.*, 2021; Li, Janssens, *et al.*, 2021), and diseases (Ofengeim, Giagtzoglou, *et al.*, 2017; Wang and Song, 2017; Chen, Teichmann, and Meyer, 2018). Other projects have combined single-cell RNA-sequencing with complementary techniques such as patch-clamp recordings (Cadwell, Palasantza, *et al.*, 2016; Földy,

Darmanis, *et al.*, 2016; Fuzik, Zeisel, *et al.*, 2016), proteomics (Jha, Valekunja, *et al.*, 2020), or viral tracings (Cembrowski, Phillips, *et al.*, 2018; Han, Kebschull, *et al.*, 2018; Huang, Ochandarena, *et al.*, 2019) to integrate multiple modalities of data to address a specific question (Boldog, Bakken, *et al.*, 2018; Moffitt, Bambah-Mukku, *et al.*, 2018; Muñoz-Manchado, Bengtsson Gonzales, *et al.*, 2018; Bai, Mesgarzadeh, *et al.*, 2019; Gouwens, Sorensen, *et al.*, 2020; Xie, Wang, *et al.*, 2021). Each approach has its own advantages and disadvantages, and it is imperative to carefully consider them in the light of one's experimental aims to choose the most suitable method.

A typical single-cell RNA-sequencing experiment consists of several steps. First, individual cells must be isolated from the tissue of interest. Next, the mRNA of each cell needs to be extracted, reverse transcribed into cDNA, and amplified. After this, the resulting material can be used to prepare the sequencing library and subjected to high-throughput sequencing. Only then a dataset is produced, and analysis can begin. But to ensure the resulting dataset puts researchers in the best position to try to answer the questions they are interested in, one first needs to decide the best approach for each of the main steps of the experiment: cell isolation, sample preparation, and sequencing depth (i.e. the number of raw reads per sample).

4.1.1 Cell isolation

Besides establishing how the cells will be selected, the cell isolation strategy will determine how many cells can obtained (experiment throughput) and what kind of information can be added to the sequencing itself. Typically, the choice of cell isolation approach divides single-cell RNA-sequencing experiments in either low-throughput or high-throughput (Poulin, Tasic, *et al.*, 2016).

Low-throughput methods rely on manual or automated micropipetting of cells from a suspension or culture, cytoplasmic aspiration via patch pipettes, or laser capture microdissection, typically leading to datasets of tens to hundreds of cells (Poulin, Tasic, *et al.*, 2016). An advantage of these approaches is that they can provide additional data

modalities such as the morphology of the cell, electrophysiological recordings, or cell location in a tissue. On the other hand, high-throughput single-cell RNA-sequencing methods usually rely on the dissociation of brain tissue followed by fluorescence activated cell sorting (FACS) and microfluidic or droplet-based isolation techniques (Pollen, Nowakowski, *et al.*, 2014; Klein, Mazutis, *et al.*, 2015; Macosko, Basu, *et al.*, 2015; Zheng, Terry, *et al.*, 2017), and allow the capture of thousands to tens of thousands of cells. Unfortunately, tissue dissociation is incompatible with preserving information about the precise anatomical origin of the cells, and FACS has been recently shown to introduce oxidative stress and alter the metabolic state of cells (Llufrio, Wang, *et al.*, 2018).

One of the goals of my thesis was to relate the single-cell RNA-sequencing data from GABAergic and glutamatergic neurons of the PAG to their anatomical location, and eventually integrate it with biophysical properties measured with whole-cell patch-clamp recordings. The fact that I already had the expertise to obtain acute midbrain slices from transgenic mice made it easier to adapt the patch-clamp recording pipeline and repurpose the rig and patch pipettes to be able to isolate PAG neurons. I thus opted for a low-throughput approach that would allow me to manually isolate fluorescently labelled neurons from acute midbrain slices of transgenic mice.

In my case, the advantages of going down this path clearly outweighed the disadvantage of only being able to capture a few hundred cells. First, by using transgenic animals I would be able to know the identity of the cell type I was isolating without having to dissociate the tissue or subject the cells to any potential artifacts introduced by FACS. Second, by using visually guided aspiration via patch pipettes, I would be able to record the anatomical location of each cell within the slice and, in the future, have the possibility of integrating the resulting dataset with others obtained with the *patch-seq* technique, which combines electrophysiological recordings, morphological reconstructions, and single-cell RNA-sequencing (Cadwell, Palasantza, *et al.*, 2016; Fuzik, Zeisel, *et al.*, 2016). Finally, by assessing the quality of the tissue and

applying similar criteria to those I used to select neurons for patch-clamp recordings, I would be able to maximise the chances of isolating mainly good quality neurons.

4.1.2 Sample preparation protocols

Once the cells of interest have been isolated, there are a variety of protocols to choose from for the processing steps. These can mainly be classified as either full-length or tag-based protocols. Full-length protocols provide a more even coverage of the transcripts and allow the detection of splice variants and exome mutations. Tag-based protocols only capture the 5' or the 3' end of the transcript, which makes it harder to distinguish isoforms, but can be combined with unique molecular identifiers to help improve transcript quantification accuracy and mitigate PCR amplification noise.

Comparisons of several single-cell RNA-sequencing methods have shown that Smart-seq2, a protocol to generate full-length cDNA libraries from the transcriptome of single cells (Picelli, Faridani, *et al.*, 2014), is the most sensitive method and shows the most even read coverage across transcripts, making it the most suitable when annotation of single-cell transcriptomes is the focus (Svensson, Natarajan, *et al.*, 2017; Ziegenhain, Vieth, *et al.*, 2017; Ding, Adiconis, *et al.*, 2020). Smart-seq2 is also the most accurate method, which means that the detected differences in expression values across transcripts provide a good representation of the actual proportions present in the cell (Svensson, Natarajan, *et al.*, 2017; Ziegenhain, Vieth, *et al.*, 2017). Whereas a high sensitivity will allow the detection of weakly expressed genes in the samples, a high accuracy will increase the confidence in the results reflecting true biological traits rather than technical factors.

For the experimental aims of this thesis, I wanted to detect as many genes as possible from each isolated cell. This would allow me to obtain a faithful representation of the genes expressed in PAG neurons to try to get an idea of their ion channel repertoire, the receptors for neurotransmitters and neuromodulators they express, and any potential markers that would grant further access to putative subpopulations. In

addition, I wanted a method with high accuracy to be able to make comparisons between the two main cell types in the PAG and its subdivisions and leverage any differences observed to design further experiments. Finally, I also needed a protocol that was compatible with the chosen isolation method. I decided to implement the Smart-seq2 protocol as it fulfils all the criteria above and was the best suited to my experimental needs.

4.1.3 Sequencing depth

Having decided how the cells of interest are to be isolated and processed, one needs to make the critical decision of how many cells should be captured and at which depth they should be sequenced. Sequencing depth is a measure of sequencing capacity spent on a single sample or, in other words, the number of raw reads per cell (Haque, Engel, *et al.*, 2017). Although the optimal trade-off between the number of samples and the sequencing depth is still actively investigated and debated in the field (Streets and Huang, 2014; Lei, Ye, *et al.*, 2015; Torre, Dueck, *et al.*, 2018), the experimental aims and the choices made for the isolation and processing steps will be critical to reach a decision. If the main objective is to catalogue the different cell types in a tissue, detect rare cell types, and find molecular markers for them, the best option would be to try to capture thousands or tens of thousands of cells and sequence them at around 10,000 to 50,000 reads per sample. This option would be best combined with microfluidics or droplet-based methods in which the tissue would have been dissociated and potentially subjected to FACS to enrich specific subpopulations.

If, on the other hand, the main interest is to investigate the subtle differences between pre-established conditions or pre-identified cell types, one should favour sequencing at a higher depth at the expense of capturing fewer cells. Although a sequencing depth of ~50,000 reads per cell is sufficient for unbiased cell type classification and biomarker identification (Pollen, Nowakowski, *et al.*, 2014), at least one million reads per cell are required to accurately measure transcript abundance (Lei, Ye, *et al.*, 2015; Svensson, Natarajan, *et al.*, 2017; Ziegenhain, Vieth, *et al.*, 2017). In

addition, the sensitivity to detect weakly expressed genes critically depends on sequencing depth and saturates at 4.5 million reads per cell, with the gains between 1 and 4.5 million reads per cell being marginal but with the gains between 50,000 and 1 million reads being significant (Wang, Gerstein, and Snyder, 2009; Svensson, Natarajan, *et al.*, 2017; Ziegenhain, Vieth, *et al.*, 2017).

In my case, I was not interested in identifying and classifying the different types of cells present in the PAG. Instead, I wanted to use transgenic animals to identify and capture either glutamatergic or GABAergic neurons from an area of interest and obtain as much information as possible from them. I thus opted for the low-throughput, high sequencing depth approach.

Importantly, having decided the throughput-depth balance appropriate for the experiment at hand, one needs to account for the loss of useful reads that usually occurs during any sequencing run. Most studies find that around 60% of the reads in a given sequencing run will map to a single location in the genome (uniquely mapping reads), with the remaining reads either multimapping (20%) or not matching at all (20%) (Picelli, Faridani, *et al.*, 2014). Out of the uniquely mapping reads, around 60-70% will usually map to annotated exons, with the rest of reads split between intronic and intergenic sequences. These values suggest that if the sequencing depth is set to 1 million reads per sample, around 600,000 reads will uniquely map to the genome, from which 360,000 reads will ultimately map to annotated exons (and will therefore be useful to our experiment). Furthermore, the total amount of cDNA inputted on a given sequencing run tends to err on the conservative side to avoid saturating the platform, which usually means that one will never use the full 100% of the available reads in the kit of choice.

Overall, this means that only a fraction of the reads originally set as target will get used, and only a fraction of the reads used will generate useful data. To circumvent this caveat, I decided to sequence our samples to a target depth of ~4 million reads per sample, which should yield results close to saturated gene detection accuracy and

sensitivity even after accounting for the loss of reads to multimapping and non-exonic sequences.

4.1.4 Experimental approach

To sum up, I designed pipeline to obtain detailed transcriptomic profiles from $VGAT^{+}$ and $VGluT2^{+}$ neurons across PAG subdivisions by individually isolating fluorescently labelled neurons from acute midbrain slices of transgenic mice and processing them with the Smart-seq2 protocol and a target sequencing depth of over 4 million reads per sample.

4.2 A PIPELINE TO PERFORM SINGLE-CELL RNA-SEQUENCING WHILE PRESERVING THE ANATOMICAL ORIGIN OF EACH NEURON

4.2.1 Aspiration of single neurons from acute midbrain slices of transgenic mice

To isolate fluorescently labelled single neurons using visually guided aspiration via patch pipettes, I prepared acute midbrain slices from transgenic mice following the same procedure used for electrophysiological recordings (see section 2.2). The main difference between recording from a PAG neuron or aspirating it for sequencing lied in the size and resistance of the glass capillary: the patch pipettes pulled for recording purposes had a tip resistance of 4-7 MΩ, whereas the aspiration pipettes were pulled to a final resistance of 1-2 MΩ. In addition, and prior to pulling, the glass capillaries used for single cell aspiration were baked at 200°C for 2 hours to sterilise them. Once pulled, and right before aspiration, pipettes were backfilled with recording ACSF containing 2 U/μL recombinant RNase inhibitor to prevent RNA degradation.

Once a slice had been transferred to the recording chamber (Figure 4.1), I identified $VGAT^{+}$ or $VGluT2^{+}$ neurons based on fluorescence from EYFP or tdTomato expression upon LED illumination (Figure 4.2, central image). Importantly, I acquired a low magnification image of the aspiration pipette positioned directly above the target neuron before aspirating it (Figure 4.1). This allowed me to record the anatomical location of each aspirated neuron within the PAG, which was later used to confirm the PAG subdivision each neuron belonged to (see section 4.3).

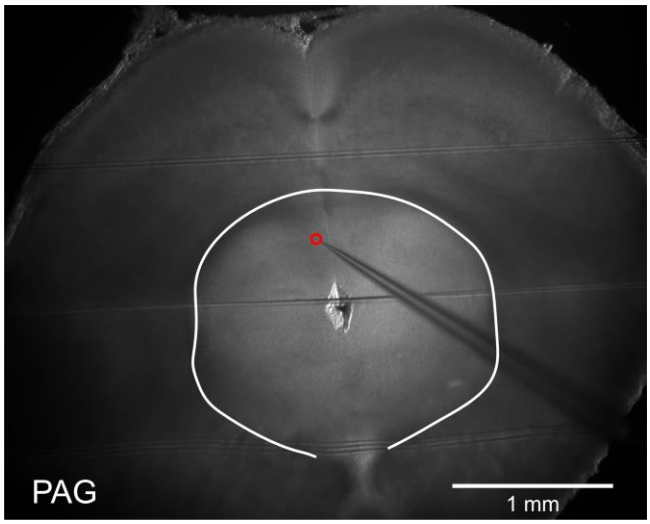

Figure 4.1. Anatomical location of an aspirated neuron within the PAG. Example image of an acute midbrain slice, obtained with a 4× objective prior to aspiration. The red circle indicates the tip of the pipette, positioned just above the target neuron. The white line delimitates the PAG. Scale bar is 1 mm.

Having confirmed the location of the target neuron, I proceeded to aspirate it. To that end, I applied positive pressure to the pipette to prevent any dirt or unwanted tissue from being aspirated and proceeded to approach the soma of the target neuron. I carefully positioned the tip of the pipette in gentle contact with the cell membrane and checked its fluorescence expression to confirm the identity of the target neuron one last time (Figure 4.2, central image). Next, I released the positive pressure and applied gentle suction to slowly aspirate the neuron into the tip of the glass pipette. Once this was accomplished, I immediately stopped the suction and proceeded to carefully retract the pipette from the slice to minimise aspirating neuronal processes or

cellular debris from the surrounding tissue. Lastly, I examined the pipette tip, where the aspirated cell typically remained attached, to obtain visual confirmation of the neuron having been successfully aspirated. An image sequence illustrating the full procedure can be found in Figure 4.2.

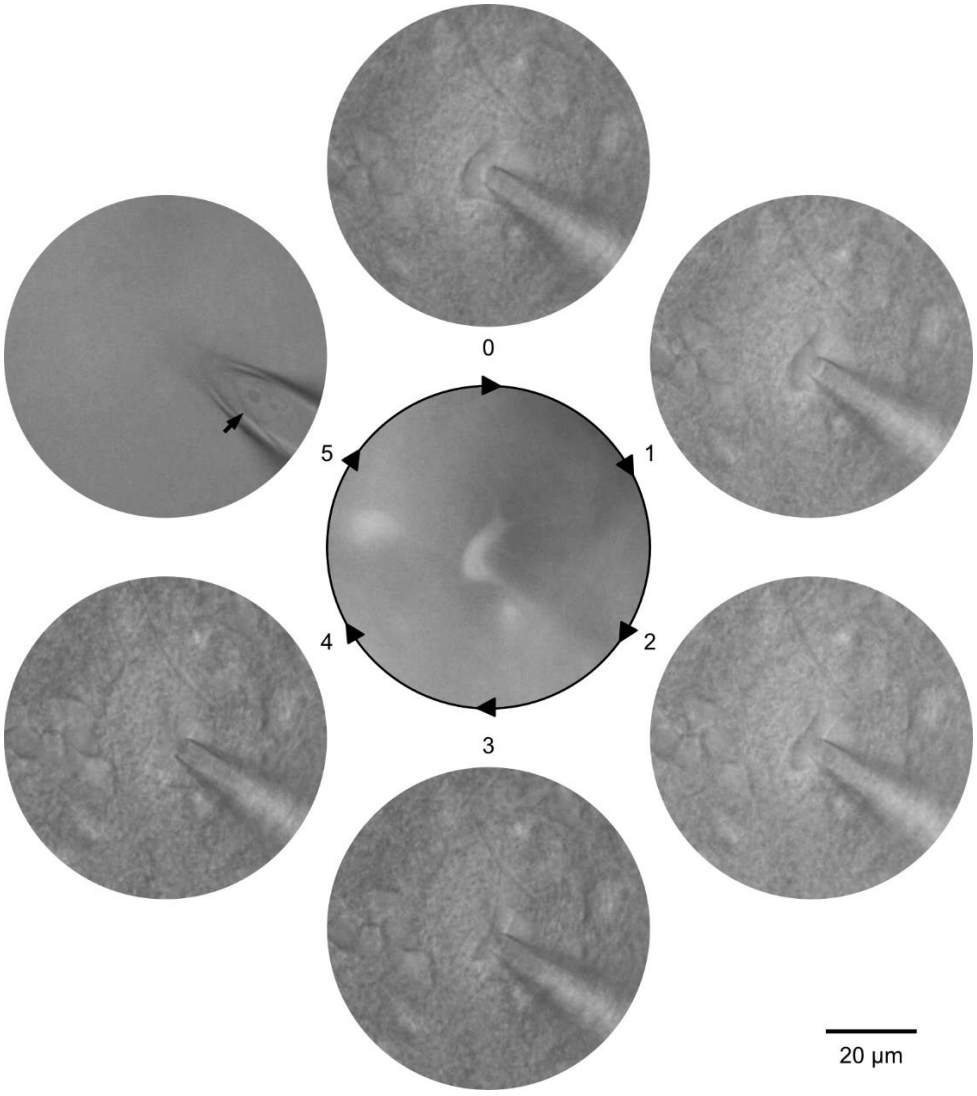

Figure 4.2. Visually guided aspiration of a single PAG neuron. Image sequence illustrating the isolation of a target neuron by visually guided aspiration with a patch pipette. The central image shows the fluorescence emitted by the fluorophores expressed by the genetically labelled neuron. The aspiration sequence starts at the top image and develops in a clockwise order: (0) pipette tip in contact with the soma of the target neuron, (1-4) release of positive pressure and application of gentle suction to aspirate the neuron, (5) aspirated neuron inside the pipette. Arrow in (5) points to the aspirated neuron. Scale bar is 20 µm for all images.

After confirming the aspiration of the target neuron had been successful, I proceeded to retract the pipette all the way out of the bath, detach it from the holder, and break its tip into the bottom of a PCR tube containing a small amount of lysis buffer. Once broken, I quickly pulled the pipette out to avoid drawing the lysis buffer and the sample back into it by capillary action. I then securely closed the PCR tube, vortexed the sample, and spun it down before placing it on dry ice, where it was kept until the remaining samples had been collected.

In a typical experiment, I would collect a total of 24 neurons in equal proportions from each hemisphere and PAG subdivision (dmPAG, dlPAG, lPAG, vlPAG), following a sequence pseudo-randomised for each animal. As a positive control, I added ERCC spike-ins (RNA transcripts of known sequence and quantity) to the lysis buffer of each PCR tube. For each batch of 24 neurons, I also included a negative control containing only lysis buffer to assess DNA contamination during the Smart-seq2 processing steps. In earlier experiments, to assess the amount of ambient mRNA that was added by my sample collection approach, I obtained negative ("stab") controls by inserting the glass pipette into the slice tissue without aspirating any cell. In a small subset of samples, I used pipettes with a 4-7 MΩ tip resistance filled with intracellular solution (see section 0) to trial the *patch-seq* method and obtain whole-cell patch-clamp recordings from the target neuron prior to aspiration.

I collected a total of 588 neurons from 25 mice (13 female, 12 male): 257 $VGAT^+$ neurons from 11 mice (7-9 weeks old, five females, six males) and 331 $VGluT2^+$ neurons from 14 mice (6-9 weeks old, eight females, six males). The breakdown of all collected neurons by cell type and PAG subdivision can be found in Table 4.1.

	dmPAG	**dlPAG**	**lPAG**	**vlPAG**	**TOTAL**
$VGAT^+$	72	65	60	60	**257**
$VGluT2^+$	83	84	82	82	**331**
	155	**149**	**142**	**142**	**588**

Table 4.1. Summary of aspirated neurons by cell type and PAG subdivision.

4.2.2 Smart-seq2 processing workflow

The PCR tube where I transferred each aspirated neuron contained mild lysis buffer to lyse the cellular membrane and ribonuclease inhibitors to prevent RNA degradation (see section 2.4.1 for full details). After briefly vortexing and spinning the samples down, I kept the lysates on dry ice until the end of the experiment and subsequently at −80°C until Smart-seq2 processing (Figure 4.3). The Smart-seq2 protocol uses oligo(dT) primers that bind to the poly(A)$^+$ tail of mRNA molecules and Moloney murine leukaemia virus reverse transcriptase that generates the first strand cDNA. Once the reverse transcription process reaches the 5' end of the RNA transcript, a short sequence of additional anchoring bases is added at the end (CCC). Locked nucleic acid (LNA)-containing template-switching oligonucleotides (TSOs) then bind these anchoring bases and allow the reverse transcriptase to switch template and synthetise a complementary sequence to the TSO, providing full-length coverage of mRNA transcripts (Picelli, Faridani, *et al.*, 2014). Every full-length cDNA molecule carries the entire 5' end of the transcript and an additional artificial sequence, which in this case is the same as the one located at the 5' end of the oligo(dT) primer. The resulting cDNA can thus be amplified using a single ISPCR primer (for a detailed list of all primers used see Table 2.1).

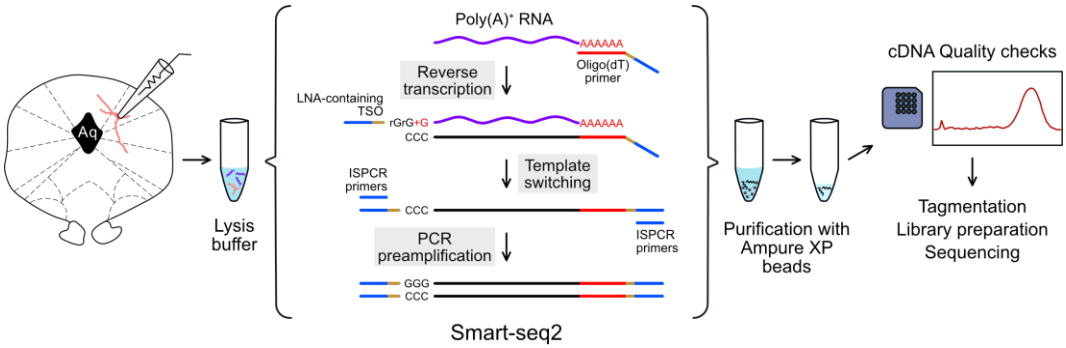

Figure 4.3. Smart-seq2 protocol workflow. Overview of the Smart-seq2 protocol. Aspirated neurons are immediately transferred to a PCR tube containing lysis buffer and subsequently processed using Smart-seq2. The resulting cDNA is purified, subjected to quality checks, and finally sequenced.

At the end of the Smart-seq2 protocol, I purified the samples using magnetic beads and subjected the cDNA to several quality checks to assess its purity, concentration, and integrity (see sections 2.4.2.4 and 0 for details). Finally, samples that passed all quality controls were deemed of good quality and submitted to an external facility for tagmentation, library preparation, and sequencing.

4.2.2.1 Batch and experimental design

Processing samples in different batches has the risk of introducing uncontrollable differences due to factors unrelated to the questions one wants to address. These factors include, but are not limited to, slight modifications in the approach when different people do the same experiment, differences in reagent quality, or differences in the machine used for processing the samples. In single-cell RNA-sequencing experiments, this can result in systematic differences in the observed gene expression profiles in cells from different batches, which are often referred to as *batch effects*. Batch effects are problematic as they can be major drivers of heterogeneity in the data, masking the relevant biological differences and making the interpretation of the results more complicated. Having a good experimental design can help avoid the most common pitfalls and confounding factors and ensure the data can be used to answer the biological questions at hand.

The experimental approach I followed to isolate PAG neurons meant that all the neurons collected on a given experimental day came from the same animal. This introduced a series of confounding factors that I was not able to correct for, as each batch of aspirated neurons was linked to the sex, age, and genotype of a particular animal. However, there were other factors I tried to account for. First, given that I was collecting one cell type (i.e. either VGluT2$^+$ or VGAT$^+$) from different subdivisions within the same brain area in the same animal, I took care to equally sample each variable (in this case, PAG subdivision) in a pseudo-randomised order. In any given experimental day, if I was able to aspirate a total of 24 VGAT$^+$ neurons, I proceeded to collect 6 dmPAG neurons, 6 dlPAG neurons, 6 lPAG neurons, and 6 vlPAG

neurons, with half the neurons in each subdivision coming from each of the hemispheres.

Similar to the limit in the number of neurons I could aspirated during one experiment (collection batch), there was a limit in the number of samples that could be processed at once with the Smart-seq2 protocol (processing batch). If, for example, I was only able to process 20 samples at once, the sample distribution should equally cover different cell types, PAG subdivisions, animals, and experimental days. In addition, given that I used transgenic animals to collect different cell types on different experimental days (e.g. I collected VGluT2^{+} neurons from animal 1, VGAT^{+} neurons from animal 2, etc.), each animal could be treated as a separate batch in their own right, reflecting (presumably uninteresting) biological differences due to genotype, age, sex, or other factors that inherent to this experimental design. What should be avoided is that one processing batch contains only samples from the same cell type and animal, as this would mean that these three variables (batch, cell type, animal) are confounded, making it very difficult to know which one is driving the biological effects observed in the data.

Unfortunately, I learned all this half-way through our data collection and sample processing, which resulted in nearly half of our processing batches following an unbalanced design (i.e. all the samples in a processing batch came from the same animal and experimental day, and belonged to the same cell type), with the other half being successfully balanced (i.e. samples within a processing batch came from different animals and experimental days, and belonged to each cell type and PAG subdivision in the same proportions). I attempted to account for this partial unbalance in the data analysis steps in the best possible way that I could.

4.2.3 cDNA quality control

I used three independent measures to assess the quality of the samples after Smart-seq2 and purification. First, I used a NanoDrop 2000 spectrophotometer to estimate the purity of each sample. The ratio of absorbance at 260 and 280 nm ($A_{260/280}$ ratio) is routinely used to assess the purity of RNA and DNA preparations (Wilfinger, Mackey, and Chomczynski, 1997; Walton and O'Connor, 2018). Typically, a DNA sample is considered pure if it has a $A_{260/280}$ ratio of ~1.8, whereas an $A_{260/280}$ ratio of less than 1.8 is indicative of the presence of unwanted compounds such as proteins. I considered samples with an $A_{260/280}$ ratio below 1.8 to have failed this first quality check.

Second, I determined the concentration of cDNA in the purified samples using a Qubit 2.0 fluorometer. The fluorometer uses specific fluorescent dyes that emit only when bound to their target molecules to measure the concentration of RNA or cDNA. This method is more sensitive than UV spectrophotometry and allows users to detect and accurately measure samples with lower concentrations of RNA or cDNA. I considered samples with a Qubit-measured concentration below 1 ng/μL to have failed this second quality check.

Third, I determined the size distribution of the cDNA of each sample using Agilent High-Sensitivity DNA chips run in an Agilent 2100 Bioanalyzer. A good sample in which cDNA synthesis and amplification were successful should produce a cDNA library spanning 400-9,000 bp with a bioanalyzer profile with a peak in the 1500-3000 bp range, a small number of fragments below 500 bp, and a small number of primer dimers (see below). Such a profile indicates that the majority of cDNA has been produced from intact mRNA and the resulting cDNA is of good quality (Figure 4.4A-D). On the other hand, a sub-optimal mRNA capture and preamplification would generate a profile in which the peak of primer dimers is higher than the cDNA library (Figure 4.4E), whereas a cDNA sample prepared from degraded mRNA would produce a profile with a shift towards short fragments (Figure 4.4G) (Picelli, Faridani, *et al.*, 2014).

Examples of samples with good and sub-optimal quality are shown in Figure 4.4. The test runs using commercially available mouse brain total RNA as starting material produced samples with a good size distribution (Figure 4.4AB). Similarly, most aspirated cells were successfully processed and yielded good size distribution profiles (Figure 4.4CD). Some samples had a bioanalyzer profile in which the peak in the 1500-3000 bp range was very low and a higher peak was observed in the 100-200 bp range, which corresponds to an amplification of primer dimers (Figure 4.4E). Negative controls in which no cell was collected had a mainly flat profile apart from the peak corresponding to the primer dimers (Figure 4.4F). Negative controls are essential and were added to each Smart-seq2 processing run to evaluate the results and to identify potential contamination problems.

In earlier experiments, I also collected and processed "stab" controls consisting of the material that would get stuck on the outside of the aspiration pipette after penetrating the slice tissue without aspirating a neuron. Such samples produced bioanalyzer profiles compatible with those obtained from libraries prepared from degraded mRNA: the main peak corresponded to primer dimers and the profile showed a low, broad peak spread throughout short fragment sizes and some long fragments (Figure 4.4G). This suggested that the ambient mRNA added by my sample collection approach was mainly degraded and of low quality and would signify a small proportion of the cDNA generated from good quality samples.

Samples that passed the NanoDrop and Qubit quality checks and showed good Bioanalyzer profiles were deemed of good quality and submitted for sequencing.

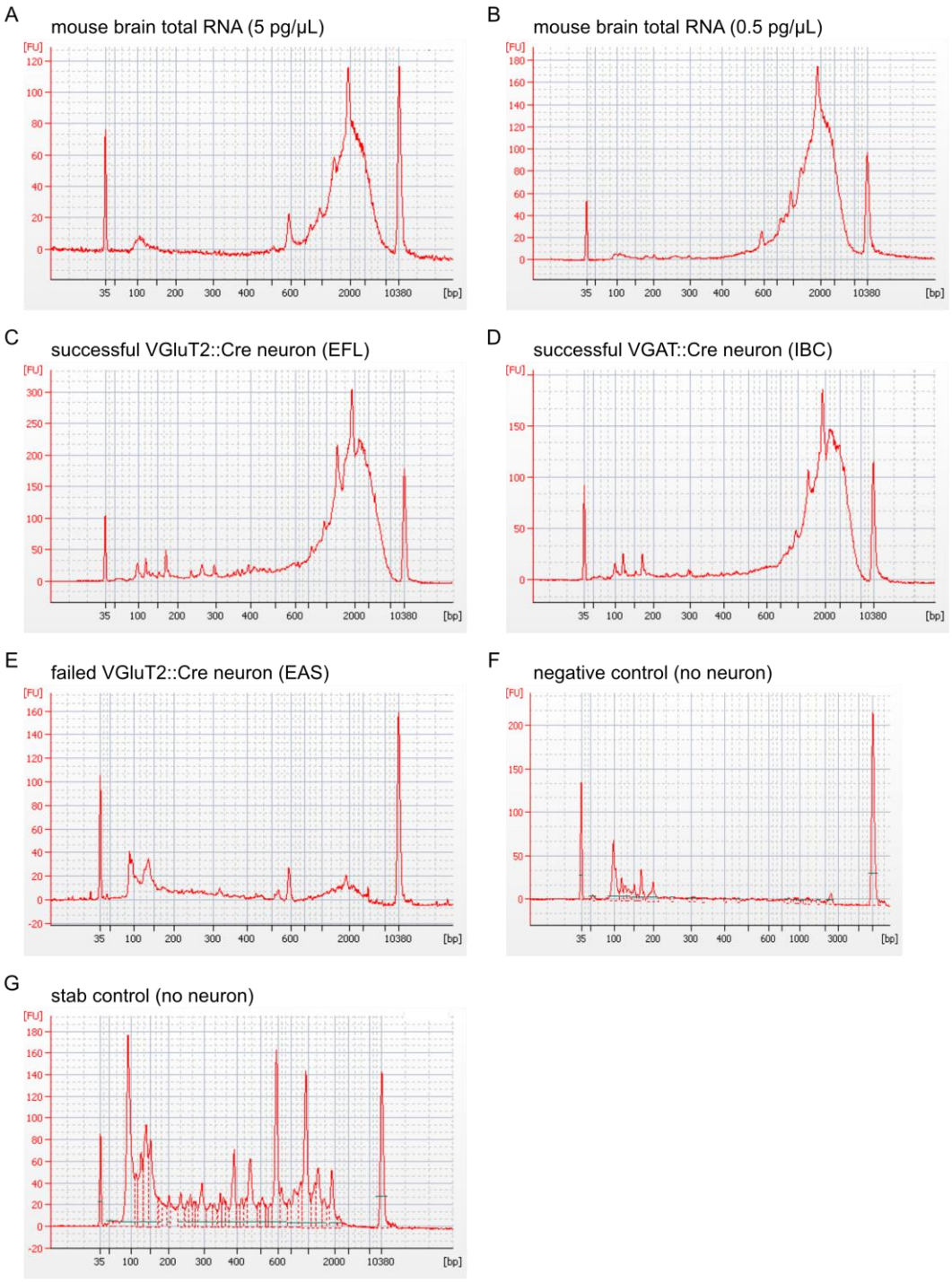

Figure 4.4. Bioanalyzer electropherograms of pre-amplified cDNA libraries. (**A-D**) Representative examples of the cDNA size distribution obtained from the successful capture, reverse transcription, pre-amplification, and purification of mRNA from commercially available mouse brain total RNA at different concentrations (A, B) and from a single VGluT2$^+$ (C) or VGAT$^+$ (D) PAG neuron. (**E-G**) Representative examples of the cDNA size distribution

obtained from the unsuccessful capture, reverse transcription, pre-amplification, and purification of mRNA from a single VGluT2$^+$ PAG neuron (E), from a negative control containing lysis buffer alone (F), and from a stab control containing the material that got stuck on the outside of the aspiration pipette after penetrating the slice tissue without aspirating a neuron (G). In all images, the first and last sharp peaks correspond to the lower (35 bp) and upper (10,380 bp) markers of the electropherogram ladder. A couple of smaller sharp peaks around 100-150 bp can usually be observed, corresponding to the pre-amplification of primer dimers. EFL, IBC, and EAS indicate the unique three-letter identifier assigned to the samples. The units of the X axis are base pairs (bp). The units of the Y axis are fluorescence units (FU).

4.2.4 Summary of aspirated neurons submitted for sequencing

Out of the 588 collected and processed PAG neurons, a total of 516 neurons (253 VGAT$^+$ and 263 VGluT2$^+$) were deemed of good quality and selected for sequencing. A breakdown of all sequenced neurons by cell type and PAG subdivision can be found in Table 4.2.

	dmPAG	**dlPAG**	**lPAG**	**vlPAG**	**TOTAL**
VGAT$^+$	70	64	61	58	**253**
VGluT2$^+$	67	66	68	62	**263**
	137	**130**	**129**	**120**	**516**

Table 4.2. Summary of sequenced neurons by cell type and PAG subdivision.

4.2.5 cDNA library preparation and sequencing

The final steps of this pipeline, namely cDNA library preparation and sequencing, were performed externally by the Barts London Genome Centre at the Blizard Institute, Queen Mary University of London. Briefly, libraries were prepared using the Illumina Nextera XT Sample Preparation Kit with an input of 150 pg of cDNA per sample, equimolar quantities of each sample library were pooled together, and 75 bp paired-end reads were generated for each library using the Illumina NextSeq 500 High-output sequencing kit, with a target sequencing depth of ~4 million reads per sample (see section 2.4.2.5 for full details).

4.3 REGISTRATION OF A NEURON'S ANATOMICAL LOCATION TO THE COMMON COORDINATE FRAMEWORK

As I explained in section 4.2.1, before penetrating the slice tissue and proceeding with sample collection, I positioned the tip of the aspiration pipette right above the target neuron and confirmed its anatomical location by taking a low magnification image (Figure 4.1). Such images allowed me to check I was in the correct PAG subdivision (Figure 4.5A) and ensured I collected each sample according to the pseudo-randomised order established for each experiment. To obtain an overview of all aspirated neurons submitted for sequencing, I visually compared each image to the coronal plates of the Franklin and Paxinos mouse brain atlas (Franklin and Paxinos, 2008), and marked the location of the neuron in the closest coronal section (Figure 4.5B).

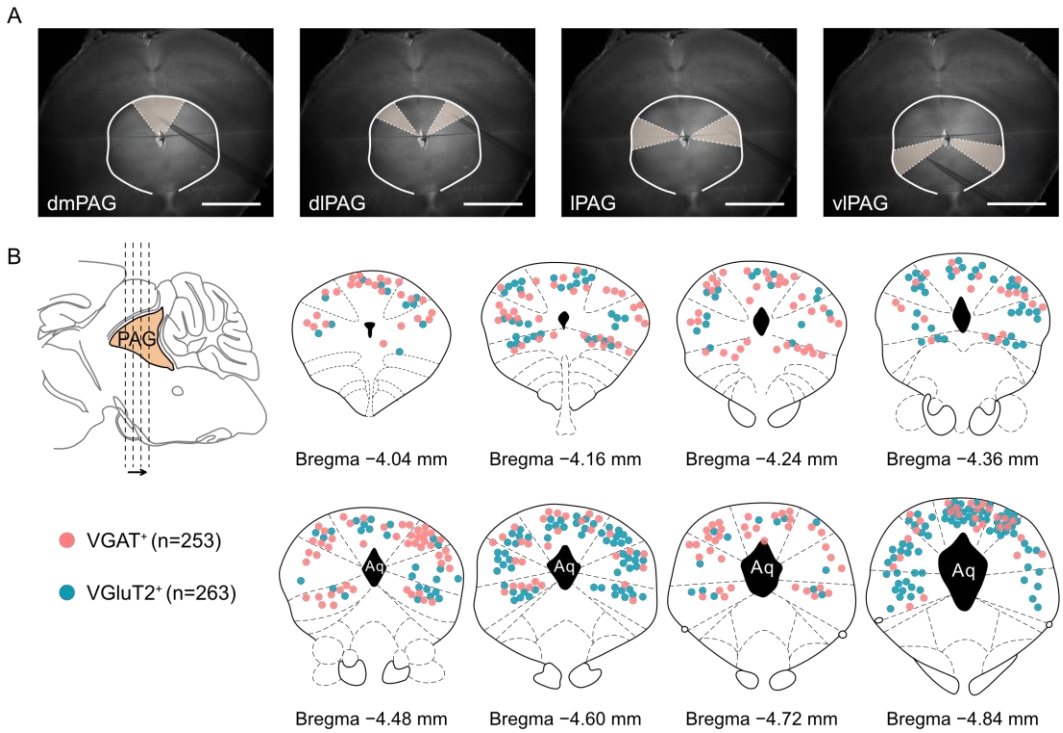

Figure 4.5. Overview of the anatomical location of all sequenced PAG neurons. (**A**) Representative images illustrating the aspiration of target neurons located at different PAG subdivisions as described in Franklin and Paxinos (2008). Yellow shadings mark each of the PAG subdivisions, from left to right: dorsomedial (dmPAG), dorsolateral (dlPAG), lateral (lPAG), and ventrolateral (vlPAG). The white line delimitates the PAG. All scale bars are 1 mm. (**B**) The inset in the top left represents a sagittal section of the posterior half of a mouse brain. The PAG is highlighted in yellow, dashed lines represent different coronal sections along the rostro-caudal axis, and the arrow indicates the direction followed by the sequence of larger sections on the right. The schematics on the right show the distribution of all sequenced neurons within coronal sections of the PAG along the rostro-caudal axis, coloured by cell type. Aq, aqueduct. Adapted from Franklin and Paxinos (2008).

The development of the Allen Mouse Brain Common Coordinate Framework (CCF) signified the creation of a standardised 3D reference atlas that could be used to integrate the results of many different types of experiments (Wang, Ding, *et al.*, 2020). Recent advances in user-friendly computational tools have made it possible to interact and work with this resource. For instance, the Slice Histology Alignment, Registration, and Probe Track analysis tool (SHARP-Track) allows users to geometrically transform

slice histology images, register them to the CCF, and extract the anatomical coordinates of a particular point of the image (Shamash, Carandini, *et al.*, 2018).

I used SHARP-Track to register all the low-magnification images and extract the CCF coordinates for the anatomical location of each PAG neuron I had aspirated and sequenced. I then used these coordinates to generate 3D visualisations with *brainrender* (Claudi, Tyson, *et al.*, 2021) and the BrainGlobe Atlas API (Claudi, Petrucco, *et al.*, 2020). Figure 4.6 shows some examples of the versatility of this tool, which allowed me to visualise the position of all the neurons in the single-cell RNA-sequencing dataset and their anatomical position within the full mouse brain and the PAG itself (Figure 4.6AB). Furthermore, I was able to enhance these plots by colouring each neuron according to specific metadata and explore whether I achieved a homogeneous distribution of each cell type across PAG subdivisions (Figure 4.6C-F, left) or of each subdivision along the rostro-caudal axis (Figure 4.6C-F, right).

In addition, image registration enabled me to curate the PAG subdivision assigned to each aspirated neuron. When finding the target neuron to aspirate, I initially decided the location by comparing the image of the brain slice under the microscope to an atlas by eye (Figure 4.5). However, this approach is prone to errors, especially since not all acute brain slices will be cut at a perfectly coronal angle and the boundaries between PAG subdivisions can be a bit subjective. By using SHARP-Track to geometrically transform and register the images to the CCF I could minimise such errors. Unfortunately, unlike the Franklin-Paxinos atlas (Franklin and Paxinos, 2008), the Allen Mouse Brain Atlas does not subdivide the PAG into columns, and the coordinates of each neuron would be labelled as PAG and not dmPAG, dlPAG, lPAG or vlPAG.

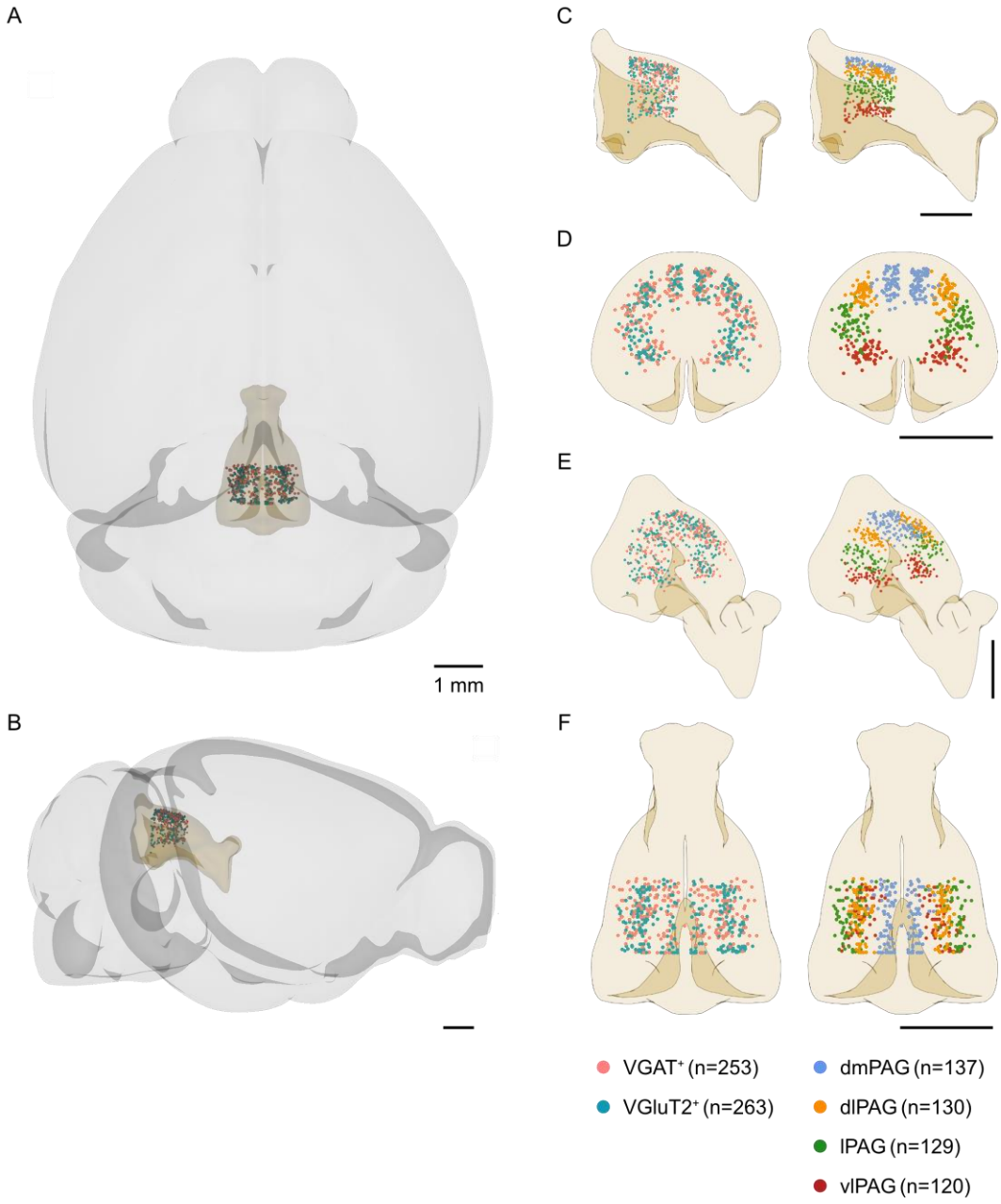

Figure 4.6. Overview of the anatomical location of all sequenced PAG neurons after registration to the CCF. (**A-B**) Distribution of all the aspirated and sequenced PAG neurons within the full CCF. Outline of the brain is in grey. Outline of the PAG is in yellow. Each dot represents a neuron, coloured by cell type. All scale bars are 1 mm. (**C-F**) Distribution of all the aspirated and sequenced neurons within the PAG, coloured by cell type (left column) or PAG subdivision (right column). Outline of the PAG is in yellow. All scale bars are 1 mm.

To overcome this problem, I turned to the recently published enhanced and unified anatomical labelling (Chon, Vanselow, *et al.*, 2019), which merges the Franklin-Paxinos labels (containing PAG subdivisions) into the Allen Mouse Brain Atlas CCF to produce a common atlas framework. Fortunately, this enhanced and unified atlas had been incorporated into the BrainGlobe Atlas API (Claudi, Petrucco, *et al.*, 2020), which meant I could use the registered coordinates to curate the PAG subdivision assigned to each aspirated neuron. To achieve this, I used the function *"structure_from_coords()"* from the BrainGlobe Atlas API, which returns the name of the brain area label that corresponds to a set of CCF coordinates. Lastly, I used a supervised approach in which I compared the original images, the registered labels, and the Franklin-Paxinos atlas to reach a consensus and obtain the final and curated PAG subdivision labels for each sequenced neuron (Table 4.2).

4.4 DATA PRE-PROCESSING AND QUALITY CONTROL

4.4.1 RNA sequence alignment and quantification

The analysis steps described in this section, including read alignment and quantification, were performed externally by the Barts London Genome Centre at the Blizard Institute, Queen Mary University of London. Before performing the read alignment, the quality of the raw reads was assessed with `FastQC` (Andrews, 2010), a quality control tool for raw sequence data coming from sequencing pipelines. The reads were then trimmed from adaptor sequences and low-quality bases. Before proceeding with read alignment, custom genome reference sequences were created for the transgenes used to label neurons (Cre, EYFP, and tdTomato), the ERCC spike-in Mix 1, and TSO concatemers. Reads were aligned to the mouse genome (mm10, GRCm38.96) and the custom reference sequences using `STAR` (Dobin, Davis, *et al.*, 2013). A mapping quality of `MAPQ=255` was specified to identify and keep only the

reads that uniquely map to one genome locus. Reads with a mapping quality value below 255 (multimapping reads) were filtered out. Duplicated and unaligned reads were also removed.

Uniquely mapping reads were quantified using the `RefSeq Transcripts 83` annotation model, generating counts for both genes and transcripts (i.e. how many copies of each gene or transcript were detected in each sample). To avoid losing any reads, the minimum number of counts required for a read to be classified as detected was set to 0. The output of the RNA sequence alignment and quantification process was a table in which each column is a PAG neuron, and each row contains the number of counts for each gene or transcript. This table can also be referred to as a *count matrix* or *gene expression matrix*. I used the table containing gene counts for downstream analysis.

	min.	1st Qu.	median	mean	3rd Qu.	max.
Total reads per sample (millions)	0.119	3.398	4.076	4.065	4.752	7.787
Uniquely mapping reads (millions)	0.099	2.785	3.401	3.382	4.010	6.759
Uniquely mapping reads (% of total reads)	22.21	80.86	84.39	82.86	86.54	89.80
Reads mapped to annotated genes (millions)	0.069	1.672	2.143	2.161	2.625	4.928
Reads mapped to annotated genes (% of total reads)	19.39	47.48	53.54	52.79	58.90	78.84
Total genes detected	2,635	8,692	9,584	9,447	10,358	13,890

Table 4.3. Sequencing output summary across all neurons.

In summary, the generated dataset contained 516 PAG neurons sequenced to a median depth of ~4 million reads (Table 4.3). Out of these, a median of ~3.4 million reads uniquely mapped to the mouse genome (approximately 84% of the total reads, the rest of the reads mainly being multimapping or with no match), with over 95% of samples having at least 70% of reads uniquely mapping to the reference genome. A

median of ~2.1 million reads mapped to annotated genes (approximately 53% of the total reads, the rest of the reads mainly mapping to intronic or intergenic sequences), and these were the ones used to generate the output table containing the gene expression matrix used for downstream analysis. Overall, a median of 9,584 genes were detected per sample. A full breakdown of the dataset can be found in Table 4.3. These values illustrate that, although being a low-throughput approach, manual aspiration of neurons followed by Smart-seq2 resulted in high-quality samples that could be sequenced at the depth required to pursue the experimental goals of my project.

4.4.2 Importing and pre-processing the data

After obtaining the gene expression matrix from the sequencing results, I proceeded to load and pre-process the data. I imported the results from the `.txt` file provided by the sequencing facility into R and created a matrix where each entry represented the number of reads mapped to a particular gene (rows) in a particular neuron (columns). I also loaded the metadata from a `.csv` file I had previously curated, in which each column contained information about a particular neuron (rows). The metadata included details about the neuron (ID, cell type, fluorophore, anatomical coordinates, PAG subdivision), the mouse it originated from (genotype, age, sex), and the experiment (date of collection, date processed, batch number, sequencing round). In addition, I prepared and imported another `.csv` file containing several manually curated lists of genes (ion channel subfamilies, transcription factors, receptors for different families of neurotransmitters, neuropeptides, and neuromodulators) that I could use during later analysis steps.

I next proceeded to curate both the data and metadata, ensuring that the gene expression data and the cell metadata followed the same order (i.e. the ID of the neuron in column 1 of the count matrix corresponded to the ID of the neuron in row 1 of the metadata, and so on and so forth). This was a critical step as otherwise there is a risk of assigning incorrect metadata to each cell. Finally, I used the ENSEMBL

identifiers to obtain the corresponding gene symbols, which are easier to interpret, and their chromosomal location.

Once I had imported and curated the data, I created an object of the `SingleCellExperiment` class, a lightweight Bioconductor container designed for storing and manipulating single-cell genomics data (Amezquita, Lun, *et al.*, 2020). Importantly, this class implements a structure that allows the user to store and manipulate all aspects of the single-cell data in one single object: the gene-by-cell expression data, the per-cell metadata, the per-gene annotations, and many other types of results that have been generated in advance (such as the lists of genes) or that will be generated during the course of the analysis (such as dimensionality reduced representations of the data, clustering IDs, or differentially expressed genes).

4.4.3 Quality control

Despite attempting to detect and remove any low-quality samples before sequencing, there is always a risk of having sub-optimal libraries in the final dataset. Such samples can complicate the analysis and interpretation of the results and need to be identified and removed before the main analysis is carried out. The Bioconductor package *scater* (McCarthy, Campbell, *et al.*, 2017) allows users to define several control metrics to identify low-quality samples.

4.4.3.1 Defining cell-based quality metrics

There are several metrics that can be used to quality check a single-cell RNA-sequencing dataset. The first of such metrics is the *library size*, defined as the total sum of counts that have been uniquely mapped to known features (genes, transgenes, ERCC spike-ins, etc.) in each sample. A relatively small library size is indicative of low quality before isolation (e.g. the cell membrane was compromised before aspiration) or poor cDNA capture and amplification (e.g. one or more of the processing steps

failed). The second metric that can be used is the *number of detected genes* in each library, defined as the number of features with non-zero counts for each sample. Samples in which the diverse transcript population has not been successfully captured tend to have very few detected genes and are likely to be of poor quality. Similarly, any sample with way more genes detected than the average is likely to contain mRNA molecules from two cells instead of just one.

The proportion of reads mapped to sequences corresponding to *mitochondrial genes* can also be used for quality control. A relatively high proportion of reads mapped to mitochondrial genes has been linked to cell damage resulting in loss of cytoplasmic RNA and relative enrichment of mitochondrial transcripts (Islam, Zeisel, *et al.*, 2014; Ilicic, Kim, *et al.*, 2016). A possible explanation for this would be that if the cell membrane is partially damaged, cytoplasmic RNA transcripts would be small enough to flow through the holes and escape, but transcripts enclosed in mitochondria would not. Similarly, a relatively high percentage of reads mapped to *ribosomal genes* or to a small number of highly expressed genes can indicate uneven capture and amplification of RNA transcripts.

Another useful quality metric is the proportion of reads mapped to *ERCC spike-in sequences*. The quantity of spike-in RNA added to each sample before processing should be constant, which means that one should only observe an increased proportion of spike-in counts if endogenous RNA was lost during sample isolation or processing. A somewhat similar strategy is to turn to the template switching oligonucleotides (TSOs) used in the Smart-seq2 protocol. During the processing steps, TSOs can concatenate and form longer DNA sequences, or *TSO concatemers*, that can get amplified along with the sample's cDNA. Knowing this, I added the TSO concatemer sequence to the customised genome reference and was able to quantify the proportion of reads mapped to these sequences and use it as a quality metric. Similar to the spike-ins metric, a high ratio of TSO concatemers in comparison to endogenous transcripts would be indicative of a low-quality sample.

In addition to these commonly used metrics, I leveraged the experimental approach I used to isolate cells for quality control. Given that I isolated cells from transgenic animals expressing either EYFP or tdTomato as a reporter, all cells should express Cre, but a given cell should only express either EYFP or tdTomato. To check everything was as it should be I looked at whether each cell expressed only the fluorophore it should according to the transgenic line it was acquired from. A simple scatter or violin plot of log-transformed counts of EYFP and tdTomato was enough to reveal this (Figure 4.7). As it is apparent in the figure, a minority of samples expressed both fluorophores when they should only express one. The safest option, and the one I followed, was to exclude any sample with counts assigned to the wrong fluorophore, as there may have been a contamination at one of the processing steps of that sample.

In all experiments, I isolated neurons expressing either EYFP or tdTomato as a reporter under the VGAT or VGluT2 promoter. One may be tempted to extend the approach followed with the fluorophores to the promoters used to target the neurons. However, even though it has been shown that VGAT and VGluT2 Cre mice specifically target GABAergic and glutamatergic neurons and that these form segregated neuronal subpopulations in the vlPAG (Samineni, Grajales-Reyes, *et al.*, 2017), many studies have reported neurons that co-express and co-release GABA and glutamate in a variety of brain areas (Shabel, Proulx, *et al.*, 2014; Yoo, Zell, *et al.*, 2016; Granger, Wallace, and Sabatini, 2017; Romanov, Zeisel, *et al.*, 2017; Root, Barker, *et al.*, 2020; Kim, Wallace, *et al.*, 2021). In my dataset, the scatter and violin plots of log-transformed counts of VGAT and VGluT2 expression showed that approximately half of the VGAT::Cre neurons also express VGluT2, and approximately half of the VGluT2::Cre neurons also express VGAT (Figure 4.8). Given that further experiments outside the scope of this thesis would be required to clarify whether PAG neurons co-release GABA and glutamate and what would the physiological effects of such an attribute be, I decided to refrain from using the expression levels of VGAT and VGluT2 as a quality control metric.

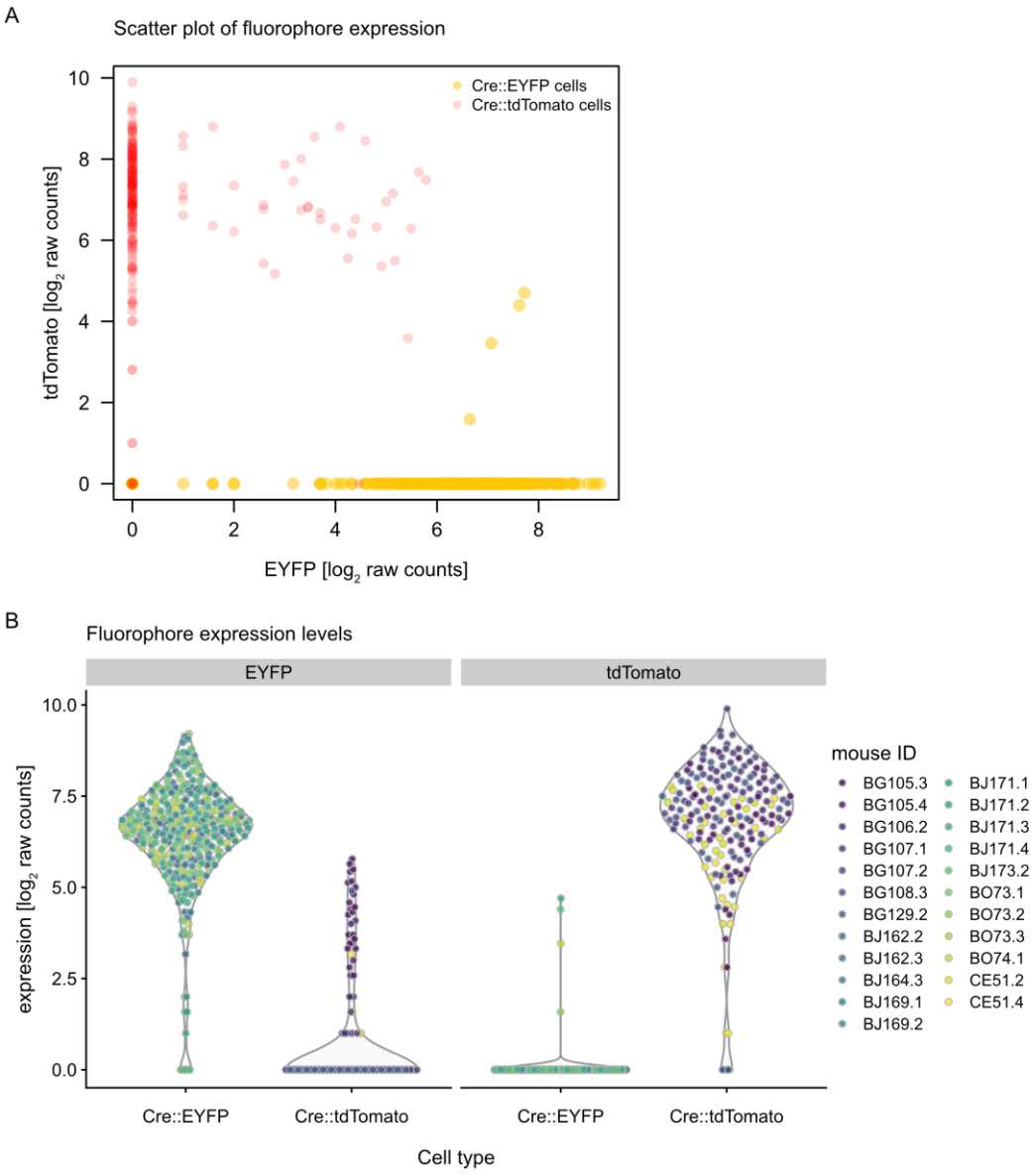

Figure 4.7. Expression levels of the fluorophores used to target neurons. (**A**) Scatter plot of the log_2-transformed raw expression values of EYFP and tdTomato for each sequenced neuron. Each circle represents a neuron, coloured according to its genotype (Cre::EYFP neurons in yellow and Cre::tdTomato neurons in red). (**B**) Violin plot of the log_2-transformed raw expression values of EYFP (left facet) or tdTomato (right facet) for all Cre::EYFP (left violin) or Cre::tdTomato (right violin) neurons. Each circle represents a neuron, coloured according to the ID of the mouse it originated from (BG indicates VGAT::tdTomato mice, BO indicates VGAT::EYFP mice, CE indicates VGluT2::tdTomato mice, and BJ indicates VGluT2::EYFP mice).

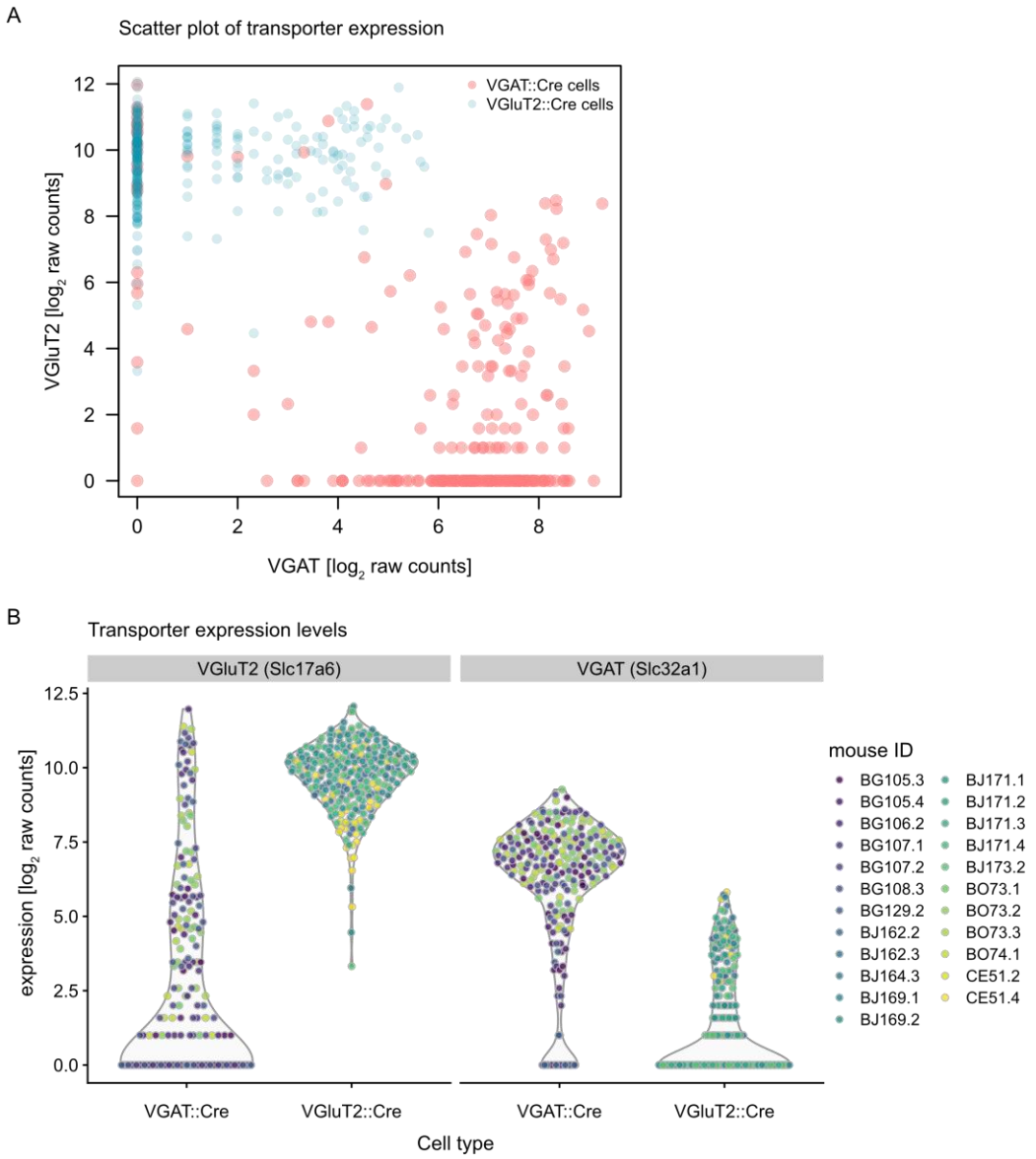

Figure 4.8. Expression levels of the transporters used to target neurons. (**A**) Scatter plot of the log_2-transformed raw expression values of VGAT and VGluT2 for each sequenced neuron. Each circle represents a neuron, coloured according to its genotype (VGAT::Cre neurons in salmon and VGluT2::Cre neurons in light blue). (**B**) Violin plot of the log_2-transformed raw expression values of VGluT2 (Slc17a6 gene, left facet) or VGAT (Slc32a1 gene, right facet) for all VGAT::Cre (left violin) or VGluT2::Cre (right violin) neurons. Each circle represents a neuron, coloured according to the ID of the mouse it originated from (BG indicates VGAT::tdTomato mice, BO indicates VGAT::EYFP mice, CE indicates VGluT2::tdTomato mice, and BJ indicates VGluT2::EYFP mice).

4.4.3.2 Identifying and excluding low-quality samples

There are several ways to use the quality metrics I just defined to identify and exclude low-quality cells from the dataset. The most flexible approach and the one that grants a higher degree of control and interpretability over the results is to define a threshold for each of the metrics based on their observed distribution. This avoids any assumptions associated with the use of outliers to identify low-quality cells and ensures the reason behind removing each cell is clear.

I first filtered samples that had libraries with low complexity by removing those with less than 400,000 reads uniquely mapping to annotated genes and those with less than 5,000 genes detected (Figure 4.9AB). I also filtered samples that could potentially contain more than one cell by removing those with more than 4.6 million reads uniquely mapping to annotated genes and those with more than 13,000 genes detected (Figure 4.9AB). Next, I removed samples with more than 15% of reads mapping to mitochondrial genes (Figure 4.9C). I also removed any sample with more than 20% (in the case of VGAT::Cre neurons) or 30% (in the case of VGluT2::Cre neurons) of reads mapping to ribosomal genes. In this case, I applied a different threshold depending on the cell type due to the difference in the distributions of this particular metric (Figure 4.9D), which may reflect the actual size difference between GABAergic and glutamatergic neurons (see section 1.1.2). In addition, I discarded any sample with more than 1% of reads mapping to ERCC spike-ins or more than 5% of reads mapping to TSO concatemers (Figure 4.9EF). To rule out any potential contamination, I excluded any sample with reads mapping to the wrong fluorophore: Cre::EYFP neurons expressing tdTomato and Cre::tdTomato neurons expressing EYFP (Figure 4.9GH). Finally, I excluded samples in which more than 60% of reads were consumed by the 100 most expressed genes (Figure 4.9I).

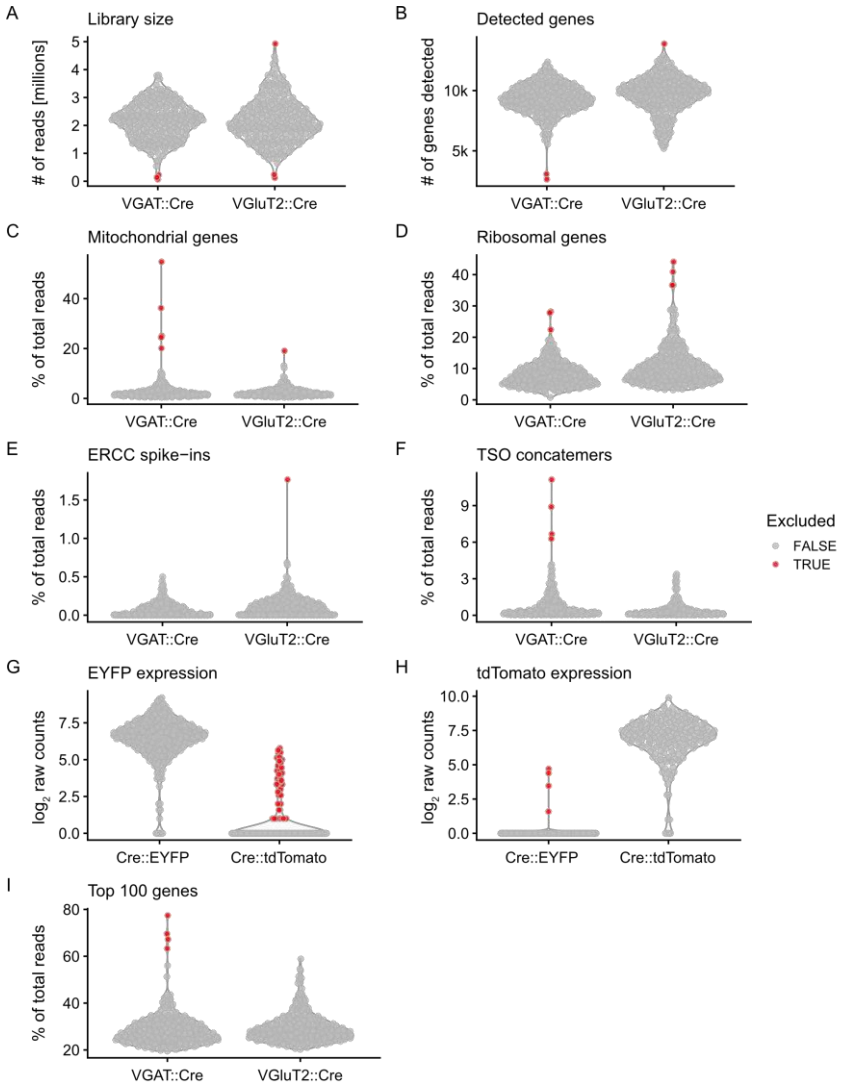

Figure 4.9. Distribution of quality control metrics. Each panel represents the distribution of a particular quality metric in the form of two violin plots, one for VGAT::Cre or Cre::EYFP neurons (left) and one for VGluT2::Cre or Cre::tdTomato neurons (right). Each dot represents the value of the relevant quality metric for a particular sequenced neuron, coloured according to whether it passes (grey) or fails (red) the pertinent quality check. (**A**) Library size, quantified as the number of reads (in millions) uniquely mapping to annotated genes in each sample. (**B**) Number of detected genes in each sample. (**C**) Percentage of reads uniquely mapping to mitochondrial genes in each sample. (**D**) Percentage of reads uniquely mapping to ribosomal genes in each sample. (**E**) Percentage of reads uniquely mapping to ERCC spike-in sequences in each sample. (**F**) Percentage of reads uniquely mapping to TSO concatemer sequences in each sample. (**G**) Log_2-transformed raw expression values of EYFP in each sample. (**H**) Log_2-transformed raw expression values of tdTomato in each sample. (**I**) Percentage of reads uniquely mapping to the top 100 most expressed genes in each sample.

To complete the cell-based quality control, I further excluded one sample that was aspirated from the ependymal cell layer surrounding the cerebral aqueduct, six samples that were subjected to whole-cell recordings before being aspirated, and two VGAT::Cre samples that did not express neither VGAT nor any fluorophore but expressed VGluT2. Overall, I excluded 69 cells from the initial 516, a little over 13% of the full dataset. A breakdown of the sequenced neurons by cell type and PAG subdivision that passed the quality control can be found in Table 4.4.

	dmPAG	**dlPAG**	**lPAG**	**vlPAG**	**TOTAL**
VGAT$^+$	53	50	46	51	**200**
VGluT2$^+$	63	61	63	60	**247**
	116	**111**	**109**	**111**	**447**

Table 4.4. Summary of sequenced neurons by cell type and PAG subdivision after quality control.

4.4.3.3 Removing uninteresting genes

In addition to removing low-quality cells, genes that offer little or no information can also be excluded from the dataset to reduce the computational complexity of downstream analysis. To that end, I first removed predicted genes from the dataset, which could be identified by having "Gm" (for Gene model) at the start of their name. Next, I excluded all the genes that were not detected in any cell, as they provide no information. Finally, I kept only the genes that were expressed (i.e. were detected at least once) in at least 3 or more cells. The rest were classified as weakly expressed genes and were discarded. In the end, I was left with a little over 20,000 genes.

4.4.4 Normalisation of cell-specific biases

The final step before moving on to quantitative analysis consisted of applying a normalisation strategy to remove or ameliorate cell-specific biases inherent to single-cell RNA-sequencing. The difficulty of preparing cDNA libraries in a consistent manner when starting from really low amounts of mRNA typically leads to technical differences across samples. This can translate into variability in the efficiency of cDNA capture or PCR amplification, which in turn can lead to systematic differences in sequencing coverage between libraries (Stegle, Teichmann, and Marioni, 2015). In addition, single-cell RNA-sequencing samples are often sequenced on highly multiplexed platforms, and the total reads derived from each cell may differ substantially. A successful normalisation will remove these differences, avoid any interference with the comparisons made regarding the expression profiles between cells, and ensure the results stem from biology and not technical biases.

To normalise the data, I used the normalisation by deconvolution approach implemented by the *scran* package, which has been specifically adapted to the characteristics of single-cell data (L. Lun, Bach, and Marioni, 2016; Vallejos, Risso, *et al.*, 2017). Briefly, the method pools the counts from groups of cells and estimates a size factor for that pool. Assuming that most genes in the dataset are not differentially expressed between cells, the size factor represents the extent to which counts should be scaled to remove technical bias. The method repeats the process for many different pools of different sizes. Given that each cell has been assigned to many different pools, the pool-based size factors can be deconvolved into cell-based factors. Each cell-based size factor represents the estimate of the relative bias in that cell and is used to normalise the expression profile of each sample.

In my data, the estimated size factors are tightly correlated with the library size for all cells (Figure 4.10). This suggested that the systematic differences between cells were primarily driven by differences in capture efficiency or sequencing depth, as any strong differential expression between cells would yield a non-linear trend between the total

count and size factor, and/or increased scatter around the trend. To normalise the data using the estimated size factors, I used *scater* to calculate normalised expression values for each sample (McCarthy, Campbell, *et al.*, 2017). Each value was defined as the $\log_2$-ratio of each count to the size factor for the corresponding cell, after adding a pseudo-count of 1 to avoid undefined values at zero counts. As mentioned above, dividing the counts of each gene by its appropriate size factor ensured that any cell-specific biases were removed. In addition, the log-transformation provided some measure of variance stabilization so that high-abundance genes with large variances did not dominate downstream analyses (Law, Chen, *et al.*, 2014). Log-transforming the data also meant that any differences in the values represented $\log_2$-fold changes in expression between cells, which is important for the clustering and dimensionality reduction analysis steps based on Euclidean distances. The resulting normalised expression values were used for the analysis steps described in the next chapter.

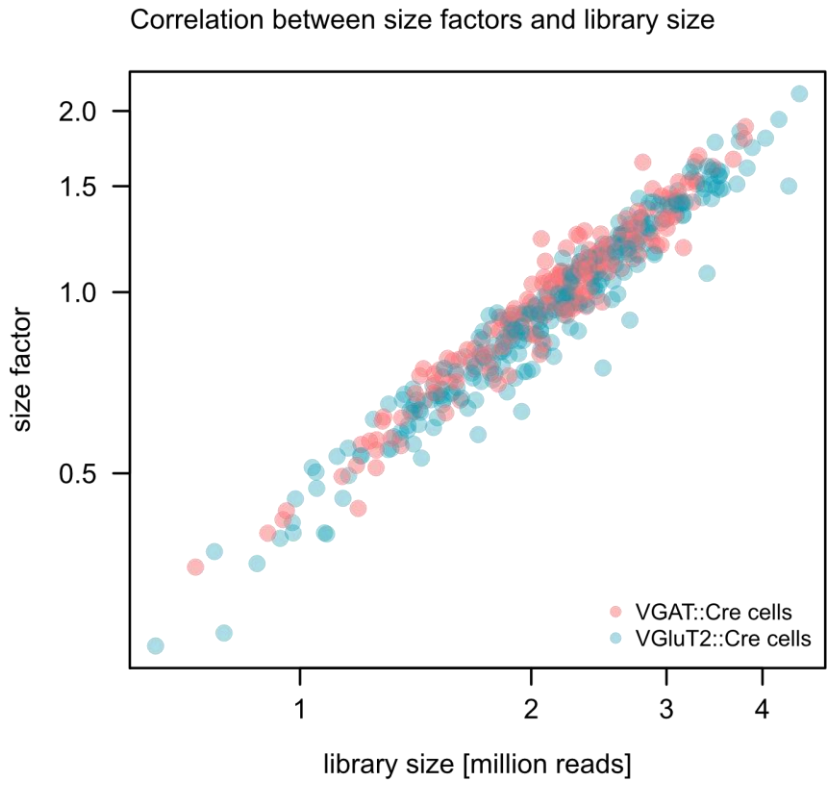

Figure 4.10. Normalisation size factors correlate with library size. Scatter plot showing the relationship between the estimated size factors and the library size for VGAT$^+$ neurons (salmon) and VGluT2$^+$ neurons (light blue).

4.5 SUMMARY

A big part of this thesis project has been dedicated to research, identify, and implement the approach best suited to characterise the molecular complexity of neurons across PAG subdivisions. Notably, neither the technique (single-cell RNA-sequencing) nor the approach (aspiration of genetically labelled neurons from acute slices) had been previously used in the laboratory or the host institute. A great deal of effort was invested in considering and comparing different protocols, in troubleshooting the chosen method, and in ensuring that this expertise would remain available to present and future colleagues (Pavón Arocas, Olesen, and Branco, 2021). The results of this chapter demonstrate I have successfully established a pipeline to perform topographic and cell type-specific deep transcriptomic profiling of PAG neurons.

To recapitulate, I implemented a method to carry out single-cell RNA-sequencing while preserving the anatomical origin of each neuron. By using visually guided aspiration via patch pipettes I isolated fluorescently labelled neurons from acute midbrain slices of transgenic mice. I processed the samples with Smart-seq2 and subjected them to deep sequencing to obtain detailed gene expression profiles from $VGAT^{+}$ and $VGluT2^{+}$ neurons across the different PAG subdivisions. I registered the anatomical location of each neuron to the common coordinate framework of the Allen Mouse Brain Atlas and obtained standardised coordinates to curate the PAG subdivision of each sequenced neuron. Finally, I pre-processed the resulting single-cell RNA-sequencing dataset and subjected it to stringent quality control and normalisation. In the next chapter, I proceed with analysis of the dataset and biological interpretation of the results.

5 GENE EXPRESSION PROFILING OF SINGLE PERIAQUEDUCTAL GRAY NEURONS

The results from chapter 3 suggested that $VGAT^+$ and $VGluT2^+$ neurons in the PAG differ in one important electrophysiological parameter: the ability to spontaneously fire action potentials in a slice. This hallmark of $VGAT^+$ neurons was independent from the presence of synaptic inputs and from the PAG subdivision where the neuron was found. To expand these findings and to characterise the molecular profile of both cell types, I implemented a method to carry out single-cell RNA-sequencing while preserving the anatomical origin of each neuron. In chapter 4, I described the steps I followed to successfully obtain detailed gene expression profiles from $VGAT^+$ and $VGluT2^+$ neurons across PAG subdivisions.

In this final results chapter, I proceeded with the downstream analysis of the dataset and the biological interpretation of the results. I first selected a subset of highly variable genes and applied dimensionality reduction techniques to capture the main factors driving the heterogeneity in the dataset while discarding the random technical and biological noise inherent to my experimental design. I next used unsupervised clustering methods to identify putative subpopulations of neurons that highlight the underlying biological structure of the data. Finally, I performed differential expression

analysis to identify potentially interesting genes that are specific to cell type, PAG subdivision, or the subpopulations identified by the unsupervised clustering approach.

Importantly, any results and biological insights derived from this analysis need to be interpreted bearing in mind the electrophysiological blueprint of PAG neurons described in chapter 3. Only by doing this will it be possible to understand the implications of the results and generate data-driven hypotheses to test how the different circuits of the PAG can be modulated to give rise to the behavioural output that maximises an individual's survival.

5.1 FEATURE SELECTION AND DIMENSIONALITY REDUCTION

The choice of genes to keep for downstream analysis can have a major impact in the results obtained from procedures like dimensionality reduction and clustering. Ideally, one needs to keep only the genes that contain interesting biological information and discard those whose expression varies due to technical noise or uninteresting factors. Thus, before proceeding with dimensionality reduction and other analyses, the variation in the expression of each gene across the dataset needs to be quantified so that the most variable genes can be selected. In addition, the systematic differences in gene expression arising from batch effects should be removed or corrected (see sections 2.4.2.2 and 4.2.2.1 for more details). Finally, principal component analysis can be applied to the corrected expression values of the highly variable genes and used to select the top principal components. Restricting the downstream analysis to these top principal components ensures that the main factors driving the heterogeneity in the dataset are captured, while the random technical and biological noise concentrated in the later principal components is discarded.

5.1.1 Modelling the technical variance and selecting highly variable genes

The variability in the observed gene expression values can be driven by biological factors or uninteresting technical noise. To distinguish between both possibilities, I used the squared coefficient of variation (CV^2), a widely used metric for describing variation in non-negative data, to model the technical component of the variability of gene expression. For each gene, I calculated the CV^2 and the mean of the expression values across all cells and fitted a trend to the relationship between both metrics (Figure 5.1A).

Under the assumption that most genes exhibit low baseline levels of variation that is not biologically interesting, one can interpret the fitted trend as an estimate of the technical variance as a function of abundance. Under this assumption, large CV^2 values that deviate strongly from the fitted trend are likely to represent genes whose expression is affected by biological structure. The total variance of each gene can thus be broken into a technical component, defined as the fitted value of the trend at that abundance, and a biological component, defined as the ratio of the total CV^2 to the fitted value of the trend. In this scenario, calculating the ratio is more appropriate than directly subtracting the trend from the CV^2, as the magnitude of the ratio is not affected by the mean. I used the ratio to rank genes according to their biological component, with large ratios being indicative of strong biological heterogeneity. Once ranked, I selected the top 15% of genes with the largest ratio as my set of highly variable genes (Figure 5.1).

Before proceeding with downstream analysis, and as discussed in section 2.4.4, I removed the measurements corresponding to spike-ins, TSO concatemers, fluorophores, and the transporters used to label and target the PAG neurons from the dataset, as some of them are not biologically informative and others have been used to select the cells. To reduce the chances of keeping genes related to uninteresting factors, I also removed mitochondrial genes, ribosomal genes, and sex-specific genes.

From the 19,574 genes left in the dataset, I selected the 2,910 most highly variable genes and used them for downstream analysis (Figure 5.1A, highlighted in orange).

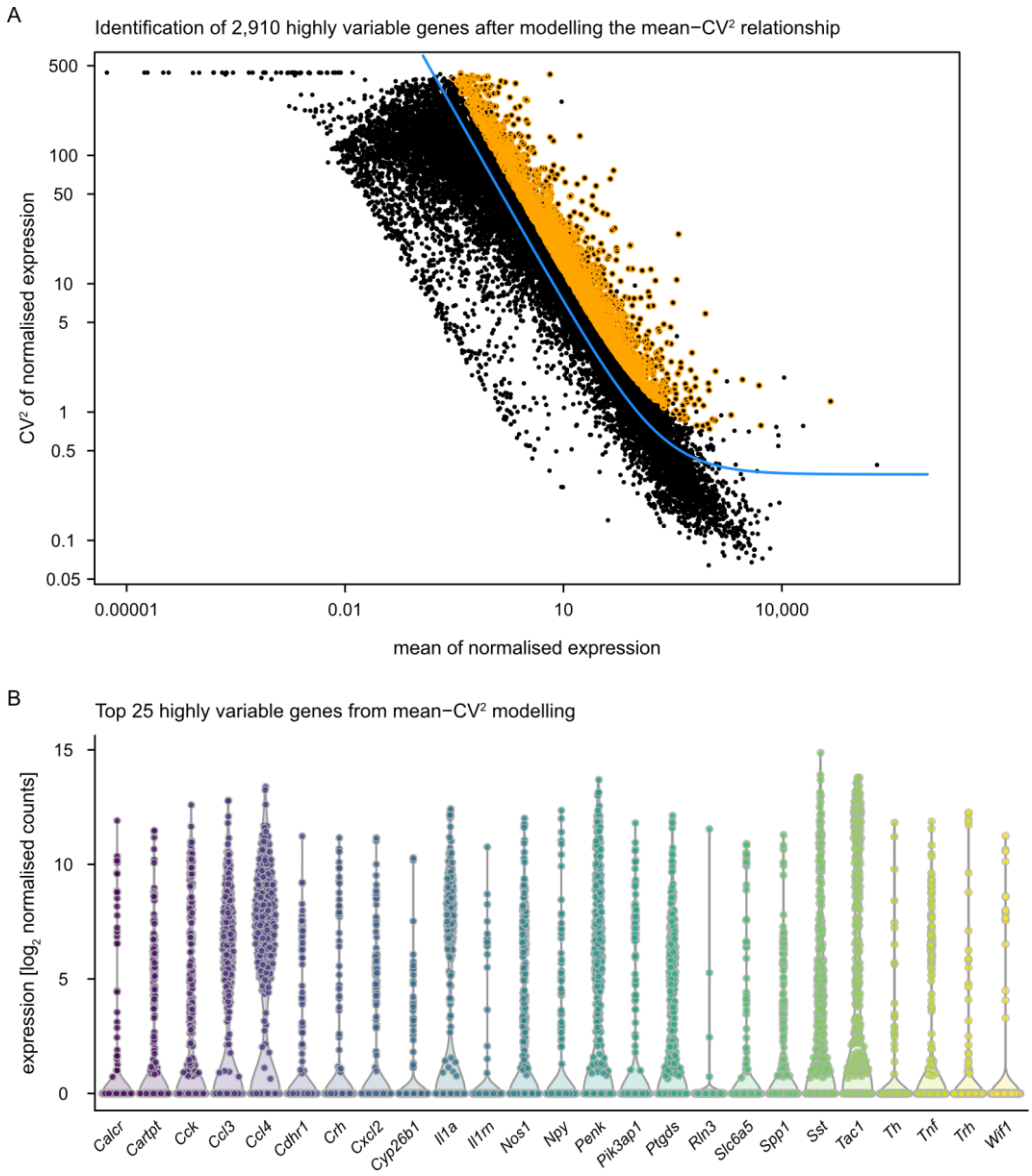

Figure 5.1. Modelling the mean-CV² relationship of expression values to select highly variable genes. (**A**) Relationship between the calculated CV² and the mean of the expression values of all the genes in the dataset. Each dot represents a gene. The blue line indicates the fitted trend representing the estimate of the technical variance as a function of gene abundance. Orange circles highlight the top 15% of genes with the largest ratio of the total CV² to the fitted value of the trend. (**B**) Expression levels of the top 25 most highly variable genes. Each circle represents the expression value of a given gene in each neuron. Each colour represents a gene.

From this selection, I quickly checked the distribution of expression values for the 25 genes with the largest biological components to ensure that the CV^2 estimate was not dominated by one or two outlier cells (Figure 5.1B). I observed how genes like *Cartpt* (encoding the Cocaine And Amphetamine Regulated Transcript prepropeptide), *Cck* (encoding the neuropeptide Cholecystokinin), *Nos1* (encoding the Nitric Oxide Synthase 1), *Npy* (encoding the Neuropeptide Y), and *Tac1* (encoding the Tachykinin Precursor 1) appeared in this shortlist, suggesting that the chosen approach successfully selected many genes with potentially interesting physiological roles.

5.1.2 Correction of batch effects

The most prominent technical covariates in single-cell data are *count depth* (library size) and *processing batch* (Luecken and Theis, 2019). Although it is possible to computationally correct systematic differences arising from such factors, the best batch correction method is preventing the effect with clever experimental design (Hicks, Townes, *et al.*, 2018). For instance, batch effects can be avoided by balancing cells across experimental conditions and samples in each batch. Unfortunately, only half of my processing batches were successfully balanced (i.e. samples within a processing batch came from different animals and experimental days, and belonged to each cell type and PAG subdivision in the same proportions), with the other half following an unbalanced design (i.e. all the samples in a processing batch came from the same animal and experimental day, and belonged to the same cell type).

In bulk RNA-sequencing experiments, batch correction is commonly performed with linear regression. This involves fitting a linear model to the expression profile of each gene, setting the unwanted batch term to zero, and recalculating the expression values without the batch effect. The result of this approach is a set of corrected expression values from which the batch effects have been eliminated. This type of linear modelling is implemented by the `removeBatchEffect` function from the *limma* package (Ritchie, Phipson, *et al.*, 2015).

This method is effective provided that the population composition within each batch is either identical across batches or known in advance. In this case, the composition of the cell population is not identical across batches, as each batch of aspirated neurons inevitably comes from one transgenic mouse and thus has only one out of two possible cell types. However, individually aspirating cells based on expression of a transgene has the advantage of knowing the exact composition of each batch, and `removeBatchEffect` accepts a design matrix that describes the comparisons between the samples which should not be removed.

I used `removeBatchEffect` to perform a linear regression on the data and set the coefficients corresponding to the blocking factor `batch.processing` to zero. As a design matrix, I provided the combination of both the type of cell and the PAG subdivision each sample corresponded to. Unfortunately, and as I have already mentioned, only half of the batches followed a balanced design. This meant that, although `batch.processing` was an important variable (and I certainly had batch effects, inherent to this type of experiments), the fact that I didn't have properly balanced batches made it hard to remove the batch effect while leaving the biology intact, as by removing it I would also be removing some of its confounds linked to biology (such as the identity of the mouse or the type of cell). I thus limited the use of the batch corrected expression values to dimensionality reduction and visualisation and continued using the log-normalised values for clustering and downstream analysis.

5.1.3 Principal component analysis

I performed principal component analysis (PCA) to obtain the first 50 principal components (PC) capturing the most variation of the gene expression data. To do that, I used the `runPCA` function from *scater* (McCarthy, Campbell, *et al.*, 2017) on (1) the log-normalised and (2) log-normalised and batch corrected gene expression values of the set of highly variable genes identified in section 5.1.1.

At this point, I needed to decide the number of PCs to keep for downstream analysis. Keeping more PCs would avoid discarding potentially meaningful biological signal at the cost of retaining more noise. Instead of choosing an arbitrary number, I used `getClusteredPCs` from *scran* (Lun, McCarthy, and Marioni, 2016) to try to make an informed decision. This method performs graph-based clustering on the samples using a varying number of PCs and suggests the number of PCs to keep based on the detected number of clusters. The idea is that keeping more PCs should capture more biological signal, allowing the clustering algorithm to detect more subpopulations, up until the point that adding more signal starts to increase the noise, making it harder for the algorithm to distinguish between subpopulations. Upon examination of the results from using `getClusteredPCs` on the dataset, I kept the suggested top 17 PCs from the log-normalised values and the suggested top 14 PCs from the batch corrected values for dimensionality reduction and unsupervised clustering.

5.1.4 Dimensionality reduction with uniform manifold approximation and projection

The uniform manifold approximation and projection (UMAP) method is a non-linear dimensionality reduction technique widely used to map high dimensional data to a 2-dimensional space while trying to preserve local and global distances between samples (McInnes, Healy, and Melville, 2018; Becht, McInnes, *et al.*, 2019). Non-linear methods like UMAP or t-stochastic neighbour embedding (t-SNE) (van der Maaten and Hinton, 2008) tend to work better than PCA for the highly dimensional datasets obtained in single-cell RNA-sequencing experiments. This is because the former can directly capture non-linear relationships in high-dimensional space, whereas the latter must represent them (suboptimally) as linear components.

UMAP has a suite of hyperparameters that affect the final visualisation. Of these, the number of neighbours (`n_neighbors`) and the minimum distance between embedded points (`min_dist`) have the greatest effect on the granularity of the output.

If these values are too low, random noise will be incorrectly treated as high-resolution structure. If the values are too high, the method will discard fine structure altogether in favour of obtaining an accurate overview of the entire dataset.

I applied UMAP to the dataset using the `runUMAP` function implemented in *scater* (McCarthy, Campbell, *et al.*, 2017). Similar to what I did for PCA, I performed UMAP on the log-normalised and batch corrected gene expression values of the set of highly variable genes identified in section 5.1.1. To mitigate the computational intensity of this approach and leverage the noise removal provided by the PCA, I instructed the function to perform the UMAP calculations on the top 14 PCs. Given that the algorithm is not deterministic, I repeated the approach using different seeds for the random number generator to ensure the results could be reproducible. Importantly, before settling for a given visualisation, I tested a range of values for the main hyperparameters to ensure the results were consistent and any conclusions were not compromised by a poor hyperparameter choice. I found that setting `n_neighbors` to 15 and `min_dist` to 0.01 resulted in a clear visualisation that captured the main features obtained across hyperparameters and seeds (Figure 5.2).

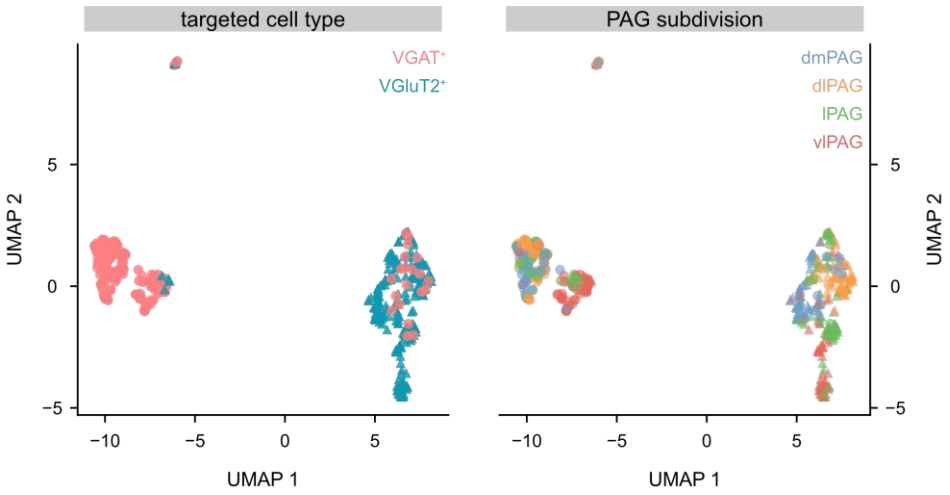

Figure 5.2. Dimensionality reduction with UMAP separates VGAT$^+$ and VGluT2$^+$ neurons and captures some underlying substructure related to PAG subdivisions (**Left**) UMAP plot representation of the dataset, coloured by cell type. (**Right**). UMAP plot representation of the dataset, coloured by PAG subdivision. Circles indicate VGAT$^+$ neurons. Triangles indicate VGluT2$^+$ neurons.

Examination of the UMAP plot suggested that VGAT^{+} and VGluT2^{+} neurons could be clearly separated by their gene expression profile (Figure 5.2, left panel). In addition, UMAP seemed to identify fainter gene expression signatures capturing variability across PAG subdivisions (Figure 5.2, right panel). This was clearer in the case of VGluT2^{+} neurons, which grouped by anatomical location, with vlPAG VGluT2^{+} neurons at the bottom right, followed by lPAG VGluT2^{+} neurons going upwards, and then a slight separation between dmPAG and dlPAG VGluT2^{+} neurons. For VGAT^{+} neurons, the clearest separation was between dorsal (dm/dl) and ventral (l/vl) PAG neurons.

I also observed a small and very distinct subset of neurons that cohabited at the top of the UMAP plot. This cluster of 12 cells showed a high expression of genes like *Cd33*, *Cd68*, *Plaur*, and *Cxcl16*, all genes typically expressed by cells from the monocyte lineage, by circulating macrophages, and by tissue macrophages. This suggested that this subset of cells may have been contaminated by immune cells, perhaps indicating that those neurons were damaged and in the process of being phagocytised by tissue macrophages at the time of aspiration.

Even though it may be tempting to take the UMAP results as an indication of the existence of clusters or subpopulations of neurons in the dataset, one should refrain from doing so. Instead, one should use methods specifically designed for clustering and project the results on the UMAP plot. This approach repurposes the UMAP plot as a diagnostic tool to assess the clustering output and check whether two clusters are actually neighbouring each other or whether a cluster can be further split into smaller subclusters. Major discrepancies between the clustering results and the UMAP visualisation can highlight parts of the dataset where the results are ambiguous and motivate further investigation into that direction. Conversely, the lack of discrepancies between UMAP and clustering results will increase the confidence and trust in the results.

5.2 UNSUPERVISED CLUSTERING IDENTIFIES PUTATIVE SUBPOPULATIONS OF VGAT$^+$ AND VGLUT2$^+$ PAG NEURONS

Clustering is an unsupervised learning procedure that is used in single-cell RNA-sequencing data analysis to empirically define groups of cells with similar gene expression profiles. This allows researchers to describe population heterogeneity in terms of discrete labels, rather than attempting to comprehend the high-dimensional manifold on which the cells truly reside. It is worth noting that, although a cell type can be defined as a true biological class, clusters are but an empirical construct derived from data analysis. As such, different clustering algorithms can be used to obtain as many clusters as one wants, with each approach allowing the inspection of a dataset from a different perspective or at a different resolution. Some of the most popular approaches are *graph-based clustering*, *k-means clustering*, and *hierarchical clustering*. I used the first two to continue the analysis of my dataset.

5.2.1 Graph-based clustering

Graph-based clustering is an approach that first builds a graph where each node is a cell connected to its nearest neighbours in the high-dimensional space. The edges of the graph are then weighted according to the similarity between the cells involved, with a higher weight assigned to cells with more similar expression profiles. Once the graph is built, community-detection algorithms can be used to identify groups of cells that are more connected between each other than with cells of other groups. In this scenario, each community represents a cluster that can be used for downstream analysis and interpretation.

An advantage of this approach is that graph construction does not make strong assumptions about the shape of the clusters, unlike methods like k-means which favour spherical clusters. In addition, each cell gets connected to a minimum number of

neighbouring cells, which minimises the risk of ending up with uninformative clusters of one or two outlier cells. The main drawback of graph-based methods is that after graph construction no information is retained about relationships beyond the neighbouring cells. In datasets with varying levels of cell density, this may inflate high-density regions and occasionally lead to the formation of subclusters that overstate the heterogeneity of the data.

The function `buildSNNgraph` from the *scran* package (Lun, McCarthy, and Marioni, 2016) provides several graph construction methods based on shared nearest neighbours (Xu and Su, 2015), after which methods from the *igraph* package (Csardi and Nepusz, 2006) can be used to identify clusters. For each cell, the `buildSNNgraph` method identifies its "k" nearest neighbours based on the Euclidean distances between their expression profiles. An edge is then drawn between all pairs of cells that share at least one neighbour and weighted according to the method of choice.

To cluster the data, I used `buildSNNgraph` with `k=5` on the log-normalised expression values of the set of highly variable genes and the top 17 PCs, and I set the edge weighting scheme to the Jaccard approach. This uses the Jaccard similarity index to weight the edges between nodes, assigning a weight from 0 to 1 based on the number of nearest neighbours shared between two cells. The closer to 1, the more similar the two cells are. I then used the Louvain algorithm (Blondel, Guillaume, *et al.*, 2008) implemented in the *igraph* package to extract the community structure of the graph.

The results of this approach yielded 11 clusters: 4 putative $VGAT^+$ clusters, 6 putative $VGluT2^+$ clusters, and the cluster enriched with macrophage-related genes (Figure 5.3A). As it can be seen on the UMAP projection, these clusters matched well with the structure captured by the UMAP itself, tracking the main PAG subdivisions for both $VGAT^+$ and $VGluT2^+$ neurons.

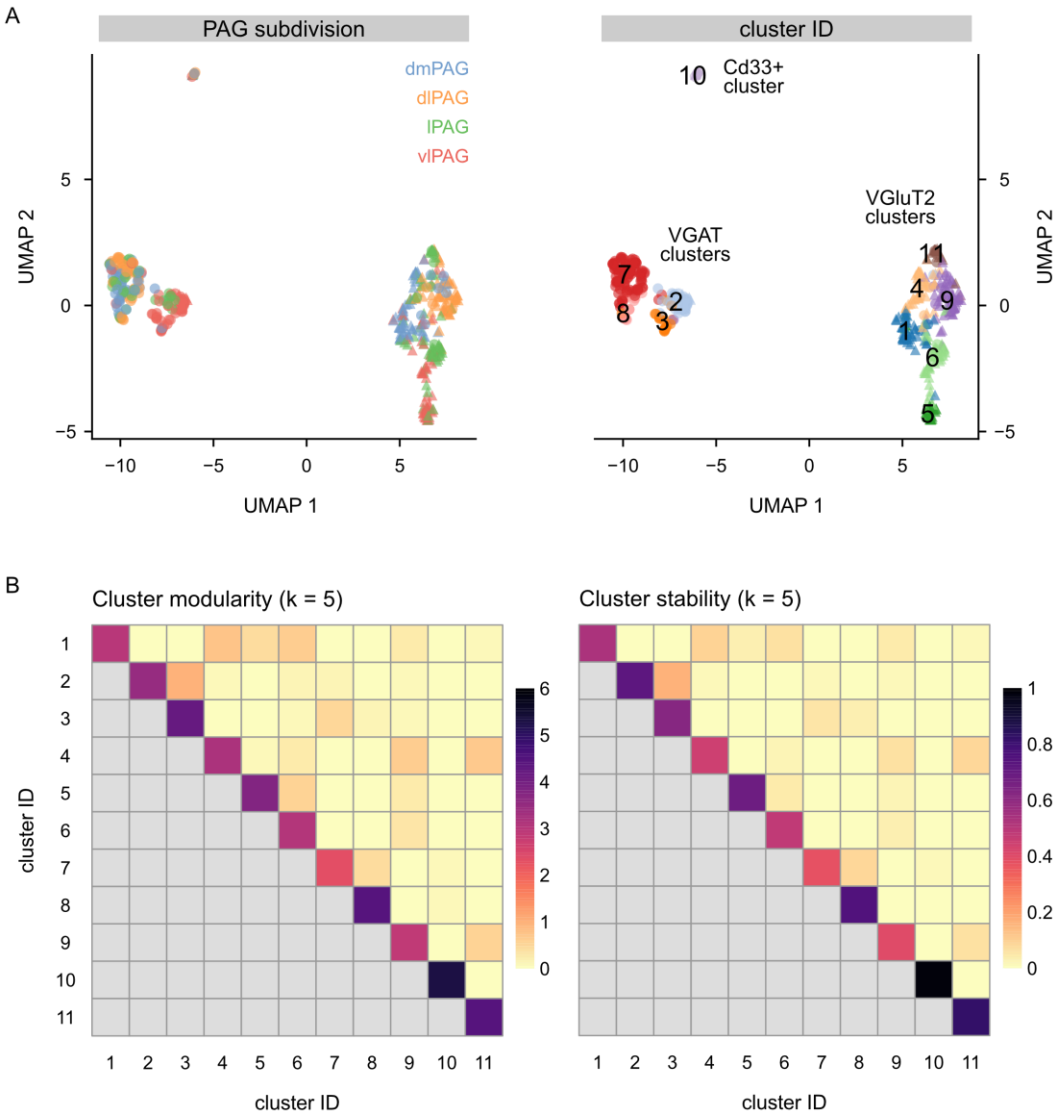

Figure 5.3. Graph-based clustering identifies 11 putative subpopulations. (**A**) UMAP plot representation of the dataset, coloured by PAG subdivision (left) and by cluster identity (right). Circles indicate VGAT$^+$ neurons. Triangles indicate VGluT2$^+$ neurons (**B**) Cluster modularity matrix (left) and cluster stability matrix (right). Each row and column correspond to a cluster. For the modularity matrix, the colour of each entry indicates the ratio of the observed to total weight of edges between cells in the respective clusters. For the stability matrix, the colour of each entry indicates the co-assignment probability of the cells in each pair of clusters.

To evaluate the separation between the identified clusters, I calculated the modularity of the graph with the `clusterModularity` function of the *scran* package (Lun, McCarthy, and Marioni, 2016) (Figure 5.3B, left). The modularity metric is

defined as the scaled difference between (1) the observed total weight of edges between nodes in the same cluster and (2) the expected total weight if edge weights were randomly distributed across all pairs of nodes. Larger modularity values indicate that most edges occur within clusters, suggesting that the identified clusters are sufficiently separated to avoid edges forming between neighbouring cells in different clusters. A well-separated cluster should have mostly intra-cluster edges and a high modularity score on the corresponding diagonal entry (e.g. cluster 10 in Figure 5.3B, left), while two closely related clusters that are weakly separated will have many inter-cluster edges and a high off-diagonal score (e.g. clusters 2 and 3 in Figure 5.3B, left).

I observed that cluster 10 had the highest score and did not relate to any other cluster, which makes sense as it is the one enriched with macrophage-related markers. On the other hand, clusters 2 and 3 had a relatively high off-diagonal entry, suggesting they were closely related. Indeed, upon inspecting the UMAP projection I could see they were neighbouring clusters composed mainly by ventral PAG VGAT$^+$ neurons. Clusters 7 and 8 showed a similar pattern, which made sense as they were nearly undistinguishable in the UMAP plot and consisted mainly of dorsal VGAT$^+$ neurons. I observed a similar trend in VGluT2$^+$ clusters, with clusters 5 and 6, as well as 4, 9, and 11 showing relatively high off-diagonal modularity values, again suggesting they were closely related to each other (Figure 5.3B, left).

Further to examining the modularity of the resulting graph, I used the bootstrapping approach implemented by the `bootstrapCluster` function from *scran* to evaluate the stability of the graph-based clustering solution (Figure 5.3B, right). This algorithm samples cells with replacement to create a "bootstrap replicate" dataset and repeats the clustering on this replicate to see if the same clusters can be reproduced. I repeated the bootstrapping 1000 times and calculated the co-assignment probability for each pair of original clusters. The co-assignment probability between a given cluster X and a given cluster Y represents the probability that a randomly chosen cell from X and a randomly chosen cell from Y are assigned to the same cluster in the bootstrap replicate. A high co-assignment probability between a pair of clusters indicates that the

original clusters were not stably separated, given that their cells ended up clustering together in the bootstrap replicates. Conversely, the co-assignment probability of each cluster to itself provides a measure of its stability: a probability of 1 would indicate that all cells were always assigned to the same cluster across bootstrap iterations, while the existence of internal structure that leads to the formation of subclusters would lower this probability. Ideally, a good clustering solution would have high co-assignment probabilities on the diagonal and low probabilities off the diagonal.

Similar to what I observed with the modularity metric, I found that the less stable clusters where those directly next to each other in the UMAP plot (Figure 5.3B, right). Together with the modularity analysis, this suggested that the VGAT^{+} clusters 2 and 3 or 7 and 8 may actually be the result of over-clustering, or that they are at least closely related. The same could be said for some of the VGluT2^{+} clusters, with clusters 5 and 6 and clusters 4, 9, and 11 being seemingly related to each other. On the other hand, cluster 10 stably identified a subset of cells that are different from the rest, again strengthening the idea that it is composed of macrophage-contaminated samples.

5.2.2 Consensus clustering with SC3

As an alternative clustering approach, I used Single-Cell Consensus Clustering (SC3), a tool developed for unsupervised clustering of single-cell RNA-sequencing data (Kiselev, Kirschner, *et al.*, 2017). As a purely clustering tool, SC3 achieves high accuracy and robustness by consistently integrating different k-means clustering solutions through a consensus approach. I repeated the analysis with different values of `k` and found that the best results were those obtained with `k=4`. SC3 identified 4 main clusters: 2 for VGAT^{+} neurons and 2 for VGluT2^{+} neurons (Figure 5.4A). In both cases, and upon examination of the results on the UMAP plot, the clusters seemed to separate the neurons coming from dorsal PAG (dmPAG and dlPAG) and ventral PAG (lPAG and vlPAG).

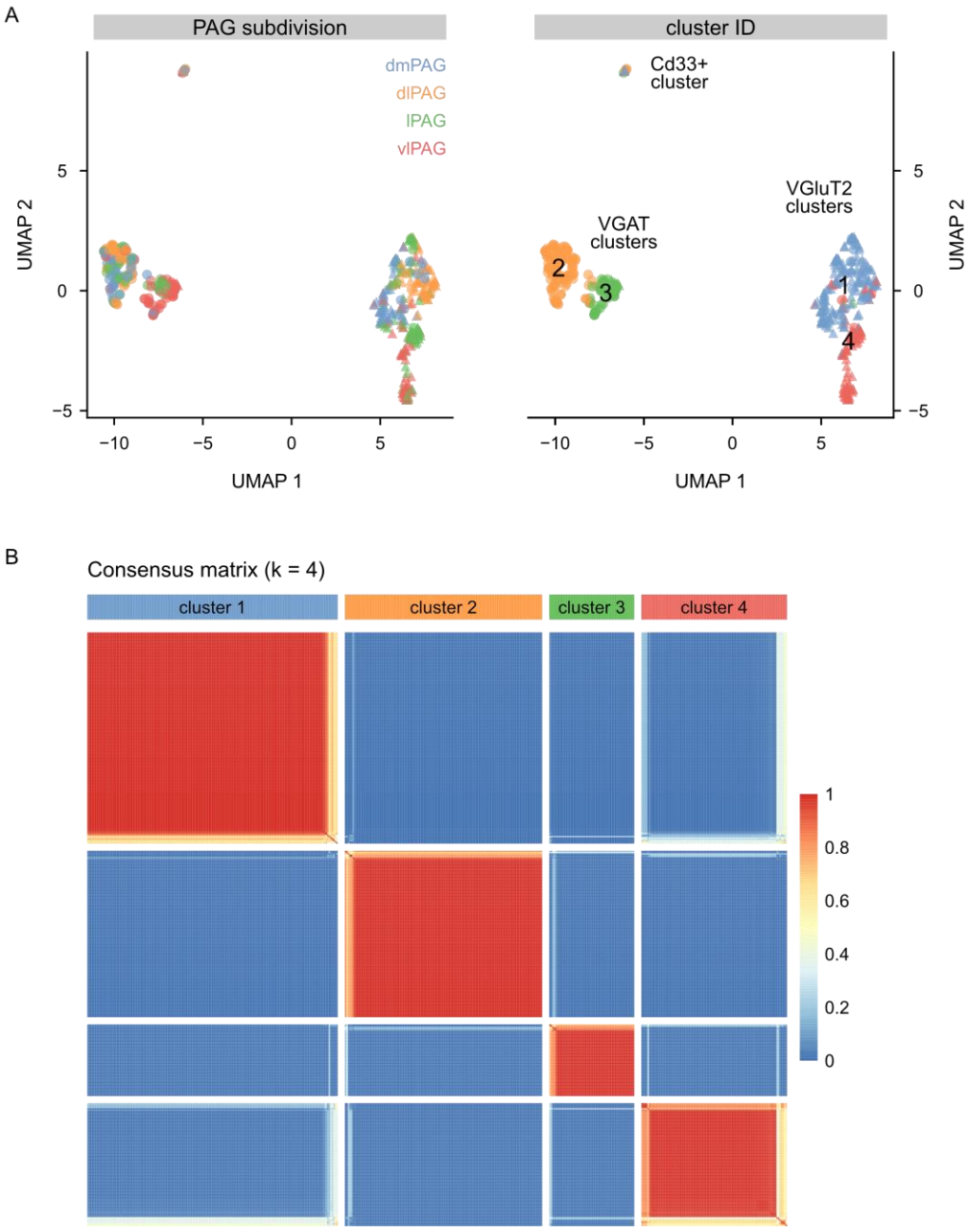

Figure 5.4. Consensus clustering with SC3 identifies 4 putative subpopulations. (**A**) UMAP plot representation of the dataset, coloured by PAG subdivision (left) and by cluster identity (right). Circles indicate VGAT^{+} neurons. Triangles indicate VGluT2^{+} neurons (**B**) Consensus matrix of the clustering solution. A N×N matrix where N is the number of cells. The colour represents the similarity between each pair of cells based on the averaging of clustering results from all combinations of clustering parameters. A similarity of 0 (blue) indicates that the two cells were always assigned to different clusters, whereas a similarity of 1 (red) indicates that the two cells were always assigned to the same cluster.

To examine the stability of the clusters, SC3 calculates a consensus matrix, a N×N matrix where N is the number of cells (Figure 5.4B). The matrix represents the similarity between each pair of cells based on the averaging of clustering results from all combinations of clustering parameters. A similarity of 0 (blue) means that the two cells were always assigned to different clusters, whereas a similarity of 1 (red) means that the two cells were always assigned to the same cluster. In addition, the consensus matrix is clustered by hierarchical clustering and has a diagonal-block structure, with the perfect clustering achieved when all diagonal blocks are completely red and all off-diagonal elements are completely blue.

The consensus matrix obtained for the results of SC3 with `k=4` suggested that this clustering solution was nearly perfect, as the diagonal blocks were almost completely red (Figure 5.4B). This was very interesting and, together with the modularity and stability analysis of the graph-based clustering results from section 5.2.1, suggested that the graph-based clusters may have indeed been the result of slight over-clustering. The results from SC3 would very much resemble those from graph-based clustering were I to combine the clusters that had relatively high off-diagonal modularity and similarity values. For instance, cluster 2 from SC3 would match the combination of clusters 7 and 8 from graph-based clustering. Similarly, cluster 3 from SC3 would be equivalent to the combination of clusters 2 and 3 from graph-based clustering. And clusters 1 and 4 from SC3 would match the combination of clusters 1-4-9-11 and 5-6 from graph-based clustering (Figure 5.3A and Figure 5.4A). Together, both approaches concurred on one observation: the main axis of variation within each cell type seemed to be whether a neuron belonged to the dorsal or to the ventral PAG.

The only downside of the SC3 approach was that it failed to identify the small cluster enriched with macrophage markers. In fact, some of the cells with low similarity values in the consensus matrix most likely correspond to the ones that would belong to this cluster. After considering both clustering solutions, I decided to proceed with a combination of both approaches: I kept the results from the graph-based clustering

approach to label the macrophage-enriched cells and used the identity of the SC3 clusters for the rest of cells in the dataset.

5.3 DIFFERENTIALLY EXPRESSED GENES IN PAG NEURON CELL TYPES AND SUBPOPULATIONS

One of the most common types of analyses when working with RNA-sequencing data is to identify differentially expressed genes between conditions or subpopulations of cells. By comparing the genes whose expression levels differ between two groups of cells one can begin to characterise their molecular differences and generate hypothesis to investigate the impact these can have for their physiological function.

For the differential expression analysis, I used the Wilcoxon rank sum test implemented by the `findMarkers` function from the *scran* package (Lun, McCarthy, and Marioni, 2016). The Wilcoxon rank sum test is a widely used method for pairwise comparisons between groups of observations, which directly assesses the separation between the expression distributions of different groups of cells. Its test statistic is proportional to the area-under-the-curve (AUC) or concordance probability, which is the probability of a random cell from one group having a higher expression of the tested gene than a random cell from another group. In a pairwise comparison, AUCs of 1 or 0 indicate that the two groups have perfectly separated expression distributions. A value greater than 0.5 indicates that the tested gene is upregulated in the current group compared to the other, while values less than 0.5 correspond to downregulation. AUC values above 0.7 or 0.8 typically indicate strongly upregulated candidate marker genes. Importantly, the resulting p-values were only used to rank the genes and I only considered genes with a Benjamini-Hochberg adjusted p-value of less than 0.05. This cut-off, together with the AUC value, was used to select potentially interesting genes.

I focused the analysis on three main comparisons. First, I compared the gene expression differences of $VGAT^{+}$ and $VGluT2^{+}$ neurons, as they can provide insights

about the molecular toolkit available to each cell type and help generate testable hypothesis aimed at contextualising and probing their physiological function. Second, I attempted to identify marker genes for the clusters identified in section 5.2 to aid me in their biological interpretation. Finally, I used the factor resulting from the combination of *cell type* and *PAG subdivision* to investigate the potential differences between $VGAT^+$ and $VGluT2^+$ neurons across PAG subdivisions. Before performing the differential expression analysis and to avoid masking any effects related to the desired conditions, the cells belonging to the small cluster labelled with a high expression of macrophage-related genes (cluster 10 in Figure 5.3A) were excluded from the dataset.

5.3.1 Cell type-specific marker genes

A main feature of my experimental design is that I knew in advance the type of cell I was going to aspirate and sequence. I thus took advantage of my metadata to perform pairwise comparisons between $VGAT^+$ and $VGluT2^+$ neurons. I found 289 genes that were upregulated in $VGAT^+$ neurons and 1117 genes that were upregulated in $VGluT2^+$ neurons. To examine the genes with the potential to identify each cell type, I focused on those with an AUC value above 0.8 (Figure 5.5).

Further to the expected high expression of *Gad1* and *Gad2* (the genes encoding for the Glutamate Decarboxylase enzyme) in $VGAT^+$ neurons, I found several transcription factors among the shortlist of PAG cell type-specific genes. These included *Gata3*, *Lhx5*, and *Tal1* for $VGAT^+$ neurons and *Lhx9*, *Tcf7l2*, *Shox2*, and *Pou4f1* for $VGluT2^+$ neurons.

Besides transcription factors, I found other genes with the potential to contribute to the physiology of either cell type or impact the function of synaptic partners and neighbouring cells. Two of the most differentially expressed genes were encoding ion channel subunits. *Asic4*, a gene encoding the Acid Sensing Ion Channel Subunit Family Member 4, was a hallmark for $VGAT^+$ neurons, whereas *Cacna2d1*, a gene encoding

the Voltage-Gated Calcium Channel Auxiliary Subunit α2δ1, was the top marker gene for VGluT2$^+$ neurons in the PAG. I will take a closer look at them in the following sections.

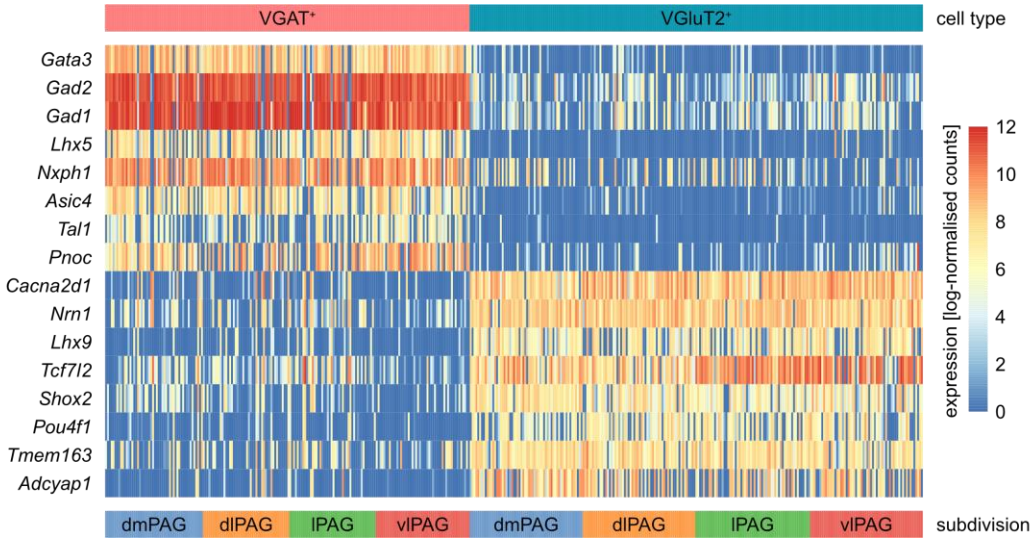

Figure 5.5. Differential expression of cell type-specific marker genes. Heatmap summarising the expression levels of the upregulated genes with the highest AUC value in VGAT$^+$ (left) and VGluT2$^+$ neurons (right). Each row represents a gene. Red colours indicate high expression. Blue colours indicate low expression. Each column represents a neuron, ordered by PAG subdivision and cell type. For each neuron, the identity of the cell type and PAG subdivision it belongs to is indicated in the row above or below the plot, respectively.

In addition, I found several genes that could hint at some of the effects VGAT$^+$ and VGluT2$^+$ neurons in the PAG can exert on downstream targets. GABAergic neurons showed a high expression of *Nxph1*, a gene encoding the neuropeptide-like Neurexophilin 1, and *Pnoc*, which encodes Prepronociceptin, a preproprotein that can give rise to the neuropeptides Nociceptin, Nocistatin, and Orphanin FQ2. On the other hand, glutamatergic neurons had a high expression of *Tmem163*, a gene encoding the Transmembrane Protein 163, which has been recently identified as a zinc transporter (Sanchez, Ali, *et al.*, 2019; Styrpejko and Cuajungco, 2021), and *Adcyap1*, which encodes the Pituitary Adenylate Cyclase Activating Polypeptide 1 (PACAP). As before, I will come back and examine these in more detail in the subsequent sections.

5.3.1.1 *Asic4*, an acid-sensing ion channel modulatory subunit, is a marker gene for VGAT$^+$ neurons in the PAG

To examine some of the most interesting genes in more detail, I used dot plots to summarise the data (Figure 5.6). This type of visualisation provides an intuitive understanding of how the expression of a subset of genes changes across conditions. The size of the dot encodes the percentage of cells in the group that express a particular gene of interest. The colour intensity of the dot indicates the average expression level across all cells in that group, with white being no expression and the colour used to identify VGAT$^+$ or VGluT2$^+$ neurons representing high expression (Figure 5.6). For all the subsequent dot plots, I first showed the expression of the selected genes for VGAT$^+$ or VGluT2$^+$ neurons (Figure 5.6A), and then I further split the comparison into PAG subdivisions (Figure 5.6B).

When using the dot plots to zoom in on the expression profile of acid-sensing ion channels in PAG neurons, I appreciated the striking difference in the expression levels of *Asic4* between VGAT$^+$ and VGluT2$^+$ neurons, with this gene being strongly enriched in GABAergic neurons (Figure 5.6A). Conversely, *Asic1* and *Asic2* had very similar expression levels between cell types. I observed the same pattern when further subgrouping the data by PAG subdivision (Figure 5.6B). This suggested that the strong enrichment of *Asic4* in VGAT$^+$ neurons was independent of PAG subdivision and could have strong implications for the functions carried out by GABAergic neurons.

Acid-sensing ion channels are voltage-insensitive, proton-gated channels activated by a drop in the extracellular pH. They are mainly permeable to Na^+, although some channels with ASIC1 subunits have some Ca^{2+} permeability. ASIC1 and ASIC2 are pore forming subunits that activate at different levels of acidosis, with the former responding to values around pH 6 and the latter responding to values around pH 4.5 (Kweon and Suh, 2013). While ASIC4 does not seem to form a proton-gated channel, it does appear to have a modulatory function on other ASIC channels (Akopian, Chen,

et al., 2000). It has been suggested that ASIC4 reduces the number of functional ASICs located at the plasma membrane, effectively diminishing the current mediated by ASIC1 (Donier, Rugiero, *et al.*, 2008). My results suggest that, in the PAG, this effect could be specific to VGAT^{+} neurons, thus biasing the effects of a drop in pH towards VGluT2^{+} neurons.

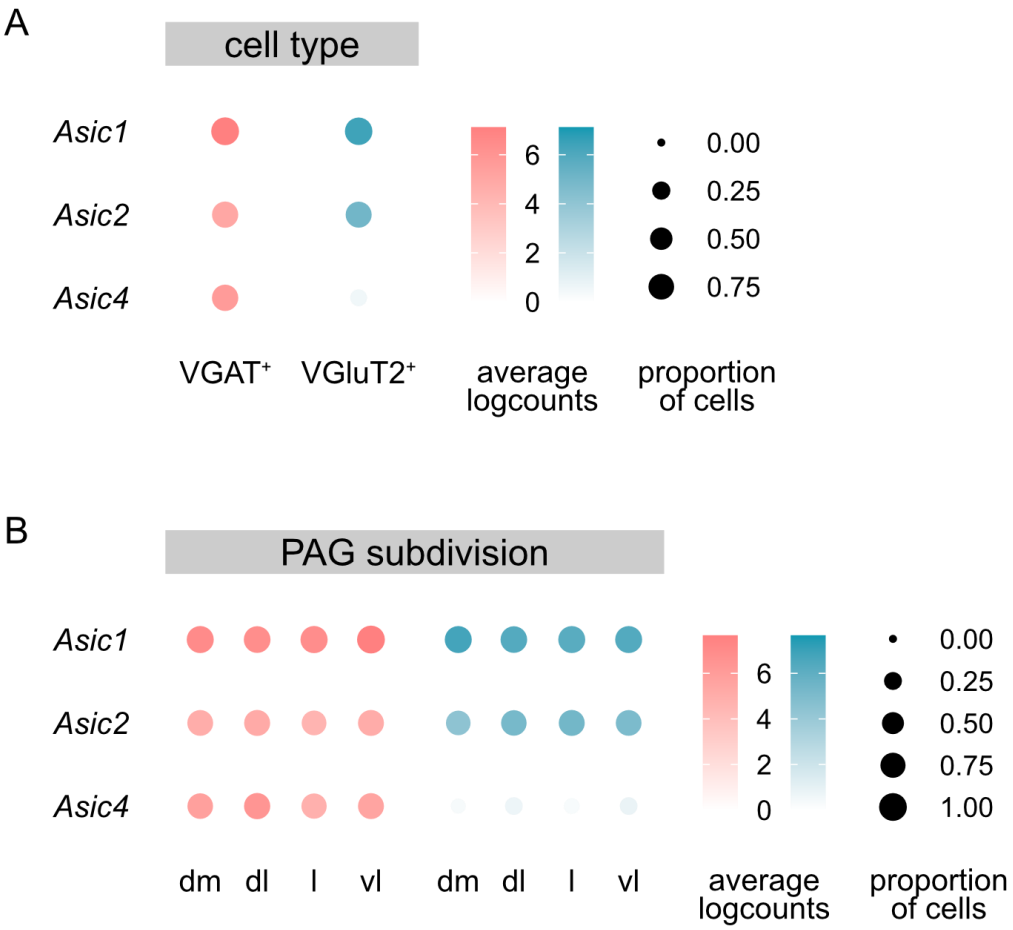

Figure 5.6. Gene expression profile of acid-sensing ion channel subunits across cell types and PAG subdivisions. (**A**) Dot plot summarising the average expression of each gene (rows) in all VGAT^{+} (left column) and in all VGluT2^{+} neurons (right column). (**B**) Dot plot summarising the average expression of each gene (rows) in all VGAT^{+} (left-side columns) and in all VGluT2^{+} neurons (right-side columns) across PAG subdivisions. *dm* indicates dmPAG, *dl* indicates dlPAG, *l* indicates lPAG, *vl* indicates vlPAG. The size of each dot indicates the proportion of neurons in each group that express a given gene. The colour intensity of the dot represents the average expression of a given gene across all neurons in that group.

5.3.1.2 *Cacna2d1*, an auxiliary subunit of voltage-gated calcium channels and the target of gabapentinoid drugs, is a marker gene for VGluT2$^+$ neurons in the PAG

The top marker gene for glutamatergic neurons in the PAG was *Cacna2d1*, a gene encoding the Voltage-Gated Calcium Channel Auxiliary Subunit α2δ1. Similar to what I observed in the case of ASIC channels, the main pore-forming α subunits showed a similar expression profile both between cell type (Figure 5.7A) and across PAG subdivisions (Figure 5.7B), but the α2δ1 subunit was strikingly enriched in VGluT2$^+$ neurons.

α2δ subunits have been showed to enhance the trafficking of α1 subunits to the cell membrane, increase their maximum current density, accelerate their activation and inactivation kinetics, and shift the voltage dependence of inactivation towards a more hyperpolarised potential (Dolphin and Lee, 2020). They have also been shown to form heteromeric complexes with NMDA receptors and to play a role in neuropathic pain (Chen, Li, *et al.*, 2018). My data suggest that in the case of PAG neurons, the effects mediated by α2δ1 would be specific to VGluT2$^+$ neurons.

An interesting fact about the α2δ1 and α2δ2 subunits is that they are the binding site for gabapentinoids, a class of drugs that includes gabapentin and pregabalin used to treat epilepsy, neuropathic pain, anxiety, and other neurological disorders (Dolphin, 2012). Gabapentinoids are derivatives of the inhibitory neurotransmitter GABA and specifically block α2δ-containing voltage-gated calcium channels, without binding to GABA receptors or affecting GABA metabolism. My results suggest that the pharmacological effects of gabapentinoids could in part be derived from differentially dampening the excitability of VGluT2$^+$ neurons in the PAG.

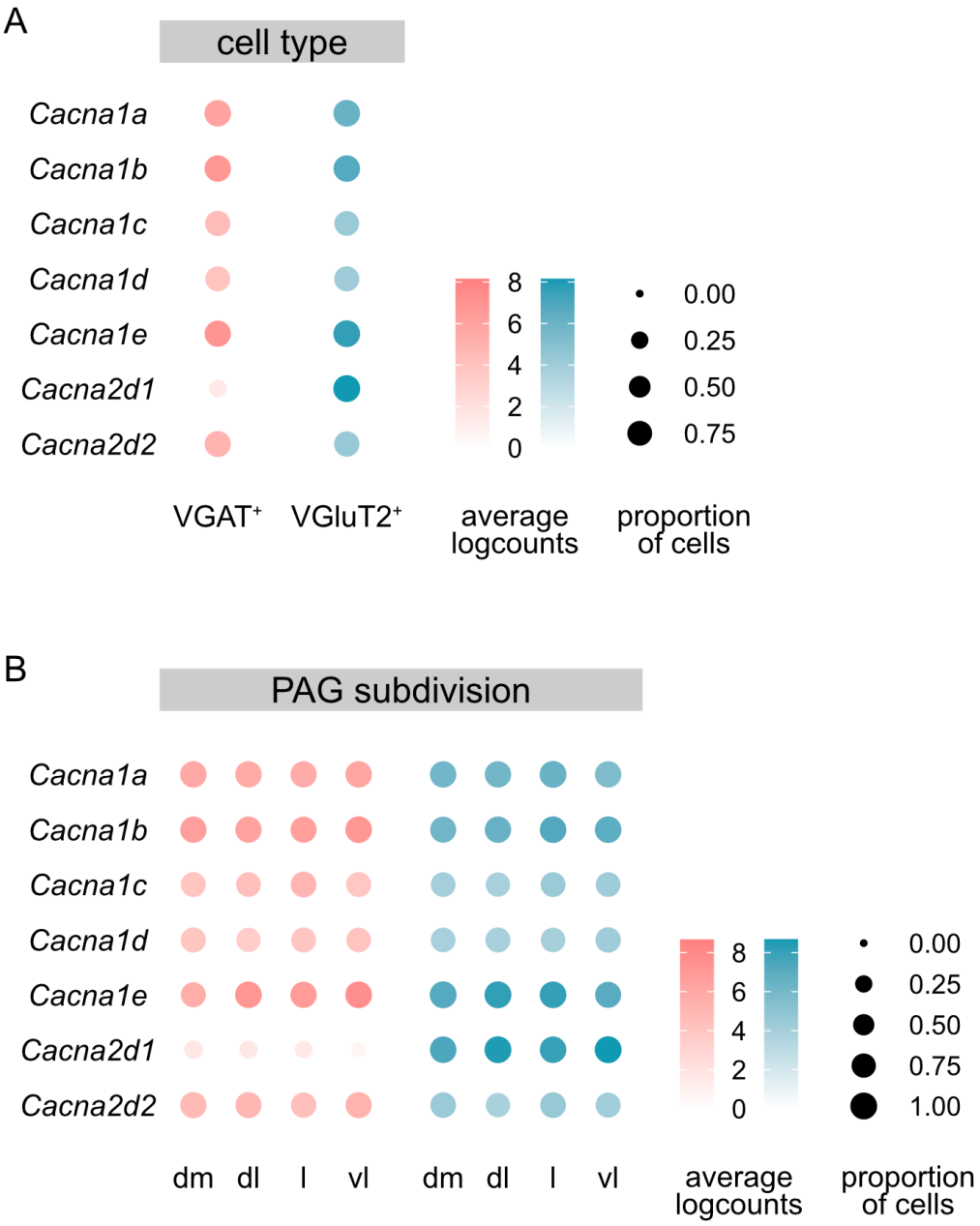

Figure 5.7. Gene expression profile of voltage-gated calcium channel subunits across cell types and PAG subdivisions. (**A**) Dot plot summarising the average expression of each gene (rows) in all VGAT+ (left column) and in all VGluT2+ neurons (right column). (**B**) Dot plot summarising the average expression of each gene (rows) in all VGAT+ (left-side columns) and in all VGluT2+ neurons (right-side columns) across PAG subdivisions. *dm* indicates dmPAG, *dl* indicates dlPAG, *l* indicates lPAG, *vl* indicates vlPAG. The size of each dot indicates the proportion of neurons in each group that express a given gene. The colour intensity of the dot represents the average expression of a given gene across all neurons in that group.

5.3.1.3 Differential expression of potassium channels

The main electrophysiological difference between VGAT$^+$ and VGluT2$^+$ neurons in acute midbrain slices was the ability of VGAT$^+$ neurons to spontaneously fire action potentials. I thus searched the list of cell type-specific differentially expressed genes for those encoding ion channels involved in pacemaking or in regulating neuronal excitability. Although I did not find genes with the clear differences observed for *Asic4* and *Cacna2d1*, I found a subset of potassium channels that were slightly upregulated in VGluT2$^+$ neurons (Figure 5.8).

Two of these genes, *Kcnh1* and *Kcnh5*, encode the pore-forming α subunit of two classes of Ether-A-Go-Go potassium channel, typically involved in repolarising the cell after an action potential. The former corresponds to a non-inactivating voltage-gated delayed rectifier, while the latter corresponds to a non-inactivating voltage-gated outward rectifier.

Another gene, *Kcnq5*, also showed a slight upregulation in VGluT2$^+$ neurons. This gene encodes a potassium channel that gives rise to a slowly activating and slowly deactivating voltage-dependent potassium conductance that contributes to the M-type current. It plays a critical role in determining the subthreshold excitability of neurons and is important for raising the threshold for eliciting an action potential. This was potentially interesting as I did observe a slightly higher action potential threshold in VGluT2$^+$ neurons in my whole-cell patch-clamp recordings (Figure 3.14).

Finally, I found that *Kcnj3*, which gives rise to the G-protein activated inward rectifying potassium channel GIRK1, and *Kcnk9*, which encodes the pH-dependent, voltage-insensitive, two-pore potassium channel TASK3 responsible for a background leak potassium current, were also slightly upregulated in VGluT2$^+$ neurons and may contribute to setting their resting membrane potential.

Although none of these genes offers an obvious explanation of why VGAT$^+$ neurons are able to elicit spontaneous action potentials whereas VGluT2$^+$ neurons are

not, taken together they may be able to add up and contribute to the observed electrophysiological blueprint of PAG neurons. At the very least, they offer a clear path to further investigate the role these potassium channels have in PAG neurons.

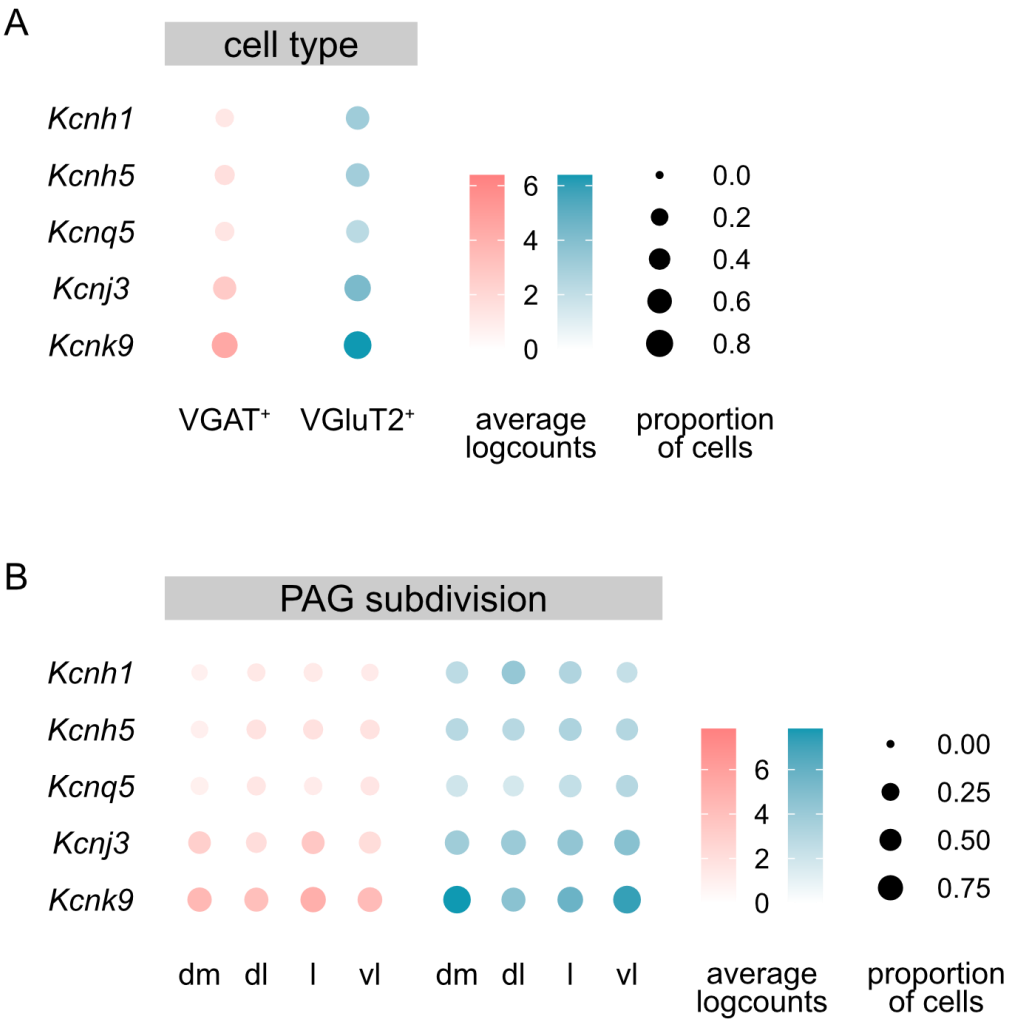

Figure 5.8. Gene expression profile of potassium channel subunits across cell types and PAG subdivisions. (**A**) Dot plot summarising the average expression of each gene (rows) in all VGAT+ (left column) and in all VGluT2+ neurons (right column). (**B**) Dot plot summarising the average expression of each gene (rows) in all VGAT+ (left-side columns) and in all VGluT2+ neurons (right-side columns) across PAG subdivisions. *dm* indicates dmPAG, *dl* indicates dlPAG, *l* indicates lPAG, *vl* indicates vlPAG. The size of each dot indicates the proportion of neurons in each group that express a given gene. The colour intensity of the dot represents the average expression of a given gene across all neurons in that group.

5.3.2 Subpopulation-specific marker genes

After examining the main drivers of gene expression heterogeneity between VGAT$^+$ and VGluT2$^+$ neurons in the PAG, I set out to investigate whether I could find similar signatures for PAG subdivisions and putative subpopulations identified by the unsupervised clustering approaches.

To identify marker genes across PAG subdivisions while accounting for cell type, I grouped the cells according to the metadata factor resulting from the combination of cell type and PAG subdivision. This yielded pairwise comparisons between eight groups: dmPAG, dlPAG, lPAG, and vlPAG for either VGAT$^+$ and VGluT2$^+$ neurons. On this occasion, however, I did not find any genes that were uniquely upregulated in one of the groups with a Benjamini-Hochberg adjusted p-value of less than 0.05. This is reminiscent of the results I obtained with patch-clamp recordings, in which most of the electrophysiological properties I examined showed no significant differences between PAG subdivisions.

I next seeked to find marker genes for the subpopulations identified by the graph-based clustering approach (Figure 5.3). After excluding the cells belonging to the macrophage-enriched cluster, I was left with 10 putative subpopulations, four belonging to VGAT$^+$ neurons and six belonging to VGluT2$^+$ neurons. Again, I was unable to find unique marker genes for most clusters. The only hits were *Tac1*, a gene that encodes the Tachykinin Precursor 1 (which can give rise to the peptide hormones substance P, neurokinin A, neuropeptide K, and neuropeptide gamma) and was upregulated in cluster 5, mainly composed by VGluT2$^+$ vlPAG neurons, and *Pax5* and *En1*, both genes that regulate transcription during early development and that seemed to specifically label cluster 2, mainly composed by VGAT$^+$ vlPAG neurons (Figure 5.3A).

Lastly, I set out to find marker genes for the subpopulations identified by the alternative consensus clustering approach (Figure 5.4). In this case, I had a total of four putative subpopulations, roughly consisting of either glutamatergic or GABAergic

neurons in either the dorsal or ventral PAG. The results from the pairwise comparisons of these four groups did yield a few marker genes: 9 for cluster 1 (VGluT2$^+$ neurons from dm/dlPAG), 30 for cluster 2 (VGAT$^+$ neurons from dm/dlPAG), 62 for cluster 3 (VGAT$^+$ neurons from l/vlPAG), and 31 for cluster 4 (VGluT2$^+$ neurons from l/vlPAG). As I did for the cell type comparison, to examine the genes with the potential to identify each subpopulation, I focused on those with an AUC value above 0.8 (Figure 5.9).

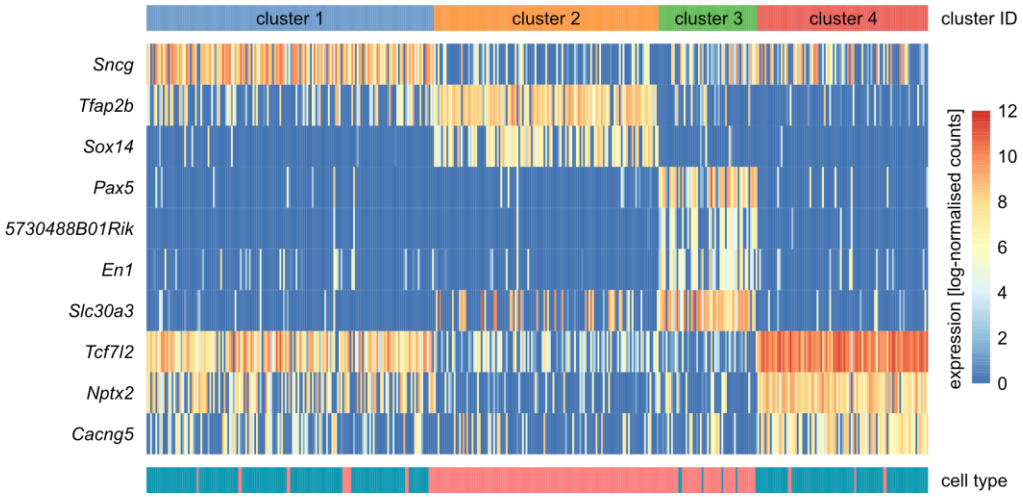

Figure 5.9. Differential expression of subpopulation-specific marker genes. Heatmap summarising the expression levels of the upregulated genes with the highest AUC value in each of the clusters. Each row represents a gene. Red colours indicate high expression. Blue colours indicate low expression. Each column represents a neuron. For each neuron, the identity of the cluster and cell type it belongs to is indicated in the row above or below the plot, respectively.

From the subset of potential marker genes, I found that the cleanest genes to separate clusters 2 and 3 were once again transcription factors: *Sox14* was a very specific marker of neurons in cluster 2 (VGAT$^+$ neurons from dm/dlPAG), whereas *Pax5* and *En1* were specific for cluster 3 (VGAT$^+$ neurons from l/vlPAG). These last two are the same I already found in the results from the graph-based clustering results, also being remarkably specific for the smaller cluster 2 composed mainly of VGAT$^+$ vlPAG neurons. For both genes, though, the AUC values were higher in the graph-

based clustering scenario, suggesting they were more specific for the subpopulation of vlPAG neurons identified there.

From the rest of the potential markers, two stood out. On one hand, *Slc30a3*, a gene encoding a zinc transporter involved in the accumulation of zinc in synaptic vesicles, seemed to be enriched in cluster 3 ($VGAT^+$ neurons from l/vlPAG), although it was also expressed by other $VGAT^+$ neurons. On the other hand, *Cacng5*, a gene encoding the Transmembrane AMPA receptor Regulatory Protein γ-5, was specific for cluster 4 ($VGluT2^+$ neurons from l/vlPAG). The rest of the potential marker genes did not show a very clear expression pattern, with most being expressed in several cells in other clusters.

Taken together, the results from this section suggest that although there is some substructure within the glutamatergic and GABAergic neurons of the PAG that seems to faintly correlate with PAG subdivisions, I have not managed to identify a clear set of marker genes that would classify PAG neurons according to their cell type and anatomical location.

5.4 NEUROPEPTIDES AND RECEPTORS FOR NEUROMODULATORS CAN SEGREGATE BY CELL TYPE AND PAG SUBDIVISION

An alternative approach to trying to identify marker genes with a high AUC value would be to follow a more nuanced and targeted approached. This could consist of considering any gene with a Benjamini-Hochberg adjusted p-value of less than 0.05 in the chosen pairwise comparisons. I could then use customised gene lists to select those belonging to different families of ion channels, neuropeptides, or neuromodulator receptors and examine their expression pattern in the selected groups in search of potentially interesting effects.

Given that I did not find marker genes specific to clusters or to the combination of cell type and PAG subdivision, I decided to return to the list of genes identified by comparing VGAT$^+$ to VGluT2$^+$ neurons. I argued that, even if the differences in gene expression were not clear or large enough to be picked up by my previous analysis, both the clustering results and the UMAP visualisation seemed to indicate there was sub-structure worth investigating. For example, a gene highly expressed in a given PAG subdivision for GABAergic neurons but also in a different PAG subdivision for glutamatergic neurons may not have been detected by the analysis approach used so far but could have strong implications on the physiology and function of the PAG.

In this last section, I investigated the expression profile of a subset of genes encoding neuropeptides and neuromodulator receptors with the potential to open new lines of research into the neural circuits underpinning behavioural control by the PAG.

5.4.1 Neuropeptides and neuromodulators differentially expressed in VGAT$^+$ and VGluT2$^+$ neurons in the PAG

From the genes showing a clear upregulation in either VGAT$^+$ and VGluT2$^+$ neurons in the PAG (Figure 5.5), I found five genes encoding for different peptides and hormones. *Nxph1* and *Pnoc* were enriched in VGAT$^+$ neurons, whereas *Acyap1*, *Nxph4*, and *Tac1* were enriched in VGluT2$^+$ neurons (Figure 5.10). In both cases, this effect was irrespective of PAG subdivision (Figure 5.10B).

Nxph1 is a gene encoding the secreted peptide Neurexophilin 1, whereas *Nxph4* encodes the secreted peptide Neurexophilin 4. Neurexophilins may be signalling molecules that resemble neuropeptides and bind to α-neurexins, but their signalling function is not clear (Petrenko, Ullrich, *et al.*, 1996; Missler and Südhof, 1998). The high specificity for either VGAT$^+$ or VGluT2$^+$ neurons suggests that the functional

implications of these proteins may help better understand the architecture of the neuronal circuits within the PAG.

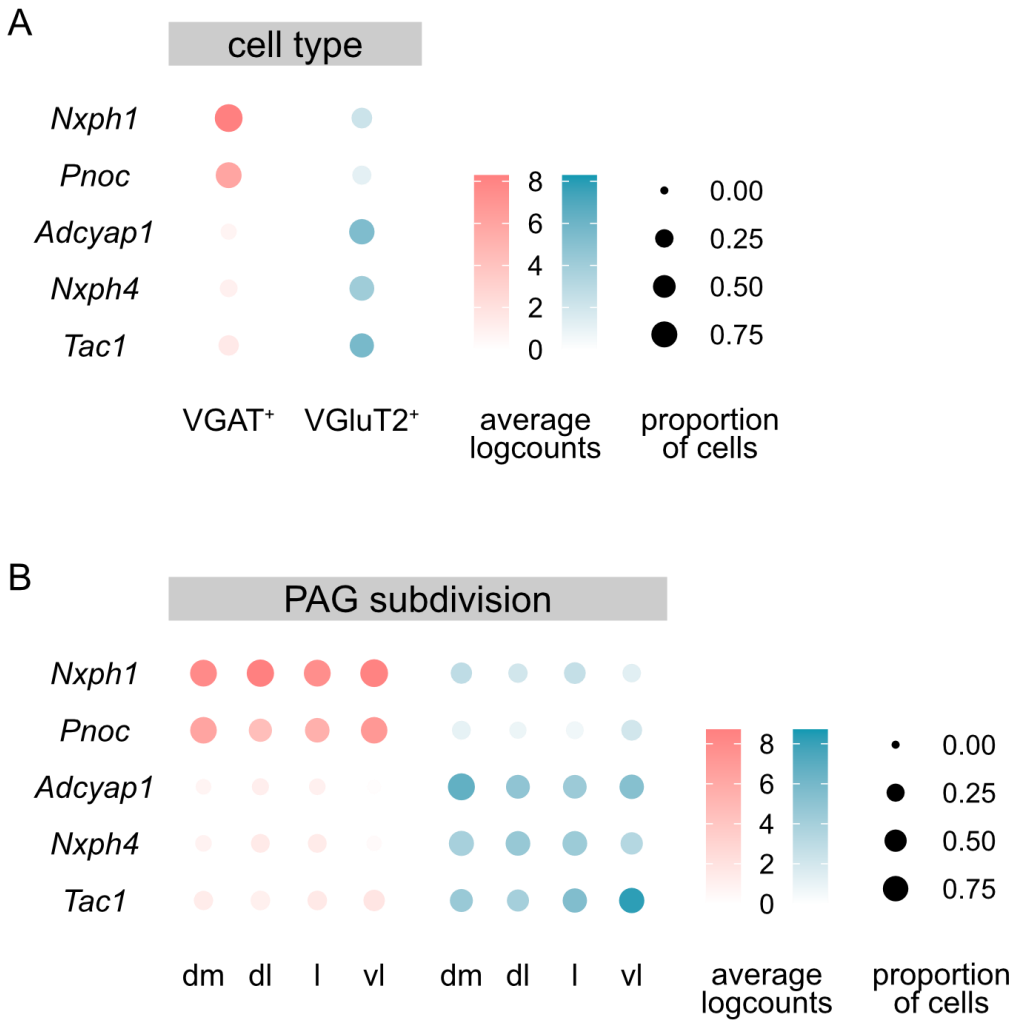

Figure 5.10. Gene expression profile of neuropeptides across cell types and PAG subdivisions. (**A**) Dot plot summarising the average expression of each gene (rows) in all VGAT+ (left column) and in all VGluT2+ neurons (right column). (**B**) Dot plot summarising the average expression of each gene (rows) in all VGAT+ (left-side columns) and in all VGluT2+ neurons (right-side columns) across PAG subdivisions. *dm* indicates dmPAG, *dl* indicates dlPAG, *l* indicates lPAG, *vl* indicates vlPAG. The size of each dot indicates the proportion of neurons in each group that express a given gene. The colour intensity of the dot represents the average expression of a given gene across all neurons in that group.

Pnoc encodes Prepronociceptin, a preproprotein that can give rise to the neuropeptides Nociceptin, Nocistatin, and Orphanin FQ2. The products of this gene have been repeatedly implicated in pain sensitivity and analgesia (Martin, Malmberg, and Basbaum, 1998; Amodeo, López Méndez, *et al.*, 2000; Okuda–Ashitaka and Ito, 2000; Andero, 2015; Gavioli, Holanda, *et al.*, 2021). My data suggest that their effects could be specifically mediated by a subset of $VGAT^{+}$ PAG neurons.

In $VGluT2^{+}$ neurons, I found two other upregulated genes very relevant to the function of the PAG. The first was *Adcyap1*, which encodes the Pituitary Adenylate Cyclase Activating Polypeptide 1 (PACAP). This peptide has been implicated in stress and anxiety (Ferragud, Velazquez-Sanchez, *et al.*, 2021; Zhang, Hernandez, *et al.*, 2021), as well as with autonomic responses, feeding, and reproduction (Farnham, Lung, *et al.*, 2012; Krashes, Shah, *et al.*, 2014; Tan, Cooke, *et al.*, 2016; Ross, Leon, *et al.*, 2018; Sureshkumar, Saenz, *et al.*, 2021). The second was *Tac1*, a gene that encodes the Tachykinin Precursor 1, a precursor protein that can give rise to the peptide hormones substance P and neurokinin A and may label a subset of PAG neurons involved in itch-induced scratching behaviour (Gao, Chen, *et al.*, 2019). Tachykinins have also been suggested to play a role in pain, anxiety, stress, and aggression in rodents (Severini, Improta, *et al.*, 2002), all functions widely linked to the PAG.

The fact that these peptides can be synthesised and released in a cell type-specific manner, together with the electrophysiological traits of $VGAT^{+}$ and $VGluT2^{+}$ neurons in the PAG I described in chapter 3, may help clarify and contextualise the effects these molecules exert on downstream targets. Furthermore, identifying subpopulations that express the receptors for these peptides may help discover specific pathways and bring new opportunities to disentangle the heterogeneous functionality of the PAG.

5.4.2 Neuromodulator receptors and neuropeptides expressed in distinct PAG subdivisions

Lastly, I asked whether there were any genes showing expression patterns that would slightly bias their effects to a PAG subdivision in a cell type-specific manner. Indeed, I identified a subset of genes with the potential to label or modulate the function of subsets of neurons in specific PAG subdivisions (Figure 5.11). Of note, I found that *Drd1* and *Rxfp2* were strikingly specific for $VGAT^+$ neurons in the dmPAG. *Drd1* encodes the dopamine receptor D1, whose activation by dopamine stimulates adenylyl cyclase and activates cyclic AMP-dependent protein kinases. *Rxfp2* encodes the relaxin receptor 2, whose activation by the peptide relaxin also leads to the stimulation of adenylate cyclase and an increase of cyclic AMP. Thus, in both cases the release of either dopamine or relaxin in the dmPAG would specifically stimulate GABAergic neurons, strengthening the inhibitory tone in that circuit module.

A second set of genes seemed to be selectively expressed in subpopulations of $VGluT2^+$ neurons in the dlPAG. These included *Rxfp3*, encoding the relaxin receptor 3, and *Galr1*, encoding the galanin receptor 1. In this case, though, the activation of the receptor by its ligand would lead to the inhibition of adenylate cyclase, thus having the opposite effect than *Drd1* and *Rxfp2*. Another gene also expressed in a subpopulation of $VGluT2^+$ neurons in the dlPAG was *Prokr2*, encoding the Prokineticin receptor 2, a G_q-coupled receptor that would lead to the activation of phospholipase C.

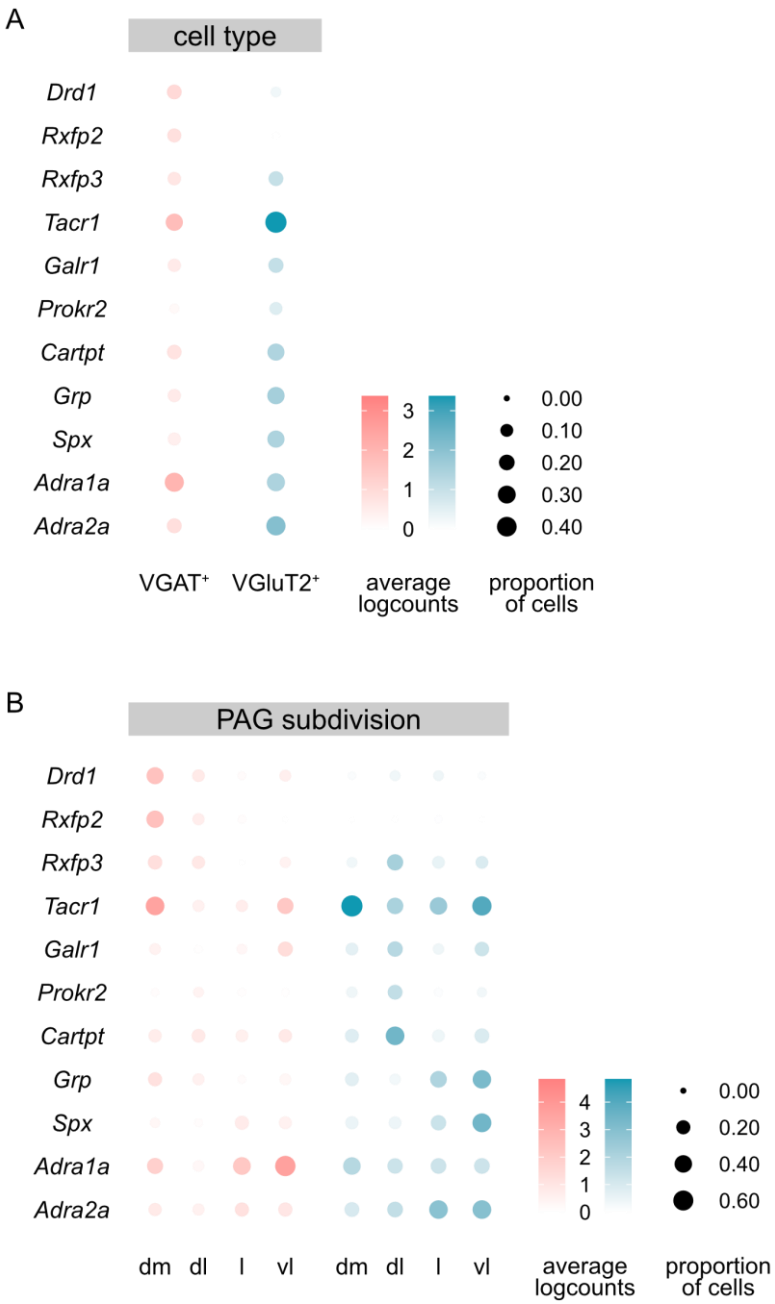

Figure 5.11. Gene expression profile of neuromodulator receptors and neuropeptides across cell types and PAG subdivisions. (**A**) Dot plot summarising the average expression of each gene (rows) in all VGAT$^+$ (left column) and in all VGluT2$^+$ neurons (right column). (**B**) Dot plot summarising the average expression of each gene (rows) in all VGAT$^+$ (left-side columns) and in all VGluT2$^+$ neurons (right-side columns) across PAG subdivisions. *dm* indicates dmPAG, *dl* indicates dlPAG, *l* indicates lPAG, *vl* indicates vlPAG. The size of each dot indicates the proportion of neurons in each group that express a given gene. The colour intensity of the dot represents the average expression of a given gene across all neurons in that group.

I also identified a few neuropeptides enriched in a subset of VGluT2$^+$ neurons. *Cartpt*, a gene encoding the Cocaine And Amphetamine Regulated Transcript prepropeptide, had a higher expression in dlPAG VGluT2$^+$ neurons and could label a subpopulation implicated in energy homeostasis, feeding, and stress. *Grp*, a gene encoding the Gastrin-Releasing Peptide, and *Spx*, a gene encoding the neuropeptide Spexin, were upregulated in a subset of vlPAG and lPAG VGluT2$^+$ neurons. Neurons expressing *Grp* could contribute to the perception of prurient stimuli and the transmission of itch signals to the spinal cord. Spexin, on the other hand, has been shown to bind Galanin receptors 2 and 3 (but not 1) and may play a role in energy metabolism, cardiovascular and renal function, and nociception.

Finally, I observed inverted expression patterns of two α-adrenergic receptors in VGAT$^+$ and VGluT2$^+$ neurons of the lPAG and vlPAG columns: *Adra1a*, encoding the α_{1A}-adrenergic receptor, was enriched in VGAT$^+$ neurons, whereas *Adra2a*, encoding the α_{2A}-adrenergic receptor, was enriched in VGluT2$^+$ neurons. Interestingly, while the effects of the former are mediated by G_q proteins, the latter would act via G_i proteins. This suggested that in the lPAG and vlPAG, noradrenaline would lead to opposing effects in VGAT$^+$ and VGluT2$^+$ neurons, resulting in a net inhibitory effect.

I found a similar dichotomy when looking at the expression of the full set of dopamine receptors (Figure 5.12). In this case, the G_s-coupled D1-like receptors encoded by *Drd1* and *Drd5* showed a marked expression in a subset of VGAT$^+$ neurons of the dmPAG and dlPAG, respectively. Conversely, some VGluT2$^+$ neurons in the vlPAG showed a higher expression of the G_i-coupled D2-like receptor encoded by *Drd2* and the G_s-coupled D1-like receptor encoded by *Drd5*, but not by *Drd1*. This suggested that the effects of dopamine in the dorsal PAG would result in a stimulation of the already tonically active GABAergic neurons, whereas in the vlPAG the effects of dopamine would depend on which receptor the target neuron expressed, with both stimulation and inhibition being a possible outcome.

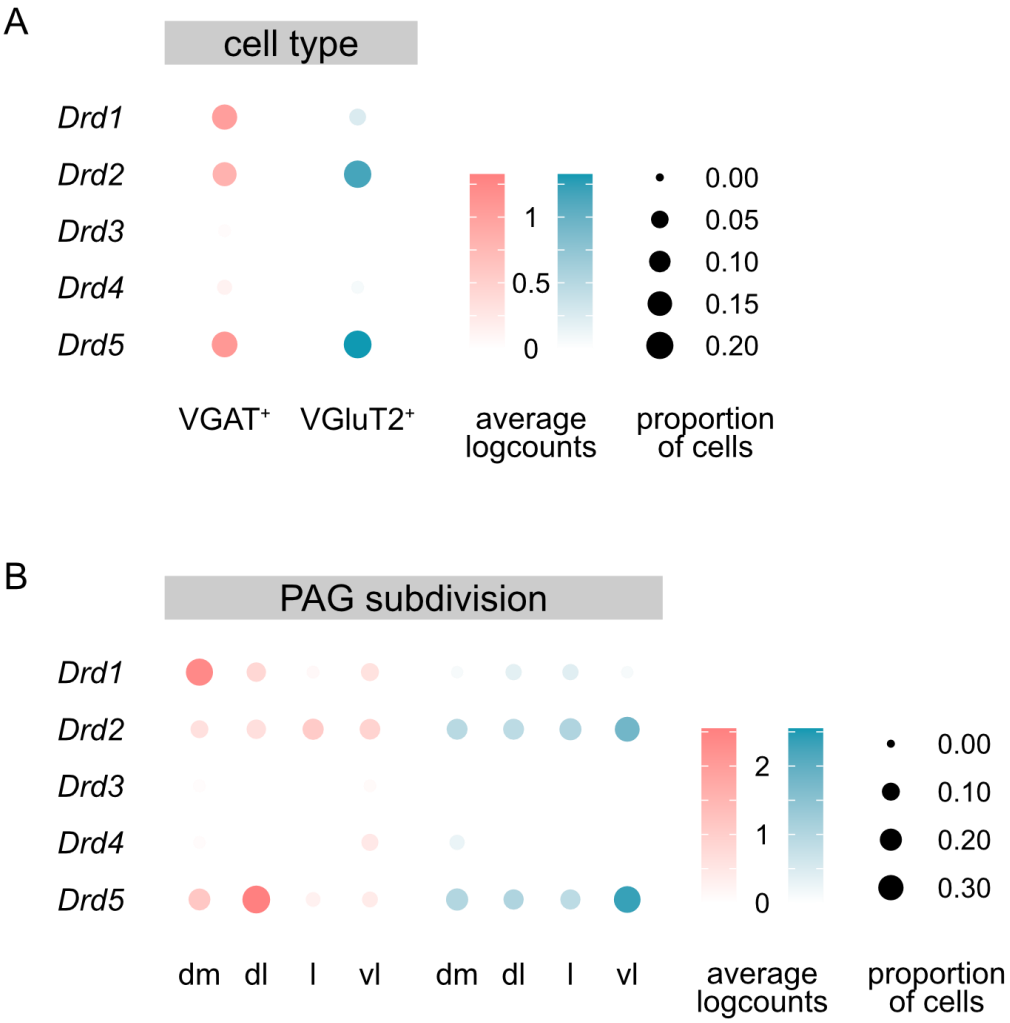

Figure 5.12. Gene expression profile of dopamine receptors across cell types and PAG subdivisions. (**A**) Dot plot summarising the average expression of each gene (rows) in all VGAT+ (left column) and in all VGluT2+ neurons (right column). (**B**) Dot plot summarising the average expression of each gene (rows) in all VGAT+ (left-side columns) and in all VGluT2+ neurons (right-side columns) across PAG subdivisions. *dm* indicates dmPAG, *dl* indicates dlPAG, *l* indicates lPAG, *vl* indicates vlPAG. The size of each dot indicates the proportion of neurons in each group that express a given gene. The colour intensity of the dot represents the average expression of a given gene across all neurons in that group.

Overall, these results suggested that the high level of functional heterogeneity in the different cell types and PAG subdivisions can be partially explained by the complex expression profiles of different subpopulations of neurons.

5.5 SUMMARY

In this last chapter, I have used unsupervised clustering and differential expression analysis to extract biological insights from the gene expression profiles of $VGAT^{+}$ and $VGluT2^{+}$ neurons across PAG subdivisions. My results identify an array of molecular motifs that would enable different brain circuits to discretely modulate and exploit the underlying electrophysiological properties of glutamatergic and GABAergic neurons in a cell type and even PAG subdivision specific manner to elicit the behavioural output that maximises an individual's survival.

6 Discussion

The midbrain PAG is a longitudinal columnar structure that regulates and coordinates the execution of a plethora of instinctive behaviours, from predator avoidance, reproductive behaviour, and hunting to analgesia, stress, and cardiovascular function (Bandler and Depaulis, 1991; Behbehani, 1995; Benarroch, 2012; Keay and Bandler, 2015; Silva and McNaughton, 2019). Even though its functional heterogeneity has been known for decades, a systematic biophysical and molecular characterisation of the different cell types across PAG subdivisions was still lacking. In this study I began to address this gap.

I first combined the preparation of acute midbrain slices with the use of transgenic lines and pharmacology to obtain patch-clamp recordings from genetically labelled subsets of neurons in the PAG and its anatomical subdivisions. By using loose-seal cell-attached recordings, I found that the baseline firing properties of GABAergic and glutamatergic neurons were strikingly different: $VGAT^{+}$ neurons spontaneously generated action potentials even in the absence of synaptic inputs, whereas $VGluT2^{+}$ neurons were mostly silent. In addition, the results from a complementary set of experiments using whole-cell patch-clamp recordings suggested that $VGAT^{+}$ neurons have a higher input resistance and a lower action potential threshold than $VGluT2^{+}$ neurons. Importantly, these results were irrespective of the PAG subdivision the recorded neuron was found in, as well as of other variables such as the age or the sex

of the mouse. Together, these results suggested a common electrophysiological trait upon which the different neural circuits within the PAG are built.

In an attempt to better understand the main cellular components of the neuronal circuits within the PAG, I established a pipeline to perform topographic and cell type-specific deep transcriptomic profiling of PAG neurons. By using visually guided aspiration via patch pipettes I successfully isolated fluorescently labelled neurons from acute midbrain slices of transgenic mice while preserving their anatomical origin. To the best of my knowledge, this study is the first to use such targeted approach to link the expression of ion channels, receptors, and molecular effectors to specific PAG subdivisions.

The results of my analysis are a stepping stone towards dissecting the complexity underlying PAG circuits. I identified two ion channel subunits as the most differentially expressed genes between $VGAT^{+}$ and $VGluT2^{+}$ neurons, one of them (*Asic4*) with an unknown function and the other (*Cacna2d1*) being the main target of gabapentinoids, a class of drugs that includes gabapentin and pregabalin used as a first-line medication for epilepsy and neuropathic pain. I also found evidence of a complex biological substructure, with many neuropeptides and neuromodulator receptors showing expression patterns biased to different cell types and PAG subdivisions. Of note, I found that the expression profile of a subset of dopamine, relaxin, and noradrenaline receptors places them in a privileged position to regulate some of the functions mediated by the PAG. These are some examples of molecular motifs that could enable different brain regions to modulate and exploit the underlying electrophysiological properties of glutamatergic and GABAergic neurons in a cell type or PAG subdivision-specific manner to elicit the behavioural output that maximises an individual's survival.

In these last few pages, I discuss the implications of the major findings presented in the previous results chapters and propose several experiments with the potential to open new lines of investigation. I hope that, by interpreting the gene expression data in light of the electrophysiological properties of the two main cell types in the PAG,

these results will prove to be an asset to the field and will ultimately lead to a better understanding of the many roles of this fascinating brain area.

6.1 A CELL TYPE-SPECIFIC ELECTROPHYSIOLOGICAL BLUEPRINT FOR PAG CIRCUITS

Several studies have reported a baseline firing frequency close to 4 Hz in the PAG. For example, *in vitro* extracellular recordings in rats found a firing rate of ~3 Hz, whereas extracellular recordings in anesthetised rats reported a baseline firing frequency of ~7 Hz (Behbehani, Jiang, *et al.*, 1990), and single-unit recordings in awake rats have reported baseline firing rates of ~3 Hz (Halladay and Blair, 2015; Watson, Cerminara, *et al.*, 2016). However, most of the studies using extracellular recordings were blind to the type of cell recorded. It is only recently that the development of recording techniques has allowed the identification of the type of neuron being recorded. Experiments using such an approach have reported that the baseline firing rate of lPAG neurons *in vivo* was higher in $VGAT^+$ neurons (~7 Hz) than in $VGluT2^+$ neurons (~3 Hz) (Yu, Xiang, *et al.*, 2021).

I set out to conduct a systematic study of the baseline firing properties of PAG neurons in a genetically addressable manner. I obtained targeted loose-seal cell-attached recordings from a total of 60 $VGAT^+$ and 76 $VGluT2^+$ neurons, spanning the different PAG subdivisions, and found that $VGAT^+$ neurons in the PAG are spontaneously active, with an average firing frequency of 4.59 ± 0.55 Hz, whereas $VGluT2^+$ neurons are mostly silent, with an average firing frequency of 0.12 ± 0.05 Hz (Figure 3.3). These results held when removing the effects of synaptic activity within the slice, with $VGAT^+$ neurons maintaining an average firing frequency of 5.98 ± 0.73 Hz and $VGluT2^+$ maintaining an average firing frequency of 0.03 ± 0.02 Hz (Figure 3.3), and were consistent across PAG subdivisions (Figure 3.7). This suggests

that, at least in part, the baseline firing frequencies reported in the PAG when using experimental techniques agnostic to the type of cell being recorded could correspond to the intrinsic activity of $VGAT^+$ neurons.

In addition, I used whole-cell patch-clamp recordings to further characterise the biophysical properties of PAG neurons in the dmPAG and dlPAG. I found differences in two parameters directly related to the excitability of a neuron: the input resistance (Figure 3.12) and the action potential threshold (Figure 3.14). I found that, in control conditions, $VGAT^+$ neurons in the dorsal PAG had an average input resistance of 684.4 ± 36.0 MΩ, whereas $VGluT2^+$ neurons in the dorsal PAG had an average input resistance of 338.0 ± 44.7 MΩ. Interestingly, when blocking synaptic inputs in the slice $VGAT^+$ and $VGluT2^+$ neurons exhibited similar values of input resistance, with $VGAT^+$ neurons having an average input resistance of 795.0 ± 98.3 MΩ and $VGluT2^+$ neurons having an average input resistance of 675.4 ± 116.8 MΩ. Furthermore, I found that the average action potential threshold was slightly lower in $VGAT^+$ neurons (−38.2 ± 0.6 mV in control conditions and −36.6 ± 0.9 mV in synaptic blockers) than in $VGluT2^+$ neurons (−35.3 ± 1.2 mV in control conditions and −32.9 ± 0.9 mV in synaptic blockers).

These results further support the idea that $VGAT^+$ and $VGluT2^+$ neurons in the PAG have profoundly different electrophysiological profiles and could help contextualise the mixed results from early electrical stimulation and lesion studies that began to characterise the physiological roles of the PAG. In line with what recent experiments suggest (La-Vu, Sethi, *et al.*, 2022), it is paramount that future studies wishing to dissect the function of the PAG in a particular behaviour use cell type-specific approaches to record and manipulate the activity of neurons in this area.

As striking as the difference in baseline firing frequency was, I found no evidence for a higher level of expression of pacemaking ion channels in $VGAT^+$ neurons, with both cell types exhibiting similar expression levels of sodium channels, of hyperpolarisation-activated cation channels, and of low and high-voltage activated calcium channels. This suggests that, at least at the mRNA level, both cell types are

equipped with the necessary conductances to generate spontaneous action potentials, but a yet to be described feature of VGluT2$^+$ neurons prevents them from doing so. In the final section I propose a first set of experiments that could help identify it.

Our results from recordings obtained in the presence of synaptic blockers further suggest that the firing frequency, the input resistance, and the action potential threshold of PAG neurons can be modulated by incoming inputs. By being spontaneously active, having a higher input resistance, and having a lower action potential threshold, VGAT$^+$ neurons are in an ideal position to control the output of VGluT2$^+$ neurons and therefore the amount of neuronal activity needed to reach VGluT2$^+$ neurons in order to generate PAG output. Indeed, unpublished data from colleagues in the Branco Lab have shown that in the dorsal PAG, VGAT$^+$ neurons provide synaptic inputs onto neighbouring glutamatergic cells and exert local phasic inhibition on the dorsal PAG network. Optogenetic inactivation of VGAT$^+$ dorsal PAG neurons in freely behaving mice increased the probability of initiating escape from innately aversive stimuli. Conversely, optogenetic activation of the same neurons during threat presentation inhibited escape initiation. These results suggest that both the activity of glutamatergic neurons in the dorsal PAG and the initiation of instinctive escape are controlled by the local GABAergic network that was described in earlier studies. A similar blueprint seems to be in place in the other PAG subdivisions (Behbehani, Jiang, *et al.*, 1990; Behbehani, 1995; Lee and Gammie, 2010; Kohl, Babayan, *et al.*, 2018; Hao, Yang, *et al.*, 2019) and may underpin the computation and coordination of the different behaviours controlled by the PAG.

6.2 THE EXPRESSION OF *CACNA2D1* AND *ASIC4* AS A HALLMARK OF GLUTAMATERGIC AND GABAERGIC NEURONS IN THE PAG

The top marker gene for glutamatergic neurons in the PAG was *Cacna2d1*, a gene encoding the Voltage-Gated Calcium Channel Auxiliary Subunit α2δ1. While the main pore-forming α subunits and the α2δ2 subunit showed a similar expression profile both between cell type (Figure 5.7A) and across PAG subdivisions (Figure 5.7B), the α2δ1 subunit showed an expression pattern strikingly restricted to VGluT2$^+$ neurons.

As I discussed earlier, α2δ subunits enhance the trafficking of α1 subunits to the cell membrane, increase their maximum current density, and accelerate their activation and inactivation kinetics (Dolphin and Lee, 2020). My data suggest that the effects mediated by α2δ1 would be specific to VGluT2$^+$ neurons. However, the most interesting fact about the α2δ1 and α2δ2 subunits is that they are the binding site for gabapentinoids, a class of drugs that include gabapentin and pregabalin used to treat epilepsy, neuropathic pain, anxiety, and other neurological disorders (Dolphin, 2012). Gabapentinoids achieve their effect by specifically blocking α2δ-containing voltage-gated calcium channels, without binding to GABA receptors or affecting GABA metabolism. Given the role of PAG in pain processing, analgesia, stress, and anxiety, my results suggest that the pharmacological effects of gabapentinoids could in part be derived from selectively dampening the excitability of VGluT2$^+$ neurons in the PAG.

However, gabapentinoids have many side effects and are not equally effective in all patients. Some of the main side effects include drowsiness, increased appetite, irritability, dysarthria, dry mouth, urinary incontinence, withdrawal symptoms and even suicidal thoughts. The fact that *Cacna2d1* was also found to be the top marker gene for glutamatergic neurons in the superior colliculus (Xie, Wang, *et al.*, 2021) and other brain areas (Cole, Lechner, *et al.*, 2005), together with the many functions that have been ascribed to the PAG (see section 1.1.3), could highlight a potential reason for the

many side effects that gabapentinoids have. For example, oral administration of gabapentin or pregabalin to treat chronic pain, an ailment the PAG has been implicated in, would lead to off-target effects by dampening the excitability of glutamatergic neurons in other brain areas. These data could help improve the therapeutic efficacy and reduce off-target effects of these drugs by aiding the development of more specific drugs and delivery strategies.

A hypothesis potentially worth exploring would be the following. Given that (1) $VGAT^+$ neurons are spontaneously active, constantly release GABA, and synapse onto neighbouring $VGluT2^+$ neurons, that (2) the α2δ1 subunit is differentially expressed in $VGluT2^+$ neurons in the PAG and is the specific target of a class of drugs that were synthetised as GABA analogues, and that (3) the effect of this drugs is to block α2δ-containing voltage-gated calcium channels and reduce the excitability of the affected neuron, I hypothesised that if the tonically released GABA could bind the α2δ1 subunit it could partly contribute to the fact that $VGluT2^+$ neurons are not spontaneously active. However, GABA does not seem to bind the product of *Cacna2d1* as gabapentinoids do, and its K_d is suggested to be on the mM range (Cole, Lechner, *et al.*, 2005; Li, Taylor, *et al.*, 2011).

> *Although there are various amino acids that do bind the a2δ1 subunit (e.g. leucine and isoleucine), the EM structures have nothing in the binding pocket where gabapentin would bind. But their affinity is quite low, and they might have been easily removed during purification. The apparent affinity for gabapentin increases with a2δ1 purification, suggesting there may be something bound in native tissues that is being removed. The function of whatever is bound physiologically is unknown.*
>
> *Annette C. Dolphin (personal correspondence)*

Interestingly, it seems that α2δ1 double knock out mice could be less anxious than their wild-type siblings, as "*they are the ones normally picked first from the cage when collecting the ear notches*" (Annette C. Dolphin, personal correspondence). Even if my far-fetched hypothesis suggesting that α2δ1 subunits could contribute to the electrophysiological profile of $VGluT2^+$ neurons does not hold, the fact that this calcium channel subunit is the top marker for $VGluT2^+$ neurons suggests it can indeed play a key role in

modulating the physiological function of PAG circuits. The most pressing experiments should be directed at identifying the endogenous ligand, if there is one, that binds this subunit in physiological conditions and at characterising the effects that α2δ1 and α2δ2 blockers have in $VGAT^+$ and $VGluT2^+$ neurons. The latter could be achieved by combining whole-cell recordings and pharmacology to test the effects of gabapentin and pregabalin and compare them to other ligands like spermine or the amino acid leucine that bind the subunit without having the anxiolytic effect of gabapentin (Dissanayake, Gee, *et al.*, 1997; Brown, Dissanayake, *et al.*, 1998). Furthermore, a set of behavioural experiments could be performed on α2δ1 knock out mice to test whether there are any obvious differences in the defensive behaviours mediated by dorsal PAG neurons by examining their response to the presentation of overhead expanding dots that simulate the imminent danger of a predator (Yilmaz and Meister, 2013; De Franceschi, Vivattanasarn, *et al.*, 2016; Vale, Evans, and Branco, 2017; Evans, Stempel, *et al.*, 2018).

In the case of $VGAT^+$ neurons, one of the most differentially upregulated genes was *Asic4* (Figure 5.6). Similar to what I observed in the case of voltage-gated calcium channels, the expression levels of the pore-forming subunits encoded by *Asic1* and *Asic2* were very similar between $VGAT^+$ and $VGluT2^+$ neurons across PAG subdivisions. Acid-sensing ion channels are voltage-insensitive, proton-gated channels activated by a drop in the extracellular pH. They are mainly permeable to Na^+, although some channels with ASIC1 subunits have some Ca^{2+} permeability. ASIC1 and ASIC2 are pore forming subunits that activate at different levels of acidosis, with the former responding to values around pH 6 and the latter responding to values around pH 4.5 (Kweon and Suh, 2013).

While ASIC4 does not seem to form a proton-gated channel, it does appear to have a modulatory function on other ASIC channels (Akopian, Chen, *et al.*, 2000). It has been suggested that ASIC4 reduces the number of functional ASICs located at the plasma membrane, effectively diminishing the current mediated by ASIC1 (Donier, Rugiero, *et al.*, 2008). According to my single-cell RNA-sequencing data, this effect

would be specific to $VGAT^+$ neurons. Thus, the expression of ASIC4 in $VGAT^+$ neurons would lead to the internalisation of ASIC1-2, something that would not occur in $VGluT2^+$ neurons. This could give rise to a situation in which a drop in pH would selectively activate $VGluT2^+$ neurons, as the number of ASIC1 channels in the membrane would not be affected by ASIC4. Interestingly, the existence of a suffocation alarm system within the PAG with a link to panic attacks has been suggested in the rat (Schimitel, de Almeida, *et al.*, 2012).

A potential experiment in this direction would be to obtain whole-cell recordings from $VGAT^+$ and $VGluT2^+$ neurons and characterise the effects of applying different solutions with decreasing pH levels. These results suggest that, in the PAG, the expression, or lack thereof, of ASIC4 could have profound implications for $VGAT^+$, or $VGluT2^+$, neurons. To the best of my knowledge, the endogenous ligand and the potential modulators of ASIC4 are still unknown. Identifying them and elucidating the function that ASIC4 has in $VGAT^+$ neurons could be a big step towards better understating the function of the PAG.

6.3 THE MANY PATHS TO NEUROMODULATION IN THE PAG

Given that multiple brain regions send neuromodulatory projections to the PAG (see section 1.1.1), it is not surprising that some studies have focused on the role neuromodulators such as dopamine and noradrenaline have in this brain area (Jiang, Chandler, *et al.*, 1992; Brandão, Anseloni, *et al.*, 1999; Vander Weele, Siciliano, *et al.*, 2018; Silva and McNaughton, 2019). For instance, it has been shown that brain areas including the zona incerta, the arcuate hypothalamic nucleus, and the parabrachial nucleus send dopaminergic projections to the PAG, whereas the locus coeruleus and the dorsal raphe send noradrenergic and serotoninergic inputs to the PAG (see section 1.1.1 for more details).

Our single-cell RNA-sequencing data has identified inverted expression patterns of two α-adrenergic receptors in a subset of $VGAT^+$ and $VGluT2^+$ neurons of the lPAG and vlPAG columns (Figure 5.11): *Adra1a*, encoding the α_{1A}-adrenergic receptor, was preferentially expressed in $VGAT^+$ neurons, whereas *Adra2a*, encoding the α_{2A}-adrenergic receptor, was preferentially expressed in $VGluT2^+$ neurons. I found a similar dichotomy when looking at the expression pattern of the full set of dopamine receptors (Figure 5.12). In this case, the G_s-coupled D1-like receptors encoded by *Drd1* and *Drd5* showed a marked expression in a subset of $VGAT^+$ neurons of the dmPAG and dlPAG, respectively. Conversely a subset of $VGluT2^+$ neurons across PAG subdivisions showed a higher expression of the G_i-coupled D2-like receptor encoded by *Drd2*, while others expressed the G_s-coupled D1-like receptor encoded by *Drd5*.

α_{1A} -adrenergic receptor signalling is mediated by $G_{q\alpha}$ and leads to the activation of phospholipase C and the subsequent opening of inositol triphosphate gated calcium channels in the endoplasmic reticulum, releasing Ca^{2+} into the cytosol and resulting in increased activation of the neuron. In contrast, α_{2A}-adrenergic receptors are $G_{i\alpha}$-coupled and lead to a reduction in neuronal excitability by inhibiting adenylyl cyclase and reducing protein kinase A activity (Molinoff, 1984).

Dopamine receptors are subdivided into two classes with opposing effects on intracellular signalling cascades: D_1-like (D_1, D_5) and D_2-like (D_2, D_3, D_4). D_1-like receptors are coupled with $G_{s\alpha}$ and stimulate adenylyl cyclase to produce cyclic AMP, leading to protein kinase A mediated phosphorylation of ionotropic glutamate receptors and inward rectifying potassium channels. By increasing the inflow of Na^+ and Ca^{2+} through ionotropic glutamate receptors and reducing K^+ currents, D_1-like receptors have a net depolarising effect when activated. On the other hand, D_2-like receptors are coupled to $G_{i\alpha}$, which inhibits the production of cyclic AMP and reduces excitability by opening GIRK channels (Missale, Nash, *et al.*, 1998).

Together with the results from the electrophysiological recordings presented in the first results chapter, I hypothesise that in the lPAG and vlPAG noradrenaline would have opposing effects in $VGAT^+$ and $VGluT2^+$ neurons, increasing the

excitability of the already tonically active GABAergic neurons and reducing that of glutamatergic neurons, resulting in a net inhibitory effect. In the case of dopamine, I hypothesise that dopamine transmission in the dorsal PAG would also lead to a net inhibitory effect also by stimulating the tonically active GABAergic neurons, whereas the effects of dopamine on VGluT2^{+} neurons in the ventral PAG would depend on which receptor is expressed, with both stimulation and inhibition of being a possible outcome. In line with this, injection of the D2-like receptor antagonist sulpiride into the dorsal PAG of rats has been shown to increase defensive behaviours (Muthuraju, Talbot, and Brandão, 2016).

A feasible follow-up experiment would thus be to combine whole-cell patch-clamp recordings and pharmacology to assess the effects that adding dopamine or noradrenaline to the recording solution has on the intrinsic properties of VGAT^{+} and VGluT2^{+} neurons in the dorsal or ventral PAG of acute midbrain slices. Ultimately, understanding the effects monoamine neuromodulators have on the electrophysiological properties of PAG neurons could lead to better treatments for anxiety disorders. In particular, the PAG has been implicated in panic attacks, post-traumatic stress disorder, and stress (Brandão and Lovick, 2019). Leveraging the gene expression dataset I generated could help design experiments with the potential to bridge the gap between neuronal physiology and neuropsycopharmacological observations in humans.

A similar approach could be followed to assess the potential effects of several other neuropeptides and neuromodulators with interesting expression patterns as observed in the single-cell RNA-sequencing dataset. The ones with a measurable effect *in vitro* could then be selected for further experiments, including cell type-specific viral tracing or neural activity recording during behaviour.

6.4 ON THE VALIDITY OF USING MRNA AS A PROXY FOR PROTEIN SYNTHESIS AND FUNCTION

An important cautionary note needs to be kept in mind when considering any hypothesis or interpretation stemming from results obtained with single-cell RNA-sequencing data: the mRNA molecules I have been measuring have not yet been translated into proteins and the correspondence between gene expression and protein density may not be great (Hansen, Markello, *et al.*, 2021). It is thus critical that any results and hypotheses are validated and tested with other methods.

Single-cell RNA-sequencing allows researchers to get a snapshot of the gene expression of a cell at a given point in time. From all the mRNA molecules I have detected, only some will be translated into a protein and be trafficked into the cellular compartment where they can carry out their function. This last point is particularly relevant in the case of neurons, as ion channels and receptors can end up in a distal dendrite, the soma, or a presynaptic bouton and impact the physiology of the cell in very different ways.

For most of the gene expression results I described, patch-clamp recordings and pharmacology could be combined to test whether the application of an agonist or antagonist leads to a measurable effect in the targeted neuron *in vitro*. If an effect is observed, one could then proceed to further develop the hypothesis and design experiments to test it. As an example, if the D1 receptor was shown to have an effect on $VGAT^{+}$ neurons in the dmPAG in slices, one could then use rabies tracing from D1-expressing neurons to investigate where the dopaminergic inputs come from. In addition, optical imaging using dopamine sensors could be used to record the dynamics of dopamine during a behavioural paradigm, and Cre-dependent short-hairpin RNA knockdown (Song, Ro, and Yan, 2010) could be used to remove the identified, functionally relevant receptor and investigate its role on escape behaviour *in vivo*.

6.5 EXPERIMENTAL OUTLOOK

Due to the descriptive and exploratory nature of the experimental approach I followed, the results of this research created many hypotheses and highlighted several questions for future studies to test and answer. In this final section, I outline some of the most interesting ones.

What is the ionic basis of spontaneous action potential generation in VGAT$^+$ neurons in the PAG?

There are many examples in the literature of neurons showing spontaneous firing (Puopolo, Raviola, and Bean, 2007; Khaliq and Bean, 2010), including Purkinje cells and molecular layer interneurons in the cerebellum (Häusser and Clark, 1997; Alcami, Franconville, *et al.*, 2012), and dopamine neurons of the vlPAG and the dorsal raphe nucleus (Dougalis, Matthews, *et al.*, 2017).

Given the absence of spontaneous firing in VGluT2$^+$ neurons, I was expecting to find one or more of the ion channel genes typically involved with pacemaking amongst the group of differentially expressed genes between VGAT$^+$ and VGluT2$^+$ PAG neurons. However, I did not find any evidence for this, with both cell types exhibiting similar expression levels of sodium channels, of hyperpolarisation-activated cation channels, and of low and high-voltage activated calcium channels. As I have already discussed, having similar expression levels of an mRNA does not equate to having the same phenotype, as the transcript can be further modified to produce different isoforms and the protein function can be regulated by mechanisms specific to only one of the cell types.

A potentially interesting line of investigation would be to design a series of voltage-clamp experiments in slices to characterise the voltage-dependent currents that are active in the subthreshold range of VGAT$^+$ neurons. Given the slight difference in

the expression levels of some potassium channels between VGAT$^+$ and VGluT2$^+$ neurons (Figure 5.8), one could begin by characterising the A-type transient currents, M-currents, delayed rectifier currents, and background leak currents present in PAG neurons. These experiments could be followed by others aimed at examining the kinetics of low- and high-voltage activated calcium currents and sodium background "persistent" currents, as well as investigating whether *Asic4* and *Cacna2d1* could have an impact on the baseline intrinsic properties of PAG neurons.

What is the dynamic range of the spontaneous activity of GABAergic neurons in the PAG?

Although I found no clear differences between the baseline firing frequency of VGAT$^+$ neurons from different PAG subdivisions, one could imagine a situation in which differentially increasing or decreasing the firing frequency of VGAT$^+$ neurons in different circuit modules could help determine which behavioural output the PAG gives rise to. This could be achieved both by projection specific inputs and by selective expression of a subset of neuromodulator receptors. Akin to having a gain knob, this would enable contextual cues or internal states to modify the level of inhibition in a given subcircuit to bias the output of the PAG towards one behaviour or another. A potentially viable first step towards investigating this would be to use Neuropixels probes and opto-tagging (Anikeeva, Andalman, *et al.*, 2012; Jun, Steinmetz, *et al.*, 2017; Vale, Campagner, *et al.*, 2020) to record the dynamics of VGAT$^+$ and VGluT2$^+$ neurons in the different PAG columns during behaviour.

Of note, I found that the expression levels of *Drd1* (encoding the dopamine receptor D1) and *Rxfp2* (encoding the relaxin receptor 2) were strikingly specific for VGAT$^+$ neurons in the dmPAG (Figure 5.11). In both cases, the activation of the receptor by its ligand leads to the stimulation of adenylate cyclase and an increase of cyclic AMP, and could thus selectively increase the inhibitory tone in that particular PAG subdivision.

What is the input-output connectivity of molecularly defined circuit modules within the PAG?

Monosynaptic rabies tracing (Callaway and Luo, 2015) could be used to map the areas that project to either $VGAT^+$ or $VGluT2^+$ neurons in different PAG subdivisions. The results from this approach could be combined and interpreted together with the insights derived from the single-cell RNA-sequencing dataset presented here. This could help identify overlapping patterns between the types of receptors expressed by the starting $VGAT^+$ or $VGluT2^+$ neurons and the neuronal types present in the areas projecting to them.

It would also be interesting to use AAV viruses to sparsely label $VGAT^+$ or $VGluT2^+$ neurons. The transfected whole brains could then be processed with serial two-photon tomography (Amato, Pan, *et al.*, 2016; Tyson, Vélez-Fort, *et al.*, 2022) to assess whether they predominantly establish local connections or long-range projections, and where these projections extend to. This approach could be repeated for subsets of glutamatergic or GABAergic neurons expressing a particular neuropeptide, hopefully revealing whether these define circuit modules with discrete projection patterns.

What is the connectivity between cell types and across subdivisions within the PAG?

An important piece of the puzzle to understand the overall function of the PAG is the connectivity within its submodules. Do GABAergic neurons in the dmPAG synapse onto GABAergic or to glutamatergic neurons of the vlPAG? Do glutamatergic neurons of one subdivision send collateral projections to both their downstream targets to elicit a particular behaviour and to GABAergic neurons of a competing subdivision to silence its potential behavioural output? Identifying the circuit motifs

of PAG microcircuits with cell type-specific approaches will be critical in the field's quest to understand this highly heterogeneous and multifaceted brain area.

What is the mechanism responsible for terminating a behaviour and how does the PAG network return to baseline once the selected behavioural output has been completed?

Does the PAG provide a sustained excitatory drive to maintain a given motor command, or is it more like an on/off signal conveyed to engage and disengage the relevant central pattern generator? In either case, where is the feedback signal computed and how is it transmitted back to the PAG?

For example, in the case of escape behaviour, once the animal has found a shelter and reached safety, who shuts down the PAG and terminates the flight? Is inhibition recruited once the animal reaches the shelter? Where does this inhibition come from? And is it even necessary to feed this information back to the PAG, or is it enough to simply remove the inputs that led the PAG to instigate the behaviour in the first place?

The continued refinement of modern techniques has made it possible to record and perturb the activity of large numbers of neurons in a cell type-specific manner, as well as to map the inputs and outputs of molecularly defined neuronal subpopulations with unprecedented detail. The methodology and the field are now ripe to begin to tackle this type of very exciting questions.

6.6 CONCLUDING REMARKS

Much is known about the involvement of the PAG in behaviours that are critical for the survival of the organism and as diverse as predator avoidance, hunting, analgesia, stress, anxiety, pup grooming, micturition, social vocalisations, and many others. However, our physiological knowledge about how the different circuit modules within the PAG interact with one another to select and implement a behavioural output is still at its infancy. The results presented in this thesis provide a biophysical framework and molecular resource for future studies trying to achieve a mechanistic understanding of how the PAG acts as an integrator, gating the behavioural output that maximises an individual's survival.

The template for this thesis is freely accessible online (Pavón Arocas, 2021).

7 References

Aitken PG, Breese GR, Dudek FF, Edwards F, *et al.* (1995) Preparative methods for brain slices: a discussion, *Journal of Neuroscience Methods*, 59(1), pp. 139–149.

Akopian AN, Chen C-C, Ding Y, Cesare P, *et al.* (2000) A new member of the acid-sensing ion channel family, *NeuroReport*, 11(10), pp. 2217–2222.

Albin RL, Makowiec RL, Hollingsworth Z, Dure LS, *et al.* (1990) Excitatory amino acid binding sites in the periaqueductal gray of the rat, *Neuroscience Letters*, 118(1), pp. 112–115.

Alcami P, Franconville R, Llano I, and Marty A (2012) Measuring the Firing Rate of High-Resistance Neurons with Cell-Attached Recording, *Journal of Neuroscience*, 32(9), pp. 3118–3130.

Allen WE, DeNardo LA, Chen MZ, Liu CD, *et al.* (2017) Thirst-associated preoptic neurons encode an aversive motivational drive, *Science*, 357(6356), pp. 1149–1155.

Amano K, Tanikawa T, Iseki H, Kawabatake H, *et al.* (1978) Single Neuron Analysis of the Human Midbrain Tegmentum, *Stereotactic and Functional Neurosurgery*, 41(1–4), pp. 66–78.

Amato SP, Pan F, Schwartz J, and Ragan TM (2016) Whole Brain Imaging with Serial Two-Photon Tomography, *Frontiers in Neuroanatomy*, 10(MAR), pp. 1–11.

Amezquita RA, Lun ATL, Becht E, Carey VJ, *et al.* (2020) Orchestrating single-cell analysis with Bioconductor, *Nature Methods*, 17(2), pp. 137–145.

Amodeo P, López Méndez B, Guerrini R, Salvadori S, *et al.* (2000) Pain peptides. Solution structure of orphanin FQ2, *FEBS Letters*, 473(2), pp. 157–160.

Andero R (2015) Nociceptin and the nociceptin receptor in learning and memory, *Progress in Neuro-Psychopharmacology and Biological Psychiatry*, 62, pp. 45–50.

Andrews S (2010) FastQC: A Quality Control Tool for High Throughput Sequence Data.

Andrews TS, Kiselev VY, McCarthy D, and Hemberg M (2021) Tutorial: guidelines

for the computational analysis of single-cell RNA sequencing data, *Nature Protocols*, 16(1), pp. 1–9.

Anikeeva P, Andalman AS, Witten I, Warden M, *et al.* (2012) Optetrode: a multichannel readout for optogenetic control in freely moving mice, *Nature Neuroscience*, 15(1), pp. 163–170.

Asp M, Giacomello S, Larsson L, Wu C, *et al.* (2019) A Spatiotemporal Organ-Wide Gene Expression and Cell Atlas of the Developing Human Heart, *Cell*, 179(7), pp. 1647-1660.e19.

Audi EA and Graeff FG (1987) $GABA_A$ receptors in the midbrain central grey mediate the antiaversive action of GABA, *European Journal of Pharmacology*, 135(2), pp. 225–229.

Bacher R and Kendziorski C (2016) Design and computational analysis of single-cell RNA-sequencing experiments, *Genome Biology*, 17(1), p. 63.

Bai L, Mesgarzadeh S, Ramesh KS, Huey EL, *et al.* (2019) Genetic Identification of Vagal Sensory Neurons That Control Feeding, *Cell*, 179(5), pp. 1129-1143.e23.

Bakken TE, Jorstad NL, Hu Q, Lake BB, *et al.* (2021) Comparative cellular analysis of motor cortex in human, marmoset and mouse, *Nature*, 598(7879), pp. 111–119.

Bakken TE, van Velthoven CT, Menon V, Hodge RD, *et al.* (2021) Single-cell and single-nucleus RNA-seq uncovers shared and distinct axes of variation in dorsal LGN neurons in mice, non-human primates, and humans, *eLife*, 10, pp. 1–20.

Bandler R and Carrive P (1988) Integrated defence reaction elicited by excitatory amino acid microinjection in the midbrain periaqueductal grey region of the unrestrained cat, *Brain Research*, 439(1–2), pp. 95–106.

Bandler R and Depaulis A (1991) *The Midbrain Periaqueductal Gray Matter*. Edited by A. Depaulis and R. Bandler. Boston, MA: Springer US.

Baran-Gale J, Chandra T, and Kirschner K (2018) Experimental design for single-cell RNA sequencing, *Briefings in Functional Genomics*, 17(4), pp. 233–239.

Barbaresi P and Manfrini E (1988) Glutamate decarboxylase-immunoreactive neurons and terminals in the periaqueductal gray of the rat, *Neuroscience*, 27(1), pp. 183–191.

Barbour B and Isope P (2000) Combining loose cell-attached stimulation and

recording, *Journal of Neuroscience Methods*, 103(2), pp. 199–208.

Barry PH and Lynch JW (1991) Liquid junction potentials and small cell effects in patch-clamp analysis, *The Journal of Membrane Biology*, 121(2), pp. 101–117.

Becht E, McInnes L, Healy J, Dutertre C-A, *et al.* (2019) Dimensionality reduction for visualizing single-cell data using UMAP, *Nature Biotechnology*, 37(1), pp. 38–44.

Behbehani MM (1995) Functional characteristics of the midbrain periaqueductal gray, *Progress in Neurobiology*, 46(6), pp. 575–605.

Behbehani MM, Jiang M, Chandler SD, and Ennis M (1990) The effect of GABA and its antagonists on midbrain periaqueductal gray neurons in the rat, *Pain*, 40(2), pp. 195–204.

Beitz AJ and Shepard RD (1985) The midbrain periaqueductal gray in the rat. II. A Golgi analysis, *The Journal of Comparative Neurology*, 237(4), pp. 460–475.

Benarroch EE (2012) Periaqueductal gray: An interface for behavioral control, *Neurology*, 78(3), pp. 210–217.

Berg J, Sorensen SA, Ting JT, Miller JA, *et al.* (2021) Human neocortical expansion involves glutamatergic neuron diversification, *Nature*, 598(7879), pp. 151–158.

Bischofberger J, Engel D, Li L, Geiger JRP, *et al.* (2006) Patch-clamp recording from mossy fiber terminals in hippocampal slices, *Nature Protocols*, 1(4), pp. 2075–2081.

Blanton MG, Lo Turco JJ, and Kriegstein AR (1989) Whole cell recording from neurons in slices of reptilian and mammalian cerebral cortex, *Journal of Neuroscience Methods*, 30(3), pp. 203–210.

Blondel VD, Guillaume J-L, Lambiotte R, and Lefebvre E (2008) Fast unfolding of communities in large networks, *Journal of Statistical Mechanics: Theory and Experiment*, 2008(10), p. P10008.

Bochet P, Audinat E, Lambolez B, Crépel F, *et al.* (1994) Subunit composition at the single-cell level explains functional properties of a glutamate-gated channel, *Neuron*, 12(2), pp. 383–388.

Boldog E, Bakken TE, Hodge RD, Novotny M, *et al.* (2018) Transcriptomic and morphophysiological evidence for a specialized human cortical GABAergic cell

type, *Nature Neuroscience*, 21(9), pp. 1185–1195.

Borgius L, Restrepo CE, Leao RN, Saleh N, *et al.* (2010) A transgenic mouse line for molecular genetic analysis of excitatory glutamatergic neurons, *Molecular and Cellular Neuroscience*, 45(3), pp. 245–257.

Braga AA, Aguiar DC, and Guimarães FS (2009) NOC-9, a selective nitric oxide donor, induces flight reactions in the dorsolateral periaqueductal gray of rats by activating soluble guanylate cyclase, *Neuroscience Letters*, 459(2), pp. 79–83.

Brahma B, Forman RE, Stewart EE, Nicholson C, *et al.* (2000) Ascorbate inhibits edema in brain slices, *Journal of Neurochemistry*, 74(3), pp. 1263–1270.

Branco T and Redgrave P (2020) The Neural Basis of Escape Behavior in Vertebrates, *Annual Review of Neuroscience*, 43(1), pp. 417–439.

Brandão ML, De Aguiar JC, and Graeff FG (1982) GABA mediation of the anti-aversive action of minor tranquilizers, *Pharmacology Biochemistry and Behavior*, 16(3), pp. 397–402.

Brandão ML, Anseloni VZ, Pandóssio JE, De Araújo JE, *et al.* (1999) Neurochemical mechanisms of the defensive behavior in the dorsal midbrain, *Neuroscience & Biobehavioral Reviews*, 23(6), pp. 863–875.

Brandão ML and Lovick TA (2019) Role of the dorsal periaqueductal gray in posttraumatic stress disorder: mediation by dopamine and neurokinin, *Translational Psychiatry*, 9(1), p. 232.

Brown JP, Dissanayake VUK, Briggs AR, Milic MR, *et al.* (1998) Isolation of the [^{3}H]Gabapentin-Binding Protein / $\alpha_2\delta$ Ca^{2+} Channel Subunit from Porcine Brain: Development of a Radioligand Binding Assay for $\alpha_2\delta$ Subunits Using [^{3}H]Leucine, *Analytical Biochemistry*, 255(2), pp. 236–243.

Buskila Y, Breen PP, Tapson J, van Schaik A, *et al.* (2015) Extending the viability of acute brain slices, *Scientific Reports*, 4(1), p. 5309.

Cadwell CR, Palasantza A, Jiang X, Berens P, *et al.* (2016) Electrophysiological, transcriptomic and morphologic profiling of single neurons using Patch-seq, *Nature Biotechnology*, 34(2), pp. 199–203.

Cadwell CR, Scala F, Li S, Livrizzi G, *et al.* (2017) Multimodal profiling of single-cell morphology, electrophysiology, and gene expression using Patch-seq, *Nature*

Protocols, 12(12), pp. 2531–2553.

Caggiano V, Leiras R, Goñi-Erro H, Masini D, *et al.* (2018) Midbrain circuits that set locomotor speed and gait selection, *Nature*, 553(7689), pp. 455–460.

Callaway EM, Dong H-W, Ecker JR, Hawrylycz MJ, *et al.* (2021) A multimodal cell census and atlas of the mammalian primary motor cortex, *Nature*, 598(7879), pp. 86–102.

Callaway EM and Luo L (2015) Monosynaptic Circuit Tracing with Glycoprotein-Deleted Rabies Viruses, *Journal of Neuroscience*, 35(24), pp. 8979–8985.

Cameron AA, Khan IA, Westlund KN, Cliffer KD, *et al.* (1995) The efferent projections of the periaqueductal gray in the rat: A Phaseolus vulgaris-leucoagglutinin study. I. Ascending projections, *The Journal of Comparative Neurology*, 351(4), pp. 568–584.

Cameron AA, Khan IA, Westlund KN, and Willis WD (1995) The efferent projections of the periaqueductal gray in the rat: A Phaseolus vulgaris-leucoagglutinin study. II. Descending projections, *The Journal of Comparative Neurology*, 351(4), pp. 585–601.

Campagnola L, Seeman SC, Chartrand T, Kim L, *et al.* (2021) Local Connectivity and Synaptic Dynamics in Mouse and Human Neocortex, *bioRxiv*, p. 2021.03.31.437553.

Canteras NS and Swanson LW (1992) The dorsal premammillary nucleus: an unusual component of the mammillary body, *Proceedings of the National Academy of Sciences*, 89(21), pp. 10089–10093.

Cao C, Lemaire LA, Wang W, Yoon PH, *et al.* (2019) Comprehensive single-cell transcriptome lineages of a proto-vertebrate, *Nature*, 571(7765), pp. 349–354.

Cao J, Packer JS, Ramani V, Cusanovich DA, *et al.* (2017) Comprehensive single-cell transcriptional profiling of a multicellular organism, *Science*, 357(6352), pp. 661–667.

Cao J, Spielmann M, Qiu X, Huang X, *et al.* (2019) The single-cell transcriptional landscape of mammalian organogenesis, *Nature*, 566(7745), pp. 496–502.

Carlson GC and Coulter DA (2008) In vitro functional imaging in brain slices using fast voltage-sensitive dye imaging combined with whole-cell patch recording,

Nature Protocols, 3(2), pp. 249–255.

Carrive P (1993) The periaqueductal gray and defensive behavior: Functional representation and neuronal organization, *Behavioural Brain Research*, 58(1–2), pp. 27–47.

Carter RA, Bihannic L, Rosencrance C, Hadley JL, *et al.* (2018) A Single-Cell Transcriptional Atlas of the Developing Murine Cerebellum, *Current Biology*, 28(18), pp. 2910-2920.e2.

Cauli B, Audinat E, Lambolez B, Angulo MC, *et al.* (1997) Molecular and Physiological Diversity of Cortical Nonpyramidal Cells, *The Journal of Neuroscience*, 17(10), pp. 3894–3906.

Cembrowski MS, Phillips MG, DiLisio SF, Shields BC, *et al.* (2018) Dissociable Structural and Functional Hippocampal Outputs via Distinct Subiculum Cell Classes, *Cell*, 173(5), pp. 1280-1292.e18.

Chen J, Li L, Chen S-R, Chen H, *et al.* (2018) The α2δ-1-NMDA Receptor Complex Is Critically Involved in Neuropathic Pain Development and Gabapentin Therapeutic Actions, *Cell Reports*, 22(9), pp. 2307–2321.

Chen R, Wu X, Jiang L, and Zhang Y (2017) Single-Cell RNA-Seq Reveals Hypothalamic Cell Diversity, *Cell Reports*, 18(13), pp. 3227–3241.

Chen X, Teichmann SA, and Meyer KB (2018) From Tissues to Cell Types and Back: Single-Cell Gene Expression Analysis of Tissue Architecture, *Annual Review of Biomedical Data Science*, 1(1), pp. 29–51.

Chiang LW (1998) Detection of gene expression in single neurons by patch-clamp and single-cell reverse transcriptase polymerase chain reaction, *Journal of Chromatography A*, 806(1), pp. 209–218.

Chiou L. and Chou H. (2000) Characterization of synaptic transmission in the ventrolateral periaqueductal gray of rat brain slices, *Neuroscience*, 100(4), pp. 829–834.

Chon U, Vanselow DJ, Cheng KC, and Kim Y (2019) Enhanced and unified anatomical labeling for a common mouse brain atlas, *Nature Communications*, 10(1), p. 5067.

Chou X, Wang X, Zhang Z, Shen L, *et al.* (2018) Inhibitory gain modulation of

defense behaviors by zona incerta, *Nature Communications*, 9(1), p. 1151.

Claudi F, Petrucco L, Tyson A, Branco T, *et al.* (2020) BrainGlobe Atlas API: a common interface for neuroanatomical atlases, *Journal of Open Source Software*, 5(54), p. 2668.

Claudi F, Tyson AL, Petrucco L, Margrie TW, *et al.* (2021) Visualizing anatomically registered data with brainrender, *eLife*, 10, pp. 1–16.

Cole RL, Lechner SM, Williams ME, Prodanovich P, *et al.* (2005) Differential distribution of voltage-gated calcium channel alpha-2 delta ($\alpha_2\delta$) subunit mRNA-containing cells in the rat central nervous system and the dorsal root ganglia, *The Journal of Comparative Neurology*, 491(3), pp. 246–269.

Csardi G and Nepusz T (2006) The igraph software package for complex network research, *InterJournal, Complex Systems*, 1965(5), p. 1/9.

Cuevas-Diaz Duran R, Wei H, and Wu JQ (2017) Single-cell RNA-sequencing of the brain, *Clinical and Translational Medicine*, 6(1), p. 20.

Deng H, Xiao X, and Wang Z (2016) Periaqueductal Gray Neuronal Activities Underlie Different Aspects of Defensive Behaviors, *Journal of Neuroscience*, 36(29), pp. 7580–7588.

Ding J, Adiconis X, Simmons SK, Kowalczyk MS, *et al.* (2020) Systematic comparison of single-cell and single-nucleus RNA-sequencing methods, *Nature Biotechnology*, 38(6), pp. 737–746.

Dissanayake VUK, Gee NS, Brown JP, and Woodruff GN (1997) Spermine modulation of specific [^{3}H]-gabapentin binding to the detergent-solubilized porcine cerebral cortex $\alpha_2\delta$ calcium channel subunit, *British Journal of Pharmacology*, 120(5), pp. 833–840.

Dobin A, Davis CA, Schlesinger F, Drenkow J, *et al.* (2013) STAR: ultrafast universal RNA-seq aligner, *Bioinformatics*, 29(1), pp. 15–21.

Dolphin AC (2012) Calcium channel $\alpha_2\delta$ subunits in epilepsy and as targets for antiepileptic drugs, in Rogawski, M.A., Delgado-Escueta, A. V, Noebels, J.L., Avoli, M., et al. (eds) *Jasper's Basic Mechanisms of the Epilepsies*. 4th editio. Oxford University Press.

Dolphin AC and Lee A (2020) Presynaptic calcium channels: specialized control of

synaptic neurotransmitter release, *Nature Reviews Neuroscience*, 21(4), pp. 213–229.

Donier E, Rugiero F, Jacob C, and Wood JN (2008) Regulation of ASIC activity by ASIC4 - new insights into ASIC channel function revealed by a yeast two-hybrid assay, *European Journal of Neuroscience*, 28(1), pp. 74–86.

Dorst MC, Tokarska A, Zhou M, Lee K, *et al.* (2020) Polysynaptic inhibition between striatal cholinergic interneurons shapes their network activity patterns in a dopamine-dependent manner, *Nature Communications*, 11(1), p. 5113.

Dougalis AG, Matthews GAC, Liss B, and Ungless MA (2017) Ionic currents influencing spontaneous firing and pacemaker frequency in dopamine neurons of the ventrolateral periaqueductal gray and dorsal raphe nucleus (vlPAG/DRN): A voltage-clamp and computational modelling study, *Journal of Computational Neuroscience*, 42(3), pp. 275–305.

Edwards FA, Konnerth A, Sakmann B, and Takahashi T (1989) A thin slice preparation for patch clamp recordings from neurones of the mammalian central nervous system, *Pflügers Archiv European Journal of Physiology*, 414(5), pp. 600–612.

Eguchi K, Velicky P, Hollergschwandtner E, Itakura M, *et al.* (2020) Advantages of Acute Brain Slices Prepared at Physiological Temperature in the Characterization of Synaptic Functions, *Frontiers in Cellular Neuroscience*, 14(March), pp. 35–37.

Elmslie KS and Yoshikami D (1985) Effects of kynurenate on root potentials evoked by synaptic activity and amino acids in the frog spinal cord, *Brain Research*, 330(2), pp. 265–272.

Estrada VB, Matsubara NK, Gomes MV, Corrêa FMA, *et al.* (2016) Noradrenaline microinjected into the dorsal periaqueductal gray matter causes anxiolytic-like effects in rats tested in the elevated T-maze, *Life Sciences*, 152, pp. 94–98.

Evans DA, Stempel AV, Vale R, Ruehle S, *et al.* (2018) A synaptic threshold mechanism for computing escape decisions, *Nature*, 558(7711), pp. 590–594.

Falkner AL, Wei D, Song A, Watsek LW, *et al.* (2020) Hierarchical Representations of Aggression in a Hypothalamic-Midbrain Circuit, *Neuron*, 106(4), pp. 637-648.e6.

Fanselow MS, Decola JP, De Oca BM, and Landeira-Fernandez J (1995) Ventral and dorsolateral regions of the midbrain periaqueductal gray (PAG) control different stages of defensive behavior: Dorsolateral PAG lesions enhance the defensive freezing produced by massed and immediate shock, *Aggressive Behavior*, 21(1), pp. 63–77.

Farnham MMJ, Lung MSY, Tallapragada VJ, and Pilowsky PM (2012) PACAP causes PAC_1/$VPAC_2$ receptor mediated hypertension and sympathoexcitation in normal and hypertensive rats, *American Journal of Physiology-Heart and Circulatory Physiology*, 303(7), pp. H910–H917.

Faull OK, Subramanian HH, Ezra M, and Pattinson KTS (2019) The midbrain periaqueductal gray as an integrative and interoceptive neural structure for breathing, *Neuroscience & Biobehavioral Reviews*, 98(August 2018), pp. 135–144.

Fenwick EM, Marty A, and Neher E (1982) A patch-clamp study of bovine chromaffin cells and of their sensitivity to acetylcholine, *The Journal of Physiology*, 331(1), pp. 577–597.

Ferragud A, Velazquez-Sanchez C, Minnig MA, Sabino V, *et al.* (2021) Pituitary adenylate cyclase-activating polypeptide (PACAP) modulates dependence-induced alcohol drinking and anxiety-like behavior in male rats, *Neuropsychopharmacology*, 46(3), pp. 509–518.

Fincher CT, Wurtzel O, de Hoog T, Kravarik KM, *et al.* (2018) Cell type transcriptome atlas for the planarian Schmidtea mediterranea, *Science*, 360(6391).

Floyd NS, Price JL, Ferry AT, Keay KA, *et al.* (2000) Orbitomedial prefrontal cortical projections to distinct longitudinal columns of the periaqueductal gray in the rat, *The Journal of Comparative Neurology*, 422(4), pp. 556–578.

Földy C, Darmanis S, Aoto J, Malenka RC, *et al.* (2016) Single-cell RNAseq reveals cell adhesion molecule profiles in electrophysiologically defined neurons, *Proceedings of the National Academy of Sciences*, 113(35), pp. E5222–E5231.

De Franceschi G, Vivattanasarn T, Saleem AB, and Solomon SG (2016) Vision Guides Selection of Freeze or Flight Defense Strategies in Mice, *Current Biology*, 26(16), pp. 2150–2154.

Franklin K and Paxinos G (2008) *The Mouse Brain in Stereotaxic Coordinates*. 3rd edn.

Academic Press.

Franklin TB (2019) Recent Advancements Surrounding the Role of the Periaqueductal Gray in Predators and Prey, *Frontiers in Behavioral Neuroscience*, 13(May), pp. 1–6.

Franklin TB, Silva BA, Perova Z, Marrone L, *et al.* (2017) Prefrontal cortical control of a brainstem social behavior circuit, *Nature Neuroscience*, 20(2), pp. 260–270.

Fratzl A, Koltchev AM, Vissers N, Tan YL, *et al.* (2021) Flexible inhibitory control of visually evoked defensive behavior by the ventral lateral geniculate nucleus, *Neuron*, 109(23), pp. 3810-3822.e9.

Fuzik J, Zeisel A, Máté Z, Calvigioni D, *et al.* (2016) Integration of electrophysiological recordings with single-cell RNA-seq data identifies neuronal subtypes, *Nature Biotechnology*, 34(2), pp. 175–183.

Gao Z-R, Chen W-Z, Liu M-Z, Chen X-J, *et al.* (2019) Tac1-Expressing Neurons in the Periaqueductal Gray Facilitate the Itch-Scratching Cycle via Descending Regulation, *Neuron*, 101(1), pp. 45-59.e9.

Gavioli EC, Holanda VAD, Calo G, and Ruzza C (2021) Nociceptin/orphanin FQ receptor system blockade as an innovative strategy for increasing resilience to stress, *Peptides*, 141(February), p. 170548.

Gibb AJ and Edwards FA (1994) Patch clamp recording from cells in sliced tissues, in Ogden, D.C. (ed.) *Microelectrode techniques, The Plymouth workshop handbook*. 2nd edn. Cambridge: The Company of Biologists Limited, pp. 255–274.

Gjorgjieva J, Drion G, and Marder E (2016) Computational implications of biophysical diversity and multiple timescales in neurons and synapses for circuit performance, *Current Opinion in Neurobiology*, 37(1), pp. 44–52.

Gouwens NW, Sorensen SA, Baftizadeh F, Budzillo A, *et al.* (2020) Integrated Morphoelectric and Transcriptomic Classification of Cortical GABAergic Cells, *Cell*, 183(4), pp. 935-953.e19.

Gouwens NW, Sorensen SA, Berg J, Lee C, *et al.* (2019) Classification of electrophysiological and morphological neuron types in the mouse visual cortex, *Nature Neuroscience*, 22(7), pp. 1182–1195.

Graeff FG (2004) Serotonin, the periaqueductal gray and panic, *Neuroscience &*

Biobehavioral Reviews, 28(3), pp. 239–259.

Granger AJ, Wallace ML, and Sabatini BL (2017) Multi-transmitter neurons in the mammalian central nervous system, *Current Opinion in Neurobiology*, 45, pp. 85–91.

Guimarães FS, Beijamini V, Moreira FA, Aguiar DC, *et al.* (2005) Role of nitric oxide in brain regions related to defensive reactions, *Neuroscience & Biobehavioral Reviews*, 29(8), pp. 1313–1322.

Halladay LR and Blair HT (2015) Distinct ensembles of medial prefrontal cortex neurons are activated by threatening stimuli that elicit excitation vs. inhibition of movement, *Journal of Neurophysiology*, 114(2), pp. 793–807.

Hamill OP, Marty A, Neher E, Sakmann B, *et al.* (1981) Improved patch-clamp techniques for high-resolution current recording from cells and cell-free membrane patches, *Pflügers Archiv - European Journal of Physiology*, 391(2), pp. 85–100.

Han X, Zhou Z, Fei L, Sun H, *et al.* (2020) Construction of a human cell landscape at single-cell level, *Nature*, 581(7808), pp. 303–309.

Han Y, Kebschull JM, Campbell RAA, Cowan D, *et al.* (2018) The logic of single-cell projections from visual cortex, *Nature*, 556(7699), pp. 51–56.

Hanemaaijer NAK, Popovic MA, Wilders X, Grasman S, *et al.* (2020) Ca^{2+} entry through Na_V channels generates submillisecond axonal Ca^{2+} signaling, *eLife*, 9, pp. 1–75.

Hansen JY, Markello RD, Tuominen L, Nørgaard M, *et al.* (2021) Correspondence between gene expression and neurotransmitter receptor and transporter density in the human brain, *bioRxiv*, p. 2021.11.30.469876.

Hao S, Yang H, Wang X, He Y, *et al.* (2019) The Lateral Hypothalamic and BNST GABAergic Projections to the Anterior Ventrolateral Periaqueductal Gray Regulate Feeding, *Cell Reports*, 28(3), pp. 616-624.e5.

Haque A, Engel J, Teichmann SA, and Lönnberg T (2017) A practical guide to single-cell RNA-sequencing for biomedical research and clinical applications, *Genome Medicine*, 9(1), p. 75.

Häusser M and Clark BA (1997) Tonic Synaptic Inhibition Modulates Neuronal

Output Pattern and Spatiotemporal Synaptic Integration, *Neuron*, 19(3), pp. 665–678.

Hicks SC, Townes FW, Teng M, and Irizarry RA (2018) Missing data and technical variability in single-cell RNA-sequencing experiments, *Biostatistics*, 19(4), pp. 562–578.

Hirono M and Obata K (2006) α-Adrenoceptive Dual Modulation of Inhibitory GABAergic Inputs to Purkinje Cells in the Mouse Cerebellum, *Journal of Neurophysiology*, 95(2), pp. 700–708.

Horn R and Marty A (1988) Muscarinic activation of ionic currents measured by a new whole-cell recording method, *Journal of General Physiology*, 92(2), pp. 145–159.

Hrvatin S, Hochbaum DR, Nagy MA, Cicconet M, *et al.* (2018) Single-cell analysis of experience-dependent transcriptomic states in the mouse visual cortex, *Nature Neuroscience*, 21(1), pp. 120–129.

Huang KW, Ochandarena NE, Philson AC, Hyun M, *et al.* (2019) Molecular and anatomical organization of the dorsal raphe nucleus, *eLife*, 8, pp. 1–34.

Huang S and Uusisaari MY (2013) Physiological temperature during brain slicing enhances the quality of acute slice preparations, *Frontiers in Cellular Neuroscience*, 7(APR), pp. 1–8.

Huber W, Carey VJ, Gentleman R, Anders S, *et al.* (2015) Orchestrating high-throughput genomic analysis with Bioconductor, *Nature Methods*, 12(2), pp. 115–121.

Ilicic T, Kim JK, Kolodziejczyk AA, Bagger FO, *et al.* (2016) Classification of low quality cells from single-cell RNA-seq data, *Genome Biology*, 17(1), p. 29.

Islam S, Zeisel A, Joost S, La Manno G, *et al.* (2014) Quantitative single-cell RNA-seq with unique molecular identifiers, *Nature Methods*, 11(2), pp. 163–166.

Jeong H-J, Lam K, Mitchell VA, and Vaughan CW (2013) Serotonergic modulation of neuronal activity in rat midbrain periaqueductal gray, *Journal of Neurophysiology*, 109(11), pp. 2712–2719.

Jha PK, Valekunja UK, Ray S, Nollet M, *et al.* (2020) Single-cell transcriptomics and cell-specific proteomics reveals molecular signatures of sleep, *bioRxiv*, p.

2020.12.18.423331.

Jiang M, Chandler SD, Ennis M, Shipley MT, *et al.* (1992) Actions of epinephrine on neurons in the rat midbrain periaqueductal gray maintained in vitro, *Brain Research Bulletin*, 29(6), pp. 871–877.

Jobson DD, Hase Y, Clarkson AN, and Kalaria RN (2021) The role of the medial prefrontal cortex in cognition, ageing and dementia, *Brain Communications*, 3(3).

Jun JJ, Steinmetz NA, Siegle JH, Denman DJ, *et al.* (2017) Fully integrated silicon probes for high-density recording of neural activity, *Nature*, 551(7679), pp. 232–236.

Kalmbach BE, Hodge RD, Jorstad NL, Owen S, *et al.* (2021) Signature morpho-electric, transcriptomic, and dendritic properties of human layer 5 neocortical pyramidal neurons, *Neuron*, 109(18), pp. 2914-2927.e5.

Keay KA and Bandler R (2001) Parallel circuits mediating distinct emotional coping reactions to different types of stress, *Neuroscience & Biobehavioral Reviews*, 25(7–8), pp. 669–678.

Keay KA and Bandler R (2015) Periaqueductal Gray, in Paxinos, G. (ed.) *The Rat Nervous System*. 4th Editio. Elsevier, pp. 207–221.

Keay KA, Feil K, Gordon BD, Herbert H, *et al.* (1997) Spinal afferents to functionally distinct periaqueductal gray columns in the rat: An anterograde and retrograde tracing study, *The Journal of Comparative Neurology*, 385(2), pp. 207–229.

Khaliq ZM and Bean BP (2010) Pacemaking in Dopaminergic Ventral Tegmental Area Neurons: Depolarizing Drive from Background and Voltage-Dependent Sodium Conductances, *Journal of Neuroscience*, 30(21), pp. 7401–7413.

Kim D-W, Yao Z, Graybuck LT, Kim TK, *et al.* (2019) Multimodal Analysis of Cell Types in a Hypothalamic Node Controlling Social Behavior, *Cell*, 179(3), pp. 713-728.e17.

Kim S, Wallace ML, El-Rifai M, Knudsen AR, *et al.* (2021) Biophysical demonstration of co-packaging of glutamate and GABA in individual synaptic vesicles in the central nervous system, *bioRxiv* [Preprint].

Kiselev VY, Kirschner K, Schaub MT, Andrews T, *et al.* (2017) SC3: consensus clustering of single-cell RNA-seq data, *Nature Methods*, 14(5), pp. 483–486.

Klein AM, Mazutis L, Akartuna I, Tallapragada N, *et al.* (2015) Droplet Barcoding for Single-Cell Transcriptomics Applied to Embryonic Stem Cells, *Cell*, 161(5), pp. 1187–1201.

Kohl J, Babayan BM, Rubinstein ND, Autry AE, *et al.* (2018) Functional circuit architecture underlying parental behaviour, *Nature*, 556(7701), pp. 326–331.

Kolodziejczyk AA, Kim JK, Svensson V, Marioni JC, *et al.* (2015) The Technology and Biology of Single-Cell RNA Sequencing, *Molecular Cell*, 58(4), pp. 610–620.

Kondo S and Marty A (1998) Synaptic currents at individual connections among stellate cells in rat cerebellar slices, *The Journal of Physiology*, 509(1), pp. 221–232.

Krashes MJ, Shah BP, Madara JC, Olson DP, *et al.* (2014) An excitatory paraventricular nucleus to AgRP neuron circuit that drives hunger, *Nature*, 507(7491), pp. 238–242.

Kweon H-J and Suh B-C (2013) Acid-sensing ion channels (ASICs): therapeutic targets for neurological diseases and their regulation, *BMB Reports*, 46(6), pp. 295–304.

Kyrozis A and Reichling DB (1995) Perforated-patch recording with gramicidin avoids artifactual changes in intracellular chloride concentration, *Journal of Neuroscience Methods*, 57(1), pp. 27–35.

L. Lun AT, Bach K, and Marioni JC (2016) Pooling across cells to normalize single-cell RNA sequencing data with many zero counts, *Genome Biology*, 17(1), p. 75.

La-Vu M, Sethi E, Maesta-Pereira S, Schuette PJ, *et al.* (2022) A genetically-defined population in the lateral and ventrolateral periaqueductal gray selectively promotes flight to safety, *bioRxiv*, p. 2022.01.19.476981.

Lafzi A, Moutinho C, Picelli S, and Heyn H (2018) Tutorial: guidelines for the experimental design of single-cell RNA sequencing studies, *Nature Protocols*, 13(12), pp. 2742–2757.

Lambolez B, Audinat E, Bochet P, Crépel F, *et al.* (1992) AMPA receptor subunits expressed by single purkinje cells, *Neuron*, 9(2), pp. 247–258.

Law CW, Chen Y, Shi W, and Smyth GK (2014) voom: precision weights unlock linear model analysis tools for RNA-seq read counts, *Genome Biology*, 15(2), p. R29.

Lee G and Gammie SC (2010) $GABA_A$ receptor signaling in caudal periaqueductal gray regulates maternal aggression and maternal care in mice, *Behavioural Brain Research*, 213(2), pp. 230–237.

Lefler Y, Campagner D, and Branco T (2020) The role of the periaqueductal gray in escape behavior, *Current Opinion in Neurobiology*, 60, pp. 115–121.

Lei R, Ye K, Gu Z, and Sun X (2015) Diminishing returns in next-generation sequencing (NGS) transcriptome data, *Gene*, 557(1), pp. 82–87.

Li H, Janssens J, De Waegeneer M, Saroja Kolluru S, *et al.* (2021) Fly Cell Atlas: a single-cell transcriptomic atlas of the adult fruit fly, *bioRxiv*, p. 2021.07.04.451050.

Li Y, Zeng J, Zhang J, Yue C, *et al.* (2018) Hypothalamic Circuits for Predation and Evasion, *Neuron*, 97(4), pp. 911-924.e5.

Li Z, Taylor CP, Weber M, Piechan J, *et al.* (2011) Pregabalin is a potent and selective ligand for $\alpha_2\delta$-1 and $\alpha_2\delta$-2 calcium channel subunits, *European Journal of Pharmacology*, 667(1–3), pp. 80–90.

Linnman C, Moulton EA, Barmettler G, Becerra L, *et al.* (2012) Neuroimaging of the periaqueductal gray: State of the field, *NeuroImage*, 60(1), pp. 505–522.

Lipton P, Aitken PG, Dudek FE, Eskessen K, *et al.* (1995) Making the best of brain slices: comparing preparative methods, *Journal of Neuroscience Methods*, 59(1), pp. 151–156.

Llufrio EM, Wang L, Naser FJ, and Patti GJ (2018) Sorting cells alters their redox state and cellular metabolome, *Redox Biology*, 16(February), pp. 381–387.

Lovick TA and Stezhka V V. (1999) Neurones in the dorsolateral periaqueductal grey matter in coronal slices of rat midbrain: electrophysiological and morphological characteristics, *Experimental Brain Research*, 124(1), pp. 53–58.

Luecken MD and Theis FJ (2019) Current best practices in single-cell RNA-seq analysis: a tutorial, *Molecular Systems Biology*, 15(6).

Lun ATL, McCarthy DJ, and Marioni JC (2016) A step-by-step workflow for low-level analysis of single-cell RNA-seq data with Bioconductor, *F1000Research*, 5(2122), p. 2122.

Luppi P-H, Aston-Jones G, Akaoka H, Chouvet G, *et al.* (1995) Afferent projections

to the rat locus coeruleus demonstrated by retrograde and anterograde tracing with cholera-toxin B subunit and Phaseolus vulgaris leucoagglutinin, *Neuroscience*, 65(1), pp. 119–160.

van der Maaten L and Hinton G (2008) Visualizing Data using t-SNE, *Journal of machine learning research* [Preprint].

MacGregor DG, Chesler M, and Rice ME (2001) HEPES prevents edema in rat brain slices, *Neuroscience Letters*, 303(3), pp. 141–144.

Macosko EZ, Basu A, Satija R, Nemesh J, *et al.* (2015) Highly Parallel Genome-wide Expression Profiling of Individual Cells Using Nanoliter Droplets, *Cell*, 161(5), pp. 1202–1214.

Madry C, Kyrargyri V, Arancibia-Cárcamo IL, Jolivet R, *et al.* (2018) Microglial Ramification, Surveillance, and Interleukin-1β Release Are Regulated by the Two-Pore Domain K^+ Channel THIK-1, *Neuron*, 97(2), pp. 299-312.e6.

Mandelbaum G, Taranda J, Haynes TM, Hochbaum DR, *et al.* (2019) Distinct Cortical-Thalamic-Striatal Circuits through the Parafascicular Nucleus, *Neuron*, 102(3), pp. 636-652.e7.

La Manno G, Gyllborg D, Codeluppi S, Nishimura K, *et al.* (2016) Molecular Diversity of Midbrain Development in Mouse, Human, and Stem Cells, *Cell*, 167(2), pp. 566-580.e19.

Mantyh PW (1982) The midbrain periaqueductal gray in the rat, cat, and monkey: A Nissl, Weil, and Golgi analysis, *The Journal of Comparative Neurology*, 204(4), pp. 349–363.

Martin WJ, Malmberg AB, and Basbaum AI (1998) Pain: Nocistatin spells relief, *Current Biology*, 8(15), pp. R525–R527.

Mason MJ, Simpson AK, Mahaut-Smith MP, and Robinson HPC (2005) The Interpretation of Current-Clamp Recordings in the Cell-Attached Patch-Clamp Configuration, *Biophysical Journal*, 88(1), pp. 739–750.

McCarthy DJ, Campbell KR, Lun ATL, and Wills QF (2017) Scater: pre-processing, quality control, normalization and visualization of single-cell RNA-seq data in R, *Bioinformatics*, 33(8), p. btw777.

McCauley JP, Petroccione MA, D'Brant LY, Todd GC, *et al.* (2020) Circadian

Modulation of Neurons and Astrocytes Controls Synaptic Plasticity in Hippocampal Area CA1, *Cell Reports*, 33(2), p. 108255.

McInnes L, Healy J, and Melville J (2018) UMAP: Uniform Manifold Approximation and Projection for Dimension Reduction, *arXiv* [Preprint].

Mereu E, Lafzi A, Moutinho C, Ziegenhain C, *et al.* (2020) Benchmarking single-cell RNA-sequencing protocols for cell atlas projects, *Nature Biotechnology*, 38(6), pp. 747–755.

Messanvi F, Eggens-Meijer E, Roozendaal B, and van der Want JJ (2013) A discrete dopaminergic projection from the incertohypothalamic A13 cell group to the dorsolateral periaqueductal gray in rat, *Frontiers in Neuroanatomy*, 7(December), pp. 1–14.

Mickelsen LE, Bolisetty M, Chimileski BR, Fujita A, *et al.* (2019) Single-cell transcriptomic analysis of the lateral hypothalamic area reveals molecularly distinct populations of inhibitory and excitatory neurons, *Nature Neuroscience*, 22(4), pp. 642–656.

Miesenböck G (2011) Optogenetic Control of Cells and Circuits, *Annual Review of Cell and Developmental Biology*, 27(1), pp. 731–758.

Missale C, Nash SR, Robinson SW, Jaber M, *et al.* (1998) Dopamine receptors: from structure to function., *Physiological reviews*, 78(1), pp. 189–225.

Missler M and Südhof TC (1998) Neurexophilins Form a Conserved Family of Neuropeptide-Like Glycoproteins, *The Journal of Neuroscience*, 18(10), pp. 3630–3638.

Mlinar B, Montalbano A, Piszczek L, Gross C, *et al.* (2016) Firing properties of genetically identified dorsal raphe serotonergic neurons in brain slices, *Frontiers in Cellular Neuroscience*, 10(AUG), pp. 1–17.

Mobbs D, Petrovic P, Marchant JL, Hassabis D, *et al.* (2007) When Fear Is Near: Threat Imminence Elicits Prefrontal-Periaqueductal Gray Shifts in Humans, *Science*, 317(5841), pp. 1079–1083.

Mobbs D, Trimmer PC, Blumstein DT, and Dayan P (2018) Foraging for foundations in decision neuroscience: insights from ethology, *Nature Reviews Neuroscience*, 19(7), pp. 419–427.

Moffitt JR, Bambah-Mukku D, Eichhorn SW, Vaughn E, *et al.* (2018) Molecular, spatial, and functional single-cell profiling of the hypothalamic preoptic region, *Science*, 362(6416), p. eaau5324.

de Molina AF and Hunsperger RW (1962) Organization of the subcortical system governing defence and flight reactions in the cat, *The Journal of Physiology*, 160(2), pp. 200–213.

Molinoff PB (1984) α- and β-Adrenergic Receptor Subtypes. Properties, Distribution and Regulation, *Drugs*, 28(Supplement 2), pp. 1–15.

Moyer JR and Brown TH (1998) Methods for whole-cell recording from visually preselected neurons of perirhinal cortex in brain slices from young and aging rats, *Journal of Neuroscience Methods*, 86(1), pp. 35–54.

Muñoz-Manchado AB, Bengtsson Gonzales C, Zeisel A, Munguba H, *et al.* (2018) Diversity of Interneurons in the Dorsal Striatum Revealed by Single-Cell RNA Sequencing and PatchSeq, *Cell Reports*, 24(8), pp. 2179-2190.e7.

Muthuraju S, Talbot T, and Brandão ML (2016) Dopamine D_2 receptors regulate unconditioned fear in deep layers of the superior colliculus and dorsal periaqueductal gray, *Behavioural Brain Research*, 297, pp. 116–123.

Nashold BS, Wilson WP, and Slaughter DG (1969) Sensations Evoked by Stimulation in the Midbrain of Man, *Journal of Neurosurgery*, 30(1), pp. 14–24.

Neher E (1992) Correction for liquid junction potentials in patch clamp experiments, *Methods in enzymology*, 207(8), pp. 123–31.

Neher E and Sakmann B (1976) Single-channel currents recorded from membrane of denervated frog muscle fibres, *Nature*, 260(5554), pp. 799–802.

Newland CF and Cull-Candy SG (1992) On the mechanism of action of picrotoxin on GABA receptor channels in dissociated sympathetic neurones of the rat., *The Journal of Physiology*, 447(1), pp. 191–213.

Norimoto H, Fenk LA, Li H-H, Tosches MA, *et al.* (2020) A claustrum in reptiles and its role in slow-wave sleep, *Nature*, 578(7795), pp. 413–418.

Ofengeim D, Giagtzoglou N, Huh D, Zou C, *et al.* (2017) Single-Cell RNA Sequencing: Unraveling the Brain One Cell at a Time, *Trends in Molecular Medicine*, 23(6), pp. 563–576.

Ogawa S, Kow L-M, and Pfaff DW (1992) Effects of lordosis-relevant neuropeptides on midbrain periaqueductal gray neuronal activity in vitro, *Peptides*, 13(5), pp. 965–975.

Ogawa S, Kow L-M, and Pfaff DW (1994) In vitro electrophysiological characterization of midbrain periaqueductal gray neurons in female rats: responses to GABA- and Met-enkephalin-related agents, *Brain Research*, 666(2), pp. 239–249.

Okuda–Ashitaka E and Ito S (2000) Nocistatin: a novel neuropeptide encoded by the gene for the nociceptin/orphanin FQ precursor, *Peptides*, 21(7), pp. 1101–1109.

Onstott D, Mayer B, and Beitz AJ (1993) Nitric oxide synthase immunoreactive neurons anatomically define a longitudinal dorsolateral column within the midbrain periaqueductal gray of the rat: analysis using laser confocal microscopy, *Brain Research*, 610(2), pp. 317–324.

Pavón Arocas O (2021) A Thesis Template in Word (1.0.0). Zenodo.

Pavón Arocas O and Branco T (2022) Preparation of acute midbrain slices containing the superior colliculus and periaqueductal Gray for patch-clamp recordings, *PLOS ONE*, 17(8), p. e0271832.

Pavón Arocas O, Olesen SF, and Branco T (2021) Visually guided aspiration of fluorescently labelled single neurons from acute midbrain slices followed by Smart-seq2, *protocols.io* [Preprint].

Perkins KL (2006) Cell-attached voltage-clamp and current-clamp recording and stimulation techniques in brain slices, *Journal of Neuroscience Methods*, 154(1–2), pp. 1–18.

Perkins MN and Stone TW (1982) An iontophoretic investigation of the actions of convulsant kynurenines and their interaction with the endogenous excitant quinolinic acid, *Brain Research*, 247(1), pp. 184–187.

Petrenko AG, Ullrich B, Missler M, Krasnoperov V, *et al.* (1996) Structure and Evolution of Neurexophilin, *The Journal of Neuroscience*, 16(14), pp. 4360–4369.

Picelli S, Faridani OR, Björklund ÅK, Winberg G, *et al.* (2014) Full-length RNA-seq from single cells using Smart-seq2, *Nature Protocols*, 9(1), pp. 171–181.

Pollen AA, Nowakowski TJ, Shuga J, Wang X, *et al.* (2014) Low-coverage single-cell

mRNA sequencing reveals cellular heterogeneity and activated signaling pathways in developing cerebral cortex, *Nature Biotechnology*, 32(10), pp. 1053–1058.

Poulin J, Tasic B, Hjerling-Leffler J, Trimarchi JM, *et al.* (2016) Disentangling neural cell diversity using single-cell transcriptomics, *Nature Neuroscience*, 19(9), pp. 1131–1141.

Puopolo M, Raviola E, and Bean BP (2007) Roles of Subthreshold Calcium Current and Sodium Current in Spontaneous Firing of Mouse Midbrain Dopamine Neurons, *Journal of Neuroscience*, 27(3), pp. 645–656.

Redgrave P, Dean P, Mitchell IJ, Odekunle A, *et al.* (1988) The projection from superior colliculus to cuneiform area in the rat, *Experimental Brain Research*, 72(3), p. 537.

Ritchie ME, Phipson B, Wu D, Hu Y, *et al.* (2015) limma powers differential expression analyses for RNA-sequencing and microarray studies, *Nucleic Acids Research*, 43(7), pp. e47–e47.

Roman-Ortiz C, Guevara JA, and Clem RL (2021) GABAergic basal forebrain projections to the periaqueductal gray promote food consumption, reward and predation, *Scientific Reports*, 11(1), p. 22638.

Romanov RA, Zeisel A, Bakker J, Girach F, *et al.* (2017) Molecular interrogation of hypothalamic organization reveals distinct dopamine neuronal subtypes, *Nature Neuroscience*, 20(2), pp. 176–188.

Root DH, Barker DJ, Estrin DJ, Miranda-Barrientos JA, *et al.* (2020) Distinct Signaling by Ventral Tegmental Area Glutamate, GABA, and Combinatorial Glutamate-GABA Neurons in Motivated Behavior, *Cell Reports*, 32(9), p. 108094.

Ross RA, Leon S, Madara JC, Schafer D, *et al.* (2018) PACAP neurons in the ventral premammillary nucleus regulate reproductive function in the female mouse, *eLife*, 7, pp. 1–18.

Sakmann B and Neher E (1984) Patch Clamp Techniques for Studying Ionic Channels in Excitable Membranes, *Annual Review of Physiology*, 46(1), pp. 455–472.

Saliba A-E, Westermann AJ, Gorski SA, and Vogel J (2014) Single-cell RNA-seq: advances and future challenges, *Nucleic Acids Research*, 42(14), pp. 8845–8860.

Samineni VK, Grajales-Reyes JG, Copits BA, O'Brien DE, *et al.* (2017) Divergent Modulation of Nociception by Glutamatergic and GABAergic Neuronal Subpopulations in the Periaqueductal Gray, *eneuro*, 4(2), p. ENEURO.0129-16.2017.

Samineni VK, Grajales-Reyes JG, Sundaram SS, Yoo JJ, *et al.* (2019) Cell type-specific modulation of sensory and affective components of itch in the periaqueductal gray, *Nature Communications*, 10(1), p. 4356.

Sánchez D and Ribas J (1991) Properties and ionic basis of the action potentials in the periaqueductal grey neurones of the guinea-pig, *The Journal of Physiology*, 440(1), pp. 167–187.

Sanchez VB, Ali S, Escobar A, and Cuajungco MP (2019) Transmembrane 163 (TMEM163) protein effluxes zinc, *Archives of Biochemistry and Biophysics*, 677(November), p. 108166.

Schimitel FG, de Almeida GM, Pitol DN, Armini RS, *et al.* (2012) Evidence of a suffocation alarm system within the periaqueductal gray matter of the rat, *Neuroscience*, 200, pp. 59–73.

Schütz MTB, de Aguiar JC, and Graeff FG (1985) Anti-aversive role of serotonin in the dorsal periaqueductal grey matter, *Psychopharmacology*, 85(3), pp. 340–345.

Sebé-Pedrós A, Saudemont B, Chomsky E, Plessier F, *et al.* (2018) Cnidarian Cell Type Diversity and Regulation Revealed by Whole-Organism Single-Cell RNA-Seq, *Cell*, 173(6), pp. 1520-1534.e20.

Semenenko FM and Lumb BM (1992) Projections of anterior hypothalamic neurones to the dorsal and ventral periaqueductal grey in the rat, *Brain Research*, 582(2), pp. 237–245.

Severini C, Improta G, Falconieri-Erspamer G, Salvadori S, *et al.* (2002) The Tachykinin Peptide Family, *Pharmacological Reviews*, 54(2), pp. 285–322.

Shabel SJ, Proulx CD, Piriz J, and Malinow R (2014) GABA/glutamate co-release controls habenula output and is modified by antidepressant treatment, *Science*, 345(6203), pp. 1494–1498.

Shamash P, Carandini M, Harris K, and Steinmetz N (2018) A tool for analyzing electrode tracks from slice histology, *bioRxiv*, p. 447995.

Shapiro E, Biezuner T, and Linnarsson S (2013) Single-cell sequencing-based technologies will revolutionize whole-organism science, *Nature Reviews Genetics*, 14(9), pp. 618–630.

Sherman-Gold R (ed.) (2008) *A Guide to Electrophysiology & Biophysics Laboratory Techniques*. 3rd edn, *The Axon Guide*. 3rd edn. Molecular Devices.

Silva C and McNaughton N (2019) Are periaqueductal gray and dorsal raphe the foundation of appetitive and aversive control? A comprehensive review, *Progress in Neurobiology*, 177(February), pp. 33–72.

Song R, Ro S, and Yan W (2010) In situ hybridization detection of microRNAs, *Methods in molecular biology (Clifton, N.J.)*. Edited by M. Sioud, 629(2), pp. 287–94.

Srinivas S, Watanabe T, Lin CS, William CM, *et al.* (2001) Cre reporter strains produced by targeted insertion of EYFP and ECFP into the ROSA26 locus, *BMC developmental biology*, 1, p. 4.

Stegle O, Teichmann SA, and Marioni JC (2015) Computational and analytical challenges in single-cell transcriptomics, *Nature Reviews Genetics*, 16(3), pp. 133–145.

Streets AM and Huang Y (2014) How deep is enough in single-cell RNA-seq?, *Nature Biotechnology*, 32(10), pp. 1005–1006.

Styrpejko DJ and Cuajungco MP (2021) Transmembrane 163 (TMEM163) Protein: A New Member of the Zinc Efflux Transporter Family, *Biomedicines*, 9(2), p. 220.

Sucher NJ and Deitcher DL (1995) PCR and patch-clamp analysis of single neurons, *Neuron*, 14(6), pp. 1095–1100.

Suchyna TM, Markin VS, and Sachs F (2009) Biophysics and Structure of the Patch and the Gigaseal, *Biophysical Journal*, 97(3), pp. 738–747.

Sureshkumar K, Saenz A, Ahmad SM, and Lutfy K (2021) The PACAP/PAC1 Receptor System and Feeding, *Brain Sciences*, 12(1), p. 13.

Svensson V, Natarajan KN, Ly L-H, Miragaia RJ, *et al.* (2017) Power analysis of single-cell RNA-sequencing experiments, *Nature Methods*, 14(4), pp. 381–387.

Svensson V, Vento-Tormo R, and Teichmann SA (2018) Exponential scaling of single-cell RNA-seq in the past decade, *Nature Protocols*, 13(4), pp. 599–604.

Tan CL, Cooke EK, Leib DE, Lin Y-C, *et al.* (2016) Warm-Sensitive Neurons that Control Body Temperature, *Cell*, 167(1), pp. 47-59.e15.

Tanaka Yasuyo, Tanaka Yasuhiro, Furuta T, Yanagawa Y, *et al.* (2008) The effects of cutting solutions on the viability of GABAergic interneurons in cerebral cortical slices of adult mice, *Journal of Neuroscience Methods*, 171(1), pp. 118–125.

Tang F, Barbacioru C, Wang Y, Nordman E, *et al.* (2009) mRNA-Seq whole-transcriptome analysis of a single cell, *Nature Methods*, 6(5), pp. 377–382.

Tasic B, Menon V, Nguyen TN, Kim TK, *et al.* (2016) Adult mouse cortical cell taxonomy revealed by single cell transcriptomics, *Nature Neuroscience*, 19(2), pp. 335–346.

Tasic B, Yao Z, Graybuck LT, Smith KA, *et al.* (2018) Shared and distinct transcriptomic cell types across neocortical areas, *Nature*, 563(7729), pp. 72–78.

The Tabula Muris Consortium (2018) Single-cell transcriptomics of 20 mouse organs creates a Tabula Muris, *Nature*, 562(7727), pp. 367–372.

Ting JT, Daigle TL, Chen Q, and Feng G (2014) Acute brain slice methods for adult and aging animals: Application of targeted patch clamp analysis and optogenetics, in Martina, M. and Taverna, S. (eds) *Methods in Molecular Biology*. New York, NY: Springer New York (Methods in Molecular Biology), pp. 221–242.

Ting JT, Kalmbach B, Chong P, De Frates R, *et al.* (2018) A robust ex vivo experimental platform for molecular-genetic dissection of adult human neocortical cell types and circuits, *Scientific Reports*, 8(1), p. 8407.

Ting JT, Lee BR, Chong P, Soler-Llavina G, *et al.* (2018) Preparation of Acute Brain Slices Using an Optimized N-Methyl-D-glucamine Protective Recovery Method, *Journal of visualized experiments : JoVE*, (132), pp. 1–13.

Torre E, Dueck H, Shaffer S, Gospocic J, *et al.* (2018) Rare Cell Detection by Single-Cell RNA Sequencing as Guided by Single-Molecule RNA FISH, *Cell Systems*, 6(2), pp. 171-179.e5.

Tovote P, Esposito MS, Botta P, Chaudun F, *et al.* (2016) Midbrain circuits for

defensive behaviour, *Nature*, 534(7606), pp. 206–212.

Tripathy SJ, Toker L, Li B, Crichlow C-L, *et al.* (2017) Transcriptomic correlates of neuron electrophysiological diversity, *PLOS Computational Biology*. Edited by J. Ayers, 13(10), p. e1005814.

Tschida K, Michael V, Takatoh J, Han B-X, *et al.* (2019) A Specialized Neural Circuit Gates Social Vocalizations in the Mouse, *Neuron*, 103(3), pp. 459-472.e4.

Tyson AL, Vélez-Fort M, Rousseau C V., Cossell L, *et al.* (2022) Accurate determination of marker location within whole-brain microscopy images, *Scientific Reports*, 12(1), p. 867.

Vaaga CE, Brown ST, and Raman IM (2020) Cerebellar modulation of synaptic input to freezing-related neurons in the periaqueductal gray, *eLife*, 9, pp. 1–28.

Vale R, Campagner D, Iordanidou P, Pavón Arocas O, *et al.* (2020) A cortico-collicular circuit for accurate orientation to shelter during escape, *bioRxiv* [Preprint].

Vale R, Evans DA, and Branco T (2017) Rapid Spatial Learning Controls Instinctive Defensive Behavior in Mice, *Current Biology*, 27(9), pp. 1342–1349.

Vallejos CA, Risso D, Scialdone A, Dudoit S, *et al.* (2017) Normalizing single-cell RNA sequencing data: challenges and opportunities, *Nature Methods*, 14(6), pp. 565–571.

Verstegen AMJ, Klymko N, Zhu L, Mathai JC, *et al.* (2019) Non-Crh Glutamatergic Neurons in Barrington's Nucleus Control Micturition via Glutamatergic Afferents from the Midbrain and Hypothalamus, *Current Biology*, 29(17), pp. 2775-2789.e7.

Vianna DML and Brandão ML (2003) Anatomical connections of the periaqueductal gray: specific neural substrates for different kinds of fear, *Brazilian Journal of Medical and Biological Research*, 36(5), pp. 557–566.

Virtanen P, Gommers R, Oliphant TE, Haberland M, *et al.* (2020) SciPy 1.0: fundamental algorithms for scientific computing in Python, *Nature Methods*, 17(3), pp. 261–272.

Vong L, Ye C, Yang Z, Choi B, *et al.* (2011) Leptin Action on GABAergic Neurons Prevents Obesity and Reduces Inhibitory Tone to POMC Neurons, *Neuron*,

71(1), pp. 142–154.

Walton K and O'Connor BP (2018) Optimized Methodology for the Generation of RNA-Sequencing Libraries from Low-Input Starting Material: Enabling Analysis of Specialized Cell Types and Clinical Samples, in, pp. 175–198.

Wang J and Song Y (2017) Single cell sequencing: a distinct new field, *Clinical and Translational Medicine*, 6(1), p. 10.

Wang Q, Ding S-L, Li Y, Royall J, *et al.* (2020) The Allen Mouse Brain Common Coordinate Framework: A 3D Reference Atlas, *Cell*, 181(4), pp. 936-953.e20.

Wang Z, Gerstein M, and Snyder M (2009) RNA-Seq: a revolutionary tool for transcriptomics, *Nature Reviews Genetics*, 10(1), pp. 57–63.

Watson TC, Cerminara NL, Lumb BM, and Apps R (2016) Neural Correlates of Fear in the Periaqueductal Gray, *The Journal of Neuroscience*, 36(50), pp. 12707–12719.

Vander Weele CM, Siciliano CA, Matthews GA, Namburi P, *et al.* (2018) Dopamine enhances signal-to-noise ratio in cortical-brainstem encoding of aversive stimuli, *Nature*, 563(7731), pp. 397–401.

Weiler S, Bauer J, Hübener M, Bonhoeffer T, *et al.* (2018) High-yield in vitro recordings from neurons functionally characterized in vivo, *Nature Protocols*, 13(6), pp. 1275–1293.

Wilfinger WW, Mackey K, and Chomczynski P (1997) Effect of pH and Ionic Strength on the Spectrophotometric Assessment of Nucleic Acid Purity, *BioTechniques*, 22(3), pp. 474–481.

Xie Z, Wang M, Liu Z, Shang C, *et al.* (2021) Transcriptomic encoding of sensorimotor transformation in the midbrain, *eLife*, 10, pp. 1–34.

Xu C and Su Z (2015) Identification of cell types from single-cell transcriptomes using a novel clustering method, *Bioinformatics*, 31(12), pp. 1974–1980.

Yilmaz M and Meister M (2013) Rapid Innate Defensive Responses of Mice to Looming Visual Stimuli, *Current Biology*, 23(20), pp. 2011–2015.

Yoo JH, Zell V, Gutierrez-Reed N, Wu J, *et al.* (2016) Ventral tegmental area glutamate neurons co-release GABA and promote positive reinforcement, *Nature Communications*, 7(1), p. 13697.

Yu H, Xiang X, Chen Z, Wang Xu, *et al.* (2021) Periaqueductal gray neurons encode

the sequential motor program in hunting behavior of mice, *Nature Communications*, 12(1), p. 6523.

Zeisel A, Hochgerner H, Lönnerberg P, Johnsson A, *et al.* (2018) Molecular Architecture of the Mouse Nervous System, *Cell*, 174(4), pp. 999-1014.e22.

Zeng H and Sanes JR (2017) Neuronal cell-type classification: challenges, opportunities and the path forward, *Nature Reviews Neuroscience*, 18(9), pp. 530–546.

Zhang L, Hernandez VS, Gerfen CR, Jiang SZ, *et al.* (2021) Behavioral role of PACAP signaling reflects its selective distribution in glutamatergic and GABAergic neuronal subpopulations, *eLife*, 10, pp. 1–77.

Zheng GXY, Terry JM, Belgrader P, Ryvkin P, *et al.* (2017) Massively parallel digital transcriptional profiling of single cells, *Nature Communications*, 8(1), p. 14049.

Zhong P, Zhang Z, Barger Z, Ma C, *et al.* (2019) Control of Non-REM Sleep by Midbrain Neurotensinergic Neurons, *Neuron*, 104(4), pp. 795-809.e6.

Ziegenhain C, Vieth B, Parekh S, Reinius B, *et al.* (2017) Comparative Analysis of Single-Cell RNA Sequencing Methods, *Molecular Cell*, 65(4), pp. 631-643.e4.